



저작자표시-비영리-변경금지 2.0 대한민국

이용자는 아래의 조건을 따르는 경우에 한하여 자유롭게

- 이 저작물을 복제, 배포, 전송, 전시, 공연 및 방송할 수 있습니다.

다음과 같은 조건을 따라야 합니다:



저작자표시. 귀하는 원저작자를 표시하여야 합니다.



비영리. 귀하는 이 저작물을 영리 목적으로 이용할 수 없습니다.



변경금지. 귀하는 이 저작물을 개작, 변형 또는 가공할 수 없습니다.

- 귀하는, 이 저작물의 재이용이나 배포의 경우, 이 저작물에 적용된 이용허락조건을 명확하게 나타내어야 합니다.
- 저작권자로부터 별도의 허가를 받으면 이러한 조건들은 적용되지 않습니다.

저작권법에 따른 이용자의 권리는 위의 내용에 의하여 영향을 받지 않습니다.

이것은 [이용허락규약\(Legal Code\)](#)을 이해하기 쉽게 요약한 것입니다.

[Disclaimer](#)

Thesis for Ph. D. degree

**Measurements of Sea Ice Thickness using
Polarimetric Radar Systems**

다중편파 레이더 시스템을 이용한

해빙두께 측정

Jin-Woo Kim

February 2014

School of Earth and Environmental Sciences

Graduate School

Seoul National University

Measurements of Sea Ice Thickness using Polarimetric Radar Systems

다중편파 레이더 시스템을 이용한
해빙두께 측정

지도교수 김 덕 진

이 논문을 이학박사 학위논문으로 제출함

2013 년 12월

서울대학교 대학원
지구환경과학부

김 진 우

김진우의 이학박사 학위论문을 인준함

2014 년 02월

위 원 장 _____ 안 진 호 _____ (인)

부위원장 _____ 김 덕 진 _____ (인)

위 원 _____ 오 이 석 _____ (인)

위 원 _____ 이 훈 열 _____ (인)

위 원 _____ 김 상 완 _____ (인)

Abstract

This thesis presents an overview of the interactions between microwaves and physical properties of sea ice and snow, such as the dielectric constant and surface roughness, in order to successfully measure sea ice thickness from polarimetric radar systems. Using a ground-based scatterometer system and various microwave scattering models, polarimetric backscattered signatures from sea ice and snow were investigated as evidence of the evolution of the physical properties during the freezing and melting seasons. Based on these results, the optimum method for measuring the thickness of sea ice covered with snow using polarimetric SAR data was explored via numerical simulations and experimental measurements.

Experiments conducted using the ground-based scatterometer system as well as the in-situ measurements showed that most of the polarimetric signatures (C-band) with relatively high incidence angles (i.e., about 40°) can be backscattered from the interface between snow cover on sea ice and the surface of the sea ice over the freezing season. Microwaves can penetrate the snow cover during this season owing to the lower dielectric properties of the snow cover (about 1.25). Conversely, the signatures were predominantly backscattered from the surface of the snow cover during the melting season due to high dielectric properties induced by surface melting water. For the freezing season, the in-situ measurements and numerical simulations showed that the number of polarimetric signatures backscattered within the sea ice volume can increase with sea ice growth due to evolutions of the dielectric

properties induced by the desalination process, and the surface roughness of sea ice can increase with sea ice growth due to superimposed and ridging processes. Based on these observations, the relationship between the depolarization effects of polarimetric signatures (C- and X-band) and sea ice thickness was investigated using various numerical simulations and a case study. A strong correlation was found between the in-situ sea ice thickness and the SAR-derived depolarization factors (i.e., the co-polarized correlation and cross-polarized ratio). These results clearly demonstrate a one-to-one relationship between the thickness and the depolarization factors, which further suggests that the depolarization factors could be effective parameters in measuring the thickness of snow-covered sea ice with space-borne polarimetric SAR data.

Keywords: Sea ice thickness, snow cover, polarimetric SAR, depolarization effect, scattering signatures, dielectric constant, surface roughness, freezing season

Student Number: 2008-30820

Table of Contents

| | |
|---|-----------|
| Chapter 1. Introduction | 1 |
| 1.1. Overview | 1 |
| 1.2. Remote sensing of ice and snow | 3 |
| 1.3. Motivation and Objectives of this thesis | 11 |
| Chapter 2. Polarimetric microwave remote sensing systems | 13 |
| 2.1. Ground Based POLarimetric SCATterometer (GB-POLSCAT) | 13 |
| A. Set-up of GB-POLSCAT..... | 14 |
| B. System calibration of GB-POLSCAT | 16 |
| B.1. Basic concept of the system calibration | 16 |
| B.2. Conventional system calibration | 18 |
| C. New system calibration of GB-POLSCAT..... | 21 |
| C.1. Background | 21 |
| C.2. New technique to extract radar distortions..... | 21 |
| C.3. Validation using field experiments and numerical simulation | 21 |
| 2.2. Space-borne SAR systems | 30 |
| A. RADARSAT-2 and TerraSAR-X..... | 30 |
| B. Radiometric calibration of the SAR systems..... | 33 |
| B.1. Background | 33 |
| B.2. Backscattering coefficient computation of TerraSAR-X and RADARSAT-2..... | 33 |
| Chapter 3. Polarimetric signatures characterized by scattering features from sea ice and snow..... | 42 |
| 3.1. Background | 42 |
| 3.2. Polarimetric scattering features of snow | 49 |
| A. Dielectric properties of snow | 49 |
| B. The scattering features from snow..... | 55 |

| | |
|--|------------|
| 3.3. Polarimetric scattering features of sea ice | 63 |
| A. Dielectric properties of sea ice | 63 |
| B. Surface roughness of sea ice..... | 70 |
| C. The scattering features from sea ice | 74 |
| 3.4. Depolarization effects based on the polarimetric scattering features of sea ice | 76 |
| A. Numerical experiments of the depolarization effects due to surface scattering from rough surface..... | 78 |
| B. Numerical experiments of the depolarization effects due to volume scattering within sea ice layer | 83 |
| C. Field experiments of the depolarization effects due to volume scattering within ice layer | 92 |
| Chapter 4. Measurement of sea ice thickness using space-borne SAR data in the Arctic Ocean | 102 |
| 4.1. In-situ measurements and SAR data acquisition..... | 102 |
| 4.2. Depolarization-to-sea ice thickness relationship using space-borne SAR data | 108 |
| Chapter 5. Conclusion..... | 111 |
| 5.1. Summary | 111 |
| 5.2. Discussion | 113 |
| Appendix | 115 |
| Reference | 127 |

List of Figures

| | |
|---|----|
| Figure 1. Classification of ice and snow at the cryosphere. [From ESA] | 7 |
| Figure 2. The spatial distribution land and sea ice in the polar region. | 8 |
| Figure 3. Abedo of ice, snow, ocean water, and vegetation and dark soil on the earth..... | 9 |
| Figure 4. Average monthly Arctic sea ice extent from Jan 1979 to 2010. [From NSIDC] .. | 10 |
| Figure 5. Change rate of the ice thickness in the Antarctic ice shelf from 2003 to 2008. [Prichard et al, 2012] | 10 |
| Figure 6. (a) External parts of the GB-POLSCAT system developed by SNU (b) Structures of the circuit. | 15 |
| Figure 7. Geometry and block diagram of Polarimetric Radar System (PRS. P is the power generated by PRS. The superscript of P denotes direction of power transmission (e.g., t: transmitted or r: received direction). The subscript of P denotes a sequence of power transmission. [S] is a scattering matrix. The superscript of [S] denotes RPI or a point calibration target. G denotes the antenna gain. r is the distance between the antenna and a point calibration target..... | 26 |
| Figure 8. The measured radar response of the PRS in the anechoic chamber..... | 27 |
| Figure 9. Active distortion estimated from field experiments. | 28 |
| Figure 10. Comparison between simulated and measured backscattering coefficients. | 29 |
| Figure 11. Various imaging modes of the space-borne SAR systems (a) TerraSAR-X (b) RADARSAT-2. [From DLR and MDA]..... | 32 |
| Figure 12. Estimated radar brightness of acquired TerraSAR-X. (a) HH (b) VV..... | 38 |
| Figure 13. Estimated backscattering coefficients of acquired TerraSAR-X data. (a) HH (b) VV | 39 |
| Figure 14. Estimated radar brightness of acquired RADARSAT-2 data. (a) HH (b) HV | 40 |
| Figure 15. Estimated backscattering coefficients of acquired RADARSAT-2 data. (a) HH (b) HV | 41 |
| Figure 16. Variations of sea ice extent for the melting and freezing season. (a) Arctic sea ice (b) Antarctic sea ice | 46 |

| | |
|---|----|
| Figure 17. Life cycles of sea ice..... | 47 |
| Figure 18. Scattering structures of sea ice and snow. | 48 |
| Figure 19. Test site of Strozzi’s measurements..... | 51 |
| Figure 20. (a) measured air temperature and (b) snow density for the melting and freezing seasons. [Strozzi, 1996]..... | 53 |
| Figure 21. Comparison of observed dielectric constant (real) of snow surface and simulated dielectric constant (real) for the melting (red box) and freezing (blue box) season. | 54 |
| Figure 22. Scheme of scattering structures from snow cover in the GB-POLSCAT measurements. | 59 |
| Figure 23. Normalized scattering intensity from snow cover with Strozzi’s data for the melting and freezing season (Incidence angle: 10°). | 60 |
| Figure 24. Normalized scattering intensity from snow cover with Strozzi’s data for the melting and freezing season (Incidence angle: 40°). | 61 |
| Figure 25. Measurement site of the ice buoy (top) and structures of the ice buoy (bottom) [from Prof. Hajo Eicken’s homepage at Alaska University]..... | 67 |
| Figure 26. (a) the salinity profiles of FYI for the freezing season (red line a-d denote averaged salinity profiles as FYI grows, and blue line is averaged salinity profile of MYI in [51]) (b) the salinity profiles of MYI for the freezing season. From MYI A to MYI D, the thickness are gradually increased [61]. | 68 |
| Figure 27. Dielectric constant (real and imaginary parts) and penetration depth as a function of sea ice thickness for C- and X-band frequencies. Left Y-axis represents the values of dielectric constant (black: real part, gray: imaginary part) and right Y-axis represents penetration depth. (a) C-band (b) X-band..... | 69 |
| Figure 28. Cross-sectional view of FYI (left) and MYI (right) during the sea ice growing season. The lower bottom photographs show typical scenes of the corresponding sea ice type. | 72 |
| Figure 29. Distributions of FYI and FYI in [69]. (a) FYI (b) MYI..... | 73 |
| Figure 30. The distribution of backscattering coefficients from FYI and MYI [70] (red real line: rough FYI, red dotted line: smooth FYI, blue real line:rough MYI, and blue dotted line: smooth MYI). | 75 |
| Figure 31. The variation of cross-polarized ratio (HV/HH) as a function of RMS height (small-scale roughness) for the C- and X-band. | 81 |
| Figure 32. The variation of depolarization factors (cross polarized ratio) as a function of | |

surface slope width (large-scale surface roughness) for the dielectric constants of thick FYI and MYI using extended-Bragg model. 82

Figure 33. Set-up of VRT model simulation. (a) flat surface (only volume scattering) (b) relatively rough surface as sea ice grows (surface + volume scattering). 85

Figure 34. In the VRT simulation, dielectric constant (real and imaginary parts) and penetration depth as a function of sea ice thickness (i.e. 0.1 ~ 5 m) for C- and X-band frequencies. Left Y-axis represents the values of dielectric constant (black: real part, gray: imaginary part) and right Y-axis represents penetration depth. 86

Figure 35. Backscattering coefficients (C-band) simulated by the VRT (Case 1, only volume scattering) as sea ice grows (red: VV, blue: HH, and green: VH). (a) incidence angle: 20° (b) incidence angle: 40° 87

Figure 36. Backscattering coefficients (X-band) simulated by the VRT (Case 1, only volume scattering) as sea ice grows (red: VV, blue: HH, and green: VH). (a) incidence angle: 20° (b) incidence angle: 40° 88

Figure 37. Backscattering coefficients (C-band) simulated by the VRT (Case 2, surface and volume scattering) as sea ice grows. Real line denotes simulated value by surface scattering, and dotted line denotes simulated value by volume scattering (red: VV, blue: HH, and green: VH). (a) incidence angle: 20° (b) incidence angle: 40° 89

Figure 38. Backscattering coefficients (X-band) simulated by the VRT (Case 2, surface and volume scattering) as sea ice grows. Real line denotes simulated value by surface scattering, and dotted line denotes simulated value by volume scattering (red: VV, blue: HH, and green: VH). (a) incidence angle: 20° (b) incidence angle: 40° 90

Figure 39. The relationship between depolarization factor (VH/VV) simulated by case 1 and 2 experiments and sea ice thickness. (a) C-band (case 1) (b) C-band (case 2) (c) X-band (case 1) (d) X-band (case 2). 91

Figure 40. GB-POLSCAT measurement of artificially frozen ice. 94

Figure 41. The measured backscattered signatures from the ice (blue real line: HH, red real line: VV). The green and black dotted line denotes the backscattered signatures from metal plate on the antenna aperture and the ice surface, respectively. 95

Figure 42. Refraction of microwave at the interface between the air and the ice based on Snell's law. 96

Figure 43. The backscattered signatures from the ice at 0°, 20°, and 40° of incidence angle. (the ice thickness = 140 cm) 98

Figure 44. The backscattered signatures from the ice at 0°, 20°, and 40° of incidence angle. (the ice thickness = 190 cm) 99

Figure 45. The normalized magnitude of surface, volume, and bottom-surface scattering from the ice at 0°, 20°, and 40° of incidence angle. 100

Figure 46. Study area off the northern coast of Greenland. The TerraSAR-X data was acquired on May 2, 2009 (black solid square). Two RADARSAT-2 data were acquired on April 28, 2009 (dotted blue square) and on April 30, 2009 (dotted red square), respectively. Ground truth data were obtained on May 01, 2009 (black star). The red line shown in lower left photograph represents the validation line on which the sea ice thickness and snow depth were measured using an EM31 instrument. 104

Figure 47. Sea ice thickness profile measured by the EM31 along the validation line (smooth thick FYI: 0~580 m, rubble MYI: 580~1500 m). 105

Figure 48. Radiometrically and geometrically calibrated SAR images (backscattering coefficients) of TerraSAR-X and RADARSAT-2. The yellow dots indicated in each figure represent the positions where sea ice thickness and snow depth were measured. 106

Figure 49. Relationship between the depolarization factors and observed sea ice thickness. (a) TerraSAR-X (5/02) (b) RADARSAT-2 (4/28) (c) RADARSAT-2 (4/30)110

Figure 50. Scattering structures of VRT model simulation. (a) surface scattering (b) volume scattering (c) bottom-surface scattering 124

Figure 51. Volume scattering structure of VRT simulation. (a)-(c) first order solution (d)-(e) second order solution..... 125

Figure 52. Geometry of incident and scattered angle at the each layer for VRT simulation. 126

List of Tables

| | |
|---|-----|
| Table 1. Global distribution of land and sea ice. | 8 |
| Table 2. Specifications of RADARSAT-2 and TerraSAR-X..... | 31 |
| Table 3. Specifications of Strozzi's measurements..... | 52 |
| Table 4. Averaged scattering intensities from snow cover for the freezing season..... | 62 |
| Table 5. Averaged scattering intensities from snow cover for the melting season..... | 62 |
| Table 6. The specifications of the GB-POLSCAT measurement. | 94 |
| Table 7. The estimated cross polarized ratio in the case studies. | 101 |
| Table 8. Specifications of acquired TerraSAR-X and RADARSAT-2..... | 107 |

Acronyms

| | |
|-------------------|--|
| | Antarctic Peninsular |
| AT | Active Transponder |
| ATM | Airborne Topographic Mapper |
| BCR | Backscattering Coefficient Ratio |
| CCT | Constrained Calibration Technique |
| CSA | Canadian Space Agency |
| CTD | Conductivity-Temperature-Depth |
| DLR | German aerospace center |
| DMI | Danish Meteorological Institute |
| DTU | Danish Technological University |
| EADS | Defense And Space Company |
| FYI | First Year Ice |
| GB-POLSCAT | Ground Based POLarimetric SCATterometer |
| GCT | Generalized Calibration Technique |
| GO | Geometrical Optics |
| GPR | Ground Penetrating Radar |
| HH | Horizontal Transmit, Horizontal Receive (Polarization) |
| HV | Horizontal Transmit, Vertical Receive (Polarization) |
| IEM | Integral Equation Method |
| MCDW | Modified Circumpolar Deep Water |

| | |
|--------------|--|
| MODIS | Moderate Resolution Imaging Spectrometer |
| MYI | Multi Year Ice |
| NA | Network Analyzer |
| NRCS | Normalized Radar Cross Section |
| OMT | OrthoMode Transducer |
| PO | Physical Optics |
| RCS | Radar Cross Section |
| RMS | Root Mean Square |
| RPI | Returned signal from Point of Interest |
| RRA | National Radio Research Agency |
| SAR | Synthetic Aperture Radar |
| SNR | Signal-to-Noise Ratio |
| SNU | Seoul National University |

Chapter 1. Introduction

1.1. Overview

The cryosphere comprises all parts of the earth including frozen water, ice, and snow cover [1]. Based on the origin, ice in the cryosphere can be divided into land ice and sea ice. Land ice represents frozen freshwater and/or snow on the earth's surface, and sea ice is frozen, salty ocean water. By definition, land ice can be additionally classified as glacier, ice sheet, river, and lake ice, or as permafrost. A glacier is a huge ice mass formed by accumulated and frozen snow on land over many years. An ice sheet is a mass of glacier ice with an area that is greater than 50,000 km²; this is also known as a continental glacier. Lake and river ice, and permafrost refer to lake, river, or soil surfaces that remain frozen for two or more years. All glaciers and ice sheets flow due to gravitational forces; when these formations pass through a coastline, they float on the sea surface. The floating ice is called an "ice shelf," and its parts are broken off due to various mechanisms, such as ocean tides and surface melt-water propagation. The broken ice masses are called "icebergs" (Figure 1).

Land and sea ice are mostly distributed within the polar region of the cryosphere (Figure 2). Indeed, the areas of the land ice of Antarctica and Greenland are 1.36×10^{13} and 1.73×10^{12} m², respectively. These represent 86% and 11% of the total area of land ice (1.58×10^{13} m²) [2]. In the case of sea ice, although areas of Arctic and Antarctic sea ice have strong seasonal variation, the averaged maximum area of

Arctic and Antarctic sea ice in the winter season is 1.5×10^{11} and 1.8×10^{13} m², respectively, and the minimum area of those regions in summer season is 7×10^{10} and 3×10^{10} m², respectively [3]. Table 1.1 summarizes the global distribution of land and sea ice.

Surfaces of land ice, sea ice, and snow have high reflectivity for incoming solar radiation (Figure 3). For example, the reflectivities (or albedos) of the ice and snow, ocean water, and vegetation and dark soil is from 85 to 90%, 10%, and 20%, respectively [4]. The reflectivity of ice and snow, therefore, is about four times more than the others (Table 1). Besides, the reflectivity of the ice and snow depends upon spectral band, the ice and snow thickness, and surface temperature [5]. Therefore, the spatial distributions of the formations (e.g., their physical extents and/or thickness) are important factors in understanding the thermal feedback process between the sun and the earth. The spatial distribution of the ice and snow has rapidly changed due to global warming over the past decades with the melting of sea ice [6] (Figure 4) and the retreat and thinning of ice shelves [7] (Figure 5); this decline is occurring faster than is predicted by current climate models [8]. Climate models predict a continued and possibly accelerated decline in the ice extent, leading to an ice-free summer in the Arctic within this century [9] or even within the next thirty years [10]. Thus, there is an increasing need for accurate modeling and observation of the spatial distribution of the ice and snow, in order to improve predictions for future global climate change.

Study and monitoring of the changes in the cryosphere is both laborious and scientifically challenging due to extreme environment. For example, direct

measurement of the ice and snow thickness can be made by drilling a hole through the ice and snow or by using electromagnetic induction systems such as the EM-31 and Ground Penetrating Radar (GPR) [11], [12]. Although these methods are accurate, they are time consuming and limited in space due to the intense weather conditions of the polar region. An autonomous ice mass balance buoy can facilitate long-term measurement of the ice and snow thickness and offer insights into the governing processes, but spatial coverage is limited. However, various air- and space-borne remote sensing techniques are useful tools for monitoring the changes temporally and spatially. Various air- and space-borne remote sensing techniques have been developed since the early 1900s. The next section of this thesis provides an overview of air- and space-borne remote sensing techniques in exploring the cryosphere.

1.2. Remote sensing of ice and snow

Expeditions to the polar region using air-borne remote sensing techniques began in the early 1900s. Mittelholzer et al. (1925) [13] discussed a glacier formation using aerial photography in Spitzbergen islands in the Svalbard archipelago to the east of northern Greenland. Wilkins (1929) [14] showed ice cover in the Antarctic Peninsula (AP) using aerial photography (i.e. a folding Kodak 3A camera). Although experiments were conducted in these challenging conditions, with great skill and considerable risk, many scientific problems await solution.

In the early 1960s, the first operational space-borne optical imaging instruments

(i.e. CORONA, ARGON, and LANYARD) were developed for both detailed reconnaissance and regional mapping [15]-[17]. These systems allowed polar researchers to acquire global scale optical imaging data covering the cryosphere. The data could be used to identify local fluctuations in glacier termini [18] and large-scale flow features on ice sheets [19]; these properties have been monitored in greater detail with the development of space-borne optical imaging instruments such as Landsat, Moderate Resolution Imaging Spectrometer (MODIS), Geoeye-1, and etc. However, the remote sensing techniques based on these systems fail to resolve the problems. Long polar nights and frequent cloudy weather conditions at the high latitudes of the cryosphere hinder the measuring activities of the systems.

Given these limitations, we consider the use of microwaves, which can penetrate through cloud, dust, and rainfall because of their long wavelengths; additionally, active microwave remote sensing can observe during both day and night since its sensors generate source power. Thus, microwave remote sensing has been widely used to monitor changes in the cryosphere. For example, space-borne microwave scatterometer and radiometer systems (e.g., QuikSCAT, Seasat-A, ERS-1/2, ADEOS-1/2, SSM/I, and AMSR-E) have been used to derive sea ice extent, concentration, and motion [18]-[20]. However, these instruments do not have high resolution capability, while space-borne Synthetic Aperture Radar (SAR) instruments (e.g., RADARSAT-1, ERS -1 and -2, and Envisat) have enhanced resolution capability. Thus, these instruments have been used to generate high resolution mapping of the sea ice edge and icebergs, and they estimate the current velocity of ice sheets using interferometric methods [21]-[22]. However, these

techniques provide only horizontal information of the spatial distribution of the cryosphere.

It was suggested that microwaves can penetrate the ice and snow due to their dielectric properties (i.e., loss factors) [23]. This suggestion proved to be a prelude to exploring vertical properties of the ice and/or snow, such as thickness and internal structure. Indeed, Waite and Schmidt (1962) [24] led the first experiments to measure the thickness of ice sheets in Antarctica and Greenland using the air-borne radar altimeter system (frequencies: 110, 220, 440, and 4300 MHz). The basic principle used to measure the ice thickness and/or snow depth is that the travel time of a radar pulse (of an appropriate wave speed) between the surface and bottom of the ice and/or snow can be converted into the distance, allowing those values to be determined. These fundamental techniques contributed to the development of space-borne radar altimeter systems such as the ERS 1/2, GEOSAT, Cryosat 1/2, etc. In addition, air- and space-borne laser altimeter systems have been developed using principles similar to those of the radar altimeter systems (i.e., ICESat, Airborne Topographic Mapper (ATM) [flown as part of the IceBridge Campaign]), in order to verify surface profiles of the ice and/or snow with greater accuracy [25]-[29].

Although the altimeter systems have successfully observed the thickness of ice sheets, lake ice, and snow, measurement of sea ice thickness is an issue that has not yet been resolved. The scattering structures of microwaves from sea ice are relatively more complicated than those of land ice and snow, because the dielectric properties of sea ice vary due to the varying stages of sea ice growth. Therefore, it is difficult to interpret various scattering structures (e.g., surface and volume scattering) of

microwaves from sea ice, and many studies attempt to resolve this issue.

Ice and snow of the Cryosphere

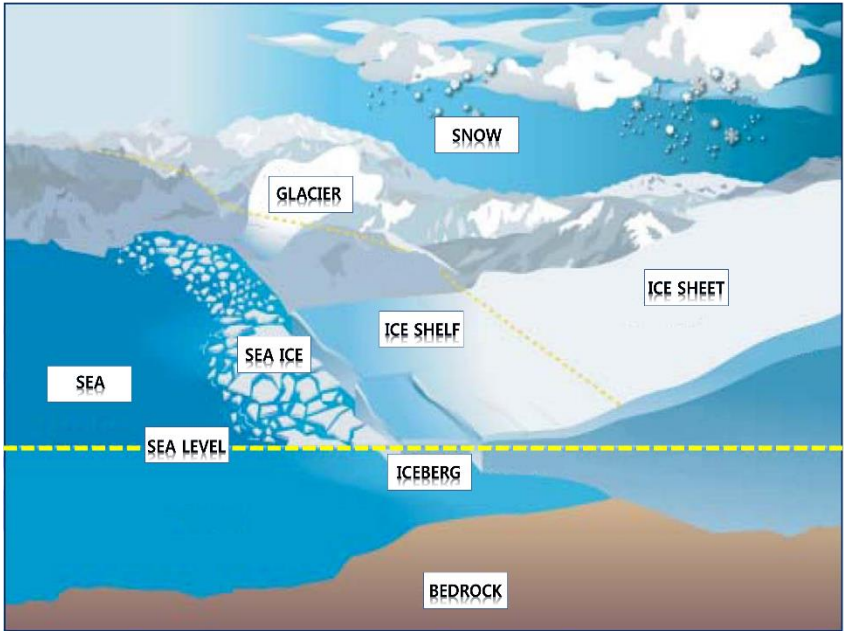


Figure 1. Classification of ice and snow at the cryosphere. [From ESA]



Figure 2. The spatial distribution land and sea ice in the polar region.

Table 1. Global distribution of land and sea ice.

| Global distribution of ice | | | | | |
|----------------------------|-------------------------|-------------|-----------|---------------|------------------------|
| Land ice | | | Sea ice | | |
| Region | Area (m ²) | Portion (%) | Region | Max./Min. | Area (m ²) |
| Antarctica | 1.36 x 10 ¹³ | 86 | Arctic | Max. (Winter) | 1.5 x 10 ¹¹ |
| Greenland | 1.73 x 10 ¹² | 11 | | Min. (Summer) | 7 x 10 ¹⁰ |
| Remainder | 5 x 10 ¹¹ | 3 | Antarctic | Max. (Winter) | 1.8 x 10 ¹¹ |
| Total | 1.58 x 10 ¹³ | 100 | | Min. (Summer) | 3 x 10 ¹⁰ |

Albedo of the earth

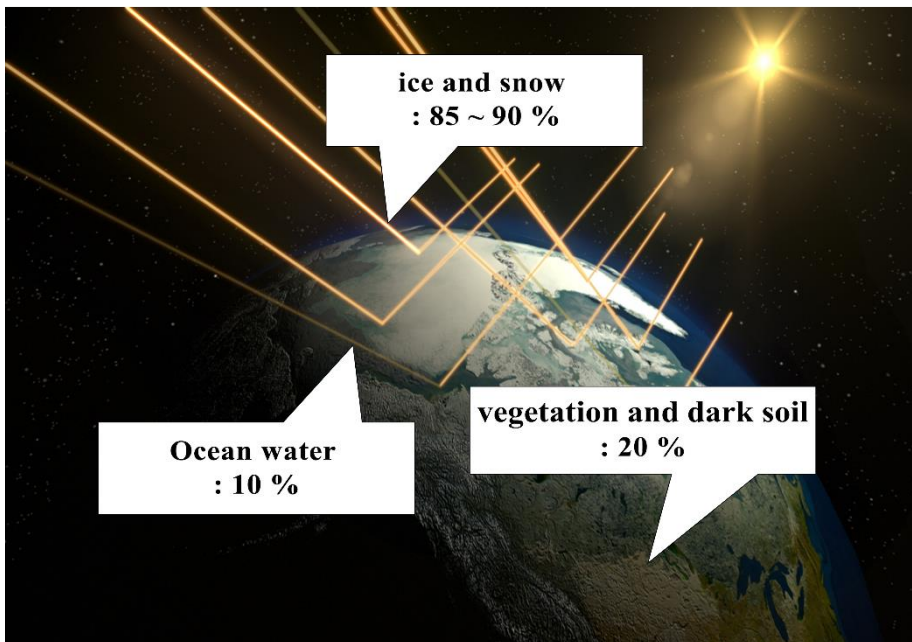


Figure 3. Albedo of ice, snow, ocean water, and vegetation and dark soil on the earth.

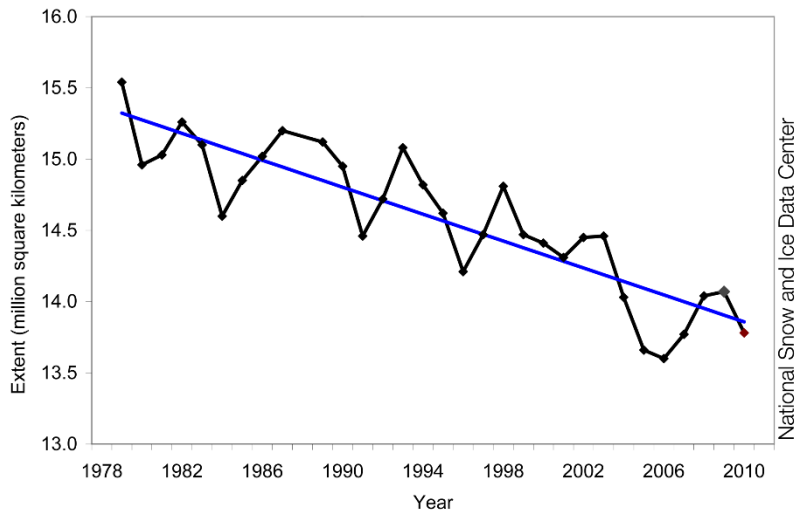


Figure 4. Average monthly Arctic sea ice extent from Jan 1979 to 2010. [From NSIDC]

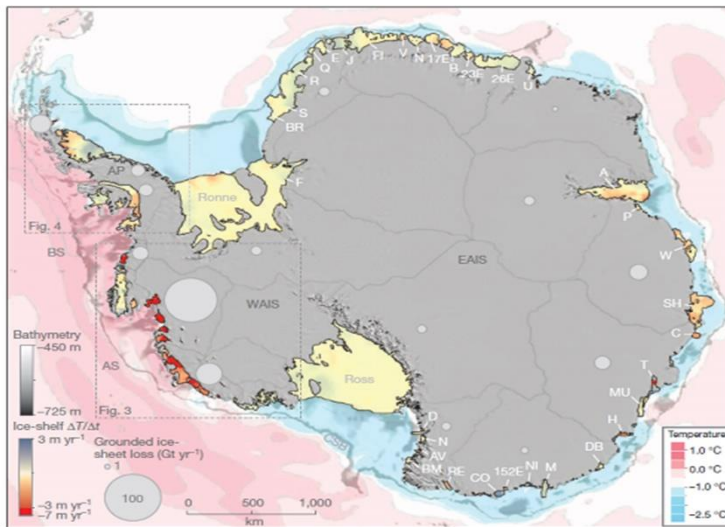


Figure 5. Change rate of the ice thickness in the Antarctic ice shelf from 2003 to 2008. [Prichard et al, 2012]

1.3. Motivation and Objectives of this thesis

The latest space-borne SAR (e.g., RADARSAT-2 and TerraSAR-X) systems offer high-resolution (up to 1 m) full polarimetric SAR data. These capabilities allow us to interpret scattering structures of microwaves using various polarimetric target decomposition methods [30]-[32]. Therefore, the latest space-borne SAR data have good potential to measure sea ice thickness with their polarimetric capabilities. An efficient method for measuring sea ice thickness can be developed if the interactions between sea ice and microwaves can be interpreted using this capability.

In this thesis, efficient methods to measure sea ice thickness using space-borne polarimetric SAR data were explored based on the interpretation of various scattering structures from sea ice and snow. A ground-based scatterometer, which can measure the return radar signals from sea ice and snow in the field, was developed in order to practically interpret the scattering structures of microwaves from sea ice and snow, and various theoretical microwave scattering model simulations were used.

Chapter 1 presents an introduction to the motivation and purpose for this thesis. Chapter 2 provides the setup of the ground-based scatterometer and space-borne SAR systems and the radiometric calibration procedures of each system to acquire reliable data. Chapter 3 explains the results of various experiments to measure sea ice thickness using measurements of the ground-based scatterometer system, in-situ measurements, and numerical simulations. Chapter 4 shows results of a

measurement in order to measure sea ice thickness using space-borne SAR data and in-situ measurements based on the results of Chapter 3. Chapter 5 summarizes the results of this thesis, and discusses limitations of proposed method to measure sea ice thickness in this thesis and future works.

Chapter 2. Polarimetric microwave remote sensing systems

2.1. Ground Based POLarimetric SCATterometer (GB-POLSCAT)

As mentioned in Chapter 1, it is well known that GB-POLSCAT is optimal tool to interpret scattering features of microwave from natural distributed targets. This system has mainly used to interpret signatures backscattered from surface of the targets with space-borne SAR data and backscattering models [33]-[35]. Furthermore, Strozzi (1996) [36] introduced the practical method to measure the signatures backscattered from snow cover with the GB-POLSCAT system at 5.3 GHz (C-band) and 35 GHz (Ka-band). This method is very useful to interpret scattering structures (i.e. surface/volume scattering) of microwave from snow covers. Detail process of the method refers to Section 6.2 of Strozzi's dissertation [36].

In this thesis, the GB-POLSCAT was developed at Seoul National University (SNU) for interpreting the signatures from sea ice and snow with Strozzi's method. In following sections, detail set-up and calibration procedures of the system are introduced.

A. Set-up of GB-POLSCAT

The GB-POLSCAT developed at SNU is based on Network Analyzer (NA), Circuit, and Antenna (Figure 6a). The NA is main device in the GB-POLSCAT as source power generator, receiver of returned signals, and signal processing unit. Anritsu MS2028B among various NA products was used. This NA can generate source signal at wide frequency range (i.e. from 5 kHz to 20 GHz), and is easy to operate being as it is hand held type. Circuit consists of isolator, power amplifier, switch controller, and circulator (Figure 6b). Isolator blocks reverse current of transmitted signal. Power amplifier controls the source power of the generated signal up to 40 dB. Switch controller and circulator decide the polarization features of transmitted and received signal through controlling the transmission line of signal transmitted into the single orthomode transducer (OMT) horn antenna or received from the one. In addition, azimuth and incidence angle of the illuminated signal can be controlled automatically by step motors.

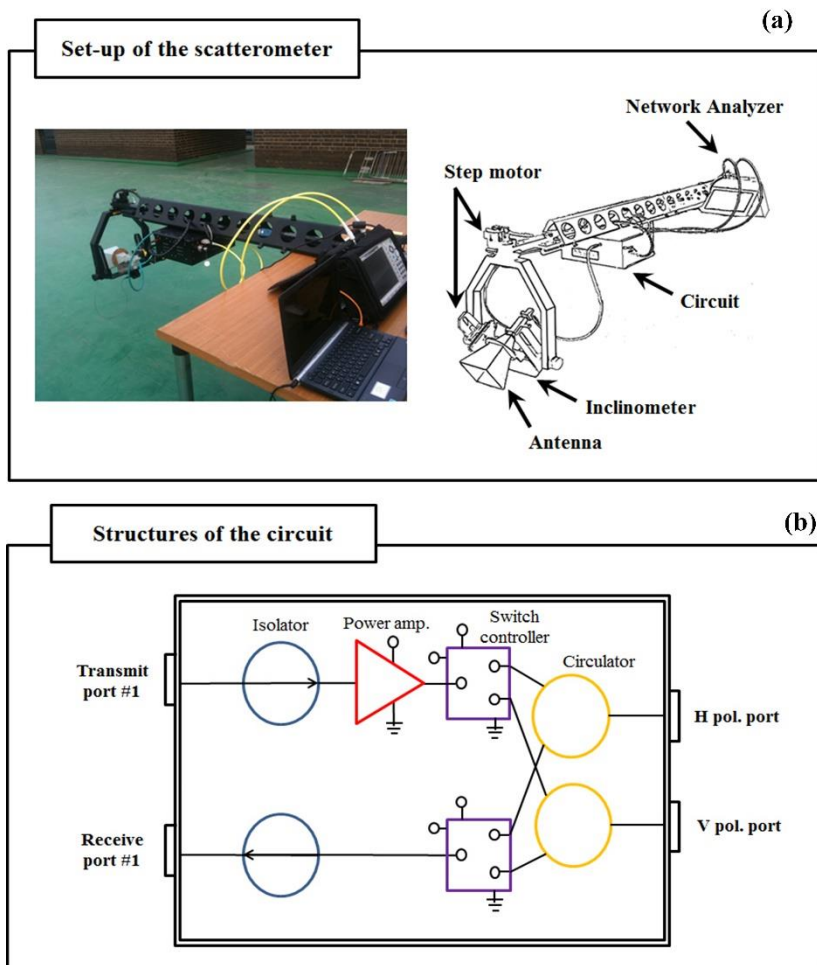


Figure 6. (a) External parts of the GB-POLSCAT system developed by SNU
 (b) Structures of the circuit.

B. System calibration of GB-POLSCAT

B.1. Basic concept of the system calibration

In the GB-POLSCAT, the radar equation associated with transmitted and received signal can be defined as following [37]

$$E_{pq}^r = e^{-j2kr} \left(\frac{P_t G_t G_r \lambda^2}{(4\pi)^2 r^4} \right)^{\frac{1}{2}} S_{pq} \quad (1)$$

where E_{pq}^r is the received electromagnetic field. G_t and G_r are the gain of transmitting and receiving antenna, respectively. P_t is transmitting power generated by the NA. λ is the wave length and r is the distance between the antenna of the GB-POLSCAT and a target. S is the scattering matrix of a target. The subscripts p and q denote the polarization of transmitted and received signal, respectively. Here, Radar Cross Section (RCS) of a target can be determined by the scattering matrix as following:

$$\sigma_{pq} = 4\pi |S_{pq}|^2 \quad (2)$$

In ideal case, it is possible to determine the scattering matrix of a target by measuring of $\frac{|E_{pq}^r|^2}{P_t} \equiv U_{pq}$ from a target. However, radar distortions are always

generated under field measuring conditions [38], so equation (1) can be simply rearrange into equation (3) and equation (4) by a corresponding four-component vector.

$$E^r = e^{-j2kr} \left(\frac{P_t G_t G_r \lambda^2}{(4\pi)^2 r^4} \right)^{\frac{1}{2}} RST \quad (3)$$

where R and T are radar distortions induced by transmitting and receiving line of signals within the GB-POLSCAT, respectively.

$$\begin{pmatrix} E_{vv}^r \\ E_{vh}^r \\ E_{hv}^r \\ E_{hh}^r \end{pmatrix} = e^{-j2kr} \left(\frac{P_t G_t G_r \lambda^2}{(4\pi)^2 r^4} \right)^{\frac{1}{2}} D \begin{pmatrix} S_{vv} \\ S_{vh} \\ S_{hv} \\ S_{hh} \end{pmatrix} \quad (4)$$

$$\text{here, } D = \begin{pmatrix} R_{vv}T_{vv} & R_{vv}T_{vh} & R_{vh}T_{vv} & R_{vh}T_{vh} \\ R_{vv}T_{hv} & R_{vv}T_{hh} & R_{vh}T_{hv} & R_{vh}T_{hh} \\ R_{hv}T_{vv} & R_{hv}T_{vh} & R_{hh}T_{vv} & R_{hh}T_{vh} \\ R_{hv}T_{hv} & R_{hv}T_{hh} & R_{hh}T_{hv} & R_{hh}T_{hh} \end{pmatrix}$$

where, D is the radar distortion matrix. In order to the system calibration, the radar distortion matrix should be exactly determined. In general, the radar distortions have been determined by measuring a point calibration target of which the RCS is well known, because it is impossible to measure directly radar distortions. From measuring the point calibration target, the radar distortions can be determined as following

$$D = e^{j2kr} \left(\frac{P_t G_t G_r \lambda^2}{(4\pi)^2 r^4} \right)^{-\frac{1}{2}} S^{-1} E^r \quad (5)$$

B.2. Conventional system calibration

Using the basic principle of the system calibration with the point calibration target, various calibration techniques have been developed. The generalized calibration technique (GCT) can be determined the radar distortion using three calibration targets [39]. The scattering matrix of the first target must have the form of identity matrix such as sphere or flat plates while the other two targets do not need any specified scattering matrix. In order to calculate the radar distortion with the calibration targets, this technique employed an eigenvalue approach. As a similar technique, constrained calibration technique (CCT) was developed. Unlike GCT, this technique uses all targets with specific scattering matrices [40]. Although these calibration techniques can fully characterize the radar distortion matrix, they are strongly affected by an alignment of the targets, and time consuming. Detail procedures of each calibration techniques are not repeated in this thesis.

Sarabandi et al. (1990; 1992) [38], [41] proposed convenient calibration techniques of the GB-POLSCAT with single OMT antenna. It can be assumed that the antenna is perfectly isolated unlike the dual antenna system. The dual antenna system can generate the cross polarized terms from not only the structure of the antenna but also unisolated features of the antenna. The cross terms of unisolated antenna system can be determined by measuring the point calibration target of which cross polarized elements of the scattering matrix are well known such as GCT or CCT. In actual, Strozzi's GB-POLSCAT was the dual antenna system, and he used GCT for the

system calibration. On the other hand, the isolated antenna assumption can lead that cross polarized terms (R_{hv} , R_{vh} , T_{hv} , and T_{vh}) of the radar distortions are only generated by structures of the antenna, and these terms can be determined by measuring of any calibration target. Thus, Sarabandi's calibration techniques can practically determine the radar distortions by only once measuring of any calibration targets. Actually, most of calibration experiments have used a metal sphere as the point calibration target because of independence of target alignment, and the radar distortion matrix can be determined as following

$$R_{vv}T_{vv} = e^{-j2kr}r^2 \frac{U_{vv}^S}{(1 + C^2)\sqrt{\frac{\sigma^S}{4\pi}}}$$

$$\beta \equiv \frac{R_{hh}}{R_{vv}} = \frac{2C}{(1 + C^2)} \frac{U_{hh}^S}{U_{vh}^S}$$

(6)

$$\alpha \equiv \frac{T_{hh}}{T_{vv}} = \frac{(1 + C^2)}{2C} \frac{U_{vh}^S}{U_{vv}^S}$$

$$C = \pm \frac{1}{\sqrt{a}} (1 - \sqrt{1 - a}) \quad \text{where,} \quad a = \frac{U_{vh}^S U_{hv}^S}{U_{vv}^S U_{hh}^S}$$

where C is the cross talk generated by single OMT antenna. σ^S is theoretical RCS of a metal sphere. The superscript S denotes measuring of a metal sphere. Using equation (6), the radar distortion matrix of equation (4) is rearranged as following

$$D = R_{vv} T_{vv} \begin{pmatrix} 1 & C\alpha & C & C^2\alpha \\ C & \alpha & C^2 & C\alpha \\ C\beta & C^2\alpha\beta & \beta & C\alpha\beta \\ C^2\beta & C\alpha\beta & C\beta & \alpha\beta \end{pmatrix} \quad (7)$$

As mentioned above, the GB-POLSCAT developed by SNU uses single OMT antenna, so all data measured by the GB-POLSCAT were basically calibrated by Sarabandi's method. However, Strozzi emphasized the necessary of improved calibration technique which can efficiently calibrate the effect of the external conditions as an issue of future study. Because the radar distortions are strongly affected by the weather conditions such as air temperature under field experiments. Therefore, practical calibration method which can give a clue of the issue are proposed in next section.

C. New system calibration of GB-POLSCAT

C.1. Background

As mentioned above, the extraction of radar distortions of polarimetric scatterometer is a key in measuring the exact backscattering coefficients of distributed targets. Radar distortions can be divided into two groups. The first group is passive distortions which are insensitive to changes of the external conditions (e.g., the passive fixed antenna structure). The second group is active distortions which are sensitive to changes of the external conditions. These can be caused mainly by active devices within radar systems such as the GB-POLSCAT (e.g. transmitter/receiver, external electronic/microwave circuits such as amplifiers) [38], [41]. These radar distortions can be determined by measuring the radar response of a point calibration target with a known Radar Cross Section (RCS) [39], [40]. In particular, Sarabandi et al. [41] proposed an improved method to extract the active distortions by using the ratios of the radar responses of a point calibration target measured within an anechoic chamber and out in the field. However, it is difficult to use this method in some locations (e.g., the cryosphere and ocean) due to the difficulties involved in installing a point calibration target. Thus, there is a need for a more versatile method.

It is highly unlikely that the antenna impedance perfectly matches the impedance of the source cable in a radar system. Due to the impedance mismatch at the antenna input, a portion of the energy reflects back to the source (this is often referred to as the “return loss”). Because of this, the scattering matrix due to the impedance

mismatch can be defined at the antenna input [42]. In this section, a practical method that can extract the active distortions using the signal returned from the antenna input is introduced. The experiments to validate the proposed method using the field measurements of PRS, space-borne SAR data, and numerical simulations are presented.

C.2. New technique to extract radar distortions

In order to effectively extract radar distortions, Sarabandi et al. [41] discretized the domain of the main antenna beam into small subdomains and measured the radar response of each subdomain from a point calibration target (e.g., a conducting sphere) in an anechoic chamber, which was well designed to prevent the loss of any signals. They then set the distortions in the anechoic chamber to 1, which can be other values under field measurements. Under field conditions, Sarabandi et al. [41] measured the radar response of a point calibration target only at the boresight direction. Then, the active distortions caused by external conditions were determined using the ratios of the radar responses of a point calibration target measured only at the boresight direction in the anechoic chamber and out in the field:

$$a_v^t a_v^r = \frac{U_{vv}^f}{U_{vv}^c}, \quad a_h^t = \frac{U_{vh}^f U_{vv}^c}{U_{vh}^c U_{vv}^f}, \quad a_h^r = \frac{U_{hh}^f U_{vh}^c}{U_{hh}^c U_{vh}^f} \quad (8)$$

where a represents the active distortion. The superscripts t and r denote transmitting and receiving channels, and the superscripts f and c are the field- and

chamber-measurements. Although this method can extract the active distortions with high accuracy, it is restricted to apply in some locations that are difficult to install a point calibration target.

Here, a more efficient and practical method to extract the active distortions without a point calibration target under field conditions is introduced. The source power of the polarimetric scatterometer reflects at the antenna input due to the impedance mismatch. The returned signal from the antenna input is named as the Returned signal from Point of Interest (RPI) and it is assumed that the transmitting and receiving antenna gains are the same ($G_t = G_r$) and the antenna structure is fixed under field conditions (Figure 7). The reflected signal from the RPI with scattering matrix, $[S_{RPI}]$, involves radar distortions except the antenna structure. Because the antenna structure is fixed such that the cross-talk and channel imbalance in the antenna are not changed under field conditions, the active distortions can be extracted using the measured value from RPI in the anechoic chamber and out in the field using Equation (8). Then, the calibration matrix elements $R_{vv}T_{vv}$, α , β of equation (6) can be modified by

$$R_{vv}^f T_{vv}^f = a_v^t a_v^r R_{vv}^c T_{vv}^c, \alpha^f = \frac{a_h^t}{a_v^t} \alpha^c, \text{ and } \beta^f = \frac{a_h^r}{a_v^r} \beta^c \quad (9)$$

Finally, the radar distortion matrix of equation (7) can be rearranged as following

$$D = R_{vv}^f T_{vv}^f \begin{pmatrix} 1 & C\alpha^f & C & C^2\alpha^f \\ C & \alpha^f & C^2 & C\alpha^f \\ C\beta^f & C^2\alpha^f\beta^f & \beta^f & C\alpha^f\beta^f \\ C^2\beta^f & C\alpha^f\beta^f & C\beta^f & \alpha^f\beta^f \end{pmatrix} \quad (10)$$

C.3. Validation using field experiments and numerical simulation

In order to validate the proposed method, radar distortions by measuring the radar responses from a point calibration target (e.g., a conducting sphere) and the RPI in the anechoic chamber (Figure 8) are derived. The radar responses of the point calibration target and the RPI at incidence angles of 20°, 30°, 40°, and 50° under field conditions are measured. Tidal flats in South Korea were selected as the field site. The Root-Mean-Square (RMS) height, correlation length, and soil moisture content at the test site are simultaneously measured. The field-measured RMS height and correlation length were 0.52 and 8.0 cm, respectively. The field-measured soil moisture content was about 0.6 m³/ m³. TerraSAR-X data (X-band: 9.65GHz) were also acquired at the test site. The acquired data was dual-polarized (VV and VH) and the incidence angle was 45°.

Figure 9 shows the estimated active distortions of the VV polarization caused by the field conditions. It shows that the estimated active distortions using the radar responses of the point calibration target and the RPI are almost the same within the margin of error (0.1%). Figure 10 shows the backscattering coefficients of the PRS, the SAR data, and the simulations from [43], [44]. These measured backscattering coefficients agree quite well with those simulated within the margin of error, which was 0.5%. Therefore, it is reasonable that the active distortions can be derived by the radar responses from the RPI under field conditions.

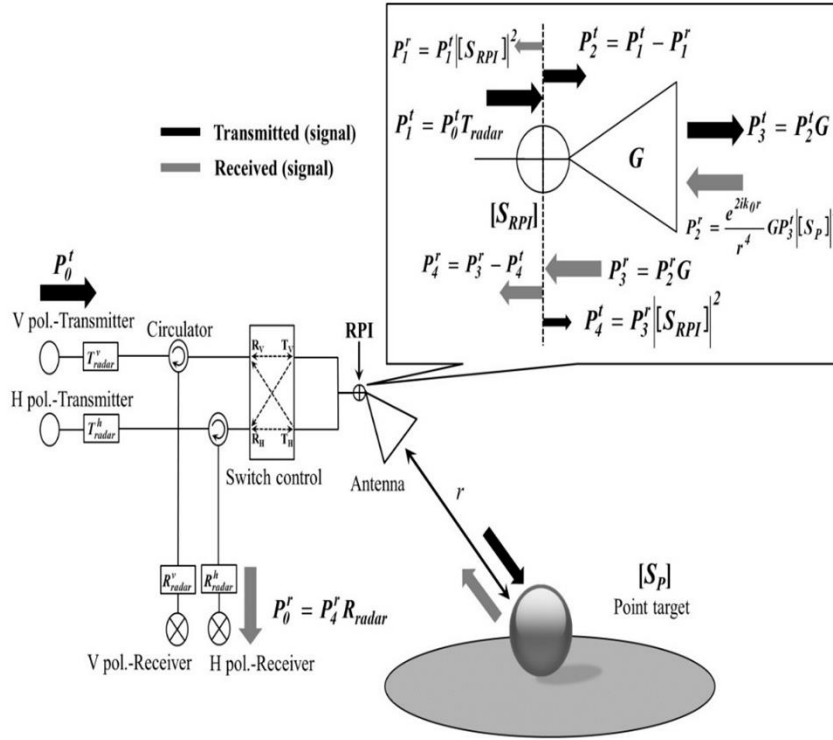


Figure 7. Geometry and block diagram of Polarimetric Radar System (PRS. P is the power generated by PRS. The superscript of P denotes direction of power transmission (e.g., t: transmitted or r: received direction). The subscript of P denotes a sequence of power transmission. [S] is a scattering matrix. The superscript of [S] denotes RPI or a point calibration target. G denotes the antenna gain. r is the distance between the antenna and a point calibration target.

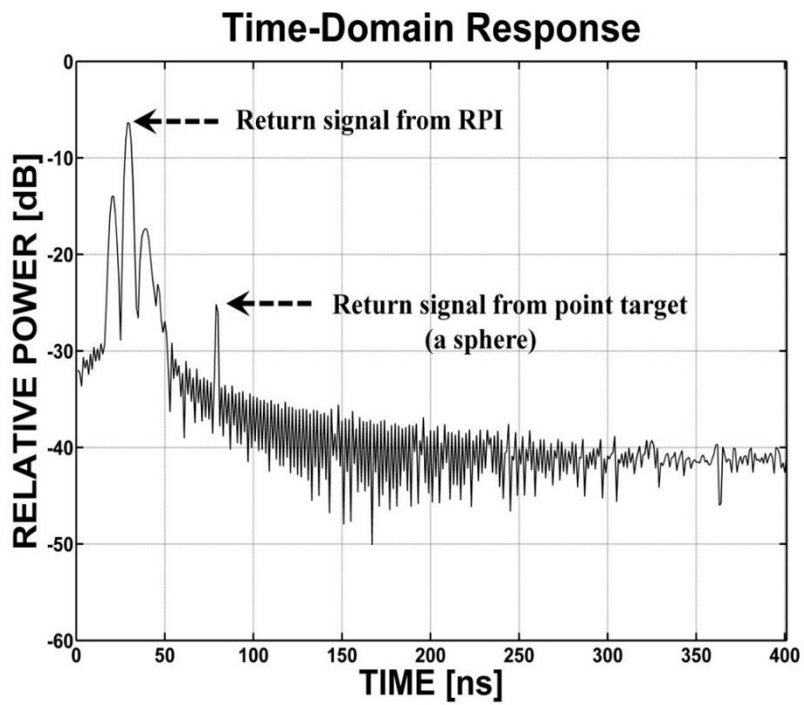


Figure 8. The measured radar response of the PRS in the anechoic chamber.

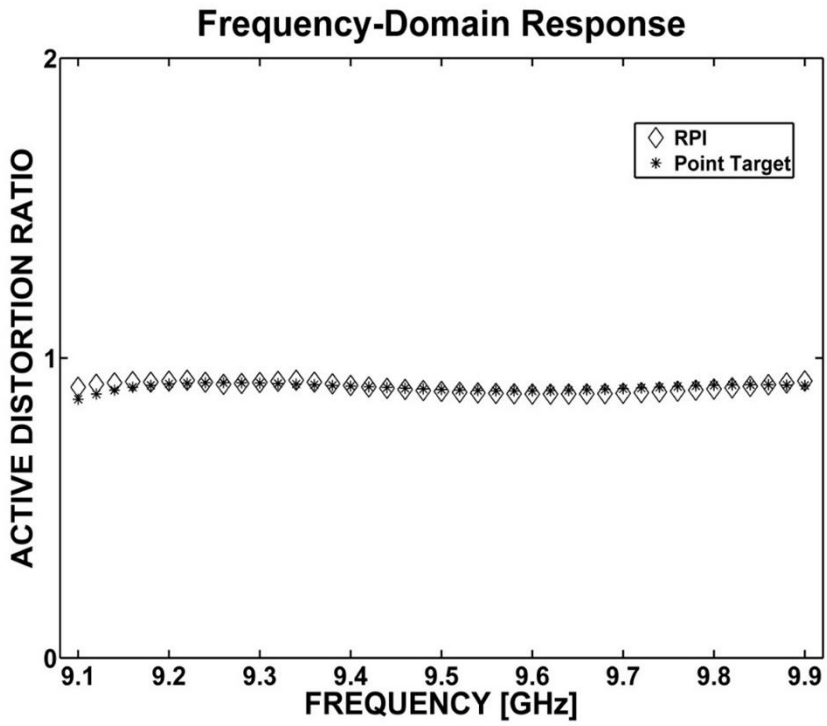


Figure 9. Active distortion estimated from field experiments.

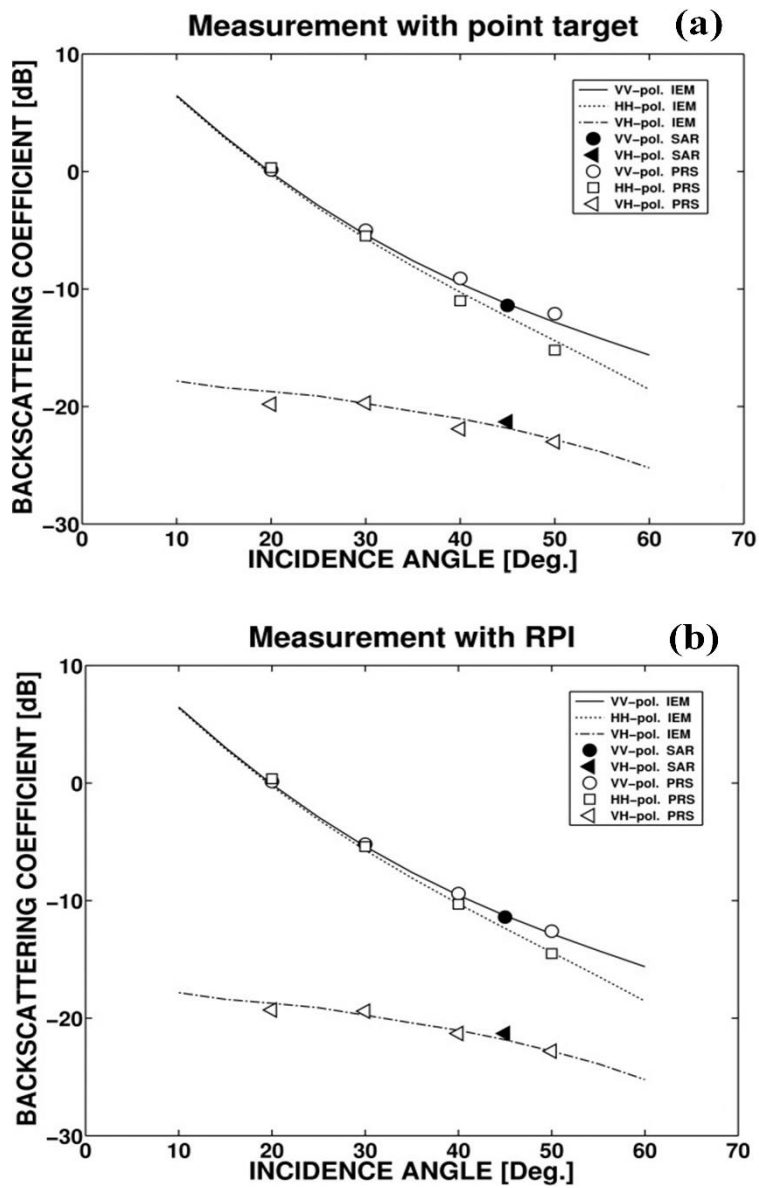


Figure 10. Comparison between simulated and measured backscattering coefficients.

2.2. Space-borne SAR systems

A. RADARSAT-2 and TerraSAR-X

In this thesis, the polarimetric space-borne SAR data were acquired by RADARSAT-2 and TerraSAR-X. RADARSAT-2 and TerraSAR-X are latest C- and X-band space-borne SAR systems, respectively. RADARSAT-2 was developed at the Canadian Space Agency (CSA), and was launched on December 14, 2007. TerraSAR-X was developed at the German Aerospace Center (DLR) and European Aeronautic Defense and Space Company (EADS) Astrium, and was launched on June 15, 2007. These radar earth observation satellites can operate with various imaging modes, combinations of full polarizations, high resolution capabilities (up to 1m), and precise radiometric and geometric accuracy (Figure 11). Detailed specifications of these systems are illustrated in Table 2. The data acquired by the space-borne SAR systems are basically calibrated by various radiometric and geometric calibration procedures. In particular, radiometric calibration is to determine the NRCS of distributed targets, and this procedure is main key to determine reliability of the acquired SAR data. The data acquired by TerraSAR-X and RADARSAT-2 need to reprocess in order to estimate exact NRCS of the data with the information which is given from MDA and DLR. Therefore, In order to reprocess exactly the data with the given information, it needs to understand basic concept of the radiometric calibration procedure. In this thesis, the procedure is explained with radiometric calibration experiments of air-borne SAR system

(NanoSAR-B, i.e. this system was used for the prospective study in chapter 4) operated by SNU since the radiometric calibration procedures of various SAR systems are similar.

Table 2. Specifications of RADARSAT-2 and TerraSAR-X.

| | <i>RADARSAT-2</i> | <i>TerraSAR-X</i> |
|-------------------------------|-------------------------------------|----------------------------|
| <i>Frequency</i> | 5.405 GHz (C-band) | 9.65 GHz (X-band) |
| <i>Polarizations</i> | HH/VV/HV/VH | HH/VV/HV/VH |
| <i>Antenna length</i> | 15m | 4.8m |
| <i>Antenna width</i> | 1.5m | 0.7m |
| <i>PRF</i> | 1.0 kHz ~ 3.8 kHz | 2.2 kHz ~ 6.5 kHz |
| <i>Range bandwidth</i> | 11.56, 17.28, 30.0, 50.0 MHz | 150 MHz and 300 MHz |
| <i>Revisit time</i> | 24 days | 11 days |
| <i>Resolution</i> | Up to 3m | Up to 1m |

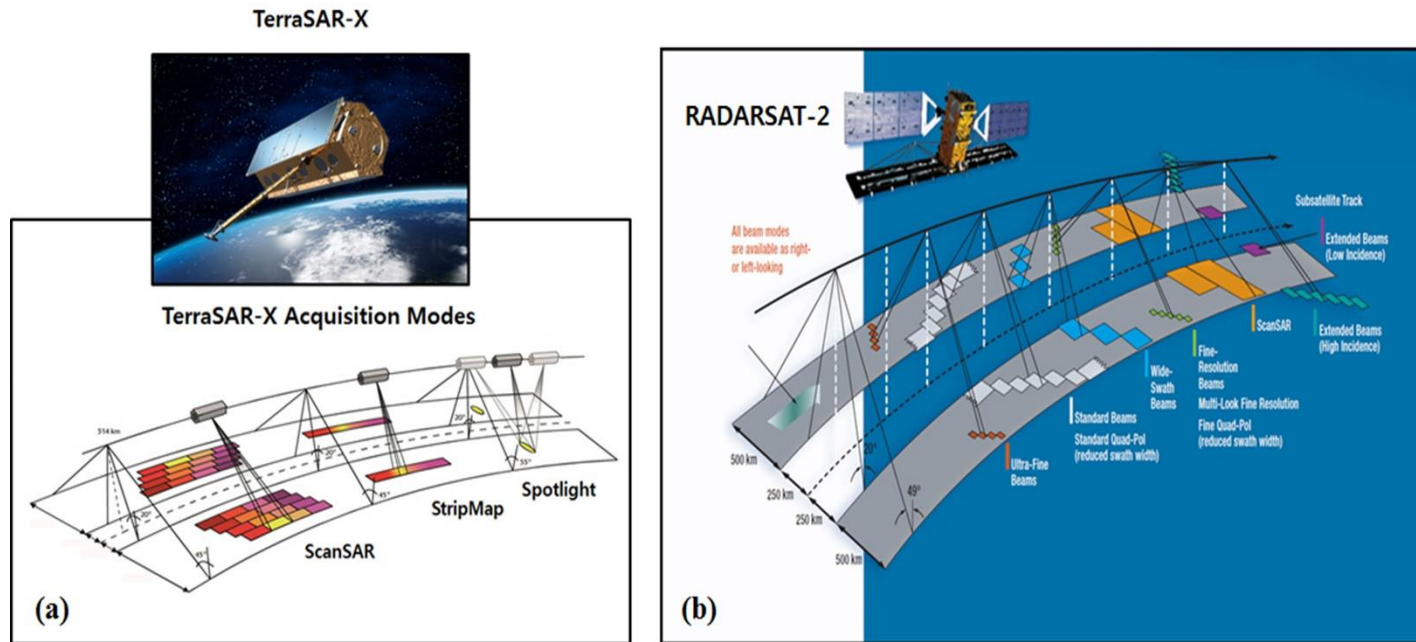


Figure 11. Various imaging modes of the space-borne SAR systems (a) TerraSAR-X (b) RADARSAT-2. [From DLR and MDA]

B. Radiometric calibration of the SAR systems

B.1. Background

Radiometric calibration allows to correct all the contributions in the radiometric values generated besides the target characteristics. This permits minimizing the differences in the image radiometry of air- and space-borne SAR system [45]. In order to acquire a highly qualified space-borne SAR data, accurate radiometric calibration is the essential procedure. Radiometric calibration is a correction for estimation of precise NRCS or backscattering coefficient (σ^0) of microwave signatures backscattered from a target. Basically, NRCS calculates with the following formula (11).

$$\sigma^0 = \frac{DN^2}{K} \frac{1}{G^2(\theta)} \left(\frac{R}{R_{ref}} \right)^3 \sin(\alpha) \quad (11)$$

where, K is the absolute calibration constant which compensates the power penalties which occurred from the internal system and the reference distance, R_{ref} , between the SAR antenna and the target. G is the unique antenna patterns transmitted and received from the antenna, which is defined as the function of elevation angle (θ). Here, it is assumed that transmitted and received antenna gain are same. R is the real distance between a target and an antenna. As K compensates the power loss from the reference distance, $(R/R_{ref})^3$ term plays the role of calibration for the power penalty

that occurred as much as the difference between the real distance and the reference distance. In general, these procedures are called “range spreading”. Lastly, α is the incidence angle of the main beam. In this regard, the antenna patterns and range spreading calibration are called “relative radiometric calibration” and the process of extracting the absolute calibration constant (K) with measuring known RCS of reference target (i.e. trihedral corner reflector) [46], [47] called “absolute radiometric calibration”.

B.2. Backscattering coefficient computation of TerraSAR-X and RADARSAT-2

Basically, DLR and MDA give to user respective radiometric calibrated TerraSAR-X and RADARSAT-2 data with above mentioned calibration procedures. However, the acquired SAR data need to be reprocessed in order to estimate exact backscattering coefficients. Here, it is explained to estimate the backscattering coefficients of the acquired TerraSAR-X and RADARSAT-2 data.

In case of TerraSAR-X, the Digital Number (DN) values are computed from the complex data given in the COSAR format file of delivered TerraSAR package files as following:

$$DN = \sqrt{I^2 + Q^2} \quad (12)$$

where I and Q are the real and imaginary parts of the complex data, respectively. Then, the radar brightness (β^0) is derived by the DN multiplying the calibration factor (K_s) given in the xml format file of delivered TerraSAR-X package files (Figure 12).

$$\beta^0 = K_s \cdot |DN|^2 \quad (13)$$

The radar brightness (β^0) is the RCS per unit area in the slant range, and the backscattering coefficient (σ^0) is the RCS per unit area in the ground range. Thus,

the relation of these values is as following

$$\beta^0 = \frac{\sigma^0}{\sin(\alpha)} \quad (14)$$

where α is a local incidence angle. Using this relationship, the backscattering coefficient is derived as following

$$\sigma^0 = \beta^0 \cdot \sin(\alpha) \quad (15)$$

DLR additionally provides the information of the system noise, Noise Equivalent Beta Naught (NEBN), in order to estimate exact radar brightness. Internal system of TerraSAR-X record the NEBN three times during the acquisition time. The acquisition start and stop times correspond to the first and last system noise records, respectively. Each NEBN is estimated as following equation

$$NEBN = K_s \cdot \sum_{i=0}^{deg} a_i (\tau - \tau_{ref})^i \quad \text{here, } \tau \in [\tau_{min}, \tau_{max}] \quad (16)$$

where i is polynomial degree. a is coefficient of the polynomial equation. τ_{ref} is reference point. τ_{min} and τ_{max} are validity range min and validity range max, respectively. The values of these parameters are given in the xml format file. At last, the NEBN is determined by the mean value of them, and then, exact backscattering coefficients of acquired TerraSAR-X data are derived as following equation (Figure 13)

$$\sigma^0 = (\beta^0 - NEBN) \cdot \sin(\alpha) \quad (17)$$

In case of RADARSAT-2, the process to estimate the backscattering coefficients is simpler than the one of TerraSAR-X. The DN values are computed from the complex data given in the tiff format file of delivered RADARSAT-2 package files, and the DN values can be selectively converted to the radar brightness (β^0) or the backscattering coefficients (σ^0) with scaling Look-up Tables (LUTs). Each LUT provides a constant offset and range dependent gain. Using these parameters, the calibrated values (i.e. the radar brightness and the backscattering coefficients) are directly derived as following equation (Figure 14 and 15)

$$\beta^0 \text{ or } \sigma^0 = \frac{(DN^2+B)}{A} \quad (18)$$

where A is the gains value. B is the constant offset

Beta naught of TerraSAR-X

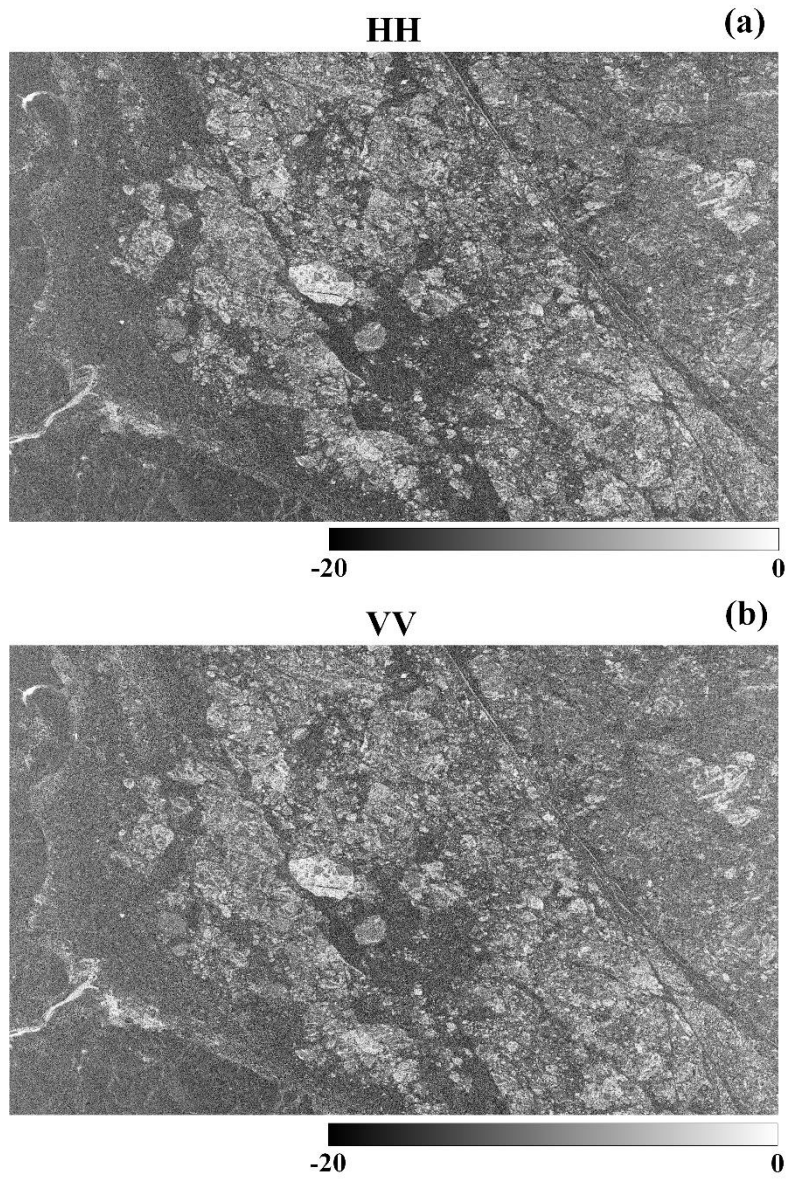


Figure 12. Estimated radar brightness of acquired TerraSAR-X. (a) HH (b) VV

Sigma naught of TerraSAR-X

HH

(a)



-20

0

VV

(b)



-20

0

Figure 13. Estimated backscattering coefficients of acquired TerraSAR-X data.
(a) HH (b) VV

Beta naught of RADARSAT-2

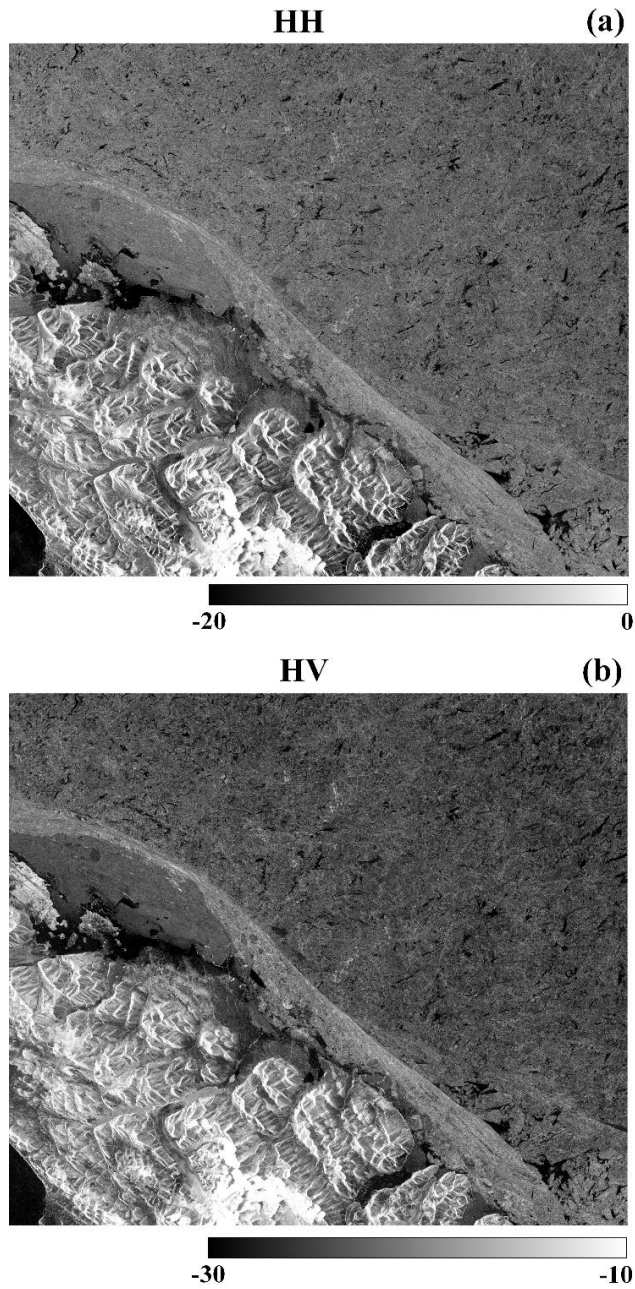


Figure 14. Estimated radar brightness of acquired RADARSAT-2 data.
(a) HH (b) HV

Sigma naught of RADARSAT-2

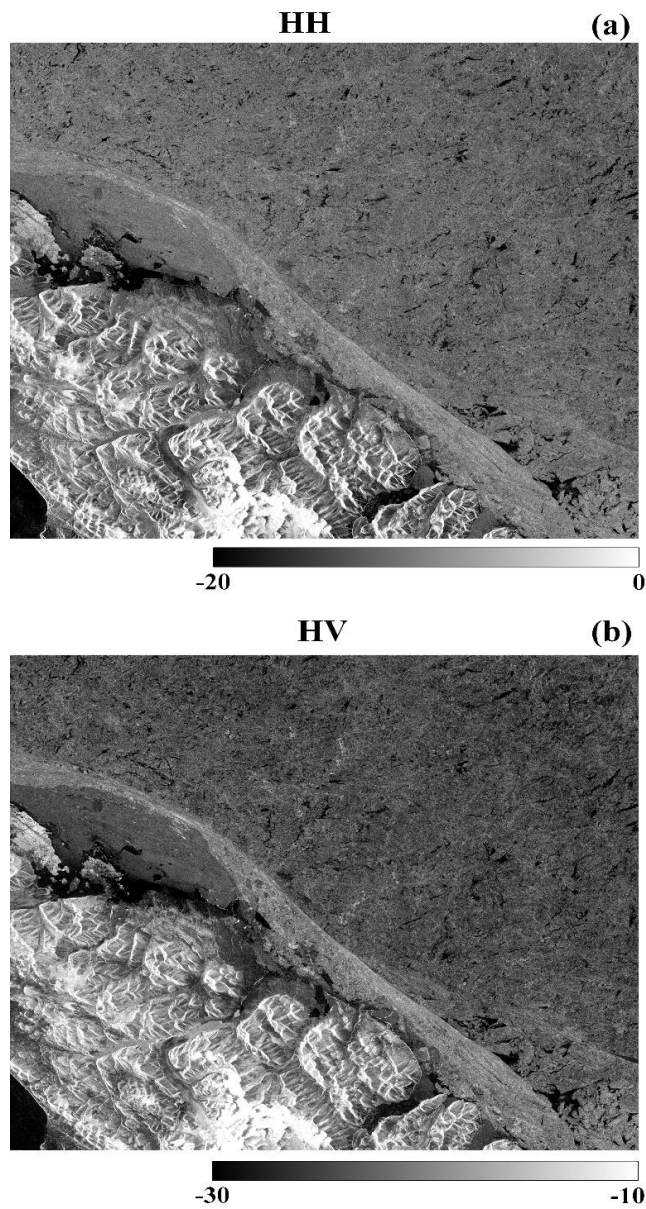


Figure 15. Estimated backscattering coefficients of acquired RADARSAT-2 data. (a) HH (b) HV

Chapter 3. Polarimetric signatures characterized by scattering features from sea ice and snow

3.1. Background

In the Arctic Ocean from the middle of September to the middle of March in next year (i.e. freezing season), sea ice is formed when the temperature of sea water decreases below its freezing point (i.e. about $-1.8\text{ }^{\circ}\text{C}$), and then, it grows. On the contrary to this, sea ice melts from the middle of March to the middle of September (i.e. melting season) due to increasing of the temperature above the freezing point (Figure 16a). In the Antarctic Ocean, the freezing season is from the middle of February to the middle of September, and the melting season is from the middle of September to the middle of February (Figure 16b). In general, sea ice formed during the freezing season can be broadly divided into First-Year ice (FYI) and Multi-Year ice (MYI). FYI has no more than one year growth while MYI has survived more than one melting season.

Figure 17 shows common life cycle of sea ice [48]. For the freezing season, FYI is formed and grows. The surface roughness of newly formed FYI is relatively smooth, and dry snow is covered on its surface. For the melting season, snow cover melts, and the surface roughness is relatively rougher. In this season, FYI are fully melted or survived. For next freezing season, the survived FYI changes into MYI, and the surface roughness of MYI is rougher and deformed due to mechanical growth processes where ice blocks collide with each other (i.e. ridging process). New dry

snow is covered on the surface. During the melting season, snow on surface of MYI becomes wet, and melting pond is formed by snow melting on surface of MYI. These processes are repeated every year. Thus, it is necessary to consider the realistic physical characteristics of sea ice such as snow cover, surface roughness, and dielectric constant in order to understand detail scattering features from sea ice under various conditions.

Polarimetric backscattering signatures from the ice are determined by various scattering features of microwave [48]. The features are simply classified into surface and volume scattering. Degree of surface scattering can be determined by surface roughness and dielectric constant of the ice surface, and the dielectric constant also decides on penetration of microwave into the ice surface. If microwave can penetrate into the ice surface due to low dielectric properties of the ice surface, degree of volume scattering must be determined by physical properties (i.e. shape, orientation, absorption, reflectivity, and etc.) of scatterers within the ice layer such as air bubbles and pockets of salty water (brine). The dielectric properties of sea ice are deeply related to the brine volume which is the fraction of brine [49], and temperature and salinity of sea ice govern the brine volume [50].

The salinity of sea ice is strongly related to its growth process. As sea ice grows, the brine within the ice layer is drained into the ice bottom, and the salinity is decreased (i.e. desalination). In addition, it was found that rapid desalination only occurs in thin sea ice (i.e. < 50 cm thickness), and the desalination slows down over time as the ice thickens, and Cox and Weeks (1973) [51] suggested that the average salinity in the Arctic Ocean is a piecewise linear decreasing function of the ice

thickness. This suggests that the variation of surface dielectric constant as the ice thickness may give us the solution to measure the ice thickness using space-borne SAR data.

As mentioned above, it is generally known that backscattering signatures from sea ice are dominated by surface roughness and complex dielectric constant of the ice surface [52]. These two factors have been decoupled to study relative contribution between these two [53]-[55]. The authors of [53]-[55] suggested the VV-to-HH backscattering coefficient ratio (BCR) of L-band air-borne SAR data could cancel out the surface roughness contribution, BCR can represent the remaining contribution from dielectric constant. They also showed a good correlation between BCR and thin FYI thickness. This relationship can be attributed to desalination of sea ice as the ice thickness increases. The rapid desalination of FYI decreases the surface dielectric constant resulting in decreasing BCR. However, as mentioned above, rapid desalination only occurs in thin FYI, and the desalination slows down over time as the ice thickens. That is, the variation of surface dielectric constant becomes very small in thicker ice (e.g. MYI). Furthermore, the ice is characterized by low-density surface layer with air bubbles, thus, unlike thin FYI, backscattering signatures from the ice are induced by not only surface scattering from surface roughness and dielectric properties but also volume scattering within the low-density layer [52]. These complexities of the scattering features from sea ice still make measuring of the ice thickness using the SAR data difficult. Therefore, it needs to understand detail scattering structures of microwave from sea ice exposed various conditions. In order to understand in detail the scattering features from sea ice, the

scattering structures of sea ice were departmentalized like Figure 18. As mentioned above, sea ice surfaces are generally covered with snow cover. Thus, the scattering structures can be classified into surface and volume scattering from snow, and surface and volume scattering from sea ice. Based on the scattering structures, it was explored optimized method to determine sea ice thickness in next section.

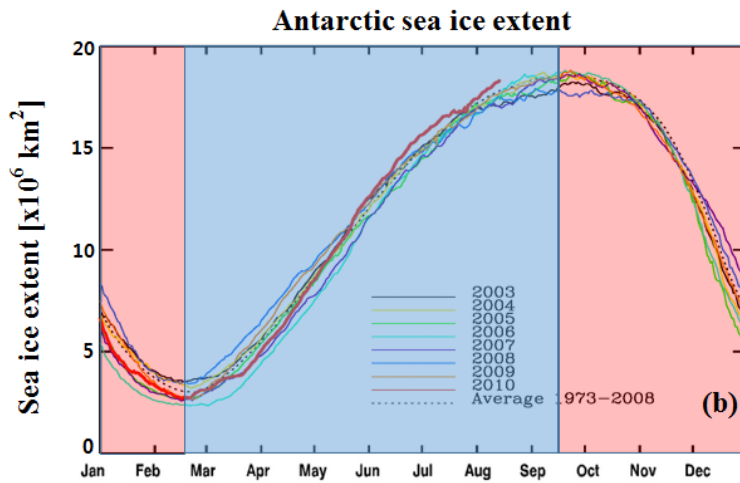
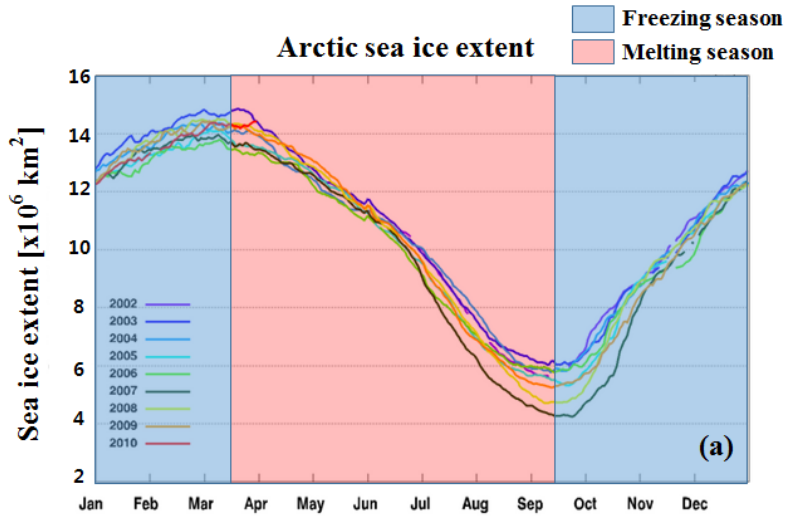


Figure 16. Variations of sea ice extent for the melting and freezing season.
 (a) Arctic sea ice (b) Antarctic sea ice

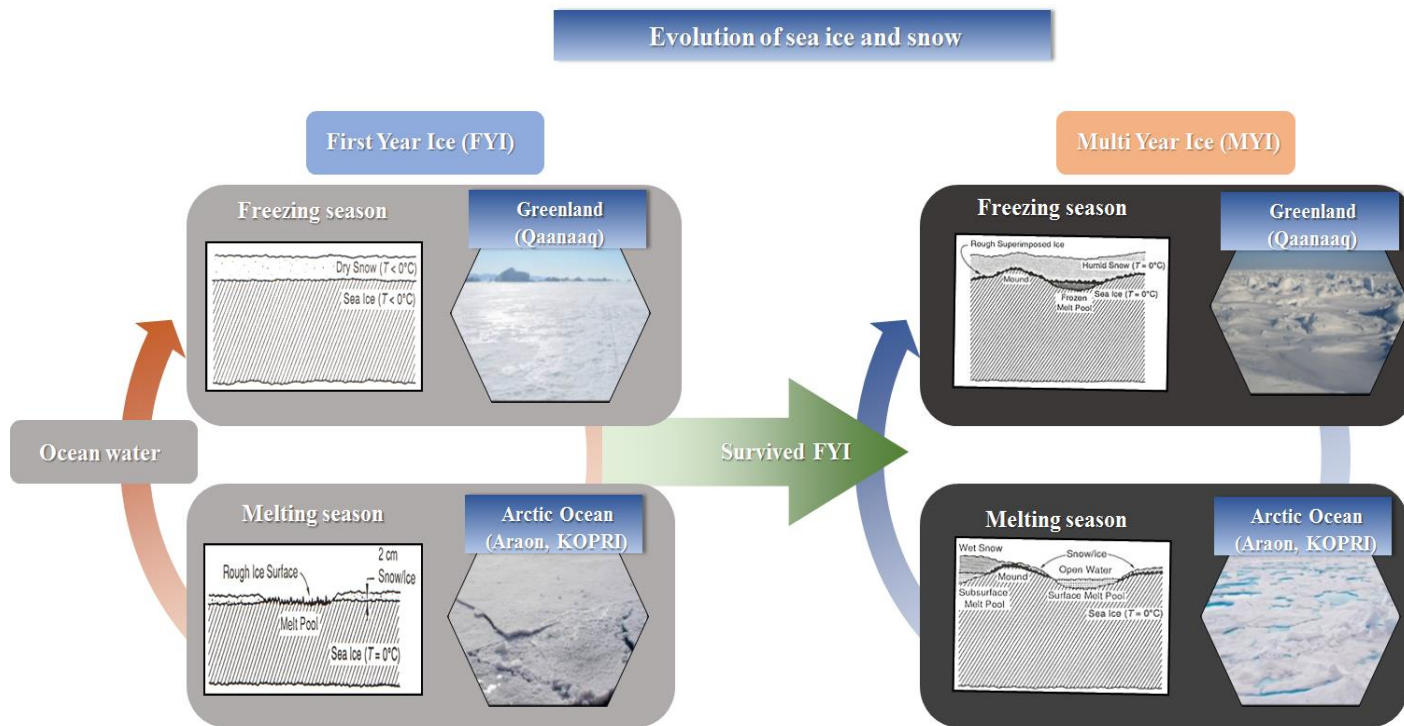


Figure 17. Life cycles of sea ice.

Backscattering structure of microwave at sea ice and snow

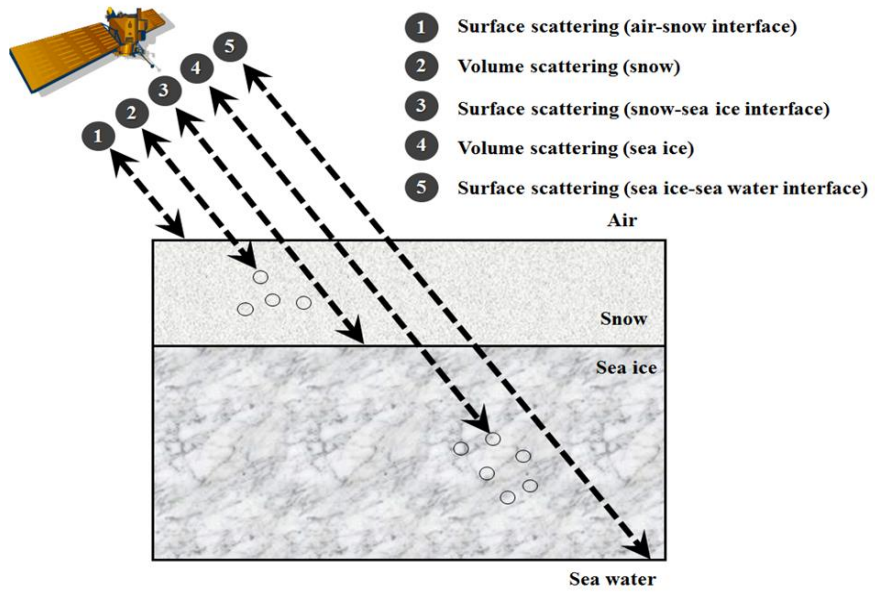


Figure 18. Scattering structures of sea ice and snow.

3.2. Polarimetric scattering features of snow

A. Dielectric properties of snow

In general, snow becomes dry when the surface temperature of snow fall below the freezing point (0 °C), causing this snow to have a minimal amount of water content. In contrast to wet snow, whose average snow to water content ratio is about ten to one, dry snow may have the ratio as high as 30 to one. There are more air pockets between the snow crystals within dry snow layer. Previous study [56] showed that the dielectric properties of dry snow are only dependent on the density of snow although wet snow is dependent on not only the density of snow but also water content [57], and it is difficult to know the amount of liquid within snow layer. Thus, many studies [58]-[59] developed the dielectric constant model of dry snow. Typical dielectric constant model is as following [60]

$$\varepsilon'_{ds} = 1.0 + 1.9\rho_s \quad (\rho_s < 0.5) \quad \varepsilon'_{ds} = 0.51 + 2.88\rho_s \quad (\rho_s \geq 0.5) \quad (19)$$

$$\varepsilon''_{ds} = \frac{\varepsilon'_i \left(\frac{\varepsilon'_{ds} - 1}{\varepsilon'_i - 1} \right)^2}{v_i} \quad , \text{ here } \varepsilon'_i = 3.15 \text{ and } v_i = \frac{\rho_s}{0.916} \quad (20)$$

where ε'_{ds} and ε''_{ds} denote real and imaginary part of dielectric constant of dry snow, respectively. ρ_s is the density of snow. ε'_i denotes real part of dielectric constant of pure ice, and this is about 3.15.

Strozzi (1996) [36] measured the air temperature, the density of snow, and the

dielectric constant of snow at Moosseedorf, Swiss from January 1994 to June 1995 (Figure 19), and these data could show the variation of the density and dielectric constant as air temperature changes (Table 3). In figure 20, mean air temperature was below 0 °C during the freezing season in 1994 and 1995, and the density of snow was distributed between 100 and 200 g/cm³. In contrast, mean air temperature was above 0 °C during the melting season, and the density of snow was rapidly increased by more than 500 g/ cm³. In a comparison between observed real part of dielectric constant and the one simulated by equation (13), the simulated values during the freezing season (blue box) were perfectly matched with the observed values unlike the simulated values during the melting season (Figure 21). Thus, it is clear that the range of dielectric constant (real part) is from 1.1 to 1.25 during the freezing season, and based on the range, it is expected that the backscattering signatures from dry snow cover may be induced by not only surface scattering from surface roughness and dielectric properties of snow cover but also volume scattering within the low-density layer during the freezing season. However, the backscattering signatures from wet snow cover may be induced by only surface scattering from surface roughness and relatively high dielectric constant of snow cover. In next section, it shows that the scattering features measured by GB-POLSCAT with Strozzi's method and newly proposed method to quantitatively estimate normalized intensity of surface, bottom-surface, and volume scattering from snow cover.

Test site : Moosseedorf, Swiss

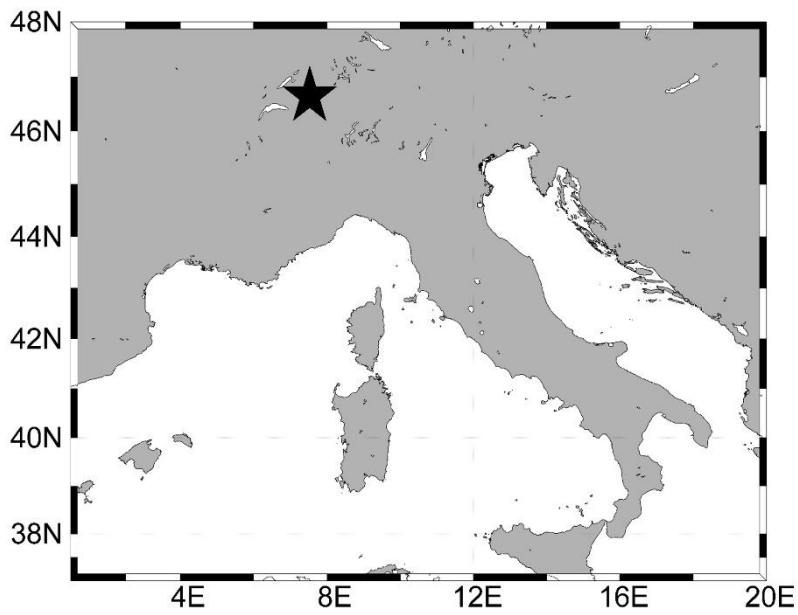


Figure 19. Test site of Strozzi's measurements.

Table 3. Specifications of Strozzi's measurements.

| Specifications | |
|---------------------------|--|
| Center Frequency | 5.3 GHz (C-band) |
| Sweep time | 1s |
| Bandwidth | 1.4 GHz |
| Transmitted Power | 10 dBm |
| Polarization | HH/VV/HV/VH |
| Incidence Angle | 0° ~ 70° |
| Platform Height | ~ 4m |
| Calibration method | GCT |
| Measurement item | Radar response / air temp. / Snow density / Dielectric constant of snow |

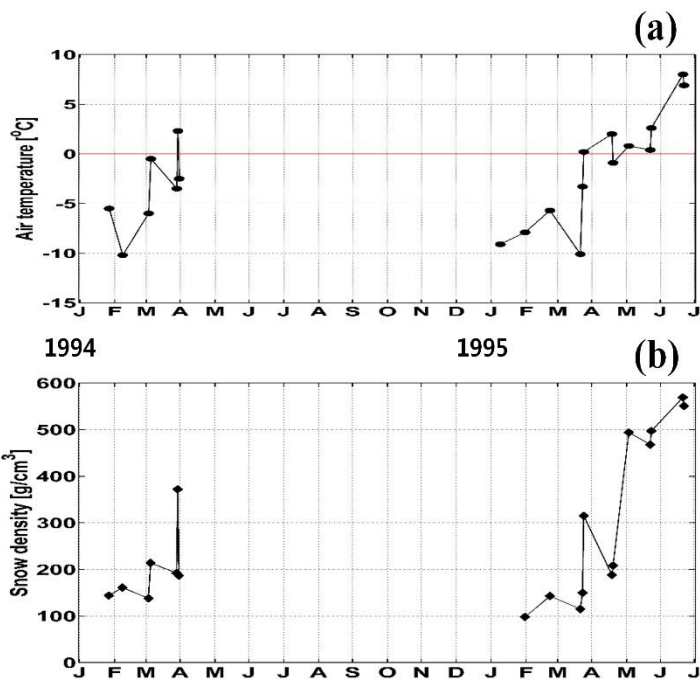


Figure 20. (a) measured air temperature and (b) snow density for the melting and freezing seasons. [Strozzi, 1996]

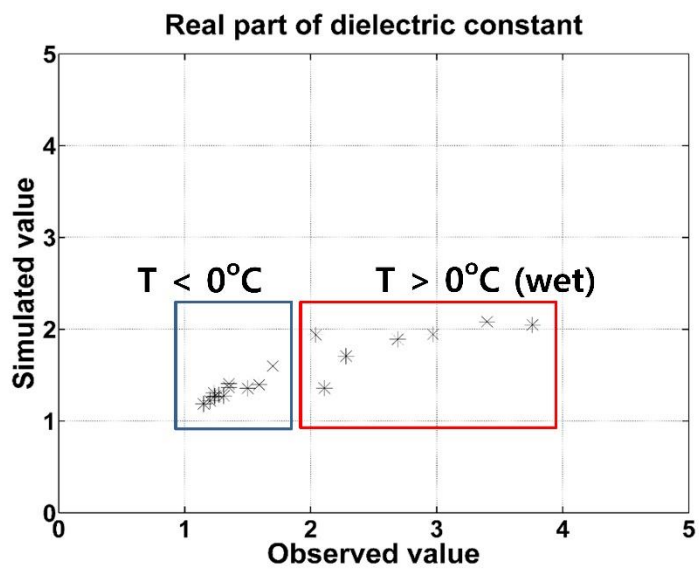


Figure 21. Comparison of observed dielectric constant (real) of snow surface and simulated dielectric constant (real) for the melting (red box) and freezing (blue box) season.

B. The scattering features from snow

It is difficult to understand the scattering features from snow cover with the conventional measurements of various GB-POLSCATs. Because the backscattering coefficient estimated by the measurements simply indicates the NRCS of snow cover, and the NRCS is determined by ensemble average of all backscattered signals induced by the surface and volume scattering from snow cover [60]. Therefore, it cannot explain in detail the scattering features from snow cover. On the other hand, Strozzi (1996) [36] showed the scattering profiles from the snow cover with the 5.3 GHz GB-POLSCAT with broad bandwidth (i.e. 1.4 GHz) (Table 3). Firstly, they measured the received electric field at 201 frequency points for the 4 polarizations (i.e. HH, VV, VH, and HV) at incidence angles between 0° and 70° on the snow cover, and converted the signal of frequency domain to the signal of time domain with inverse FFT method. They then computed the traveling times of signals from antennas to the snow surface and to the bottom at each incidence angles. To compute the correct travel times, the effect of the refraction by the snow cover was considered. Finally, they showed the scattering amplitude as a function of the snow height for the different incidence angles and polarizations.

In this study, the normalized intensity of the surface, bottom-surface, and volume scattering from snow cover was estimated with the scattering profiles. In order to distinguish each of the scattering features, time or distance range of each scattering feature was estimated by the pulse duration time (τ) of the GB-POLSCAT, and τ

can be easily determined as following

$$\tau = k_r B \quad (21)$$

where k_r is the sweep time, and B denotes the band width. These values of the GB-POLSCAT are described in Table 3.

As you can see in Figure 22, the intensity of the surface and bottom-surface scattering was estimated by the intensity summation of the backscattered signal for a pulse duration time at the snow surface and bottom, respectively, and the intensity of the volume scattering was estimated by the intensity summation of the backscattered signal between the snow surface and bottom. Finally, the normalized intensity of each scattering feature was calculated as following

$$\overline{P}_{surf} = \frac{\int_{t_{s2}}^{t_{s1}} |E_{pq}^r|^2 dt}{\int_{t_{b2}}^{t_{s1}} |E_{pq}^r|^2 dt} \quad (22)$$

$$\overline{P}_{bottom-surf} = \frac{\int_{t_{b2}}^{t_{b1}} |E_{pq}^r|^2 dt}{\int_{t_{b2}}^{t_{s1}} |E_{pq}^r|^2 dt} \quad (23)$$

$$\overline{P}_{vol} = \frac{\int_{t_{b1}}^{t_{s2}} |E_{pq}^r|^2 dt}{\int_{t_{b2}}^{t_{s1}} |E_{pq}^r|^2 dt} \quad (24)$$

where boundary conditions of each equation are described in Figure 22.

As a results, Figure 23 and Table 4 shows that the normalized intensity of each

scattering feature for 10° incidence angle and all polarizations. For the freezing season, the volume scattering (green bar) is relatively dominant than the other scattering features for HH and VV polarization. $\overline{P_{vol}}$ of HH and VV is about 55 and 56.1%, respectively. In case of cross polarizations (i.e. HV and VH), the bottom-surface scattering (red bar) is relatively dominant than the other scattering features. $\overline{P_{bottom-surf}}$ of HV and VH is about 54.3 and 56.1%, respectively. On the other hand, it shows completely different scattering patterns for the melting season. In this season, the surface scattering (blue bar) is strongly dominant for all polarizations. $\overline{P_{surf}}$ of HH, VV, HV, and VH is 88.5, 95, 76.7, and 72.5 %, respectively. In Figure 24 and Table 5, the bottom-surface scattering is predominant than the other scattering features for 40° incidence angle and all polarizations during the freezing season. $\overline{P_{bottom-surf}}$ of HH, VV, HV, and VH is 64.1, 66.4, 71.5, and 68.2 %, respectively, and the surface scattering is absolutely dominant for the melting season similar. $\overline{P_{surf}}$ is HH, VV, HV, and VH is 77.8, 84.9, 81.4, and 78.8 %, respectively.

These results show that most of the traveling signals are backscattered from the snow surface for the melting season because dielectric constant of the snow surface becomes high due to strong surface melting (Figure 21). In other words, it can say that polarimetric signatures of microwave must have been backscattered from the surface of the snow cover on sea ice for the melting season. That is, the backscattered signatures are not almost affected by the physical properties of sea ice, so it may be difficult to measure sea ice thickness using polarimetric scattering features of SAR data for the melting season. On the other hand, although the backscattered signal for low incidence angles and co-polarizations is relatively dominated by volume

scattering within the snow layer, the backscattered signal for high incidence angle and all polarizations is strongly dominated by the bottom-surface scattering from the snow cover during the freezing season. This shows that the polarimetric signatures can interact with the physical properties of sea ice for the freezing season. It is clear that first optimized condition to determine sea ice thickness is to acquire SAR data with high incidence angles (i.e. 40°) for the freezing season. In this condition, it can be ignored the scattering features from snow cover.

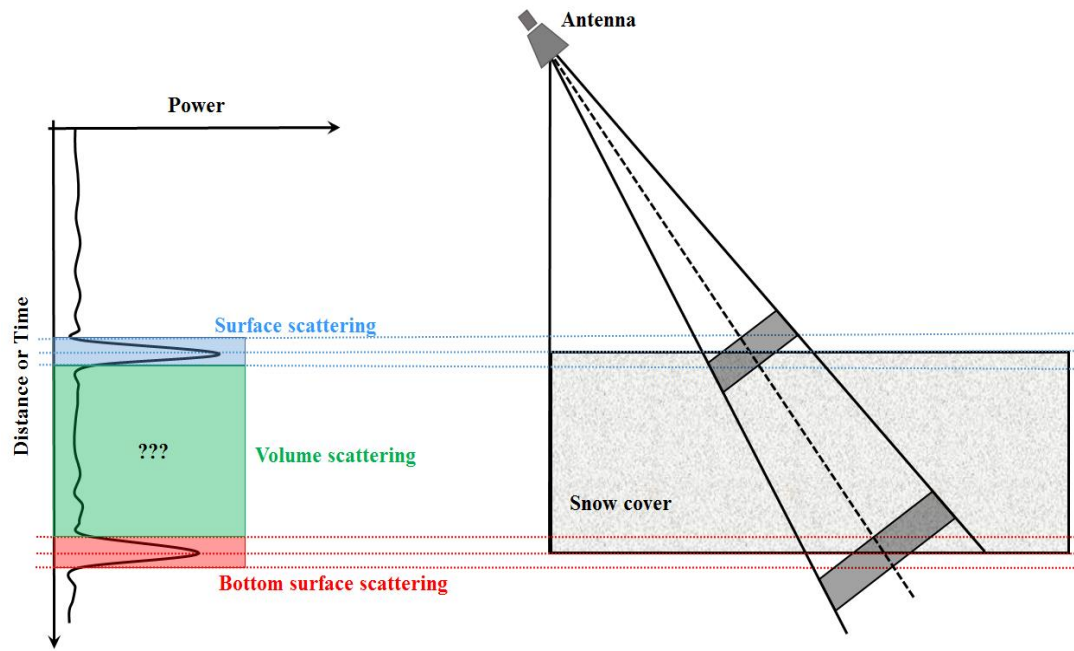


Figure 22. Scheme of scattering structures from snow cover in the GB-POLSCAT measurements.

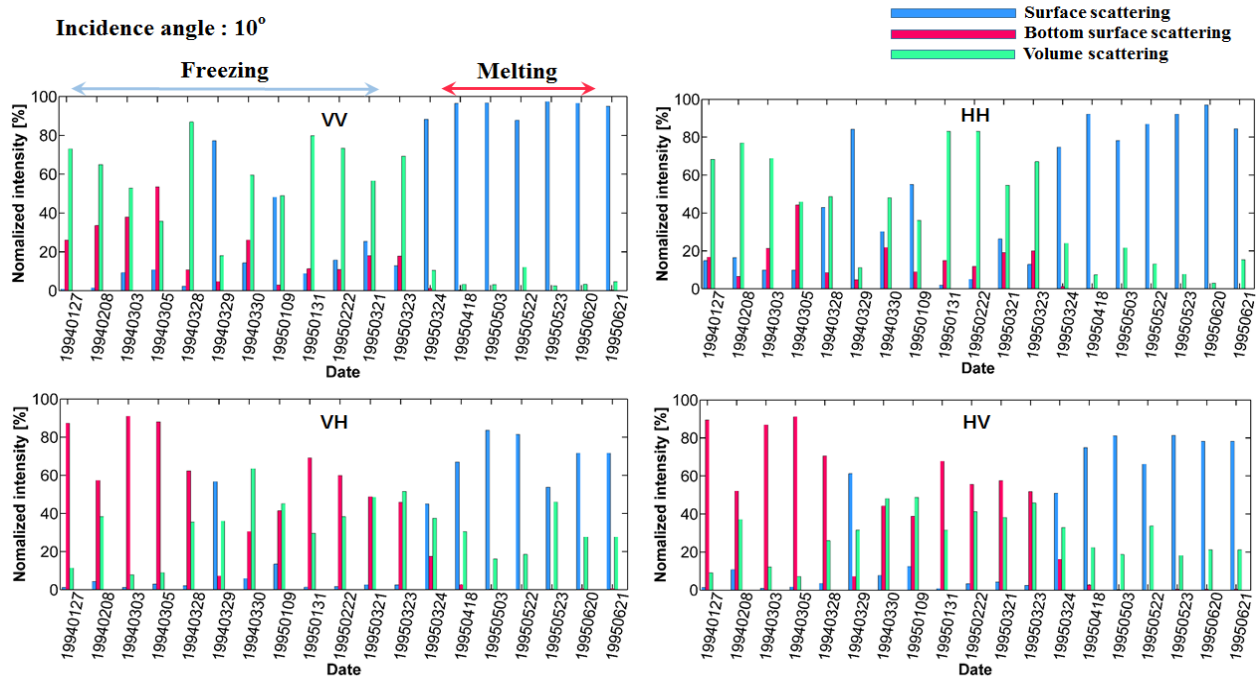


Figure 23. Normalized scattering intensity from snow cover with Strozzi's data for the melting and freezing season (Incidence angle: 10°).

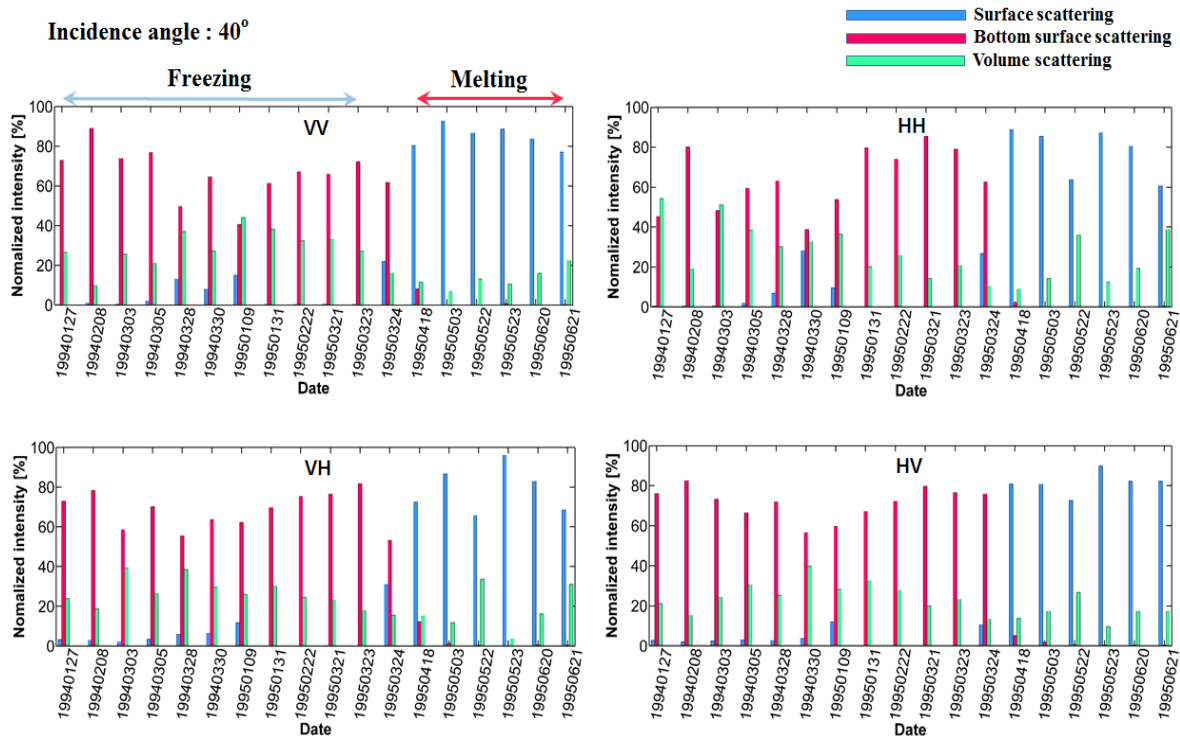


Figure 24. Normalized scattering intensity from snow cover with Strozzi's data for the melting and freezing season (Incidence angle: 40°).

Table 4. Averaged scattering intensities from snow cover for the freezing season.

| | Surface scattering | | Bottom-surface scattering | | Volume scattering | |
|-----------|--------------------|----------|---------------------------|---------------|-------------------|----------|
| | Inc. 10° | Inc. 40° | Inc. 10° | Inc. 40° | Inc. 10° | Inc. 40° |
| HH | 29.6 % | 6.3 % | 15.4 % | 64.1 % | 55 % | 29.6 % |
| VV | 24.3 % | 5.4 % | 19.6 % | 66.4 % | 56.1 % | 28.2 % |
| VH | 10.9 % | 5.6 % | 54.3 % | 68.2 % | 34.8 % | 26.2 % |
| HV | 12.4 % | 3.3 % | 56.1 % | 71.5 % | 31.5 % | 25.2 % |

Table 5. Averaged scattering intensities from snow cover for the melting season.

| | Surface scattering | | Bottom-surface scattering | | Volume scattering | |
|-----------|--------------------|---------------|---------------------------|----------|-------------------|----------|
| | Inc. 10° | Inc. 40° | Inc. 10° | Inc. 40° | Inc. 10° | Inc. 40° |
| HH | 88.5% | 77.8 % | 0.2 % | 0.6 % | 11.3 % | 21.6 % |
| VV | 95 % | 84.9 % | 0.2 % | 1.6 % | 4.8 % | 13.5 % |
| VH | 72.5 % | 78.8 % | 0.8 % | 2.6 % | 26.7 % | 18.6 % |
| HV | 76.7 % | 81.4 % | 0.7 % | 1.5 % | 22.6 % | 17.1 % |

3.3. Polarimetric scattering features of sea ice

Dielectric constant and surface roughness of sea ice can control the amount of a traveling radar signals with reflection, transmission, absorption, and dissipation. In order to understand the scattering features from the ice, it needs to understand these physical properties of sea ice. In the following sections, the physical properties were explored in detail with conditions determined in section 3.1.

A. Dielectric properties of sea ice

As mentioned above, dielectric constant of sea ice is strongly dependent on the salinity of the ice. In order to understand fluctuations of the salinity for the freezing season, it was used ice buoy data of Professor Hajo Eicken's research group at Alaska University from 1999 to 2009. The buoy was deployed on land-fast sea ice in the Chukchi Sea at Barrow, Alaska (Figure 25). Figure 26a shows the observed salinity profiles of FYI with various thicknesses for the freezing season. The profiles agree well with [51]'s results. As FYI grows, the salinity of the ice surface is rapidly decreased from 15 to 5 psu (i.e. real red line a \rightarrow d). In case of MYI, [51] showed the averaged profiles (real blue line e). The salinity of the ice surface is almost zero. In addition, [61]'s the profiles of MYI (Figure 26b) show that the salinity within the ice with MYI grows is gradually decreased from 1 to 0 psu although the salinity of all MYI surfaces is almost 0 psu.

Based on the salinity profiles as the ice grows, the dielectric constant model of sea

ice have been developed with various frequencies in several studies [49], [62]-[63]. In the frequency band of the space-borne SAR sensors introduced in Chapter 2, the models are as following

$$\varepsilon_i' = 3.04 + 0.0072 \frac{V_b}{V} \quad \varepsilon_i'' = 0.02 + 0.0033 \frac{V_b}{V} \quad (C - band) \quad (25)$$

$$\varepsilon_i' = 3.00 + 0.0120 \frac{V_b}{V} \quad \varepsilon_i'' = 0.00 + 0.010 \frac{V_b}{V} \quad (X - band) \quad (26)$$

where ε_i' and ε_i'' is the real and imaginary part of the sea ice dielectric constant, respectively. $\frac{V_b}{V}$ is the relative brine volume, and can be determined as following

$$\frac{V_b}{V} = \frac{\rho S_i}{\rho_b S_b} \quad (27)$$

Where ρ is the bulk ice density. S_b is the brine salinity. ρ_b is the brine density. S_i is the salinity of sea ice. These values can be determined as following, respectively [54].

$$\rho = \frac{\rho_i \rho_b S_b}{\rho_b S_b - S_i (\rho_b - \rho_i)} \quad (28)$$

$$\rho_b = 1 + 0.0008 S_b \quad (29)$$

$$S_i = 14.24 - 19.39 h_i \quad (h_i \leq 0.4) \quad | \quad S_i = 14.24 - 19.39 h_i \quad (h_i > 0.4) \quad (30)$$

where h_i is the thickness of sea ice

$$S_b = -3.9921 - 22.7T_i - 1.0015T_i^2 - 0.019956T_i^3 \quad (31)$$

where T_i is the temperature of sea ice, and can be determined as following [54]

$$T_i = \frac{h_s k_i T_w + h_i k_s T_a}{h_s k_i + h_i k_s} - 273.0 \quad (32)$$

where h_s is the snow depth, T_w is the sea temperature beneath the ice, T_a is the air temperature, k_s is the thermal conductivity of snow, and k_i is the thermal conductivity of the ice.

As mentioned above, thin FYI grows into thick FYI, it loses its brine (i.e., desalination), and thick FYI further loses its salinity during the melting season. These processes control the complex dielectric constants and the penetration depth of microwave into the ice. Here it is introduced a simple demonstration of evolution of complex dielectric constants as a function of ice thickness using the dielectric constant model. The penetration depth (δ) can be as following [64].

$$\delta = \frac{\lambda}{4\pi} \left\{ \left[\left(1 + \left(\frac{\varepsilon_i''}{\varepsilon_i'} \right)^2 \right) - 1 \right]^{0.5} \frac{\varepsilon_i'}{2} \right\}^{-0.5} \quad (33)$$

where λ is the wave length of microwave for the free space.

Figure 27 shows the calculated penetration depth of C- and X-band as a function of sea ice thickness. While the calculated dielectric constants decrease as the ice thickness increases, the penetration depth of C- and X-band increases as the ice thickness increases, mainly due to its lower salinity and subsequent decrease in both real and imaginary parts of complex dielectric constants. This suggests that the volume scattering within the ice can be increased as the ice grows due to the desalination process.

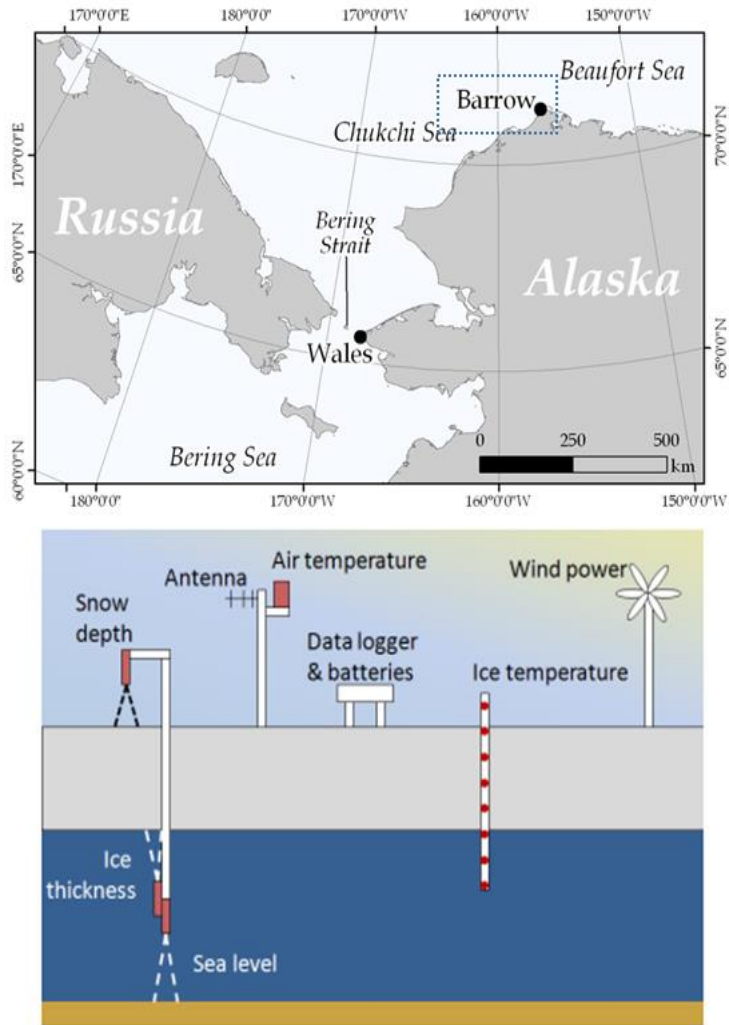


Figure 25. Measurement site of the ice buoy (top) and structures of the ice buoy (bottom) [from Prof. Hajo Eicken's homepage at Alaska University].

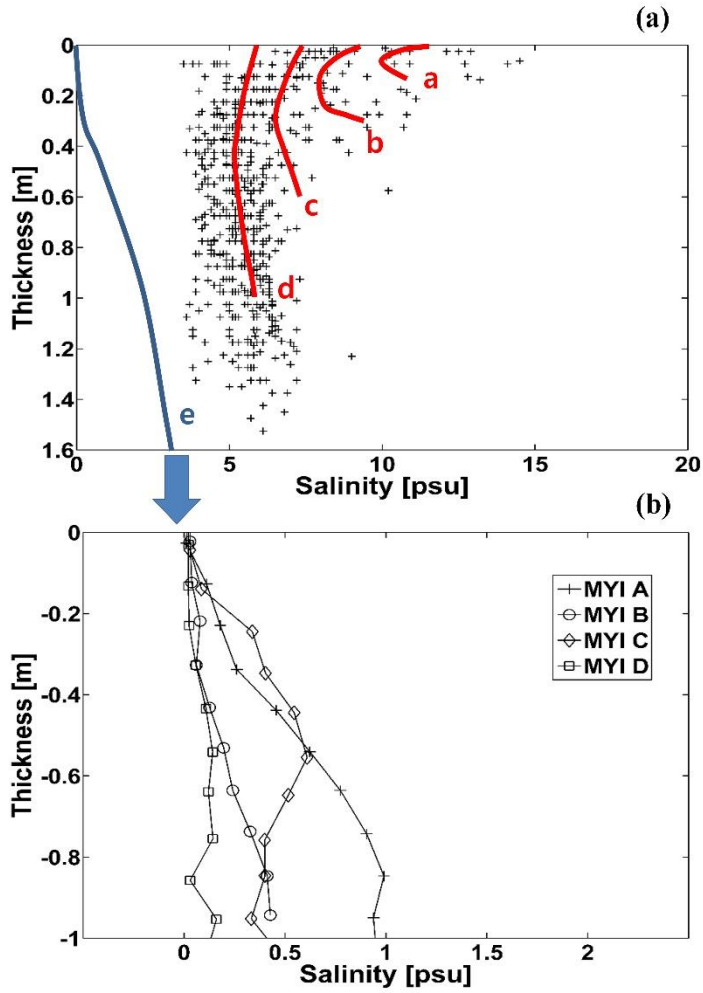


Figure 26. (a) the salinity profiles of FYI for the freezing season (red line a-d denote averaged salinity profiles as FYI grows, and blue line is averaged salinity profile of MYI in [51]) (b) the salinity profiles of MYI for the freezing season. From MYI A to MYI D, the thickness are gradually increased [61].

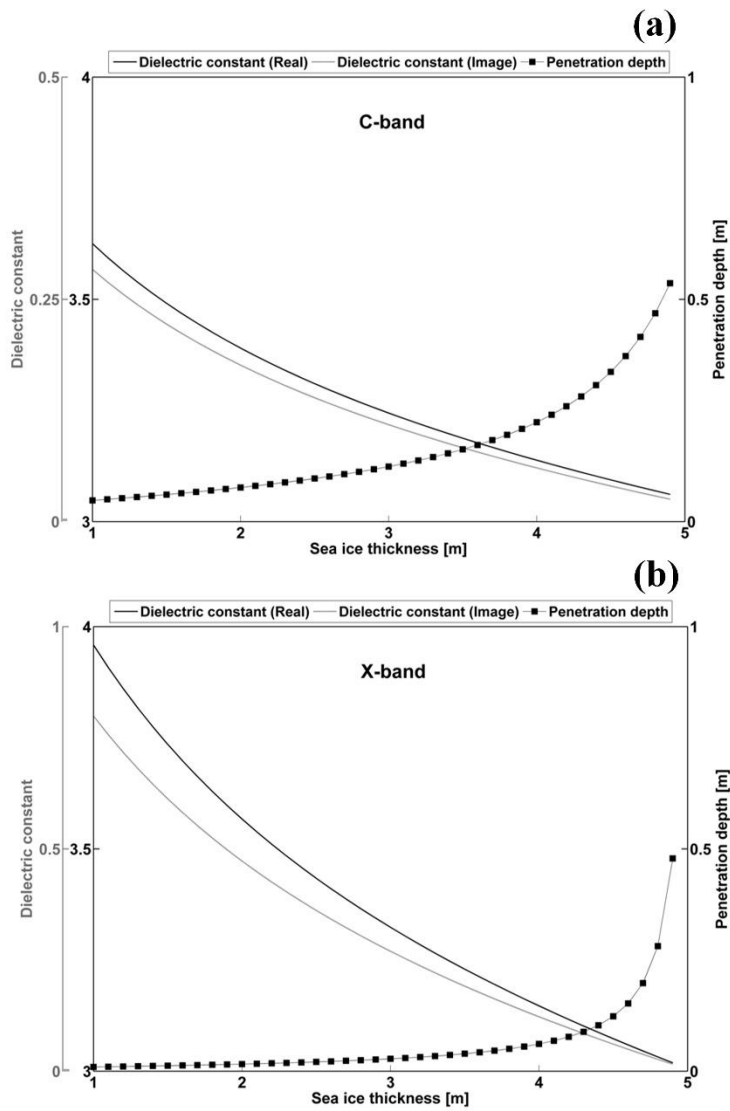


Figure 27. Dielectric constant (real and imaginary parts) and penetration depth as a function of sea ice thickness for C- and X-band frequencies. Left Y-axis represents the values of dielectric constant (black: real part, gray: imaginary part) and right Y-axis represents penetration depth. (a) C-band (b) X-band

B. Surface roughness of sea ice

The amount of surface roughness can control the amount of the backscattered signal on the ice surface. In general, small-scale (comparable with radar wavelength: a few cm) surface roughness of sea ice is important for the interpretation of SAR data. The small-scale surface roughness is usually induced by factors such as surface wind stress, snow-ice interface temperature, and so forth [65]. In particular, snow-ice interface temperature plays an important role in creating the differences in small-scale surface roughness between MYI and FYI during the sea ice growing season (Figure 28). The superimposed ice is ice created by re-frozen snow melt water at the snow-sea ice interface and can be one of the important factors in the determination of the short scale surface roughness of the sea ice [52]. Such a superimposed ice does not observe on the snow-FYI interface. Aside from small-scale surface roughness, large-scale surface (slope) can induce multiple scattering at the sea ice surface. Large-scale surface roughness (i.e., a few tens of cm) is primarily caused by sea ice compression and ridging processes, as shown in Figure 28. Peterson et al. [66] and Toyota et al. [67], [68] have showed that this scale of surface roughness is closely related to sea ice thickness due to ridging and drafting process that may occur as sea ice ages.

Gupta et al [69] showed that the distributions of surface roughness on the ice surface in the southeastern Beaufort Sea and the Amundsen Gulf in the western Canadian High Arctic with ship-based laser profiler. In case of FYI (Figure 29a), the

distribution of the surface is concentrated in Root Mean Square (RMS) height 0.02m. In case of MYI (Figure 29b), the RMS height is relatively concentrated between 0.05 and 0.08 m although the distribution is broadly dispersed. Therefore, it is reasonable to say that the scale of surface roughness is relatively increased as sea ice grows due to various process mentioned above although relationship between surface roughness and thickness of the ice thickness is relatively weak unlike dielectric properties of sea ice.

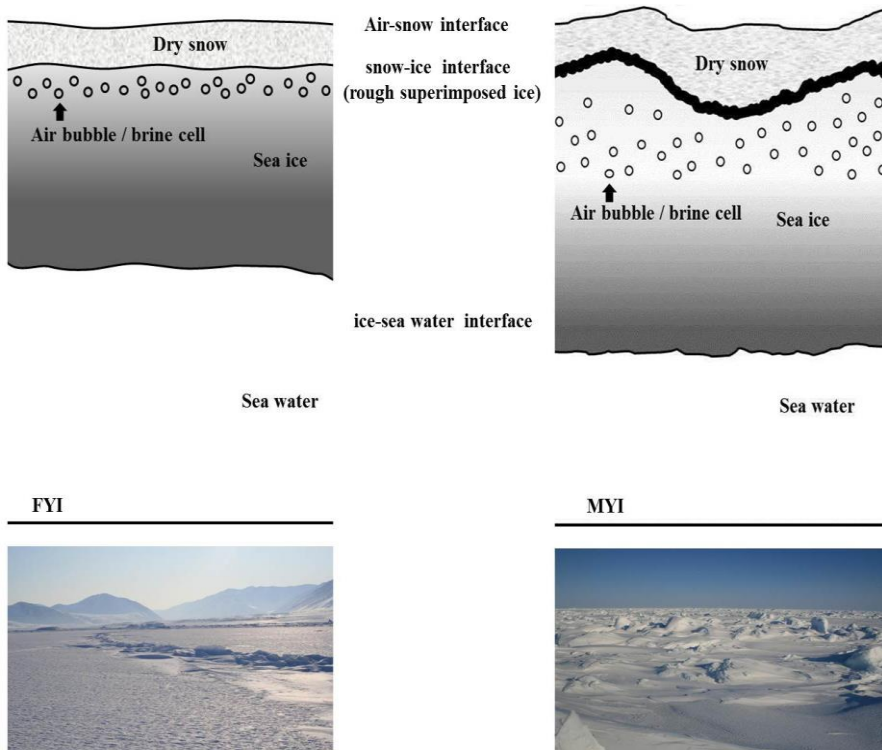


Figure 28. Cross-sectional view of FYI (left) and MYI (right) during the sea ice growing season. The lower bottom photographs show typical scenes of the corresponding sea ice type.

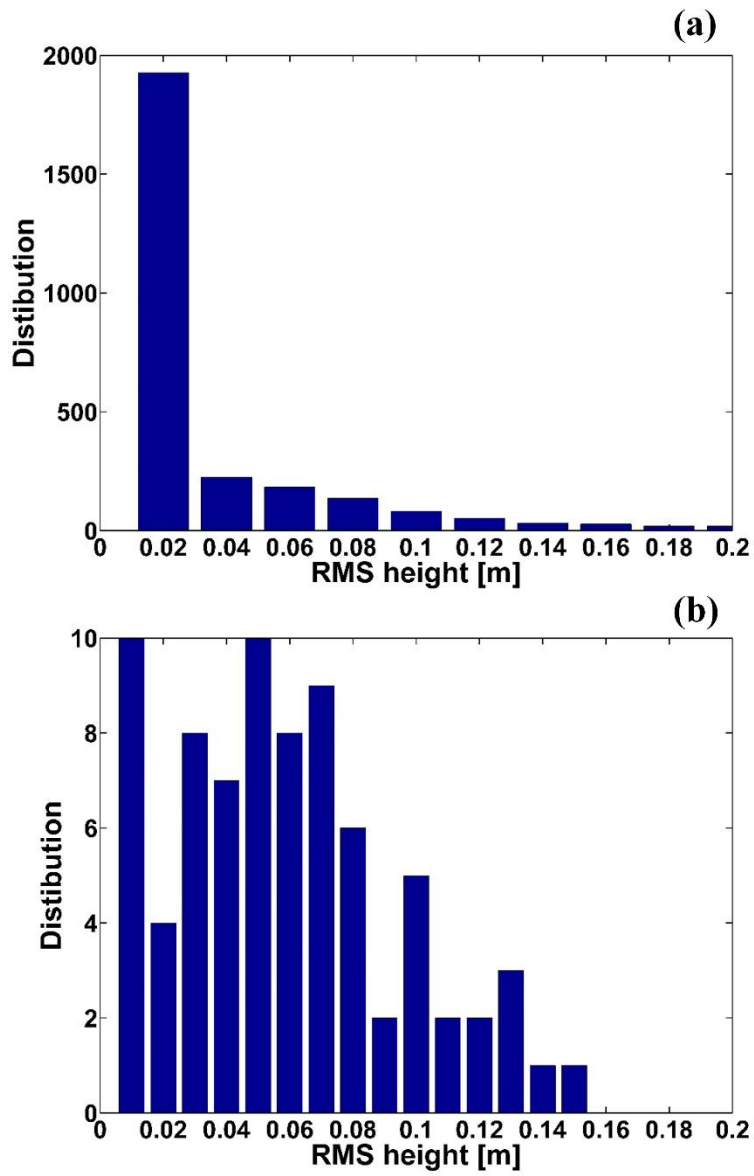


Figure 29. Distributions of FYI and FYI in [69]. (a) FYI (b) MYI

C. The scattering features from sea ice

Based on the contributions of the physical properties explained above, microwave is strongly backscattered from the surface of FYI due to high dielectric properties of the surface. Then, thicker and older sea ice tends to be rougher and less saline, and the backscattering signatures from the ice are not only originated from rough surface scattering but also from volume scattering within a low-density sub-surface layer [7],[11],[12]. Based on this, Kim et al [70] showed the NRCS distribution (5-18GHz, incidence angle: 40°, and HH polarization) of FYI and MYI with smooth and rough surface roughness estimated by field measurements and numerical simulations for the freezing season (Figure 30). The distribution can distinguish MYI from FYI for C- and X-band. That is, it is possible that the backscattering coefficient allow us to distinguish the sea ice type (i.e. FYI and MYI) in the optimized conditions. However, this result do not explain perfectly the optimized method to determine sea ice thickness. In next section, it is explored more distinct method to determine sea ice thickness using polarimetric signatures with physical interpretations.

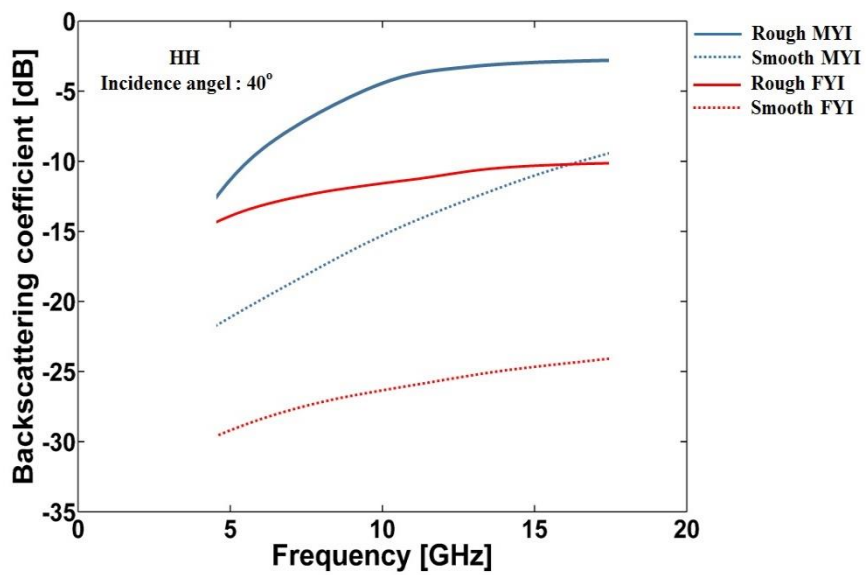


Figure 30. The distribution of backscattering coefficients from FYI and MYI [70] (red real line: rough FYI, red dotted line: smooth FYI, blue real line: rough MYI, and blue dotted line: smooth MYI).

3.4. Depolarization effects based on the polarimetric scattering features of sea ice

If the surface is rough, the scattered wave can be altered from the desired state of wave polarization – “depolarized”. The mechanism of multiple scattering at the rough surface causes the depolarization effects [71]. This depolarization effects can also be occurred within inhomogeneous bulk materials due to volume scattering. The co-polarized correlation and cross-polarized ratio have been used to measure the degree of depolarization effects [71], [72]. These depolarization factors have been used to snow mapping [72] and land classification applications [73]. For sea ice studies, Isleifson et al [74] calculated the co-polarized correlation from ship-mounted scatterometer measurements over thin FYI (2 - 69 cm) and tried to correlate the values with the ice thickness. No one-to-one relationship was found in that study, but they found two distinct the ice-thickness regimes (i.e. < 6 cm and > 8 cm). They suggested that the division of the two thickness regimes (two regimes of depolarization) was attributed to the difference in surface roughness and/or brine cells between the two thickness regimes. This experiment was however carried out only in newly formed thin sea ice (< 69 cm), and the relationship between the depolarization factors and the thickness of thicker and older sea ice has not been explored.

As mentioned above, thicker and older sea ice tends to be rougher and less saline. Small-scale surface roughness of older ice (i.e. MYI) can be higher than younger ice (i.e. FYI), mainly due to the presence of superimposed ice at the snow/ice interface

formed by re-frozen snow melt water [52]. Deformed (ridged and rafted) sea ice also tends to be thicker and rougher as previous studies [67], [68] have shown a good correlation between large-scale surface roughness and sea ice thickness due to ridging and rafting processes. MYI is thicker (mean wintertime thickness of about 3.2 m) and much less saline (about 2 ppt) than FYI (mean wintertime thickness of 2.1 m and bulk salinity of about 2-20 ppt). As the salinity of sea ice decreases, complex dielectric constants decrease, and it in turn increases the penetration depth of radar wave. Volume scattering become significantly enhanced with the presence of a low-density sub-surface layer of MYI. As surface roughness increases and desalination significantly slows down in thicker and older sea ice, it is the multiple scattering from snow/ice interface (e.g. superimposed ice, deformation-related) and volume scattering (e.g. low density layer) that affect depolarization for those ice types. Although it is a rather complex matter, these approaches were investigated via both in-situ observations and numerical modeling works. In numerical modeling works, we aim at estimating the degree of depolarization due to the multiple scattering from rough surface and volume scattering within sea ice with reasonable range of sea ice physical parameters.

A. Numerical experiments of the depolarization effects due to surface scattering from rough surface

In case of small-scale surface roughness, IEM model explained in Appendix A is used in order to simulate the depolarization factors (i.e. cross-polarization ratio) due to small-scale surface roughness. The depolarization factor of C- and X-band as a function of RMS height were simulated. The correlation length and the dielectric constant values suggested in [75] for typical sea ice types were used for the calculations. The results show increases in the calculated cross-polarized ratios with the RMS height (Figure 31). For the mean RMS values of small-scale surface roughness reported in [48] (0.48 cm for MYI and 0.27 cm for FYI), the calculated cross-polarized ratios of MYI (0.004 for C-band and 0.008 for X-band) are about two times higher than the ones of FYI (0.002 for C-band and 0.004 for X-band).

The extended Bragg model [76] would be a suitable surface scattering model that can implement the effects of those large-scale surface slopes. The coherence matrix determined from the pure Bragg scattering model cannot estimate depolarization power (i.e., HV power). However, the coherence matrix determined by the extended Bragg scattering model can estimate the depolarization power due to the azimuthally oriented surface angle (i.e., large-scale surface slopes, but less than a SAR resolution cell). Further details of extended Bragg model is described in Appendix B. In addition, we have converted the coherency matrix of the extended Bragg model to the covariance matrix using a special unitary transformation matrix in order to estimate the depolarization effects. The transformation equation is given by

$$[C] = [U][T][U]^{-1} \quad \text{here, } [U] = \frac{1}{\sqrt{2}} \begin{bmatrix} 1 & 1 & 0 \\ 1 & -1 & 0 \\ 0 & 0 & \sqrt{2} \end{bmatrix} \quad (34)$$

where C is the covariance matrix, T is the coherency matrix, and U is the special unitary transformation matrix. The converted covariance matrix of the extended Bragg model is given by the following:

$$[C] = \begin{bmatrix} \langle |S_{HH}|^2 \rangle & \langle S_{HH}S_{VV}^* \rangle & \sqrt{2}\langle S_{HH}S_{HV}^* \rangle \\ \langle S_{VV}S_{HH}^* \rangle & \langle |S_{VV}|^2 \rangle & \sqrt{2}\langle S_{VV}S_{HV}^* \rangle \\ \sqrt{2}\langle S_{HV}S_{HH}^* \rangle & \sqrt{2}\langle S_{HV}S_{VV}^* \rangle & 2\langle |S_{HV}|^2 \rangle \end{bmatrix} = \frac{m_s^2}{4} \begin{bmatrix} a & b & 0 \\ b & c & 0 \\ 0 & 0 & d \end{bmatrix} \quad (35)$$

$$\text{here, } a = C_1 + 2C_2 \text{sinc}(2\beta_1) + C_3[1 + \text{sinc}(4\beta_1)]$$

$$b = C_1 - C_3[1 + \text{sinc}(4\beta_1)]$$

$$c = C_1 - 2C_2 \text{sinc}(2\beta_1) + C_3[1 + \text{sinc}(4\beta_1)]$$

$$d = \sqrt{2}C_3[1 + \text{sinc}(4\beta_1)]$$

where C_1 , C_2 , and C_3 describe the Bragg components of the surface (Appendix B), m_s is the backscatter amplitude that contains information about the small-scale surface roughness condition of the surface, and β_1 denotes the azimuthally oriented surface angle (slope). The cross-polarized ratios and the co-polarized correlation can be estimated from the converted covariance matrix. In the simulation, the width of azimuthally oriented surface angle (β_1) was used as a measure of large-scale

roughness, because the width (range) of azimuthally oriented surface angles increases as the surface slope increases.

The results show increases in the depolarization for the higher large-scale surface roughness, showing a positive trend for cross-polarized ratios (Figure 32). It is important to note that cross-polarized ratio is almost insensitive of variations in the dielectric constant caused by changes between thick FYI and MYI. The results suggest that higher large-scale roughness (steeper surface slopes) caused by ridging or rafting could significantly increase depolarization. It should be noted that depolarization can be caused by the interaction between small-scale and large-scale roughness. These results clearly show significant depolarization due to both small-scale and large-scale surface roughness.

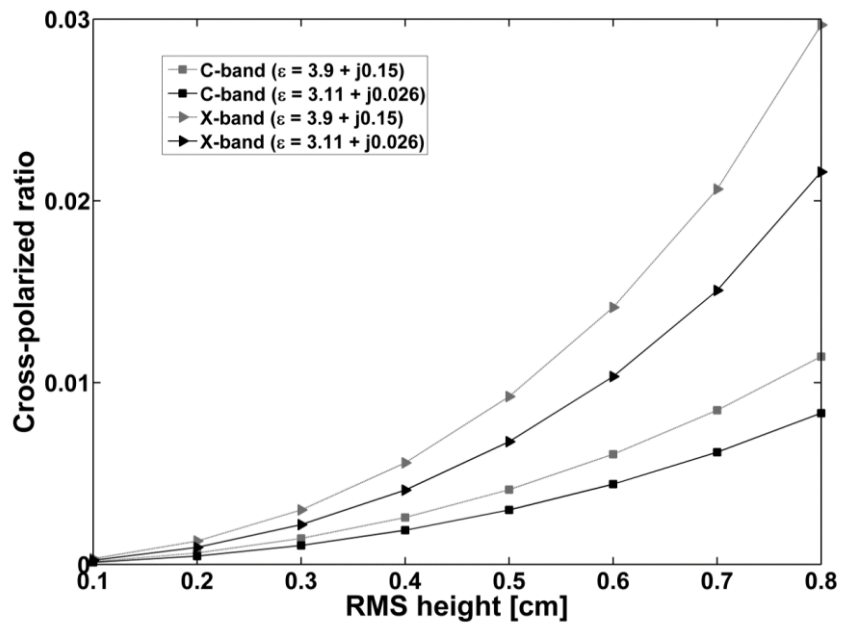


Figure 31. The variation of cross-polarized ratio (HV/HH) as a function of RMS height (small-scale roughness) for the C- and X-band.

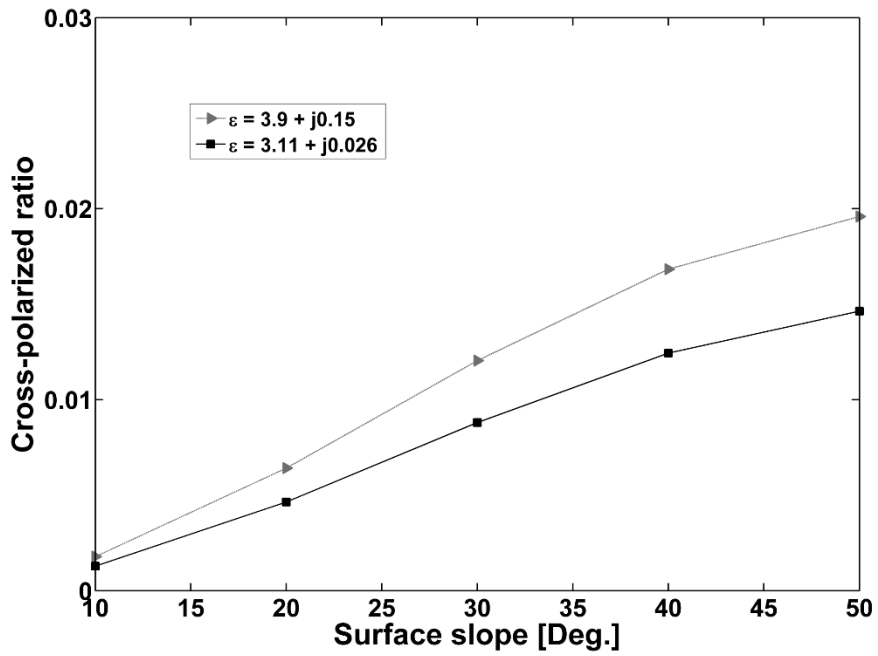


Figure 32. The variation of depolarization factors (cross polarized ratio) as a function of surface slope width (large-scale surface roughness) for the dielectric constants of thick FYI and MYI using extended-Bragg model.

B. Numerical experiments of the depolarization effects due to volume scattering within sea ice layer

As mentioned above, sea ice grows into thick ice, it loses its brine (i.e., desalination), and further loses its salinity during summer melt. These processes control the complex dielectric constants (penetration depth) and depolarization due to volume scattering. The volume scattering within sea ice have been generally simulated by Vector Radiative Transfer (VRT) theory [80],[81]. Detail description of VRT is introduced in Appendix C.

In order to simulate the relationship between the depolarization factors induced by volume scattering and sea ice thickness in the optimized conditions, the experiments of two case studies were set up. The first case is assumed that the surface of sea ice is flat, and the second case is assumed that the surface of sea ice is rougher as sea ice grows. For the simulation, changes of dielectric constant and penetration depth as sea ice grows (i.e. 0.1 ~ 5m) were first simulated by equations (19)-(27). Detail conditions of each simulation are illustrated by Figure 33a and b. Figure 34 shows that the changes of dielectric constant of C- and X-band agree well with the patterns of dielectric constant as sea ice grows explained by [77]-[79]. Using these results, polarimetric backscattering coefficients were simulated by the IEM and VRT models (Figure 35 - 38), and the cross polarized ratio (VH/VV) was estimated. The simulated cross polarized ratio (i.e. VH/VV) is increased as sea ice grows regardless of the change of incidence angle (Figure 39). In addition, the ratios simulated by case 1 and 2 experiments are almost same. That is, the ratio induced by volume scattering is

larger than the one induced by surface scattering. This shows that the backscattered signatures from sea ice can be dominantly depolarized by volume scattering within sea ice layer. Based on this, field experiments were conducted to mediate verify one-to-one relationship between the depolarization factors induced by volume scattering and the artificial ice thickness.

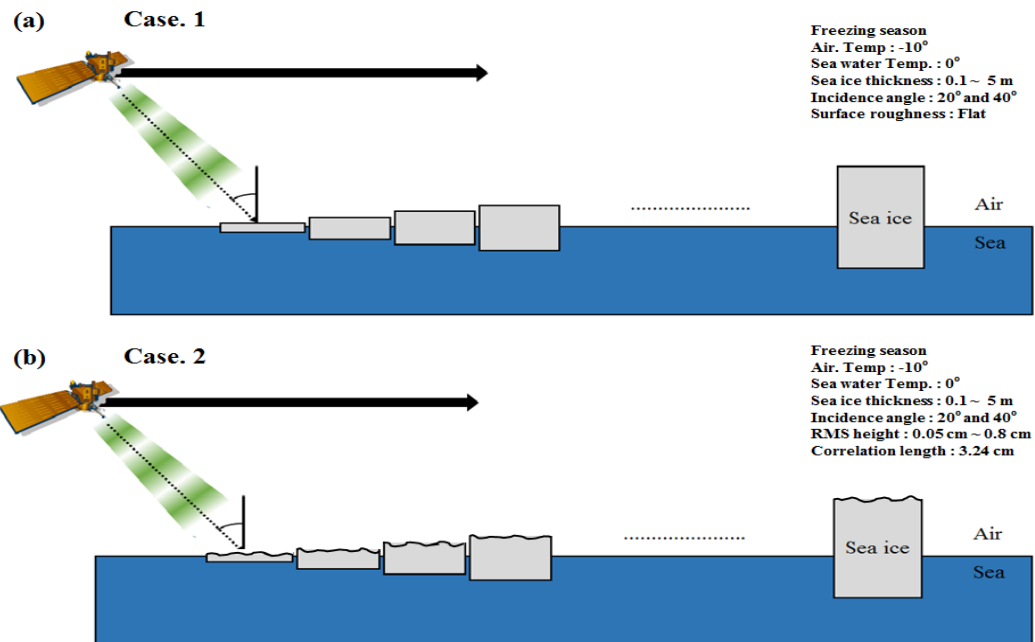


Figure 33. Set-up of VRT model simulation. (a) flat surface (only volume scattering) (b) relatively rough surface as sea ice grows (surface + volume scattering).

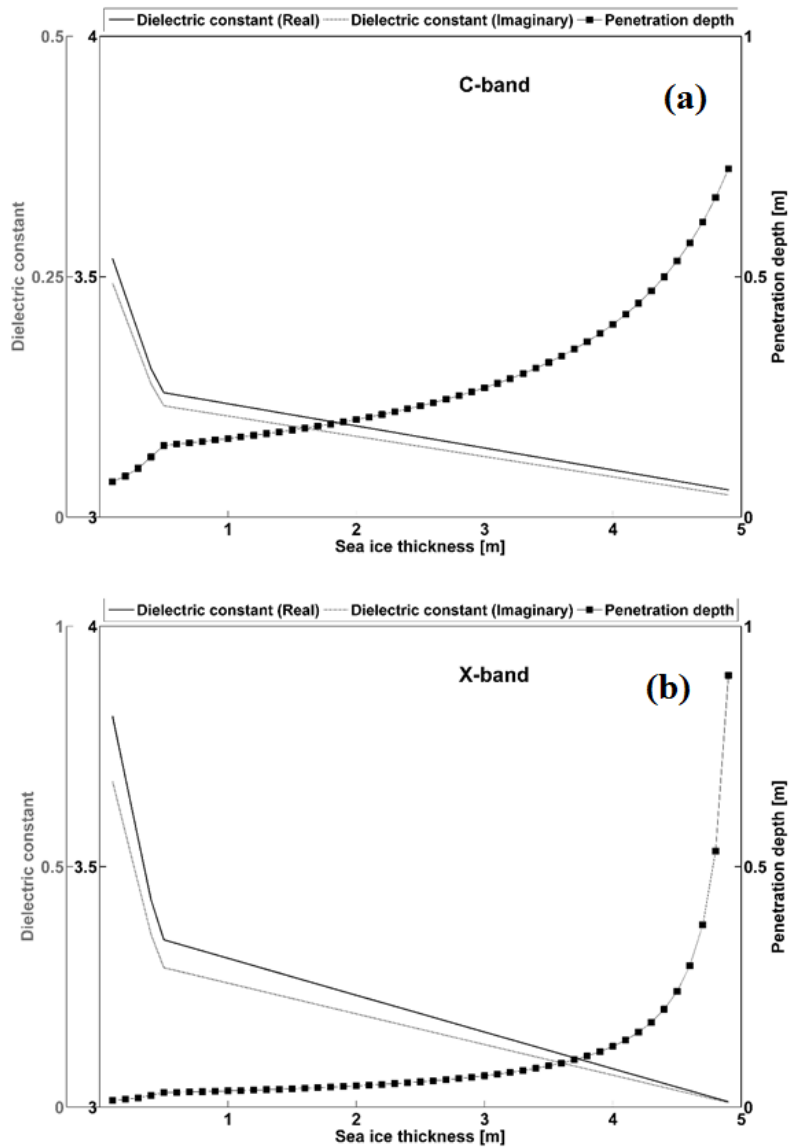


Figure 34. In the VRT simulation, dielectric constant (real and imaginary parts) and penetration depth as a function of sea ice thickness (i.e. 0.1 ~ 5 m) for C- and X-band frequencies. Left Y-axis represents the values of dielectric constant (black: real part, gray: imaginary part) and right Y-axis represents penetration depth.

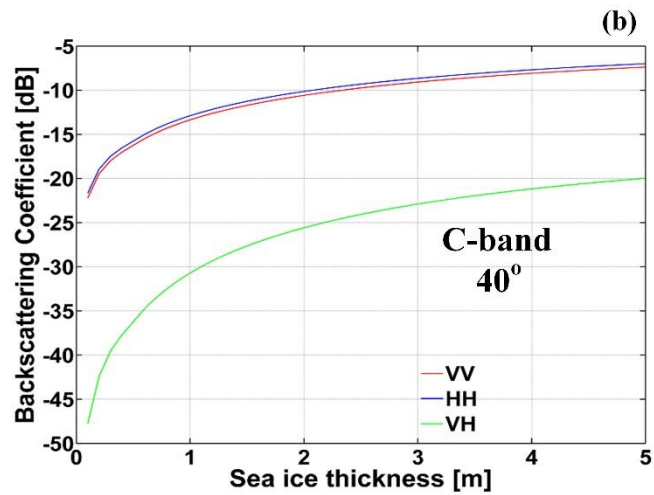
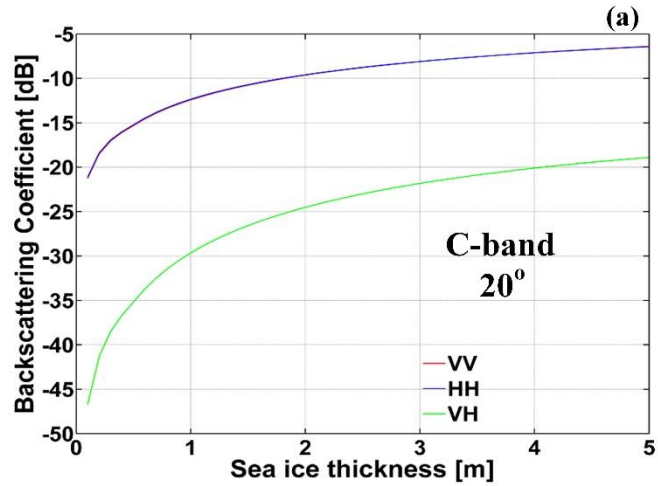


Figure 35. Backscattering coefficients (C-band) simulated by the VRT (Case 1, only volume scattering) as sea ice grows (red: VV, blue: HH, and green: VH). (a) incidence angle: 20° (b) incidence angle: 40°

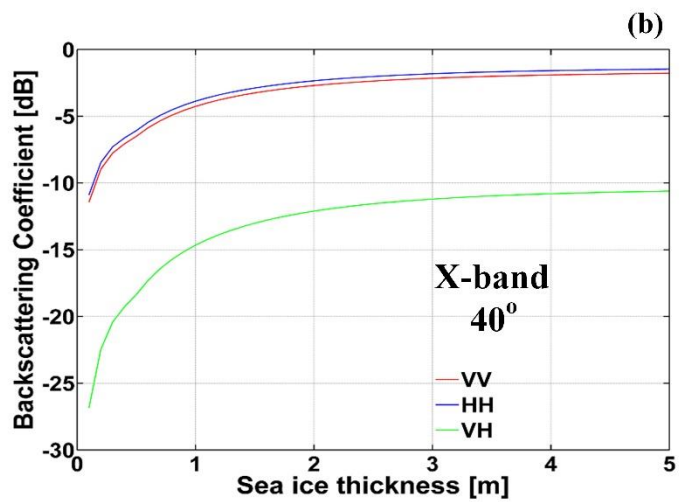
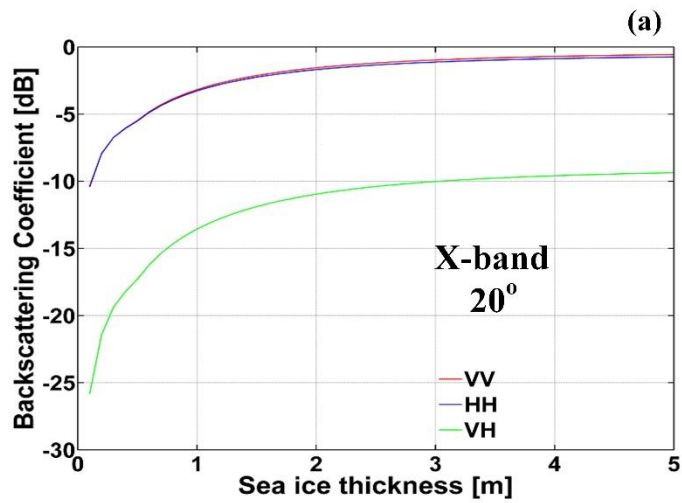


Figure 36. Backscattering coefficients (X-band) simulated by the VRT (Case 1, only volume scattering) as sea ice grows (red: VV, blue: HH, and green: VH). (a) incidence angle: 20° (b) incidence angle: 40°

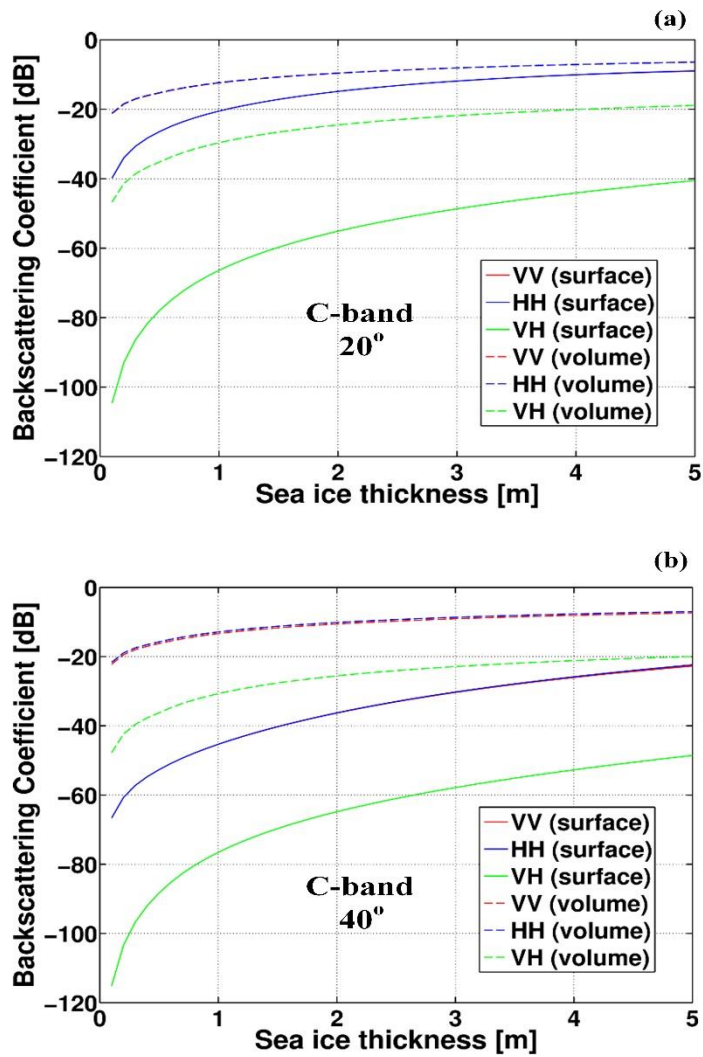


Figure 37. Backscattering coefficients (C-band) simulated by the VRT (Case 2, surface and volume scattering) as sea ice grows. Real line denotes simulated value by surface scattering, and dotted line denotes simulated value by volume scattering (red: VV, blue: HH, and green: VH). (a) incidence angle: 20° (b) incidence angle: 40°

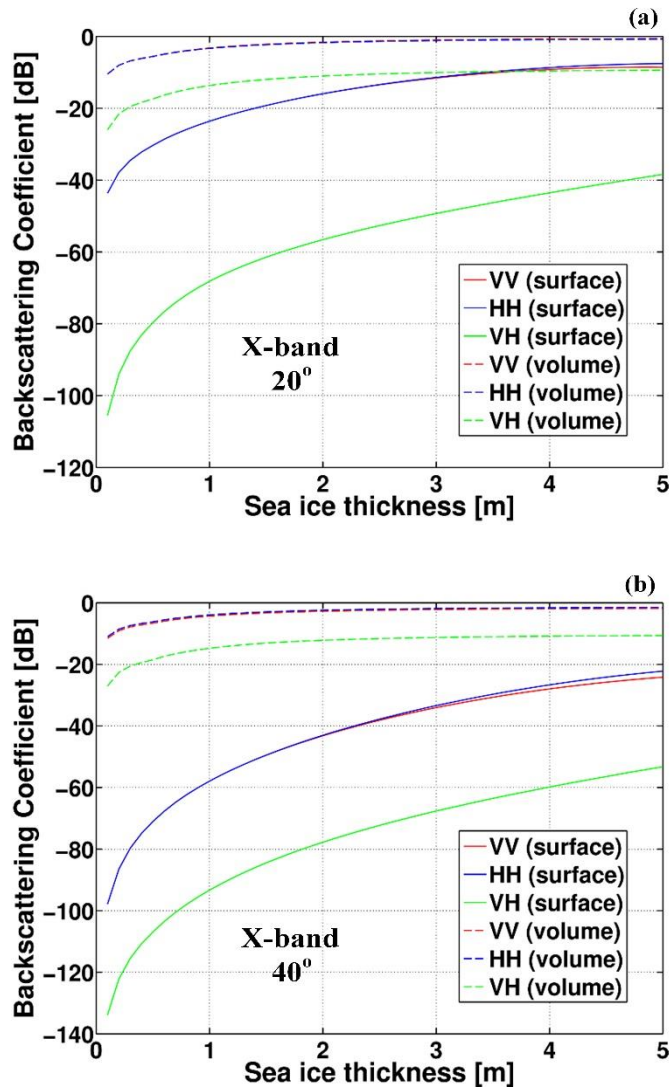


Figure 38. Backscattering coefficients (X-band) simulated by the VRT (Case 2, surface and volume scattering) as sea ice grows. Real line denotes simulated value by surface scattering, and dotted line denotes simulated value by volume scattering (red: VV, blue: HH, and green: VH). (a) incidence angle: 20° (b) incidence angle: 40°

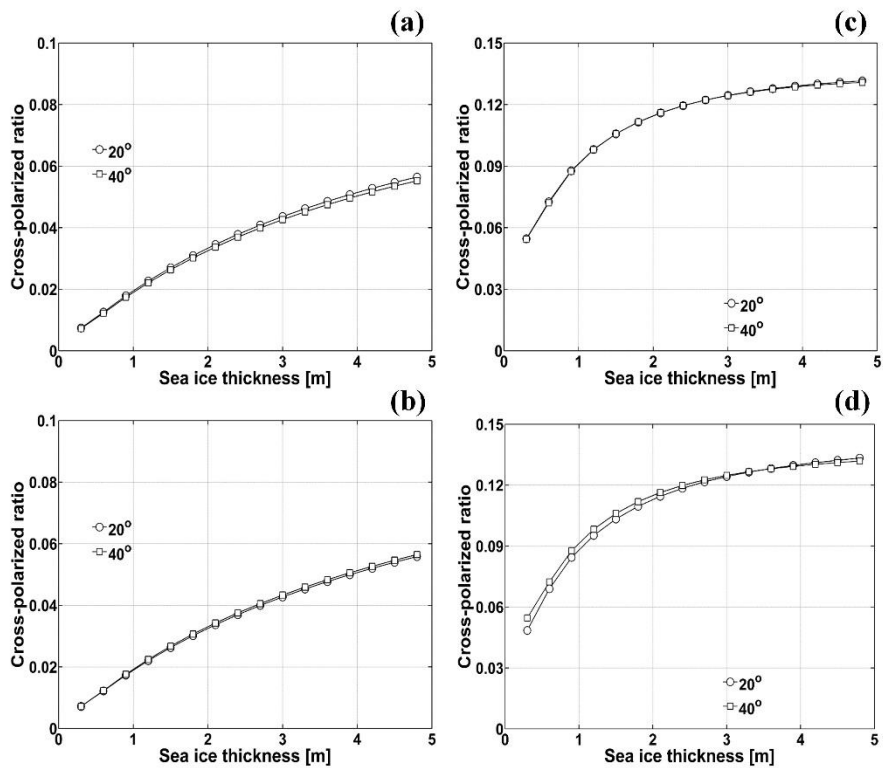


Figure 39. The relationship between depolarization factor (VH/VV) simulated by case 1 and 2 experiments and sea ice thickness. (a) C-band (case 1) (b) C-band (case 2) (c) X-band (case 1) (d) X-band (case 2)

C. Field experiments of the depolarization effects due to volume scattering within ice layer

Although the numerical simulations showed that the cross polarized ratio can be closely related to sea ice thickness due to the volume scattering within sea ice layer, it needs to verify this using field experiments. Here, the relationship between the ratio induced by volume scattering and the ice thickness was explored using measurements of artificially frozen ice with GB-POLSCAT (Figure 40). It measured the backscattered signatures from the ice with 140 and 190 cm of ice thickness, respectively. Detail specifications of the measurements are demonstrated in Table 6.

Figure 41 shows the backscattered signatures from the ice in the distance domain. In order to determine the position of ice surface, the backscattered signature was measured from the metal plate on the antenna aperture (dotted green line) and the ice surface (dotted black line). The position of ice bottom was determined by traveling distance of microwave estimated by Snell's law (Figure 42). The traveling distance within the ice (d_t) can be as following

$$\theta_t = \arcsin\left(\frac{\sqrt{\epsilon'_{air}}}{\sqrt{\epsilon'_{ice}}} \sin\theta_i\right) \quad (36)$$

$$d_t = \frac{d_i}{\cos\theta_t} \quad (37)$$

where θ_t is the transition angle. θ_i is the incidence angle. ϵ'_{air} is real part of

dielectric constant of air. ϵ'_{air} is real part of dielectric constant of ice. d_i is the ice thickness. The dielectric constant (real part) of air is 1, and of the ice is 3.15. It is assumed that the propagation velocity of microwave is same to the one of light. The backscattered signature from the antenna input was used the calibration of GB-POLSCAT based on new calibration method explained in Chapter 2.1.C

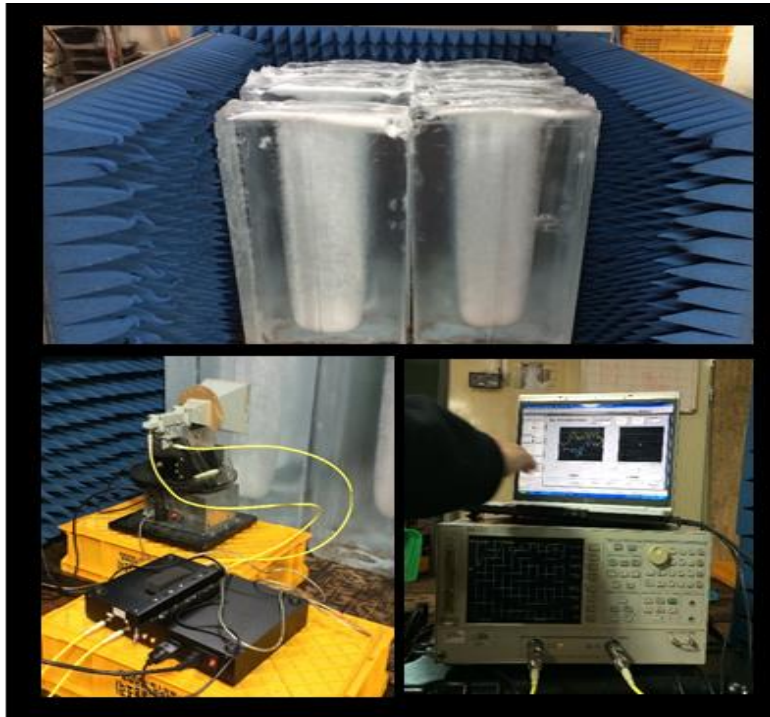


Figure 40. GB-POLSCAT measurement of artificially frozen ice.

Table 6. The specifications of the GB-POLSCAT measurement.

| Specifications | |
|---------------------------|---------------------------------------|
| Center Frequency | 5.275 GHz (C-band) |
| Sweep time | 1s |
| Bandwidth | 1.5 GHz |
| Transmitted Power | 20 dBm |
| Polarization | HH/VV/HV/VH |
| Incidence Angle | 0° ~ 40° |
| Calibration method | Kim et al [2012] |
| Measurement item | Radar response / Ice thickness |

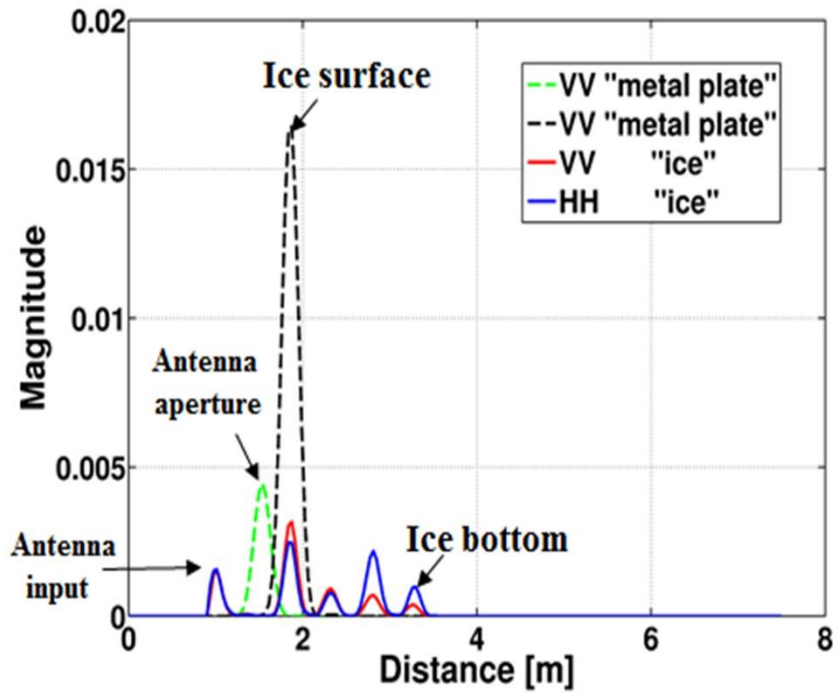


Figure 41. The measured backscattered signatures from the ice (blue real line: HH, red real line: VV). The green and black dotted line denotes the backscattered signatures from metal plate on the antenna aperture and the ice surface, respectively.

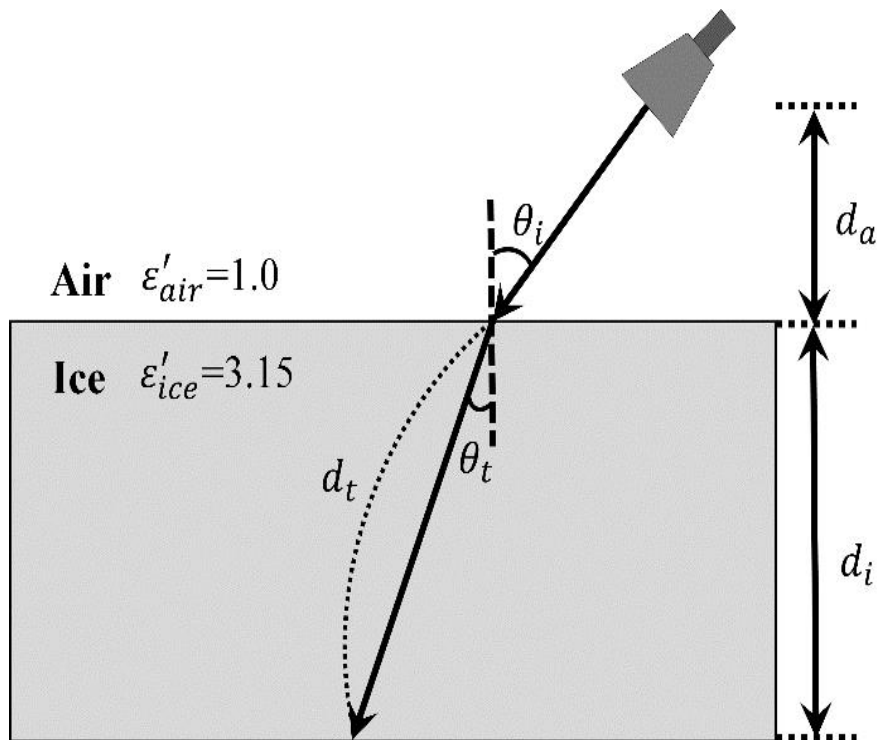


Figure 42. Refraction of microwave at the interface between the air and the ice based on Snell's law.

Figure 43 and 44 shows the backscattered signatures from each ice thickness. The range of incidence angle is from 0° to 40° (red dotted line: 0° , blue dotted line: 20° , and green dotted line: 40°). As incidence angle increases, the received power of the signals gradually decreases, and the phase is shifted due to the increase of the traveling distance. On the basis of this phase shift, each received power from surface, volume, and bottom of the ice is estimated using equation (16)-(18).

Figure 45 shows the normalized magnitude of each scattering feature. In all case experiments, volume scattering due to air bubbles within the ice is strongly dominant at 20° and 40° of incidence angle. Thus, it can be estimated that variation of the cross polarized ratio as the increase of the ice thickness. Table 7 shows the cross polarized ratio with the ice thickness. In the case 1 (the ice thickness = 140 cm), the ratio is 0.00097 and 0.00075 at 20° and 40° of incidence angle, respectively. In the case 2 (the ice thickness = 150 cm), the ratio is 0.0018 and 0.0016, respectively. That is, the increase of the ratio is 0.00083 and 0.00085 when the ice thickness increases from 140 to 190 cm. Through the numerical and the field studies, it is reasonable to say that the depolarization factors (i.e. the cross polarized ratio) are efficient parameter to determine sea ice thickness in the optimized conditions. Based on this, field experiments using space-borne SAR data were explored as case study, and it is described in next section.

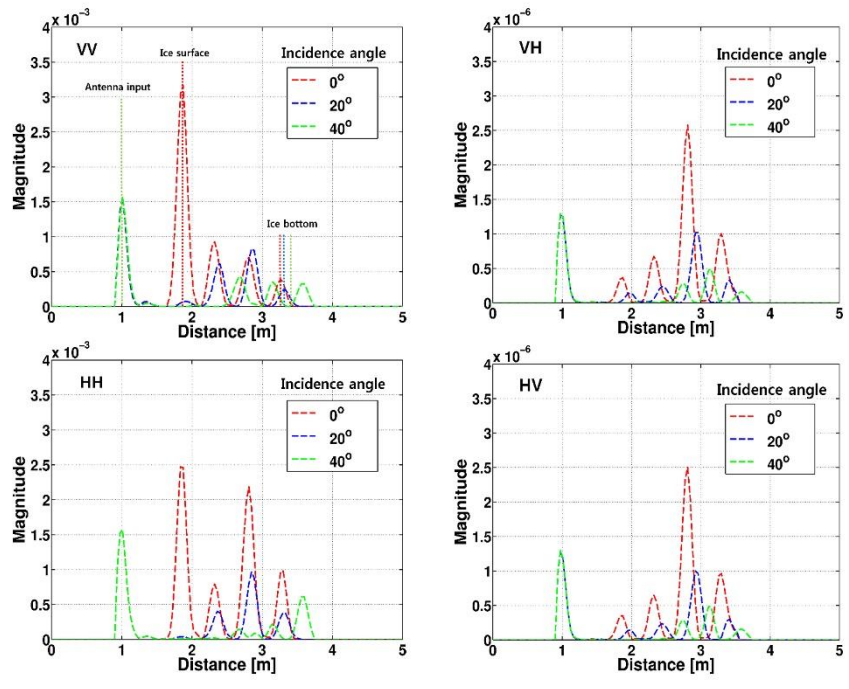


Figure 43. The backscattered signatures from the ice at 0°, 20°, and 40° of incidence angle. (the ice thickness = 140 cm)

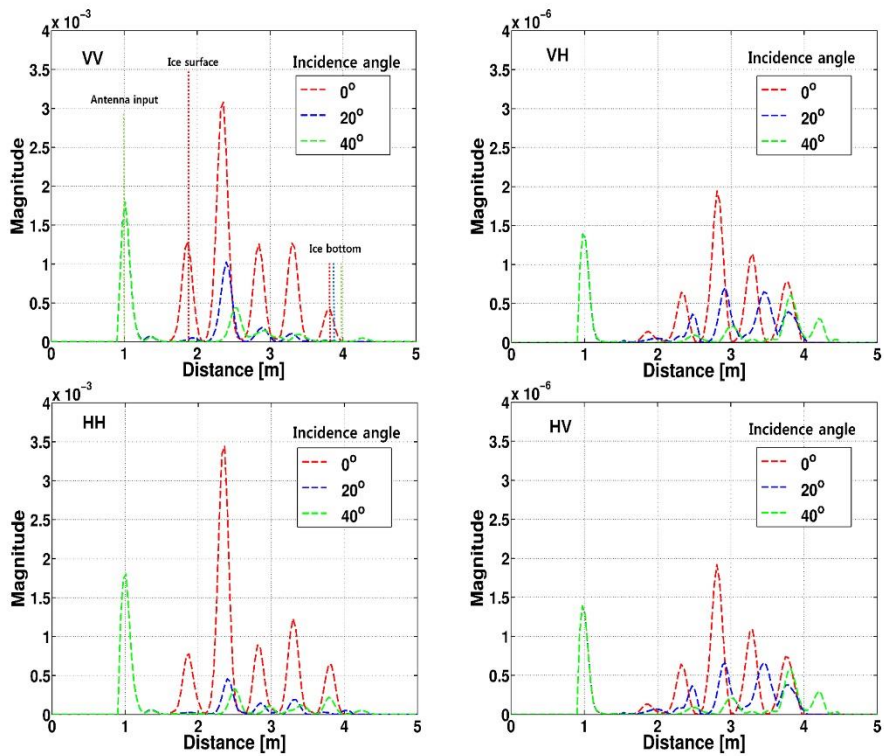


Figure 44. The backscattered signatures from the ice at 0°, 20°, and 40° of incidence angle. (the ice thickness = 190 cm)

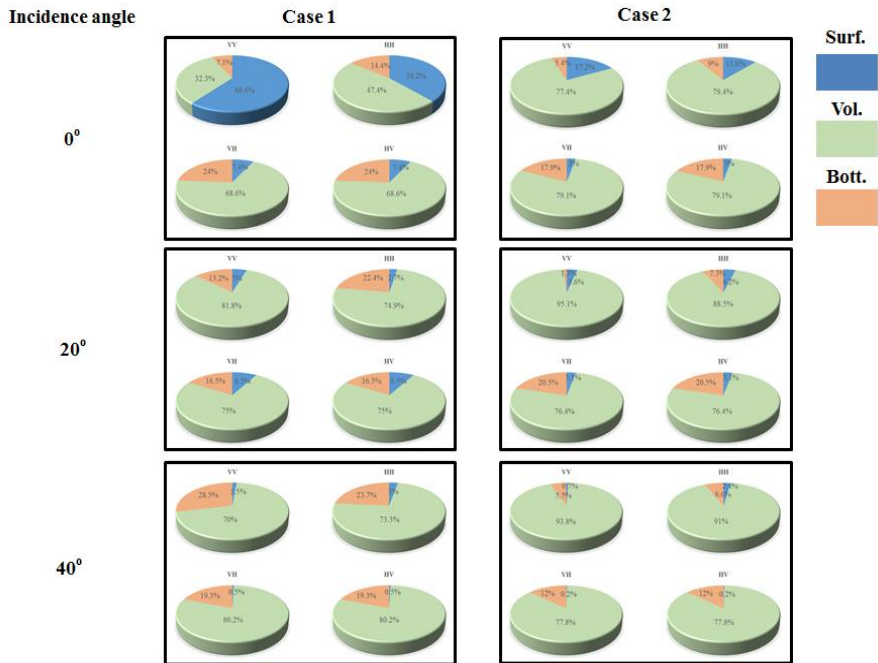


Figure 45. The normalized magnitude of surface, volume, and bottom-surface scattering from the ice at 0°, 20°, and 40° of incidence angle.

Table 7. The estimated cross polarized ratio in the case studies.

| | 20° | 40° |
|--|-----------------|-----------------|
| Case 1 (the ice thickness = 140 cm) | 0.00097 | 0.00075 |
| Case 2 (the ice thickness = 190 cm) | 0.0018 | 0.0016 |
| Difference | +0.00083 | +0.00085 |

Chapter 4. Measurement of sea ice thickness using space-borne SAR data in the Arctic Ocean

4.1. In-situ measurements and SAR data acquisition

An ice camp was set up on land-fast ice in the north of Greenland (Lat.: 83° 38.622 N, Lon.: 32° 14.245W) (Figure 46). This was part of an inter-disciplinary, scientific ice camp coordinated by the Danish Meteorological Institute (DMI) and the Danish Technological University (DTU). The land-fast ice camp was erected on May 1, 2009, and operated until May 6, 2009. Throughout the use of the ice camp, snow and ice thickness were measured using a snow probe and Electromagnetic Induction system (Model: Geonics EM31-SH). The EM31 can measure the magnitude of the in-phase and quadrature components of the secondary electro-magnetic field induced in the ground by the instrument's 9.8 kHz transmitted electro-magnetic field [22]. In the case of sea ice, the secondary field is primarily induced in the highly conductive sea water underneath the sea ice because of the low conductivity of sea ice. The magnitude of the secondary field is related directly to the distance between the instrument and the sea water below, and sea ice thickness can be estimated with known snow depth and instrument height above the snow surface.

At the ice camp, ice thickness were measured along the validation line, which stretched 1.5 km from smooth thick FYI in the south to rubble MYI in the North (Figure 47). The ice thickness of FYI was very stable at approximately 2 m, while the ice thickness of rubble MYI varied significantly. The mean air temperature was

about -18°C during ice camp. This presents an ideal case study to explore the possibility of using C- and X-band SAR data to estimate the ice thickness of both FYI and MYI.

Dual polarization TerraSAR-X data was acquired at 11:44 (UTC) on May 2, 2009, and two scenes of RADARSAT-2 were acquired at 10:42 (UTC) on April 28 and at 09:43 (UTC) on April 30, 2009, respectively (Figure 46). TerraSAR-X collected VV and HH polarization data in the Strip Map mode and RADARSAT-2 collected HH and HV (4/28), and VV and VH (4/30) dual-polarization data in the Standard Mode. All data were processed in Single-Look Complex (SLC) and slant-range projection to be used for polarimetric analysis. A speckle reduction filter (7×7 Lee filter) and radiometric calibration procedures were applied for the calculation of more accurate and reliable backscattering coefficients. Figure 48 shows the resulting backscattering coefficient images for TerraSAR-X and RADARSAT-2, respectively. The summary of the SAR data specifications are presented in Table 8.

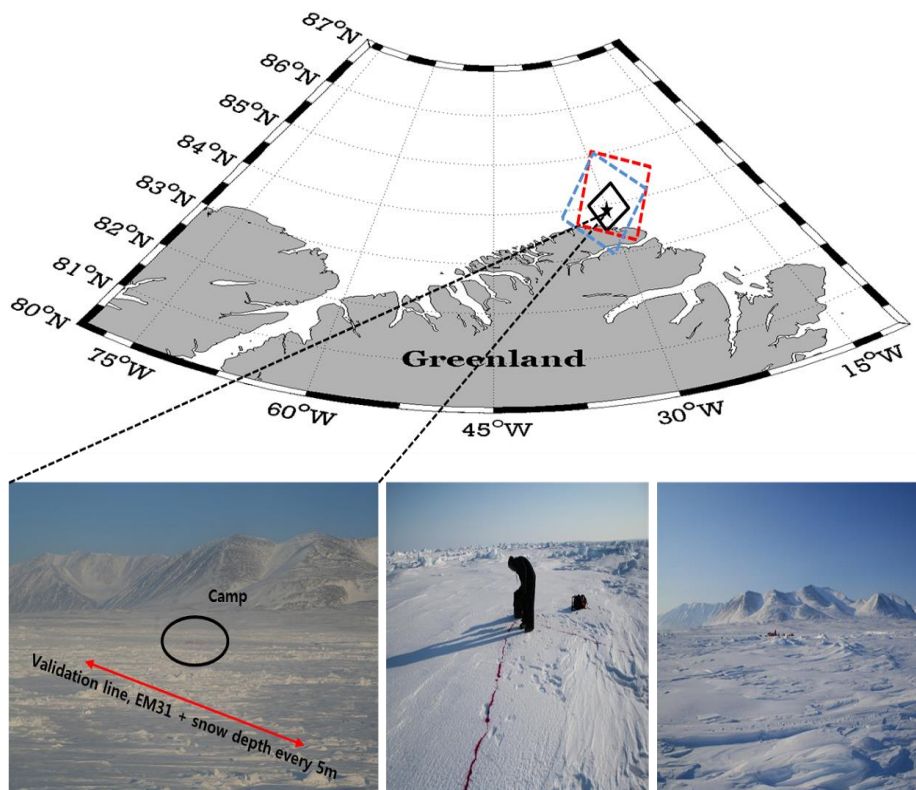


Figure 46. Study area off the northern coast of Greenland. The TerraSAR-X data was acquired on May 2, 2009 (black solid square). Two RADARSAT-2 data were acquired on April 28, 2009 (dotted blue square) and on April 30, 2009 (dotted red square), respectively. Ground truth data were obtained on May 01, 2009 (black star). The red line shown in lower left photograph represents the validation line on which the sea ice thickness and snow depth were measured using an EM31 instrument.

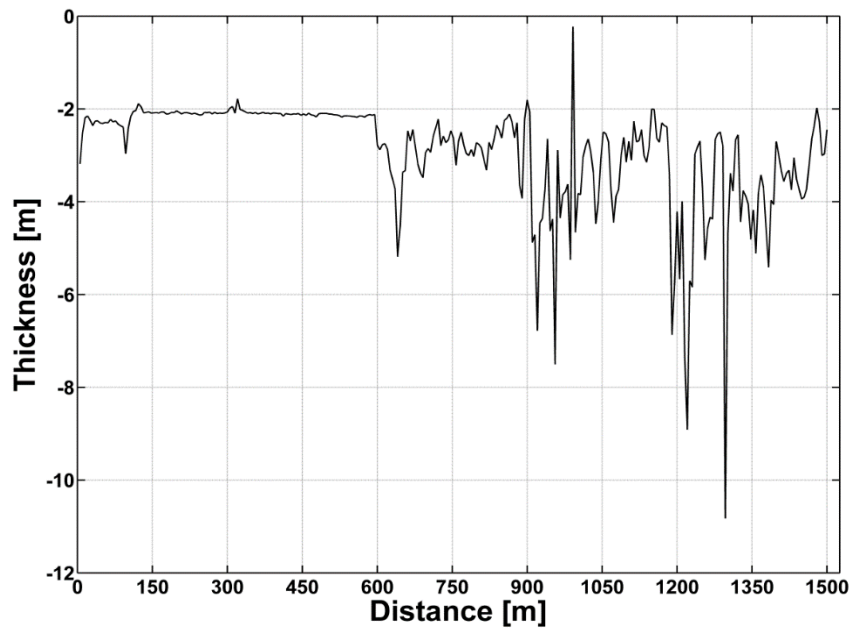


Figure 47. Sea ice thickness profile measured by the EM31 along the validation line (smooth thick FYI: 0~580 m, rubble MYI: 580~1500 m).

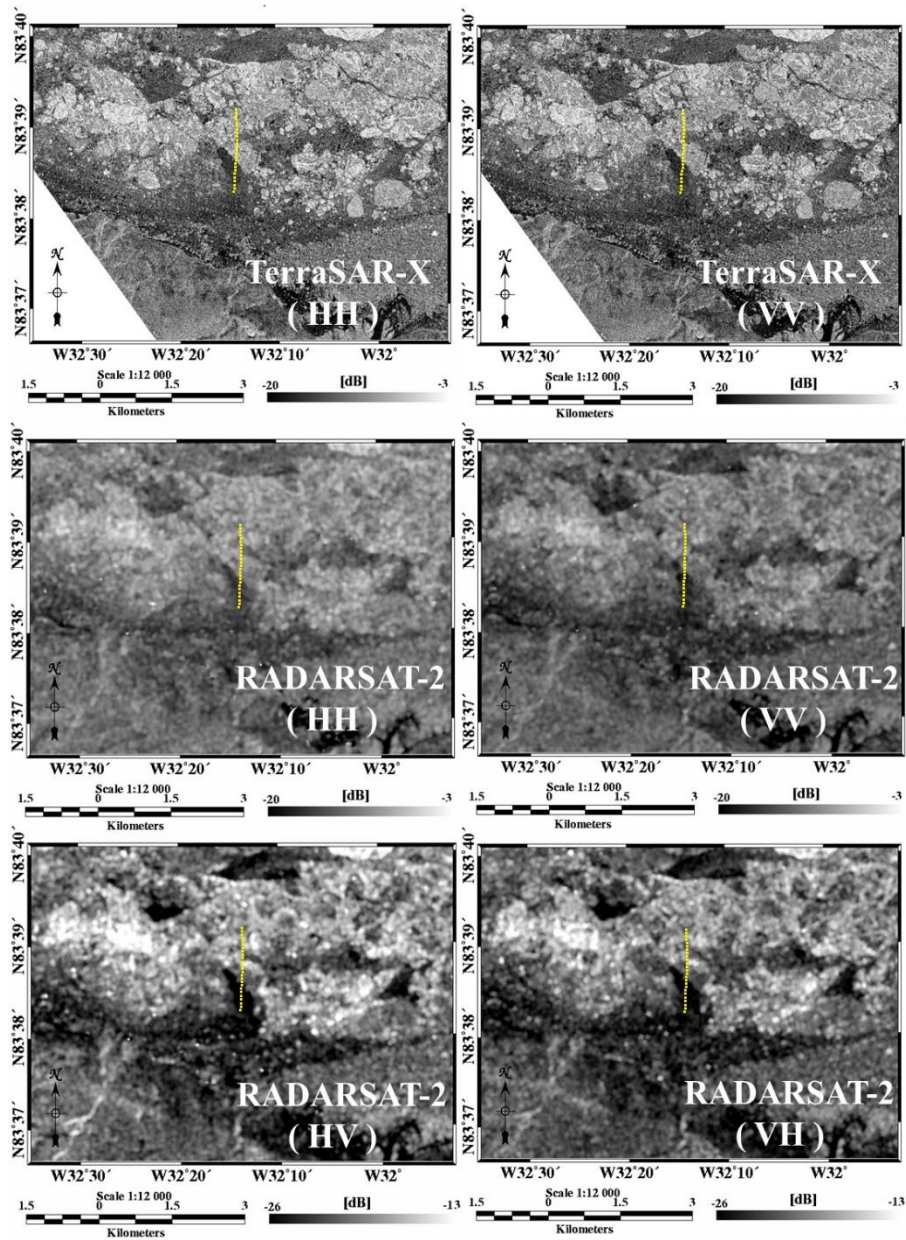


Figure 48. Radiometrically and geometrically calibrated SAR images (backscattering coefficients) of TerraSAR-X and RADARSAT-2. The yellow dots indicated in each figure represent the positions where sea ice thickness and snow depth were measured.

Table 8. Specifications of acquired TerraSAR-X and RADARSAT-2.

| <i>Acquisition date/time (UTC)</i> | <i>TerraSAR-X</i> | <i>RADARSAT-2</i> | |
|------------------------------------|------------------------------|---------------------------------|---------------------------------|
| | May 2, 2009 17:40 | April 28, 2009 10:42 | April 30, 2009 09:43 |
| <i>Center frequency</i> | 9.65 GHz (X-band) | 5.405 GHz (C-band) | 5.405 GHz (C-band) |
| <i>Polarization</i> | HH and VV | HH and HV | VV and VH |
| <i>Pixel spacing</i> | 3 m | 12.5 m | 12.5 m |
| <i>Incident angle</i> | 27.3° ~ 29.0° | 33.6° ~ 39.8° | 41.4° ~ 46.6° |

4.2. Depolarization-to-sea ice thickness relationship using space-borne SAR data

Both co-polarized correlation and cross-polarized ratio as depolarization factors were calculated from the SAR data, and the calculated values for each pixel were correlated to in-situ ice thickness. The results are presented as one-to-one scatter plots in Figure 49, showing strong and significant correlation coefficients (0.76 to 0.88) for both TerraSAR-X and RADARSAT-2. Co-polarized correlation for X-band varies 0.4 to 0.9 for the ice thickness range of 2.0 m to 5 m. Cross-polarized ratios for C-band range about 0.05 to 0.25 for the same range of sea ice thickness.

In first glance, the good correlation we found in this case study is likely due to contrast between smooth FYI and rubble MYI, however a close look reveals an interesting feature. The data points are rather continuous than clustered, especially for the case of RADARSAT-2 VH/VV. If the correlations are simply caused by a categorical difference in scattering mechanism between FYI and MYI, those data points should be more clustered. The continuous feature indicates that there might be a mechanism that thicker ice becomes rougher or higher volume scattering and in turn increases depolarization. In our case this mechanism involves ridging and rafting processes that increase the ice thickness and surface roughness as well as lower density layers within lifted ice blocks. Model simulation results for surface roughness showed a maximum of about 0.05 increases in cross-polarized ratio between FYI and

MYI, while about 0.05 (C-band) and 0.1 (X-band) increases for volume scattering. The combined value (about 0.1 ~ 0.2) from simulation is slightly smaller than the observed difference of 0.2. While considering uncertainty in model simulations, this suggests that depolarization in MYI can be attributed to both surface roughness and volume scattering which is closely related to ridging and rafting processes. Over smooth FYI, the cross-polarized ratio values are scattered at the same ice thickness. This indicates a case for de-correlation between ice thickness and roughness/volume scattering. In other words, FYI with the same ice thickness can have different surface roughness or/and volume scattering, and depolarization. In our case we observed patches of small rafting and higher snow on the surface of the smooth FYI. The effect of this scatter is relatively smaller than the correlation in MYI.

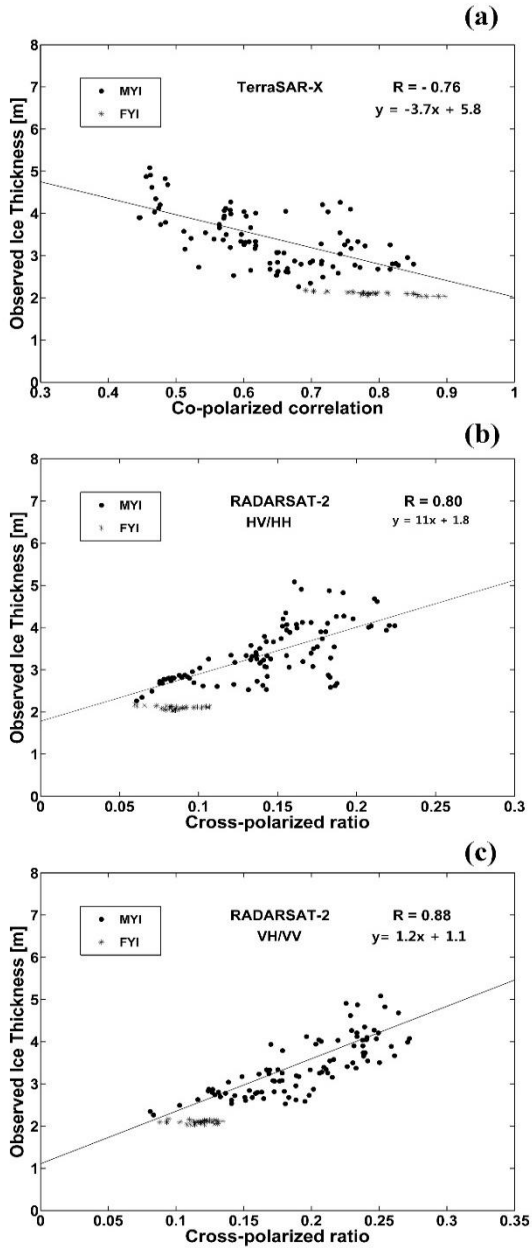


Figure 49. Relationship between the depolarization factors and observed sea ice thickness. (a) TerraSAR-X (5/02) (b) RADARSAT-2 (4/28) (c) RADARSAT-2 (4/30)

Chapter 5. Conclusion

5.1. Summary

This thesis presents numerical microwave scattering simulations and in-situ measurements with polarimetric RADAR (i.e. GB-POLSCAT and space-borne SAR) systems in order to investigate the optimum method for estimating sea ice thickness. Reanalysis of Strozzi's GB-POLSCAT measurements informed us that the backscattered signatures of microwave (C-band) from the surface of snow cover on sea ice can predominantly affect the space-borne SAR measurements for the melting season due to the high dielectric properties of the surface melting water. On the other hand, for the freezing season, the signatures with all polarization and high incidence angles can predominantly originate from the interface between the snow cover and the sea ice. Furthermore, in-situ measurements and numerical simulations of the physical properties (i.e. salinity, dielectric constant, and surface roughness) of sea ice as sea ice grows showed that sea ice tends to be rougher and less saline as sea ice grows during the freezing season. These mean that the multiple scattering of microwave from the surface and volume of sea ice can increase as the sea ice thickness increases during the freezing season. Thus, it could be proposed that relationship between sea ice thickness and the depolarization effect might exist because the depolarization effect of the backscattered signatures are strongly

dominated by the multiple scattering from a target.

Here, the degree of depolarization due to surface scattering from sea ice were simulated by dividing the roughness scales into small and large scales. IEM and extended Bragg models were used to simulate the degree of depolarization by small-scale and large-scale roughness, respectively, within a reasonable range of sea ice parameters. Furthermore, the degree of depolarization due to volume scattering was estimated by VRT simulation and GB-POLSCAT measurements. As a results, the cross-polarized ratio, one of the depolarization factors, has a distinct one-to-one relationship with sea ice thickness due to dominant depolarization effect induced by volume scattering within the ice layer. Based on these experiments, space-borne SAR data (one TerraSAR-X and two RADARSAT-2 scenes) were acquired along with in-situ sea ice thickness measurements. The depolarization factors (i.e., co-polarized correlation and cross-polarized ratio) were then calculated from acquired SAR data. At last, a strong and significant correlation between the ice thickness and the depolarization factors (correlation coefficients of 0.76 to 0.88) for both TerraSAR-X and RADARSAT-2 was found. Therefore, it is reasonable to say that the depolarization factors (i.e. the cross polarized ratio) extracted by space-borne SAR data are efficient parameters to determine sea ice thickness in the optimized conditions.

5.2. Discussion

The determination of sea ice thickness is the main issue of space-borne SAR measurements in the cryosphere, and various researches for this are being investigated. In this thesis, sensitivity studies conducted using numerical experiments and the observed results from polarimetric RADAR data have shown that the depolarization factors extracted by space-borne SAR data are effective parameters for the estimation of sea ice thickness.

However, this study restricts to conclude whether the ice thickness-to-depolarization relationship is an operational method to determine sea ice thickness. Because this relationship is not always able to satisfy under all dynamic nature of sea ice. For example, although pancake ice is a thin sea ice (i.e. its thickness is up to 10 cm), its surface roughness is relatively rougher than the one of universal thin sea ice due to periodic compressions of oceanic wave. Thus, the degree of depolarization estimated from pancake ice can be stronger than the one of universal thin sea ice due to multiple scattering from surface of the ice while the thickness of these ice are similar, and these can weaken the ice thickness-to-depolarization relationship.

Based on this view, in order to improve the operational applicability for determination of sea ice thickness using space-borne SAR data, the weakening factors of the ice thickness-to-depolarization relationship should be resolved. Although this thesis showed that the ice thickness and depolarization induced by multiple scattering

from surface of the ice can be correlated under optimized conditions, this relationship can break under specific conditions as mentioned above. On the other hand, the ice thickness and depolarization induced by volume scattering within the ice layer are strongly correlated by the desalination process as sea ice grows. That is, the operational capability can improve if depolarization effects induced by only volume scattering within the ice layer can be extracted from space-borne SAR data. Unfortunately, it is not easy because the backscattering coefficients estimated by space-borne SAR measurements are determined by the summation of the backscattered signatures induced by surface and volume scattering. Recent works have tried to quantitatively distinguish the contributions of each scattering from polarimetric SAR data with polarimetric decomposition and Polarimetric SAR Interferometry (Pol-InSAR) techniques. Therefore, future works require the investigations of capability for measuring sea ice thickness with these techniques, and if the operational method to measuring sea thickness using space-borne SAR data is successfully developed, it can be expected that global climate change process can understand more effectively such as thermal feedback between ocean, atmosphere, and the ice.

Appendix

In this appendix, the models used in this thesis are explained. The models can be classified into IEM, the extended Bragg, and VRT model. IEM and the extended Bragg model were used to simulate the backscattering features induced by the ice surface for small- and large-scale surface roughness, respectively. VRT was used to simulate the backscattering features induced within the ice layer.

A. Integral Equation Method (IEM)

This model can simulate backscattering coefficients from a target surface (σ_{pq}^S), the backscattering coefficients can be classified into single and multiple scattering ($\sigma_{pq}^S = \sigma_{pq}^s + \sigma_{pq}^m$) Single scattering can only induce the backscattering signatures of co-polarization while multiple scattering can induce the signatures of co- and cross-polarization [43]. In this model, the backscattering coefficients due to single or multiple scattering are as following

$$\sigma_{pq}^s = \frac{k^2}{2} \exp(2k_z^2 s^2) \sum_{n=1}^{\infty} |I_{pq}^n|^2 \frac{W^{(n)}(2k_x, 0)}{n!} \quad (\text{A.1})$$

$$\text{here, } |I_{pq}^n| = f_{pq} (2sk_z)^n \exp(-k_z^2 s^2) + \frac{(sk_z)^n [F_{pq}(-k_x, 0) + F_{pq}(k_x, 0)]}{2}$$

$$\sigma_{pq}^m = \frac{k^2}{16\pi} \exp(-2k_z^2 s^2) \sum_{n=1}^{\infty} \sum_{m=1}^{\infty} \frac{(k_z^2 s^2)^{n+m}}{n!m!} \quad (\text{A.2})$$

$$\cdot \int \left[|F_{pq}(u, v)|^2 + F_{pq}(u, v)F_{pq}^*(-u, -v) \right] W^{(n)}(-k_x, v)W^{(m)}(u + k_x, v)dudv$$

where superscripts s and m denote single and multiple scattering, respectively. k is the wave number. $k_x = k\sin\theta$, $k_z = k\cos\theta$, and θ is the incidence angle. u and v are scattering vector directions, s is the surface RMS height. $W^{(n)}$ and $W^{(m)}$ are the Fourier transform of the n^{th} or m^{th} power of the surface correlation function. f_{pq} is the Kirchhoff coefficient, and F_{pq} represents the complementary field coefficients.

B. Extended Bragg model

The extended Bragg model for a wider range of roughness conditions proposed by [76] is summarized. First, Bragg scattering coefficients are functions of the complex permittivity and the local incidence angle. Hence, it can write the following:

$$R_s = \frac{\cos\theta - \sqrt{\varepsilon - \sin^2\theta}}{\cos\theta + \sqrt{\varepsilon - \sin^2\theta}} \quad R_p = \frac{(\varepsilon - 1)[\sin^2\theta - \varepsilon(1 + \sin^2\theta)]}{(\varepsilon\cos\theta + \sqrt{\varepsilon - \sin^2\theta})^2} \quad (\text{B.1})$$

where R_s and R_p denote the horizontal and the vertical Bragg scattering coefficients, respectively. ε is the complex permittivity and θ is the local

incidence angle. The polarimetric scattering matrix S for a Bragg surface can be written as

$$[S] = \begin{bmatrix} S_{HH} & S_{HV} \\ S_{VH} & S_{VV} \end{bmatrix} = m_s \begin{bmatrix} R_s & 0 \\ 0 & R_p \end{bmatrix} \quad (\text{B.2})$$

where m_s is the backscatter amplitude that contains information regarding the roughness condition of the surface. The coherency matrix can be formed by employing a scattering vector \underline{k} as the vectorization of the scattering matrix using the Pauli spin matrices basis set. Its formation can be described as follows:

$$\underline{k} = \frac{1}{2} \text{Trace}([S][\Psi]) = \frac{1}{\sqrt{2}} [S_{HH+VV} \quad S_{HH-VV} \quad 2S_{HV}]^T$$

here, $[\Psi] = \left\{ \sqrt{2} \begin{bmatrix} 1 & 0 \\ 0 & 1 \end{bmatrix} \quad \sqrt{2} \begin{bmatrix} 1 & 0 \\ 0 & -1 \end{bmatrix} \quad \sqrt{2} \begin{bmatrix} 0 & 1 \\ 1 & 0 \end{bmatrix} \right\}$ (B.3)

$$[T] = \langle \underline{k} \cdot \underline{k}^{-1} \rangle = \begin{bmatrix} T_{11} & T_{12} & T_{13} \\ T_{21} & T_{22} & T_{23} \\ T_{31} & T_{32} & T_{33} \end{bmatrix}$$

where $[\Psi]$ denotes the Pauli spin matrices basis set. In order to extend the Bragg scattering model for a wider range of roughness conditions, Hajnsek et al. [76]

introduced a method of modeling the surface disturbance as a reflection symmetric depolarizer by rotating the Bragg coherency matrix about an angle, β , in the plane perpendicular to the scattering plane. This rotation of the Bragg coherency matrix can be expressed as follows:

$$[T] = m_s^2 [A] \begin{bmatrix} \langle |R_s + R_p|^2 \rangle & \langle (R_s + R_p)(R_s - R_p)^* \rangle & 0 \\ \langle (R_s - R_p)(R_s + R_p)^* \rangle & \langle |R_s - R_p|^2 \rangle & 0 \\ 0 & 0 & 0 \end{bmatrix} [A]^T \quad (\text{B.4})$$

$$\text{here, } [A] = \begin{bmatrix} 1 & 0 & 0 \\ 0 & \cos 2\beta & \sin 2\beta \\ 0 & -\sin 2\beta & \cos 2\beta \end{bmatrix}$$

Using a uniform distribution density function of β

$$P(\beta) = \begin{cases} \frac{1}{2\beta_1} & |\beta| \leq \beta_1 \\ 0 & 0 \leq \beta_1 \leq \frac{\pi}{2} \end{cases} \quad (\text{B.5})$$

The coherency matrix for a rough surface can be determined as follows:

$$\begin{aligned}
[T] &= \int_0^{2\pi} T(\beta)P(\beta)d\beta \\
&= \frac{m_s^2}{2} \begin{bmatrix} C_1 & C_2 \text{sinc}(2\beta_1) & 0 \\ C_2 \text{sinc}(2\beta_1) & C_3[1 + \text{sinc}(4\beta_1)] & 0 \\ 0 & 0 & C_3[1 - \text{sinc}(4\beta_1)] \end{bmatrix} \quad (\text{B.6})
\end{aligned}$$

The coefficients C_1 , C_2 , and C_3 describe the Bragg components of the surface and are given by

$$C_1 = |R_s + R_p|^2 \quad C_2 = (R_s + R_p)(R_s^* - R_p^*) \quad C_3 = \frac{1}{2}|R_s - R_p|^2 \quad (\text{B.7})$$

C. Vector Radiative Transfer (VRT)

In this model, the scattering and propagation of the traveling signal with a specific intensity in a medium can be defined by [77]

$$\cos\theta \frac{dI}{dz} = -\kappa_e I + \int P I dz \quad (\text{C.1})$$

where I is the specific intensity which is defined by the Stokes vector. κ_e is the extinction matrix, and P is the phase matrix of scatterer within a target layer. z denotes the penetration depth of microwave. κ_e can be estimated to sum between the scattering and the absorption coefficient of the scatterer [77]. P is strongly

connected with the shape, reflectivity, and etc. of the scatterer. In general, many sea ice simulations with VRT [60], [77], it was assumed that the scatterer within the ice layer is Rayleigh scatterer (i.e. the shape of the scatterer is a sphere and radius of the scatterer \ll wave length of microwave). The phase matrix of Rayleigh scatterer was well explained in [80]. Equation (C.1) is generally solved by iterative method with 2nd order solution [80], and the physical meanings of each order solutions were described minutely in [81].

Total backscattering coefficients simulated by VRT is as following

$$\sigma_{pq}^{total} = \sigma_{pq}^0 + \sigma_{pq}^1 + \sigma_{pq}^2 \quad (C.2)$$

where superscripts 0, 1, and 2 denote zeroth-, first-, and second-order backscattering coefficient, respectively. The zeroth-order solution is surface scattering component (Figure 50). Thus, the component was solved by IEM simulation (i.e. σ_{pq}^S) like [81]. Figure 51 shows the backscattering coefficients of first and second order solution with the physical meanings. The first order solution of VRT can be classified into three components (Figure 51a, b, and c). First and second are interaction components between bottom-surface and the scatterer within the layer, and third is single scattering component from the scatterer within the layer. Backscattering coefficients of the each component are as following

$$\sigma_{pq}^{VS} = \cos\theta_s T_p^i T_q^s \sec\theta_s^t L_p L_q \sigma_{pq}^S \quad (\text{C.3})$$

$$\begin{aligned} \sigma_{pq}^a &= \cos\theta_{t0} T_{10p}(\theta_{t0}, \theta_{i1}) T_{01q}(\theta_{t1}, \theta_{i0}) L_q(\theta_{t1}) \sec\theta_{s2} \\ &\cdot \int_0^{2\pi} \int_0^{\frac{\pi}{2}} \sin\theta \sec\theta \cdot \sum_{u=v,h} \sigma_{uq}^{VS}(\theta, \phi | \pi - \theta_{i2}, \phi_{i2}) \\ &\cdot P_{pu}(\phi_{ss1}, \theta_{ss1} | \theta, \phi) \frac{L_p(\theta_{ss1}) - L_u(\theta)}{\kappa_{eu}(\theta) \sec\theta - \kappa_{ep}(\theta_{ss1}) \sec\theta_{ss1}} d\phi d\theta \end{aligned} \quad (\text{C.4})$$

$$\begin{aligned} \sigma_{pq}^b &= \cos\theta_{t0} T_{10p}(\theta_{t0}, \theta_{i1}) T_{01q}(\theta_{t1}, \theta_{i0}) L_q(\theta_{t1}) \sec\theta_{s2} \\ &\cdot \int_0^{2\pi} \int_0^{\frac{\pi}{2}} \sin\theta \sec\theta \cdot \sum_{u=v,h} \sigma_{pu}^{VS}(\theta_{s2}, \phi_{s2} | \pi - \theta, \phi) \\ &\cdot P_{uq}(\pi - \theta, \phi | \pi - \theta_{si1}, \phi_{si1}) \frac{L_u(\theta) - L_q(\theta_{si1})}{\kappa_{eq}(\theta_{si1}) \sec\theta_{si1} - \kappa_{eu}(\theta) \sec\theta} d\phi d\theta \end{aligned} \quad (\text{C.5})$$

$$\begin{aligned} \sigma_{pq}^c &= 4\pi \cos\theta_{t0} T_{10p}(\theta_{t0}, \theta_{i1}) T_{01q}(\theta_{t1}, \theta_{i0}) \sec\theta_{ss1} \\ &\cdot P_{pq}(\theta_{ss1}, \theta_{ss1} | \pi - \theta_{si1}, \phi_{si1}) \frac{1 - L_p(\theta_{ss1}) L_q(\theta_{si1})}{\kappa_{ep}(\theta_{ss1}) \sec\theta_{ss1} - \kappa_{eq}(\theta_{si1}) \sec\theta_{si1}} \end{aligned} \quad (\text{C.6})$$

where σ_{pq}^{VS} is the backscattering coefficient of the bottom-surface. Superscripts i and s denote the incident and scattered direction, respectively. Incident or scattered angles of each layer are described in Figure 52 (i.e. $\pi - \theta$ denotes downward direction and ϕ is azimuth angle). T is the transmission coefficient on the interface of the each layer. Subscripts of T denote the propagation direction of microwave on the interface of each layer. For example, T_{01} means that the transmission coefficient

of microwave which propagates from 0 layer to 1 layer. L is power attenuation term, and can be estimated by

$$L_p(\theta) = \exp[-\kappa_{ep}d\sec\theta] \quad (\text{C.7})$$

where d is the layer depth. The second order solution of VRT can be classified into two components (Figure 51d and e). These components mean the interaction between the scatterer within the layer. Backscattering coefficients of the each component are as following

$$\begin{aligned} \sigma_{pq}^d &= 4\pi\cos\theta_{t0}T_{10p}(\theta_{t0},\theta_{i1})T_{01q}(\theta_{t1},\theta_{i0})\sec\theta_{ss2} \\ &\cdot \int_0^{2\pi} \int_0^{\frac{\pi}{2}} \sin\theta\sec\theta \cdot \sum_{u=v,h} \frac{P_{pu}(\theta_{ss2},\phi_{ss2}|\theta,\phi)P_{uq}(\theta,\phi|\pi-\theta_{si1},\phi_{si1})}{\kappa_{eq}(\theta_{si1})\sec\theta_{si1}+\kappa_{eu}(\theta)\sec\theta} \quad (\text{C.8}) \\ &\cdot \left[\frac{1-L_p(\theta_{ss2})L_q(\theta_{si1})}{\kappa_{ep}(\theta_{ss2})\sec\theta_{ss2}+\kappa_{eq}(\theta_{si1})\sec\theta_{si1}} + \frac{L_q(\theta_{si1})[L_u(\theta)-L_p(\theta_{ss2})]}{\kappa_{eu}(\theta)\sec\theta-\kappa_{ep}(\theta_{ss2})\sec\theta_{ss2}} \right] d\phi d\theta \end{aligned}$$

$$\begin{aligned} \sigma_{pq}^e &= 4\pi\cos\theta_{t0}T_{10p}(\theta_{t0},\theta_{i1})T_{01q}(\theta_{t1},\theta_{i0})\sec\theta_{ss2} \\ &\cdot \int_0^{2\pi} \int_0^{\frac{\pi}{2}} \sin\theta\sec\theta \cdot \sum_{u=v,h} \frac{P_{pu}(\theta_{ss2},\phi_{ss2}|\pi-\theta,\phi)P_{uq}(\pi-\theta,\phi|\pi-\theta_{si1},\phi_{si1})}{\kappa_{ep}(\theta_{ss2})\sec\theta_{ss2}+\kappa_{eu}(\theta)\sec\theta} \quad (\text{C.9}) \\ &\cdot \left[\frac{1-L_p(\theta_{ss2})L_q(\theta_{si1})}{\kappa_{ep}(\theta_{ss2})\sec\theta_{ss2}+\kappa_{eq}(\theta_{si1})\sec\theta_{si1}} + \frac{L_p(\theta_{ss2})[L_u(\theta)-L_q(\theta_{si1})]}{\kappa_{eu}(\theta)\sec\theta-\kappa_{eq}(\theta_{si1})\sec\theta_{si1}} \right] d\phi d\theta \end{aligned}$$

Finally, Backscattering coefficients of the volume scattering (σ_{pq}^V) within the layer can be calculated by

$$\sigma_{pq}^V = \sigma_{pq}^a + \sigma_{pq}^b + \sigma_{pq}^c + \sigma_{pq}^d + \sigma_{pq}^e \quad (\text{C.10})$$

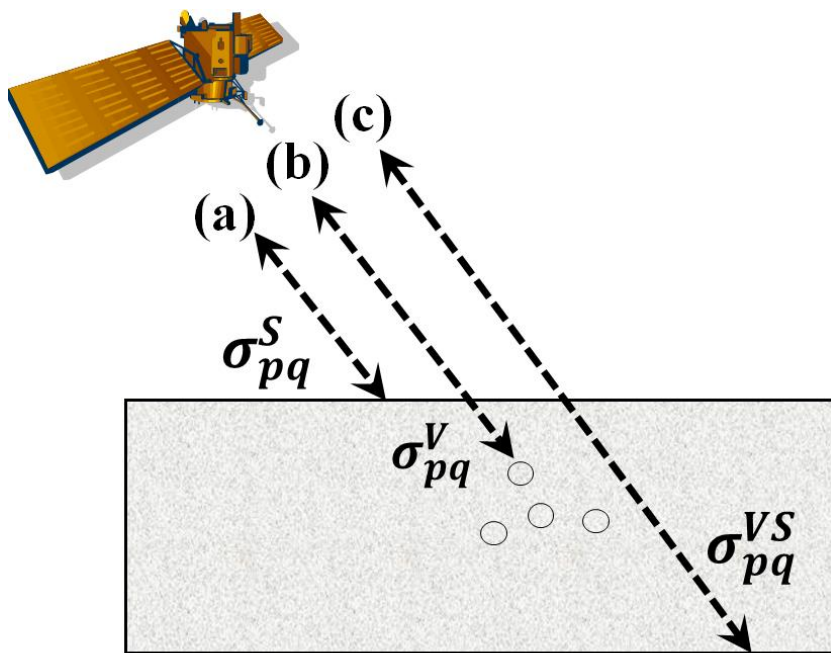


Figure 50. Scattering structures of VRT model simulation. (a) surface scattering (b) volume scattering (c) bottom-surface scattering

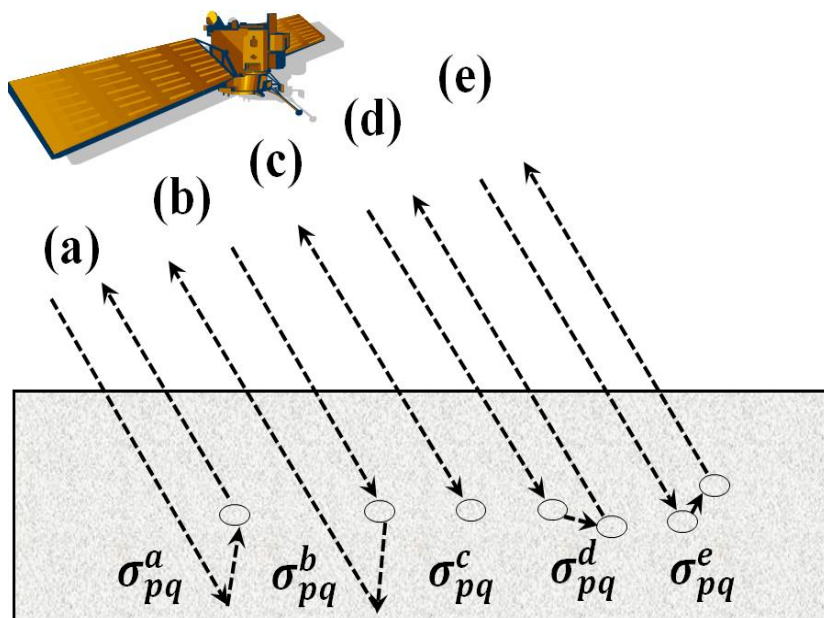


Figure 51. Volume scattering structure of VRT simulation. (a)-(c) first order solution (d)-(e) second order solution.

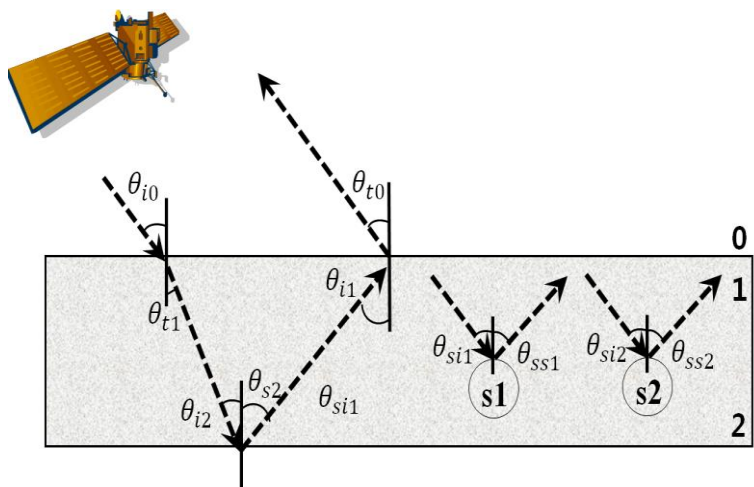


Figure 52. Geometry of incident and scattered angle at the each layer for VRT simulation.

References

1. Fitzharris, B. B. (1996). *The cryosphere: changes and their impacts*. Cambridge university press, New York, NY(USA)., pp. 241-265
2. Hall, D. K., & Martinec, J. (1985). *Remote sensing of ice and snow* (pp. 109-155). New York: Chapman and Hall.
3. Chapman, W. L., & Walsh, J. E. (1993). Recent variations of sea ice and air temperature in high latitudes. *Bulletin of the American Meteorological Society*, 74(1), 33-47.
4. <http://www.cocorahs-albedo.org/>
5. Coakley, J. A. (2002). Reflectance and albedo, surface.
6. Parkinson, C. L., & Cavalieri, D. J. (2008). Arctic sea ice variability and trends, 1979–2006. *Journal of geophysical research*, 113(C7), C07003.
7. Pritchard, H. D., Ligtenberg, S. R. M., Fricker, H. A., Vaughan, D. G., Van den Broeke, M. R., & Padman, L. (2012). Antarctic ice-sheet loss driven by basal melting of ice shelves. *Nature*, 484(7395), 502-505.
8. Stroeve, J., Holland, M. M., Meier, W., Scambos, T., & Serreze, M. (2007). Arctic sea ice decline: Faster than forecast. *Geophysical research letters*, 34(9).
9. Boé, J., Hall, A., & Qu, X. (2009). September sea-ice cover in the Arctic Ocean projected to vanish by 2100. *Nature Geoscience*, 2(5), 341-343.

10. Wang, M., & Overland, J. E. (2009). A sea ice free summer Arctic within 30 years?. *Geophysical Research Letters*, 36(7), L07502.
11. Haas, C., Gerland, S., Eicken, H., & Miller, H. (1997). Comparison of sea-ice thickness measurements under summer and winter conditions in the Arctic using a small electromagnetic induction device. *Geophysics*, 62(3), 749-757.
12. Van der Kruk, J., Arcone, S. A., & Liu, L. (2007). Fundamental and higher mode inversion of dispersed GPR waves propagating in an ice layer. *Geoscience and Remote Sensing, IEEE Transactions on*, 45(8), 2483-2491.
13. Mittelholzer W and others (1925) By airplane towards the north pole (trans: Paul E, Paul C). Houghton Mifflin, Boston, 176p
14. Wilkins, H. (1929). The Wilkins-Hearst Antarctic Expedition, 1928-1929. *Geographical Review*, 19(3), 353-376.
15. McDonald, R. A. (1995). CORONA-Success for Space Reconnaissance, a Look into the Cold-War, and a Revolution for Intelligence. *Photogrammetric Engineering and Remote Sensing*, 61(6), 689-720.
16. Peebles, C. (1997). *The CORONA project: America's first spy satellites* (p. 246). Annapolis, MD: Naval Institute Press.
17. Wheelon, A. D. (1997). Corona: The first reconnaissance satellites. *Physics today*, 50, 24.
18. Sohn, H. G., Jezek, K. C., & Van der Veen, C. J. (1998). Jakobshavn Glacier, West Greenland: 30 years of spaceborne observations. *Geophysical Research Letters*, 25(14), 2699-2702.
19. Bindshadler, R., & Vornberger, P. (1998). Changes in the West Antarctic ice sheet since 1963 from declassified satellite photography. *Science*, 279(5351),

689-692.

20. Comiso, J. C., Cavalieri, D. J., & Markus, T. (2003). Sea ice concentration, ice temperature, and snow depth using AMSR-E data. *Geoscience and Remote Sensing, IEEE Transactions on*, 41(2), 243-252.
21. Zhao, Y., Liu, A. K., & Long, D. G. (2002). Validation of sea ice motion from QuikSCAT with those from SSM/I and buoy. *Geoscience and Remote Sensing, IEEE Transactions on*, 40(6), 1241-1246.
22. Haas, C. (2001). The seasonal cycle of ERS scatterometer signatures over perennial Antarctic sea ice and associated surface ice properties and processes. *Annals of Glaciology*, 33(1), 69-73.
23. Matzler, C. (1998). Microwave properties of ice and snow. In *Solar System Ices* (pp. 241-257). Springer Netherlands.
24. Waite, A. H., & Schmidt, S. J. (1962). Gross errors in height indication from pulsed radar altimeters operating over thick ice or snow. *Proceedings of the IRE*, 50(6), 1515-1520.
25. Laxon, S. (1994). Sea ice altimeter processing scheme at the EODC. *International Journal of Remote Sensing*, 15(4), 915-924.
26. Zwally, H. J., Bindschadler, R. A., BRENNER, A. C., MAJOR, J. A., & Marsh, J. G. (1989). Growth of Greenland ice sheet: Measurement. *Science*, 246(4937), 1587-1589.
27. Wingham, D. J., Francis, C. R., Baker, S., Bouzinac, C., Brockley, D., Cullen, R., ... & Wallis, D. W. (2006). CryoSat: A mission to determine the fluctuations in Earth's land and marine ice fields. *Advances in Space Research*, 37(4), 841-871.

28. Zwally, H. J., Schutz, B., Abdalati, W., Abshire, J., Bentley, C., Brenner, A., ... & Thomas, R. (2002). ICESat's laser measurements of polar ice, atmosphere, ocean, and land. *Journal of Geodynamics*, 34(3), 405-445.
29. Koenig, L., Martin, S., Studinger, M., & Sonntag, J. (2010). Polar airborne observations fill gap in satellite data. *Eos, Transactions American Geophysical Union*, 91(38), 333-334.
30. Freeman, A., & Durden, S. L. (1998). A three-component scattering model for polarimetric SAR data. *Geoscience and Remote Sensing, IEEE Transactions on*, 36(3), 963-973.
31. Pottier, E., & Lee, J. S. (2000, March). Application of the «H/A/alpha» Polarimetric Decomposition Theorem for Unsupervised Classification of Fully Polarimetric SAR Data Based on the Wishart Distribution. In *SAR workshop: CEOS Committee on Earth Observation Satellites* (Vol. 450, p. 335).
32. Yamaguchi, Y., Moriyama, T., Ishido, M., & Yamada, H. (2005). Four-component scattering model for polarimetric SAR image decomposition. *Geoscience and Remote Sensing, IEEE Transactions on*, 43(8), 1699-1706.
33. Shi, J., Wang, J., Hsu, A. Y., O'Neill, P. E., & Engman, E. T. (1997). Estimation of bare surface soil moisture and surface roughness parameter using L-band SAR image data. *Geoscience and Remote Sensing, IEEE Transactions on*, 35(5), 1254-1266.
34. Srivastava, H. S., Patel, P., Manchanda, M. L., & Adiga, S. (2003). Use of multiincidence angle RADARSAT-1 SAR data to incorporate the effect of surface roughness in soil moisture estimation. *Geoscience and Remote Sensing, IEEE Transactions on*, 41(7), 1638-1640.
35. Rott, H. (1984). The analysis of backscattering properties from SAR data of

- mountain regions. *Oceanic Engineering, IEEE Journal of*, 9(5), 347-355.
36. Strozzi, T. (1996). *Backscattering measurements of snowcovers at 5.3 and 35 GHz*. Universitat Bern, Fakultat der Philosophisch-naturwissenschaftlichen.
 37. Barton, D. K. (2005). *Radar system analysis and modeling* (p. 122). Norwood, MA, USA: Artech House.
 38. Sarabandi, K., Ulaby, F. T., & Tassoudji, M. A. (1990). Calibration of polarimetric radar systems with good polarization isolation. *Geoscience and Remote Sensing, IEEE Transactions on*, 28(1), 70-75.
 39. Whitt, M. W., Ulaby, F. T., Polatin, P., & Liepa, V. V. (1991). A general polarimetric radar calibration technique. *Antennas and Propagation, IEEE Transactions on*, 39(1), 62-67.
 40. Barnes, R. M. (1986). Polarimetric calibration using in-scene reflectors. *Rep. TT-65, MIT Lincoln Lab, MA*.
 41. Sarabandi, K., Oh, Y., & Ulaby, F. T. (1992). Measurement and calibration of differential Mueller matrix of distributed targets. *Antennas and Propagation, IEEE Transactions on*, 40(12), 1524-1532.
 42. Bird, T. S. (2009). Definition and Misuse of Return Loss [Report of the Transactions Editor-in-Chief]. *Antennas and Propagation Magazine, IEEE*, 51(2), 166-167.
 43. Fung, A. K., Li, Z., & Chen, K. S. (1992). Backscattering from a randomly rough dielectric surface. *Geoscience and Remote Sensing, IEEE Transactions on*, 30(2), 356-369.
 44. Fung, A. K., & Chen, K. S. (2004). An update on the IEM surface backscattering model. *Geoscience and Remote Sensing Letters, IEEE*, 1(2), 75-77.

45. Matsuoka, T., Umehara, T., Nadai, A., Kobayashi, T., Satake, M., & Uratsuka, S. (2009, July). Calibration of the high performance airborne SAR system (Pi-SAR2). In *Geoscience and Remote Sensing Symposium, 2009 IEEE International, IGARSS 2009* (Vol. 4, pp. IV-582). IEEE.
46. Ruck, G., Barrick, D. E., Stuart, W. D., & Krichbaum, C. K. (1970). RCS handbook.
47. Ferrara, G., Mattia, F., & Posa, F. (1995, December). Backscattering study on non-orthogonal trihedral corner reflectors. In *Microwaves, Antennas and Propagation, IEE Proceedings* (Vol. 142, No. 6, pp. 441-446). IET.
48. Carsey, F. D. (1992). *Microwave remote sensing of sea ice* (Vol. 68, pp. 1-462). American Geophysical Union.
49. Vant, M. R., Ramseier, R. O., & Makios, V. (1978). The complex-dielectric constant of sea ice at frequencies in the range 0.1–40 GHz. *Journal of Applied Physics*, 49(3), 1264-1280.
50. Cox, G. F., & Weeks, W. F. (1982). *Equations for determining the gas and brine volumes in sea ice samples*. US Army Corps of Engineers, Cold Regions Research & Engineering Laboratory.
51. Cox, G. F., & Weeks, W. F. (1973). *Salinity variations in sea ice* (No. CRREL-RR-310). Cold Regions Research and Engineering Lab Hanover NH.
52. Onstott, R. G. (1992). SAR and scatterometer signatures of sea ice. *Microwave remote sensing of sea ice*, 73-104.
53. Wakabayashi, H., Matsuoka, T., Nakamura, K., & Nishio, F. (2004). Polarimetric characteristics of sea ice in the Sea of Okhotsk observed by airborne L-band SAR. *Geoscience and Remote Sensing, IEEE Transactions on*,

- 42(11), 2412-2425.
54. Nakamura, K., Wakabayashi, H., Naoki, K., Nishio, F., Moriyama, T., & Uratsuka, S. (2005). Observation of sea-ice thickness in the Sea of Okhotsk by using dual-frequency and fully polarimetric airborne SAR (Pi-SAR) data. *Geoscience and Remote Sensing, IEEE Transactions on*, 43(11), 2460-2469.
 55. Nakamura, K., Wakabayashi, H., Uto, S., Naoki, K., Nishio, F., & Uratsuka, S. (2006). Sea-ice thickness retrieval in the Sea of Okhotsk using dual-polarization SAR data. *Annals of Glaciology*, 44(1), 261-268.
 56. Tiuri, M., Sihvola, A., Nyfors, E., & Hallikaiken, M. (1984). The complex dielectric constant of snow at microwave frequencies. *Oceanic Engineering, IEEE Journal of*, 9(5), 377-382.
 57. Sweeny, B. D., & Colbeck, S. C. (1974). *Measurements of the Dielectric Properties of Wet Snow Using a Microwave Technique* (No. CRREL-RR-325). Cold Regions Research and Engineering Lab Hanover NH.
 58. Hallikainen, M., Ulaby, F., & Abdelrazik, M. (1986). Dielectric properties of snow in the 3 to 37 GHz range. *Antennas and Propagation, IEEE Transactions on*, 34(11), 1329-1340.
 59. Cumming, W. A. (1952). The dielectric properties of ice and snow at 3.2 centimeters. *Journal of Applied Physics*, 23(7), 768-773.
 60. Ulaby, F. T., Moore, R. K., & Fung, A. K. (1986). *Microwave Remote Sensing: Active and Passive*, vol. III, Volume Scattering and Emission Theory, Advanced Systems and Applications. *Inc., Dedham, Massachusetts*, 1797-1848.
 61. Isleifson, D., Langlois, A., Barber, D. G., & Shafai, L. (2009). C-band scatterometer measurements of multiyear sea ice before fall freeze-up in the

- Canadian Arctic. *Geoscience and Remote Sensing, IEEE Transactions on*, 47(6), 1651-1661.
62. Arcone, S. A., Gow, A. J., & McGrew, S. (1986). Structure and dielectric properties at 4.8 and 9.5 GHz of saline ice. *Journal of Geophysical Research: Oceans (1978–2012)*, 91(C12), 14281-14303.
63. Hallikainen, M. T., Toikka, M. V. O., & Hyypä, J. M. (1988, September). Microwave dielectric properties of low-salinity sea ice. In *Geoscience and Remote Sensing Symposium, 1988. IGARSS'88. Remote Sensing: Moving Toward the 21st Century., International (Vol. 1, pp. 419-420)*. IEEE.
64. Kim, J. W., Kim, D. J., & Hwang, B. J. (2012). Characterization of Arctic sea ice thickness using high-resolution spaceborne polarimetric SAR data. *Geoscience and Remote Sensing, IEEE Transactions on*, 50(1), 13-22.
65. Nghiem, S. V., Kwok, R., Yueh, S. H., & Drinkwater, M. R. (1995). Polarimetric signatures of sea ice: 1. Theoretical model. *Journal of Geophysical Research: Oceans (1978–2012)*, 100(C7), 13665-13679.
66. Peterson, I. K., Prinsenber, S. J., & Holladay, J. S. (2008). Observations of sea ice thickness, surface roughness and ice motion in Amundsen Gulf. *Journal of Geophysical Research*, 113(C6), C06016.
67. Toyota, T., Ukita, J., Ohshima, K., Wakatsuchi, M., & Muramoto, K. (1990). A measurement of sea ice albedo over the southwestern Okhotsk Sea. *Journal of the Meteorological Society of Japan. Ser. II*, 77(1), 117-133.
68. Toyota, T., Nakamura, K., Uto, S., Ohshima, K. I., & Ebuchi, N. (2009). Retrieval of sea ice thickness distribution in the seasonal ice zone from airborne L-band SAR. *International Journal of Remote Sensing*, 30(12), 3171-3189.

69. Gupta, M., Barber, D. G., Scharien, R. K., & Isleifson, D. (2012). Detection and classification of surface roughness in an Arctic marginal sea ice zone. *Hydrological Processes*.
70. Kim, Y. S., Moore, R. K., Onstott, R. G., & Gogineni, S. (1985). Towards identification of optimum radar parameters for sea ice monitoring. *Journal of Glaciology*, 31(109), 214-219.
71. Kasilingam, D., Schuler, D., & Lee, J. S. (2001). The depolarization of radar backscatter from rough surfaces due to surface roughness and slopes. In *Geoscience and Remote Sensing Symposium, 2001. IGARSS'01. IEEE 2001 International* (Vol. 2, pp. 925-927). IEEE.
72. Shi, J., Dozier, J., & Rott, H. (1994). Snow mapping in alpine regions with synthetic aperture radar. *Geoscience and Remote Sensing, IEEE Transactions on*, 32(1), 152-158.
73. Li, Z., & Guo, H. (2000). Permafrost mapping in the Tibet plateau using polarimetric SAR. In *Geoscience and Remote Sensing Symposium, 2000. Proceedings. IGARSS 2000. IEEE 2000 International* (Vol. 5, pp. 2024-2026). IEEE.
74. Isleifson, D., Hwang, B., Barber, D. G., Scharien, R. K., & Shafai, L. (2010). C-band polarimetric backscattering signatures of newly formed sea ice during fall freeze-up. *Geoscience and Remote Sensing, IEEE Transactions on*, 48(8), 3256-3267.
75. Onstott, R. G., Moore, R. K., & Weeks, W. F. (1979). Surface-based scatterometer results of Arctic sea ice. *Geoscience Electronics, IEEE Transactions on*, 17(3), 78-85.
76. Hajnsek, I., Pottier, E., & Cloude, S. R. (2003). Inversion of surface parameters

- from polarimetric SAR. *Geoscience and Remote Sensing, IEEE Transactions on*, 41(4), 727-744.
77. Fung, A. K., & Eom, H. J. (1982). Application of a combined rough surface and volume scattering theory to sea ice and snow backscatter. *Geoscience and Remote Sensing, IEEE Transactions on*, (4), 528-536.
78. Winebrenner, D. P., Tsang, L., Wen, B., & West, R. (1989). Sea-ice characterization measurements needed for testing of microwave remote sensing models. *Oceanic Engineering, IEEE Journal of*, 14(2), 149-158.
79. West, R., Tsang, L., & Winebrenner, D. P. (1993). Dense medium radiative transfer theory for two scattering layers with a Rayleigh distribution of particle sizes. *Geoscience and Remote Sensing, IEEE Transactions on*, 31(2), 426-437.
80. Jin, Y. Q. (1993). *Electromagnetic scattering modelling for quantitative remote sensing*. World Scientific.
81. Ewe, H. T., Chuah, H. T., & Fung, A. K. (1998). A backscatter model for a dense discrete medium: Analysis and numerical results. *Remote Sensing of Environment*, 65(2), 195-203.

Abstract (in Korean)

본 논문은 고해상도 다중편파 레이더 시스템의 측정자료로부터 북·남극에 존재하는 해빙두께를 효율적으로 추출할 수 있는 방법에 대한 것이다. 이를 위해, 지상기반 다중편파 산란계 시스템과 다양한 전자기파 산란 모델을 이용하여 해빙의 생성·소멸 시기에 따라 유전율과 표면 거칠기와 같은 물리적 특성에 따라 전자기파의 산란특징이 어떻게 변하는지를 이해하고자 하였다. 이를 위하여, 전자기파의 산란구조를 해빙 표면 위에 적설된 눈의 표층산란, 눈의 체적산란, 눈과 해빙의 경계면에서 발생하는 산란, 해빙의 체적산란으로 나누어 살펴 보았다.

지상기반 다중편파 산란계 시스템의 측정실험을 통하여 해빙 소멸시기에 해빙표면 위에 적설된 눈은 높은 대기온도로 인하여 눈 표면이 녹아 유전율이 높아지기 때문에 산란계로부터 송신된 대부분의 전자기파 신호가 눈 표면에서 산란(표층산란)되어 수신되는 특징을 보였다. 반면에, 해빙 생성시기에는 대기온도가 항상 영하로 유지되면서 눈 표면의 유전율이 낮아져 전자기파 신호가 눈 표면을 투과하여 눈의 체적 내부 또는 눈과 해빙 표면의 경계면에서 산란되어 수신될 수 있는 가능성을 보였다. 더욱이, 전자기파의 입사각이 작으면 HH와 VV 편파의 전자기파는 눈의 체적 내부에서 체적산란이 우세하게 발생하였고 HV와 VH 편파의 전자기파는 눈과 해빙의 경계면에서 우세하게 산란될 수 있는 가능성을 보였다. 반면에 입사각이 상대적으로 커지면 모든 편파의 전자기파가 눈과 해빙의 경계면에서 우세하게 산란될 수 있는 가능성을 보였다.

다음으로, 다양한 현장조사 자료를 통하여 해빙 생성시기가 길어질수록 해빙의 담수화 현상으로 인하여 해빙두께에 따라 해빙 표면의 유전율이 감소하고 전자기파의 투과 깊이가 증가할 수 있는 가능성을 확인 하였다. 이에 더하여, 해빙 생성시기가 길어질수록 해빙 표면 용해수의 재결빙과 유빙들의 충돌 현상으로 인해 해빙두께에 따라 표면 거칠기가 상대적으로 증가할 수 있는 가능성을 확인 하였다. 따라서, 해빙의 두께가 두꺼워질수록 해빙의 표면에서는 거친 표면으로 인하여 다중표층산란이 증가하고 해빙 체적 내부의 체적산란 또한 증가한다는 것을 다양한 전자기파 산란 모델의 수치해석 결과를 통하여 확인 하였다. 이러한 결과를 바탕으로 전자기파 산란 모델을 이용하여 해빙 두께에 따라 다중표층산란과 체적산란이 증가하고 이는 송·수신된 전자기파의 편파 손실정도 (참고, 편파손실 정도는 VH/VV 또는 HV/HH와 같은 편파비로 계산된다.)와 선형관계가 있다는 것을 확인하였다. 그리고 북극해에서 실측된 해빙 두께 정보와 동시간대에 관측된 TerraSAR-X와 RADARSAT-2 SAR 자료로부터 추출된 VH/VV와 HV/HH 편파비가 매우 높은 상관관계가 있다는 것을 추가적으로 확인 하였다. 이러한 결과를 통하여, 다중편파 레이다 시스템에서 관측된 편파 손실정도가 해빙두께를 추출하기 위한 매우 유용한 정보가 될 수 있다는 사실을 확인 하였다.

주요어: 해빙두께, 눈, 다중편파 레이다 시스템, 표층산란, 체적산란, 편파 손실 효과

학번: 2008-30820



저작자표시-비영리-변경금지 2.0 대한민국

이용자는 아래의 조건을 따르는 경우에 한하여 자유롭게

- 이 저작물을 복제, 배포, 전송, 전시, 공연 및 방송할 수 있습니다.

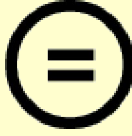
다음과 같은 조건을 따라야 합니다:



저작자표시. 귀하는 원저작자를 표시하여야 합니다.



비영리. 귀하는 이 저작물을 영리 목적으로 이용할 수 없습니다.



변경금지. 귀하는 이 저작물을 개작, 변형 또는 가공할 수 없습니다.

- 귀하는, 이 저작물의 재이용이나 배포의 경우, 이 저작물에 적용된 이용허락조건을 명확하게 나타내어야 합니다.
- 저작권자로부터 별도의 허가를 받으면 이러한 조건들은 적용되지 않습니다.

저작권법에 따른 이용자의 권리는 위의 내용에 의하여 영향을 받지 않습니다.

이것은 [이용허락규약\(Legal Code\)](#)을 이해하기 쉽게 요약한 것입니다.

[Disclaimer](#)

Thesis for Ph. D. degree

**Measurements of Sea Ice Thickness using
Polarimetric Radar Systems**

다중편파 레이더 시스템을 이용한

해빙두께 측정

Jin-Woo Kim

February 2014

School of Earth and Environmental Sciences

Graduate School

Seoul National University

Measurements of Sea Ice Thickness using Polarimetric Radar Systems

다중편파 레이더 시스템을 이용한
해빙두께 측정

지도교수 김 덕 진

이 논문을 이학박사 학위논문으로 제출함

2013 년 12월

서울대학교 대학원
지구환경과학부

김 진 우

김진우의 이학박사 학위논문을 인준함

2014 년 02월

위 원 장 _____ 안 진 호 _____ (인)

부위원장 _____ 김 덕 진 _____ (인)

위 원 _____ 오 이 석 _____ (인)

위 원 _____ 이 훈 열 _____ (인)

위 원 _____ 김 상 완 _____ (인)

Abstract

This thesis presents an overview of the interactions between microwaves and physical properties of sea ice and snow, such as the dielectric constant and surface roughness, in order to successfully measure sea ice thickness from polarimetric radar systems. Using a ground-based scatterometer system and various microwave scattering models, polarimetric backscattered signatures from sea ice and snow were investigated as evidence of the evolution of the physical properties during the freezing and melting seasons. Based on these results, the optimum method for measuring the thickness of sea ice covered with snow using polarimetric SAR data was explored via numerical simulations and experimental measurements.

Experiments conducted using the ground-based scatterometer system as well as the in-situ measurements showed that most of the polarimetric signatures (C-band) with relatively high incidence angles (i.e., about 40°) can be backscattered from the interface between snow cover on sea ice and the surface of the sea ice over the freezing season. Microwaves can penetrate the snow cover during this season owing to the lower dielectric properties of the snow cover (about 1.25). Conversely, the signatures were predominantly backscattered from the surface of the snow cover during the melting season due to high dielectric properties induced by surface melting water. For the freezing season, the in-situ measurements and numerical simulations showed that the number of polarimetric signatures backscattered within the sea ice volume can increase with sea ice growth due to evolutions of the dielectric

properties induced by the desalination process, and the surface roughness of sea ice can increase with sea ice growth due to superimposed and ridging processes. Based on these observations, the relationship between the depolarization effects of polarimetric signatures (C- and X-band) and sea ice thickness was investigated using various numerical simulations and a case study. A strong correlation was found between the in-situ sea ice thickness and the SAR-derived depolarization factors (i.e., the co-polarized correlation and cross-polarized ratio). These results clearly demonstrate a one-to-one relationship between the thickness and the depolarization factors, which further suggests that the depolarization factors could be effective parameters in measuring the thickness of snow-covered sea ice with space-borne polarimetric SAR data.

Keywords: Sea ice thickness, snow cover, polarimetric SAR, depolarization effect, scattering signatures, dielectric constant, surface roughness, freezing season

Student Number: 2008-30820

Table of Contents

| | |
|---|-----------|
| Chapter 1. Introduction | 1 |
| 1.1. Overview | 1 |
| 1.2. Remote sensing of ice and snow | 3 |
| 1.3. Motivation and Objectives of this thesis | 11 |
| Chapter 2. Polarimetric microwave remote sensing systems | 13 |
| 2.1. Ground Based POLarimetric SCATterometer (GB-POLSCAT) | 13 |
| A. Set-up of GB-POLSCAT..... | 14 |
| B. System calibration of GB-POLSCAT | 16 |
| B.1. Basic concept of the system calibration | 16 |
| B.2. Conventional system calibration | 18 |
| C. New system calibration of GB-POLSCAT..... | 21 |
| C.1. Background | 21 |
| C.2. New technique to extract radar distortions..... | 21 |
| C.3. Validation using field experiments and numerical simulation | 21 |
| 2.2. Space-borne SAR systems | 30 |
| A. RADARSAT-2 and TerraSAR-X..... | 30 |
| B. Radiometric calibration of the SAR systems..... | 33 |
| B.1. Background | 33 |
| B.2. Backscattering coefficient computation of TerraSAR-X and RADARSAT-2..... | 33 |
| Chapter 3. Polarimetric signatures characterized by scattering features from sea ice and snow..... | 42 |
| 3.1. Background | 42 |
| 3.2. Polarimetric scattering features of snow | 49 |
| A. Dielectric properties of snow | 49 |
| B. The scattering features from snow..... | 55 |

| | |
|--|------------|
| 3.3. Polarimetric scattering features of sea ice | 63 |
| A. Dielectric properties of sea ice | 63 |
| B. Surface roughness of sea ice..... | 70 |
| C. The scattering features from sea ice | 74 |
| 3.4. Depolarization effects based on the polarimetric scattering features of sea ice | 76 |
| A. Numerical experiments of the depolarization effects due to surface scattering from rough surface..... | 78 |
| B. Numerical experiments of the depolarization effects due to volume scattering within sea ice layer | 83 |
| C. Field experiments of the depolarization effects due to volume scattering within ice layer | 92 |
| Chapter 4. Measurement of sea ice thickness using space-borne SAR data in the Arctic Ocean | 102 |
| 4.1. In-situ measurements and SAR data acquisition..... | 102 |
| 4.2. Depolarization-to-sea ice thickness relationship using space-borne SAR data | 108 |
| Chapter 5. Conclusion..... | 111 |
| 5.1. Summary | 111 |
| 5.2. Discussion | 113 |
| Appendix | 115 |
| Reference | 127 |

List of Figures

| | |
|---|----|
| Figure 1. Classification of ice and snow at the cryosphere. [From ESA] | 7 |
| Figure 2. The spatial distribution land and sea ice in the polar region. | 8 |
| Figure 3. Abedo of ice, snow, ocean water, and vegetation and dark soil on the earth..... | 9 |
| Figure 4. Average monthly Arctic sea ice extent from Jan 1979 to 2010. [From NSIDC] .. | 10 |
| Figure 5. Change rate of the ice thickness in the Antarctic ice shelf from 2003 to 2008. [Prichard et al, 2012] | 10 |
| Figure 6. (a) External parts of the GB-POLSCAT system developed by SNU (b) Structures of the circuit. | 15 |
| Figure 7. Geometry and block diagram of Polarimetric Radar System (PRS. P is the power generated by PRS. The superscript of P denotes direction of power transmission (e.g., t: transmitted or r: received direction). The subscript of P denotes a sequence of power transmission. [S] is a scattering matrix. The superscript of [S] denotes RPI or a point calibration target. G denotes the antenna gain. r is the distance between the antenna and a point calibration target..... | 26 |
| Figure 8. The measured radar response of the PRS in the anechoic chamber..... | 27 |
| Figure 9. Active distortion estimated from field experiments. | 28 |
| Figure 10. Comparison between simulated and measured backscattering coefficients. | 29 |
| Figure 11. Various imaging modes of the space-borne SAR systems (a) TerraSAR-X (b) RADARSAT-2. [From DLR and MDA]..... | 32 |
| Figure 12. Estimated radar brightness of acquired TerraSAR-X. (a) HH (b) VV..... | 38 |
| Figure 13. Estimated backscattering coefficients of acquired TerraSAR-X data. (a) HH (b) VV | 39 |
| Figure 14. Estimated radar brightness of acquired RADARSAT-2 data. (a) HH (b) HV | 40 |
| Figure 15. Estimated backscattering coefficients of acquired RADARSAT-2 data. (a) HH (b) HV | 41 |
| Figure 16. Variations of sea ice extent for the melting and freezing season. (a) Arctic sea ice (b) Antarctic sea ice | 46 |

| | |
|---|----|
| Figure 17. Life cycles of sea ice..... | 47 |
| Figure 18. Scattering structures of sea ice and snow. | 48 |
| Figure 19. Test site of Strozzi’s measurements..... | 51 |
| Figure 20. (a) measured air temperature and (b) snow density for the melting and freezing seasons. [Strozzi, 1996]..... | 53 |
| Figure 21. Comparison of observed dielectric constant (real) of snow surface and simulated dielectric constant (real) for the melting (red box) and freezing (blue box) season. | 54 |
| Figure 22. Scheme of scattering structures from snow cover in the GB-POLSCAT measurements. | 59 |
| Figure 23. Normalized scattering intensity from snow cover with Strozzi’s data for the melting and freezing season (Incidence angle: 10°). | 60 |
| Figure 24. Normalized scattering intensity from snow cover with Strozzi’s data for the melting and freezing season (Incidence angle: 40°). | 61 |
| Figure 25. Measurement site of the ice buoy (top) and structures of the ice buoy (bottom) [from Prof. Hajo Eicken’s homepage at Alaska University]..... | 67 |
| Figure 26. (a) the salinity profiles of FYI for the freezing season (red line a-d denote averaged salinity profiles as FYI grows, and blue line is averaged salinity profile of MYI in [51]) (b) the salinity profiles of MYI for the freezing season. From MYI A to MYI D, the thickness are gradually increased [61]. | 68 |
| Figure 27. Dielectric constant (real and imaginary parts) and penetration depth as a function of sea ice thickness for C- and X-band frequencies. Left Y-axis represents the values of dielectric constant (black: real part, gray: imaginary part) and right Y-axis represents penetration depth. (a) C-band (b) X-band..... | 69 |
| Figure 28. Cross-sectional view of FYI (left) and MYI (right) during the sea ice growing season. The lower bottom photographs show typical scenes of the corresponding sea ice type. | 72 |
| Figure 29. Distributions of FYI and FYI in [69]. (a) FYI (b) MYI..... | 73 |
| Figure 30. The distribution of backscattering coefficients from FYI and MYI [70] (red real line: rough FYI, red dotted line: smooth FYI, blue real line:rough MYI, and blue dotted line: smooth MYI). | 75 |
| Figure 31. The variation of cross-polarized ratio (HV/HH) as a function of RMS height (small-scale roughness) for the C- and X-band. | 81 |
| Figure 32. The variation of depolarization factors (cross polarized ratio) as a function of | |

surface slope width (large-scale surface roughness) for the dielectric constants of thick FYI and MYI using extended-Bragg model. 82

Figure 33. Set-up of VRT model simulation. (a) flat surface (only volume scattering) (b) relatively rough surface as sea ice grows (surface + volume scattering). 85

Figure 34. In the VRT simulation, dielectric constant (real and imaginary parts) and penetration depth as a function of sea ice thickness (i.e. 0.1 ~ 5 m) for C- and X-band frequencies. Left Y-axis represents the values of dielectric constant (black: real part, gray: imaginary part) and right Y-axis represents penetration depth. 86

Figure 35. Backscattering coefficients (C-band) simulated by the VRT (Case 1, only volume scattering) as sea ice grows (red: VV, blue: HH, and green: VH). (a) incidence angle: 20° (b) incidence angle: 40° 87

Figure 36. Backscattering coefficients (X-band) simulated by the VRT (Case 1, only volume scattering) as sea ice grows (red: VV, blue: HH, and green: VH). (a) incidence angle: 20° (b) incidence angle: 40° 88

Figure 37. Backscattering coefficients (C-band) simulated by the VRT (Case 2, surface and volume scattering) as sea ice grows. Real line denotes simulated value by surface scattering, and dotted line denotes simulated value by volume scattering (red: VV, blue: HH, and green: VH). (a) incidence angle: 20° (b) incidence angle: 40° 89

Figure 38. Backscattering coefficients (X-band) simulated by the VRT (Case 2, surface and volume scattering) as sea ice grows. Real line denotes simulated value by surface scattering, and dotted line denotes simulated value by volume scattering (red: VV, blue: HH, and green: VH). (a) incidence angle: 20° (b) incidence angle: 40° 90

Figure 39. The relationship between depolarization factor (VH/VV) simulated by case 1 and 2 experiments and sea ice thickness. (a) C-band (case 1) (b) C-band (case 2) (c) X-band (case 1) (d) X-band (case 2). 91

Figure 40. GB-POLSCAT measurement of artificially frozen ice. 94

Figure 41. The measured backscattered signatures from the ice (blue real line: HH, red real line: VV). The green and black dotted line denotes the backscattered signatures from metal plate on the antenna aperture and the ice surface, respectively. 95

Figure 42. Refraction of microwave at the interface between the air and the ice based on Snell's law. 96

Figure 43. The backscattered signatures from the ice at 0°, 20°, and 40° of incidence angle. (the ice thickness = 140 cm) 98

Figure 44. The backscattered signatures from the ice at 0°, 20°, and 40° of incidence angle. (the ice thickness = 190 cm) 99

Figure 45. The normalized magnitude of surface, volume, and bottom-surface scattering from the ice at 0°, 20°, and 40° of incidence angle. 100

Figure 46. Study area off the northern coast of Greenland. The TerraSAR-X data was acquired on May 2, 2009 (black solid square). Two RADARSAT-2 data were acquired on April 28, 2009 (dotted blue square) and on April 30, 2009 (dotted red square), respectively. Ground truth data were obtained on May 01, 2009 (black star). The red line shown in lower left photograph represents the validation line on which the sea ice thickness and snow depth were measured using an EM31 instrument. 104

Figure 47. Sea ice thickness profile measured by the EM31 along the validation line (smooth thick FYI: 0~580 m, rubble MYI: 580~1500 m). 105

Figure 48. Radiometrically and geometrically calibrated SAR images (backscattering coefficients) of TerraSAR-X and RADARSAT-2. The yellow dots indicated in each figure represent the positions where sea ice thickness and snow depth were measured. 106

Figure 49. Relationship between the depolarization factors and observed sea ice thickness. (a) TerraSAR-X (5/02) (b) RADARSAT-2 (4/28) (c) RADARSAT-2 (4/30)110

Figure 50. Scattering structures of VRT model simulation. (a) surface scattering (b) volume scattering (c) bottom-surface scattering 124

Figure 51. Volume scattering structure of VRT simulation. (a)-(c) first order solution (d)-(e) second order solution..... 125

Figure 52. Geometry of incident and scattered angle at the each layer for VRT simulation. 126

List of Tables

| | |
|---|-----|
| Table 1. Global distribution of land and sea ice. | 8 |
| Table 2. Specifications of RADARSAT-2 and TerraSAR-X..... | 31 |
| Table 3. Specifications of Strozzi's measurements..... | 52 |
| Table 4. Averaged scattering intensities from snow cover for the freezing season..... | 62 |
| Table 5. Averaged scattering intensities from snow cover for the melting season..... | 62 |
| Table 6. The specifications of the GB-POLSCAT measurement. | 94 |
| Table 7. The estimated cross polarized ratio in the case studies. | 101 |
| Table 8. Specifications of acquired TerraSAR-X and RADARSAT-2..... | 107 |

Acronyms

| | |
|-------------------|--|
| | Antarctic Peninsular |
| AT | Active Transponder |
| ATM | Airborne Topographic Mapper |
| BCR | Backscattering Coefficient Ratio |
| CCT | Constrained Calibration Technique |
| CSA | Canadian Space Agency |
| CTD | Conductivity-Temperature-Depth |
| DLR | German aerospace center |
| DMI | Danish Meteorological Institute |
| DTU | Danish Technological University |
| EADS | Defense And Space Company |
| FYI | First Year Ice |
| GB-POLSCAT | Ground Based POLarimetric SCATterometer |
| GCT | Generalized Calibration Technique |
| GO | Geometrical Optics |
| GPR | Ground Penetrating Radar |
| HH | Horizontal Transmit, Horizontal Receive (Polarization) |
| HV | Horizontal Transmit, Vertical Receive (Polarization) |
| IEM | Integral Equation Method |
| MCDW | Modified Circumpolar Deep Water |

| | |
|--------------|--|
| MODIS | Moderate Resolution Imaging Spectrometer |
| MYI | Multi Year Ice |
| NA | Network Analyzer |
| NRCS | Normalized Radar Cross Section |
| OMT | OrthoMode Transducer |
| PO | Physical Optics |
| RCS | Radar Cross Section |
| RMS | Root Mean Square |
| RPI | Returned signal from Point of Interest |
| RRA | National Radio Research Agency |
| SAR | Synthetic Aperture Radar |
| SNR | Signal-to-Noise Ratio |
| SNU | Seoul National University |

Chapter 1. Introduction

1.1. Overview

The cryosphere comprises all parts of the earth including frozen water, ice, and snow cover [1]. Based on the origin, ice in the cryosphere can be divided into land ice and sea ice. Land ice represents frozen freshwater and/or snow on the earth's surface, and sea ice is frozen, salty ocean water. By definition, land ice can be additionally classified as glacier, ice sheet, river, and lake ice, or as permafrost. A glacier is a huge ice mass formed by accumulated and frozen snow on land over many years. An ice sheet is a mass of glacier ice with an area that is greater than 50,000 km²; this is also known as a continental glacier. Lake and river ice, and permafrost refer to lake, river, or soil surfaces that remain frozen for two or more years. All glaciers and ice sheets flow due to gravitational forces; when these formations pass through a coastline, they float on the sea surface. The floating ice is called an "ice shelf," and its parts are broken off due to various mechanisms, such as ocean tides and surface melt-water propagation. The broken ice masses are called "icebergs" (Figure 1).

Land and sea ice are mostly distributed within the polar region of the cryosphere (Figure 2). Indeed, the areas of the land ice of Antarctica and Greenland are 1.36×10^{13} and 1.73×10^{12} m², respectively. These represent 86% and 11% of the total area of land ice (1.58×10^{13} m²) [2]. In the case of sea ice, although areas of Arctic and Antarctic sea ice have strong seasonal variation, the averaged maximum area of

Arctic and Antarctic sea ice in the winter season is 1.5×10^{11} and 1.8×10^{13} m², respectively, and the minimum area of those regions in summer season is 7×10^{10} and 3×10^{10} m², respectively [3]. Table 1.1 summarizes the global distribution of land and sea ice.

Surfaces of land ice, sea ice, and snow have high reflectivity for incoming solar radiation (Figure 3). For example, the reflectivities (or albedos) of the ice and snow, ocean water, and vegetation and dark soil is from 85 to 90%, 10%, and 20%, respectively [4]. The reflectivity of ice and snow, therefore, is about four times more than the others (Table 1). Besides, the reflectivity of the ice and snow depends upon spectral band, the ice and snow thickness, and surface temperature [5]. Therefore, the spatial distributions of the formations (e.g., their physical extents and/or thickness) are important factors in understanding the thermal feedback process between the sun and the earth. The spatial distribution of the ice and snow has rapidly changed due to global warming over the past decades with the melting of sea ice [6] (Figure 4) and the retreat and thinning of ice shelves [7] (Figure 5); this decline is occurring faster than is predicted by current climate models [8]. Climate models predict a continued and possibly accelerated decline in the ice extent, leading to an ice-free summer in the Arctic within this century [9] or even within the next thirty years [10]. Thus, there is an increasing need for accurate modeling and observation of the spatial distribution of the ice and snow, in order to improve predictions for future global climate change.

Study and monitoring of the changes in the cryosphere is both laborious and scientifically challenging due to extreme environment. For example, direct

measurement of the ice and snow thickness can be made by drilling a hole through the ice and snow or by using electromagnetic induction systems such as the EM-31 and Ground Penetrating Radar (GPR) [11], [12]. Although these methods are accurate, they are time consuming and limited in space due to the intense weather conditions of the polar region. An autonomous ice mass balance buoy can facilitate long-term measurement of the ice and snow thickness and offer insights into the governing processes, but spatial coverage is limited. However, various air- and space-borne remote sensing techniques are useful tools for monitoring the changes temporally and spatially. Various air- and space-borne remote sensing techniques have been developed since the early 1900s. The next section of this thesis provides an overview of air- and space-borne remote sensing techniques in exploring the cryosphere.

1.2. Remote sensing of ice and snow

Expeditions to the polar region using air-borne remote sensing techniques began in the early 1900s. Mittelholzer et al. (1925) [13] discussed a glacier formation using aerial photography in Spitzbergen islands in the Svalbard archipelago to the east of northern Greenland. Wilkins (1929) [14] showed ice cover in the Antarctic Peninsula (AP) using aerial photography (i.e. a folding Kodak 3A camera). Although experiments were conducted in these challenging conditions, with great skill and considerable risk, many scientific problems await solution.

In the early 1960s, the first operational space-borne optical imaging instruments

(i.e. CORONA, ARGON, and LANYARD) were developed for both detailed reconnaissance and regional mapping [15]-[17]. These systems allowed polar researchers to acquire global scale optical imaging data covering the cryosphere. The data could be used to identify local fluctuations in glacier termini [18] and large-scale flow features on ice sheets [19]; these properties have been monitored in greater detail with the development of space-borne optical imaging instruments such as Landsat, Moderate Resolution Imaging Spectrometer (MODIS), Geoeye-1, and etc. However, the remote sensing techniques based on these systems fail to resolve the problems. Long polar nights and frequent cloudy weather conditions at the high latitudes of the cryosphere hinder the measuring activities of the systems.

Given these limitations, we consider the use of microwaves, which can penetrate through cloud, dust, and rainfall because of their long wavelengths; additionally, active microwave remote sensing can observe during both day and night since its sensors generate source power. Thus, microwave remote sensing has been widely used to monitor changes in the cryosphere. For example, space-borne microwave scatterometer and radiometer systems (e.g., QuikSCAT, Seasat-A, ERS-1/2, ADEOS-1/2, SSM/I, and AMSR-E) have been used to derive sea ice extent, concentration, and motion [18]-[20]. However, these instruments do not have high resolution capability, while space-borne Synthetic Aperture Radar (SAR) instruments (e.g., RADARSAT-1, ERS -1 and -2, and Envisat) have enhanced resolution capability. Thus, these instruments have been used to generate high resolution mapping of the sea ice edge and icebergs, and they estimate the current velocity of ice sheets using interferometric methods [21]-[22]. However, these

techniques provide only horizontal information of the spatial distribution of the cryosphere.

It was suggested that microwaves can penetrate the ice and snow due to their dielectric properties (i.e., loss factors) [23]. This suggestion proved to be a prelude to exploring vertical properties of the ice and/or snow, such as thickness and internal structure. Indeed, Waite and Schmidt (1962) [24] led the first experiments to measure the thickness of ice sheets in Antarctica and Greenland using the air-borne radar altimeter system (frequencies: 110, 220, 440, and 4300 MHz). The basic principle used to measure the ice thickness and/or snow depth is that the travel time of a radar pulse (of an appropriate wave speed) between the surface and bottom of the ice and/or snow can be converted into the distance, allowing those values to be determined. These fundamental techniques contributed to the development of space-borne radar altimeter systems such as the ERS 1/2, GEOSAT, Cryosat 1/2, etc. In addition, air- and space-borne laser altimeter systems have been developed using principles similar to those of the radar altimeter systems (i.e., ICESat, Airborne Topographic Mapper (ATM) [flown as part of the IceBridge Campaign]), in order to verify surface profiles of the ice and/or snow with greater accuracy [25]-[29].

Although the altimeter systems have successfully observed the thickness of ice sheets, lake ice, and snow, measurement of sea ice thickness is an issue that has not yet been resolved. The scattering structures of microwaves from sea ice are relatively more complicated than those of land ice and snow, because the dielectric properties of sea ice vary due to the varying stages of sea ice growth. Therefore, it is difficult to interpret various scattering structures (e.g., surface and volume scattering) of

microwaves from sea ice, and many studies attempt to resolve this issue.

Ice and snow of the Cryosphere

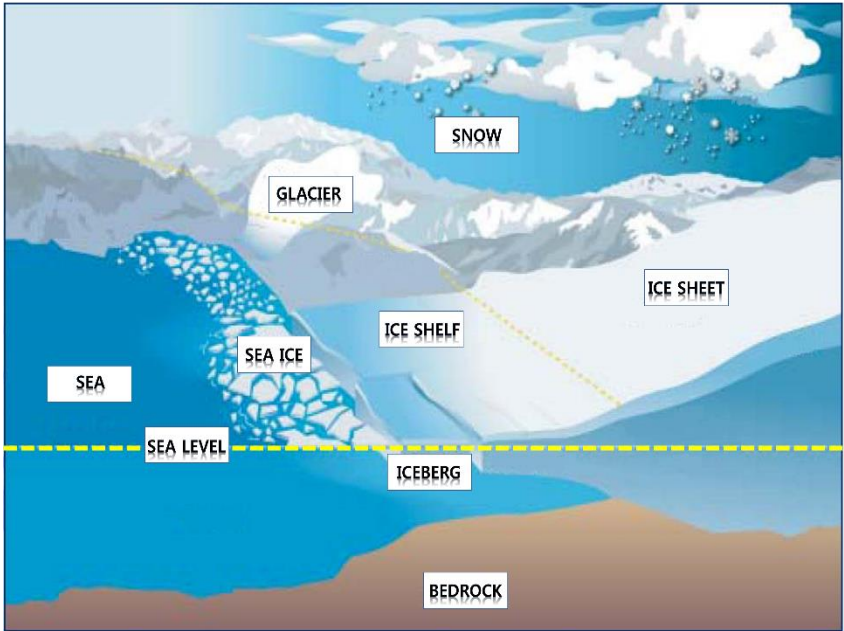


Figure 1. Classification of ice and snow at the cryosphere. [From ESA]



Figure 2. The spatial distribution land and sea ice in the polar region.

Table 1. Global distribution of land and sea ice.

| Global distribution of ice | | | | | |
|----------------------------|-------------------------|-------------|-----------|---------------|------------------------|
| Land ice | | | Sea ice | | |
| Region | Area (m ²) | Portion (%) | Region | Max./Min. | Area (m ²) |
| Antarctica | 1.36 x 10 ¹³ | 86 | Arctic | Max. (Winter) | 1.5 x 10 ¹¹ |
| Greenland | 1.73 x 10 ¹² | 11 | | Min. (Summer) | 7 x 10 ¹⁰ |
| Remainder | 5 x 10 ¹¹ | 3 | Antarctic | Max. (Winter) | 1.8 x 10 ¹¹ |
| Total | 1.58 x 10 ¹³ | 100 | | Min. (Summer) | 3 x 10 ¹⁰ |

Albedo of the earth

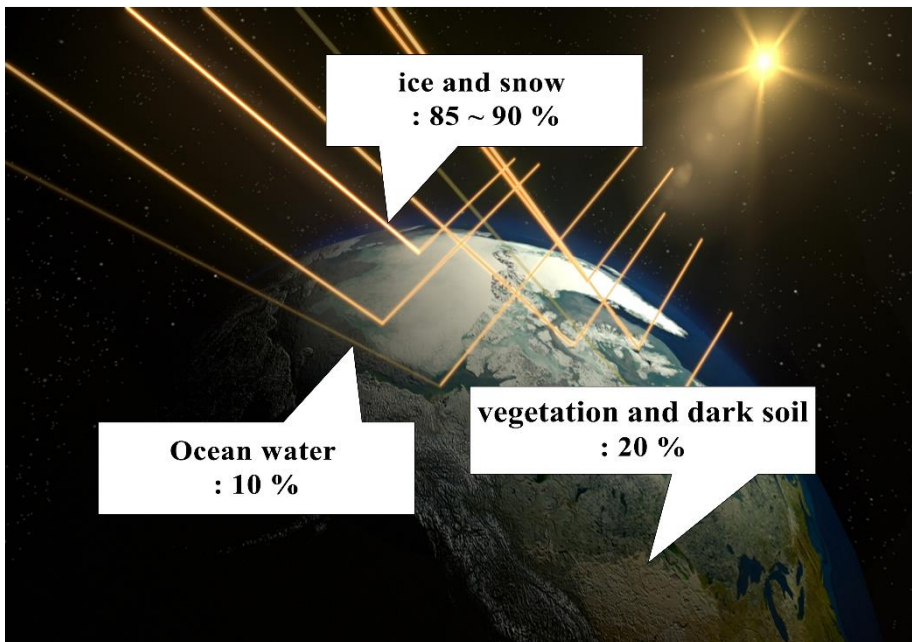


Figure 3. Albedo of ice, snow, ocean water, and vegetation and dark soil on the earth.

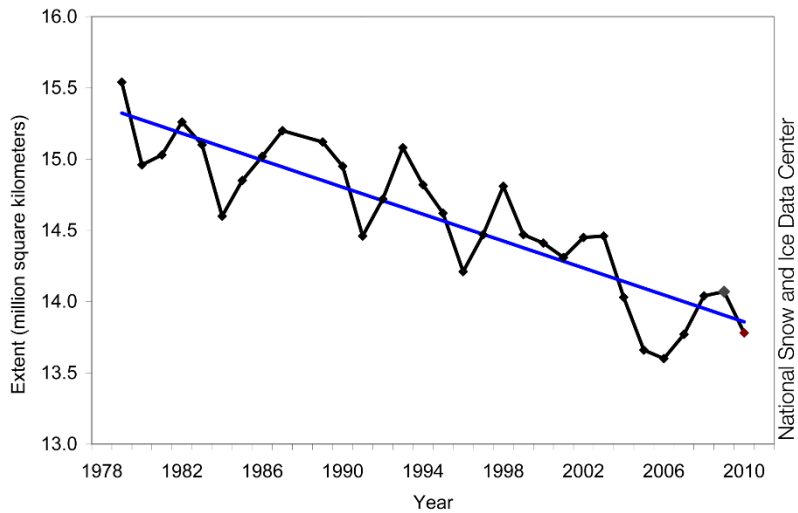


Figure 4. Average monthly Arctic sea ice extent from Jan 1979 to 2010. [From NSIDC]

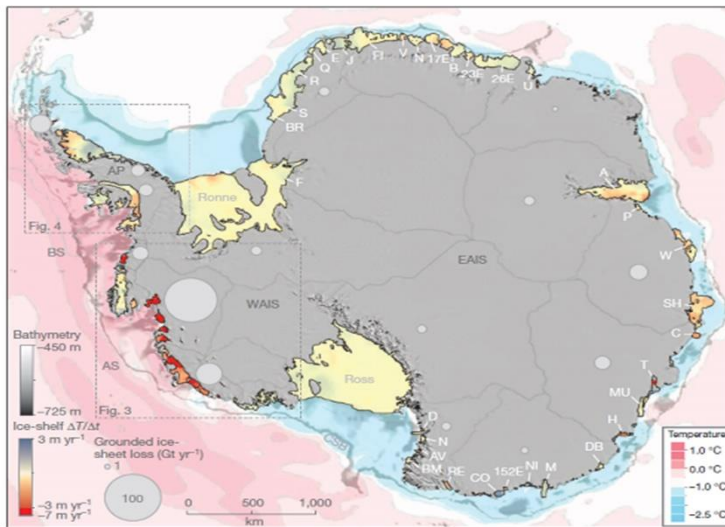


Figure 5. Change rate of the ice thickness in the Antarctic ice shelf from 2003 to 2008. [Prichard et al, 2012]

1.3. Motivation and Objectives of this thesis

The latest space-borne SAR (e.g., RADARSAT-2 and TerraSAR-X) systems offer high-resolution (up to 1 m) full polarimetric SAR data. These capabilities allow us to interpret scattering structures of microwaves using various polarimetric target decomposition methods [30]-[32]. Therefore, the latest space-borne SAR data have good potential to measure sea ice thickness with their polarimetric capabilities. An efficient method for measuring sea ice thickness can be developed if the interactions between sea ice and microwaves can be interpreted using this capability.

In this thesis, efficient methods to measure sea ice thickness using space-borne polarimetric SAR data were explored based on the interpretation of various scattering structures from sea ice and snow. A ground-based scatterometer, which can measure the return radar signals from sea ice and snow in the field, was developed in order to practically interpret the scattering structures of microwaves from sea ice and snow, and various theoretical microwave scattering model simulations were used.

Chapter 1 presents an introduction to the motivation and purpose for this thesis. Chapter 2 provides the setup of the ground-based scatterometer and space-borne SAR systems and the radiometric calibration procedures of each system to acquire reliable data. Chapter 3 explains the results of various experiments to measure sea ice thickness using measurements of the ground-based scatterometer system, in-situ measurements, and numerical simulations. Chapter 4 shows results of a

measurement in order to measure sea ice thickness using space-borne SAR data and in-situ measurements based on the results of Chapter 3. Chapter 5 summarizes the results of this thesis, and discusses limitations of proposed method to measure sea ice thickness in this thesis and future works.

Chapter 2. Polarimetric microwave remote sensing systems

2.1. Ground Based POLarimetric SCATterometer (GB-POLSCAT)

As mentioned in Chapter 1, it is well known that GB-POLSCAT is optimal tool to interpret scattering features of microwave from natural distributed targets. This system has mainly used to interpret signatures backscattered from surface of the targets with space-borne SAR data and backscattering models [33]-[35]. Furthermore, Strozzi (1996) [36] introduced the practical method to measure the signatures backscattered from snow cover with the GB-POLSCAT system at 5.3 GHz (C-band) and 35 GHz (Ka-band). This method is very useful to interpret scattering structures (i.e. surface/volume scattering) of microwave from snow covers. Detail process of the method refers to Section 6.2 of Strozzi's dissertation [36].

In this thesis, the GB-POLSCAT was developed at Seoul National University (SNU) for interpreting the signatures from sea ice and snow with Strozzi's method. In following sections, detail set-up and calibration procedures of the system are introduced.

A. Set-up of GB-POLSCAT

The GB-POLSCAT developed at SNU is based on Network Analyzer (NA), Circuit, and Antenna (Figure 6a). The NA is main device in the GB-POLSCAT as source power generator, receiver of returned signals, and signal processing unit. Anritsu MS2028B among various NA products was used. This NA can generate source signal at wide frequency range (i.e. from 5 kHz to 20 GHz), and is easy to operate being as it is hand held type. Circuit consists of isolator, power amplifier, switch controller, and circulator (Figure 6b). Isolator blocks reverse current of transmitted signal. Power amplifier controls the source power of the generated signal up to 40 dB. Switch controller and circulator decide the polarization features of transmitted and received signal through controlling the transmission line of signal transmitted into the single orthomode transducer (OMT) horn antenna or received from the one. In addition, azimuth and incidence angle of the illuminated signal can be controlled automatically by step motors.

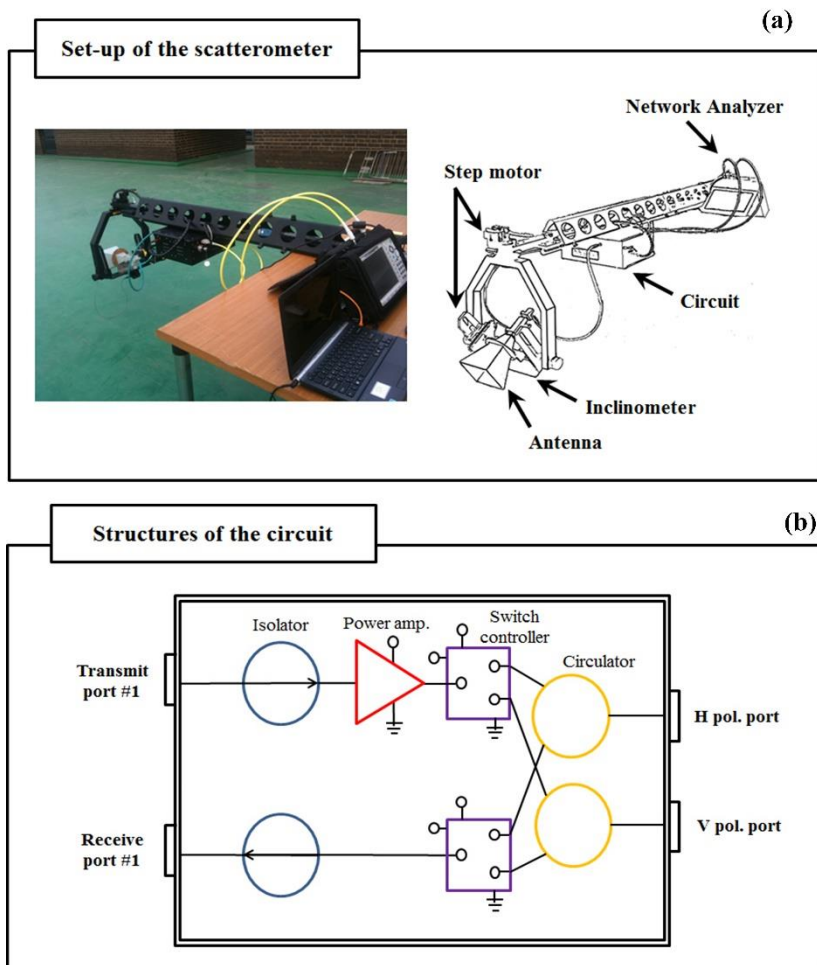


Figure 6. (a) External parts of the GB-POLSCAT system developed by SNU
 (b) Structures of the circuit.

B. System calibration of GB-POLSCAT

B.1. Basic concept of the system calibration

In the GB-POLSCAT, the radar equation associated with transmitted and received signal can be defined as following [37]

$$E_{pq}^r = e^{-j2kr} \left(\frac{P_t G_t G_r \lambda^2}{(4\pi)^2 r^4} \right)^{\frac{1}{2}} S_{pq} \quad (1)$$

where E_{pq}^r is the received electromagnetic field. G_t and G_r are the gain of transmitting and receiving antenna, respectively. P_t is transmitting power generated by the NA. λ is the wave length and r is the distance between the antenna of the GB-POLSCAT and a target. S is the scattering matrix of a target. The subscripts p and q denote the polarization of transmitted and received signal, respectively. Here, Radar Cross Section (RCS) of a target can be determined by the scattering matrix as following:

$$\sigma_{pq} = 4\pi |S_{pq}|^2 \quad (2)$$

In ideal case, it is possible to determine the scattering matrix of a target by measuring of $\frac{|E_{pq}^r|^2}{P_t} \equiv U_{pq}$ from a target. However, radar distortions are always

generated under field measuring conditions [38], so equation (1) can be simply rearrange into equation (3) and equation (4) by a corresponding four-component vector.

$$E^r = e^{-j2kr} \left(\frac{P_t G_t G_r \lambda^2}{(4\pi)^2 r^4} \right)^{\frac{1}{2}} RST \quad (3)$$

where R and T are radar distortions induced by transmitting and receiving line of signals within the GB-POLSCAT, respectively.

$$\begin{pmatrix} E_{vv}^r \\ E_{vh}^r \\ E_{hv}^r \\ E_{hh}^r \end{pmatrix} = e^{-j2kr} \left(\frac{P_t G_t G_r \lambda^2}{(4\pi)^2 r^4} \right)^{\frac{1}{2}} D \begin{pmatrix} S_{vv} \\ S_{vh} \\ S_{hv} \\ S_{hh} \end{pmatrix} \quad (4)$$

$$\text{here, } D = \begin{pmatrix} R_{vv}T_{vv} & R_{vv}T_{vh} & R_{vh}T_{vv} & R_{vh}T_{vh} \\ R_{vv}T_{hv} & R_{vv}T_{hh} & R_{vh}T_{hv} & R_{vh}T_{hh} \\ R_{hv}T_{vv} & R_{hv}T_{vh} & R_{hh}T_{vv} & R_{hh}T_{vh} \\ R_{hv}T_{hv} & R_{hv}T_{hh} & R_{hh}T_{hv} & R_{hh}T_{hh} \end{pmatrix}$$

where, D is the radar distortion matrix. In order to the system calibration, the radar distortion matrix should be exactly determined. In general, the radar distortions have been determined by measuring a point calibration target of which the RCS is well known, because it is impossible to measure directly radar distortions. From measuring the point calibration target, the radar distortions can be determined as following

$$D = e^{j2kr} \left(\frac{P_t G_t G_r \lambda^2}{(4\pi)^2 r^4} \right)^{-\frac{1}{2}} S^{-1} E^r \quad (5)$$

B.2. Conventional system calibration

Using the basic principle of the system calibration with the point calibration target, various calibration techniques have been developed. The generalized calibration technique (GCT) can be determined the radar distortion using three calibration targets [39]. The scattering matrix of the first target must have the form of identity matrix such as sphere or flat plates while the other two targets do not need any specified scattering matrix. In order to calculate the radar distortion with the calibration targets, this technique employed an eigenvalue approach. As a similar technique, constrained calibration technique (CCT) was developed. Unlike GCT, this technique uses all targets with specific scattering matrices [40]. Although these calibration techniques can fully characterize the radar distortion matrix, they are strongly affected by an alignment of the targets, and time consuming. Detail procedures of each calibration techniques are not repeated in this thesis.

Sarabandi et al. (1990; 1992) [38], [41] proposed convenient calibration techniques of the GB-POLSCAT with single OMT antenna. It can be assumed that the antenna is perfectly isolated unlike the dual antenna system. The dual antenna system can generate the cross polarized terms from not only the structure of the antenna but also unisolated features of the antenna. The cross terms of unisolated antenna system can be determined by measuring the point calibration target of which cross polarized elements of the scattering matrix are well known such as GCT or CCT. In actual, Strozzi's GB-POLSCAT was the dual antenna system, and he used GCT for the

system calibration. On the other hand, the isolated antenna assumption can lead that cross polarized terms (R_{hv} , R_{vh} , T_{hv} , and T_{vh}) of the radar distortions are only generated by structures of the antenna, and these terms can be determined by measuring of any calibration target. Thus, Sarabandi's calibration techniques can practically determine the radar distortions by only once measuring of any calibration targets. Actually, most of calibration experiments have used a metal sphere as the point calibration target because of independence of target alignment, and the radar distortion matrix can be determined as following

$$R_{vv}T_{vv} = e^{-j2kr}r^2 \frac{U_{vv}^S}{(1 + C^2)\sqrt{\frac{\sigma^S}{4\pi}}}$$

$$\beta \equiv \frac{R_{hh}}{R_{vv}} = \frac{2C}{(1 + C^2)} \frac{U_{hh}^S}{U_{vh}^S}$$

(6)

$$\alpha \equiv \frac{T_{hh}}{T_{vv}} = \frac{(1 + C^2)}{2C} \frac{U_{vh}^S}{U_{vv}^S}$$

$$C = \pm \frac{1}{\sqrt{a}} (1 - \sqrt{1 - a}) \quad \text{where,} \quad a = \frac{U_{vh}^S U_{hv}^S}{U_{vv}^S U_{hh}^S}$$

where C is the cross talk generated by single OMT antenna. σ^S is theoretical RCS of a metal sphere. The superscript S denotes measuring of a metal sphere. Using equation (6), the radar distortion matrix of equation (4) is rearranged as following

$$D = R_{vv}T_{vv} \begin{pmatrix} 1 & C\alpha & C & C^2\alpha \\ C & \alpha & C^2 & C\alpha \\ C\beta & C^2\alpha\beta & \beta & C\alpha\beta \\ C^2\beta & C\alpha\beta & C\beta & \alpha\beta \end{pmatrix} \quad (7)$$

As mentioned above, the GB-POLSCAT developed by SNU uses single OMT antenna, so all data measured by the GB-POLSCAT were basically calibrated by Sarabandi's method. However, Strozzi emphasized the necessary of improved calibration technique which can efficiently calibrate the effect of the external conditions as an issue of future study. Because the radar distortions are strongly affected by the weather conditions such as air temperature under field experiments. Therefore, practical calibration method which can give a clue of the issue are proposed in next section.

C. New system calibration of GB-POLSCAT

C.1. Background

As mentioned above, the extraction of radar distortions of polarimetric scatterometer is a key in measuring the exact backscattering coefficients of distributed targets. Radar distortions can be divided into two groups. The first group is passive distortions which are insensitive to changes of the external conditions (e.g., the passive fixed antenna structure). The second group is active distortions which are sensitive to changes of the external conditions. These can be caused mainly by active devices within radar systems such as the GB-POLSCAT (e.g. transmitter/receiver, external electronic/microwave circuits such as amplifiers) [38], [41]. These radar distortions can be determined by measuring the radar response of a point calibration target with a known Radar Cross Section (RCS) [39], [40]. In particular, Sarabandi et al. [41] proposed an improved method to extract the active distortions by using the ratios of the radar responses of a point calibration target measured within an anechoic chamber and out in the field. However, it is difficult to use this method in some locations (e.g., the cryosphere and ocean) due to the difficulties involved in installing a point calibration target. Thus, there is a need for a more versatile method.

It is highly unlikely that the antenna impedance perfectly matches the impedance of the source cable in a radar system. Due to the impedance mismatch at the antenna input, a portion of the energy reflects back to the source (this is often referred to as the “return loss”). Because of this, the scattering matrix due to the impedance

mismatch can be defined at the antenna input [42]. In this section, a practical method that can extract the active distortions using the signal returned from the antenna input is introduced. The experiments to validate the proposed method using the field measurements of PRS, space-borne SAR data, and numerical simulations are presented.

C.2. New technique to extract radar distortions

In order to effectively extract radar distortions, Sarabandi et al. [41] discretized the domain of the main antenna beam into small subdomains and measured the radar response of each subdomain from a point calibration target (e.g., a conducting sphere) in an anechoic chamber, which was well designed to prevent the loss of any signals. They then set the distortions in the anechoic chamber to 1, which can be other values under field measurements. Under field conditions, Sarabandi et al. [41] measured the radar response of a point calibration target only at the boresight direction. Then, the active distortions caused by external conditions were determined using the ratios of the radar responses of a point calibration target measured only at the boresight direction in the anechoic chamber and out in the field:

$$a_v^t a_v^r = \frac{U_{vv}^f}{U_{vv}^c}, \quad a_h^t = \frac{U_{vh}^f U_{vv}^c}{U_{vh}^c U_{vv}^f}, \quad a_h^r = \frac{U_{hh}^f U_{vh}^c}{U_{hh}^c U_{vh}^f} \quad (8)$$

where a represents the active distortion. The superscripts t and r denote transmitting and receiving channels, and the superscripts f and c are the field- and

chamber-measurements. Although this method can extract the active distortions with high accuracy, it is restricted to apply in some locations that are difficult to install a point calibration target.

Here, a more efficient and practical method to extract the active distortions without a point calibration target under field conditions is introduced. The source power of the polarimetric scatterometer reflects at the antenna input due to the impedance mismatch. The returned signal from the antenna input is named as the Returned signal from Point of Interest (RPI) and it is assumed that the transmitting and receiving antenna gains are the same ($G_t = G_r$) and the antenna structure is fixed under field conditions (Figure 7). The reflected signal from the RPI with scattering matrix, $[S_{RPI}]$, involves radar distortions except the antenna structure. Because the antenna structure is fixed such that the cross-talk and channel imbalance in the antenna are not changed under field conditions, the active distortions can be extracted using the measured value from RPI in the anechoic chamber and out in the field using Equation (8). Then, the calibration matrix elements $R_{vv}T_{vv}$, α , β of equation (6) can be modified by

$$R_{vv}^f T_{vv}^f = a_v^t a_v^r R_{vv}^c T_{vv}^c, \alpha^f = \frac{a_h^t}{a_v^t} \alpha^c, \text{ and } \beta^f = \frac{a_h^r}{a_v^r} \beta^c \quad (9)$$

Finally, the radar distortion matrix of equation (7) can be rearranged as following

$$D = R_{vv}^f T_{vv}^f \begin{pmatrix} 1 & C\alpha^f & C & C^2\alpha^f \\ C & \alpha^f & C^2 & C\alpha^f \\ C\beta^f & C^2\alpha^f\beta^f & \beta^f & C\alpha^f\beta^f \\ C^2\beta^f & C\alpha^f\beta^f & C\beta^f & \alpha^f\beta^f \end{pmatrix} \quad (10)$$

C.3. Validation using field experiments and numerical simulation

In order to validate the proposed method, radar distortions by measuring the radar responses from a point calibration target (e.g., a conducting sphere) and the RPI in the anechoic chamber (Figure 8) are derived. The radar responses of the point calibration target and the RPI at incidence angles of 20°, 30°, 40°, and 50° under field conditions are measured. Tidal flats in South Korea were selected as the field site. The Root-Mean-Square (RMS) height, correlation length, and soil moisture content at the test site are simultaneously measured. The field-measured RMS height and correlation length were 0.52 and 8.0 cm, respectively. The field-measured soil moisture content was about 0.6 m³/ m³. TerraSAR-X data (X-band: 9.65GHz) were also acquired at the test site. The acquired data was dual-polarized (VV and VH) and the incidence angle was 45°.

Figure 9 shows the estimated active distortions of the VV polarization caused by the field conditions. It shows that the estimated active distortions using the radar responses of the point calibration target and the RPI are almost the same within the margin of error (0.1%). Figure 10 shows the backscattering coefficients of the PRS, the SAR data, and the simulations from [43], [44]. These measured backscattering coefficients agree quite well with those simulated within the margin of error, which was 0.5%. Therefore, it is reasonable that the active distortions can be derived by the radar responses from the RPI under field conditions.

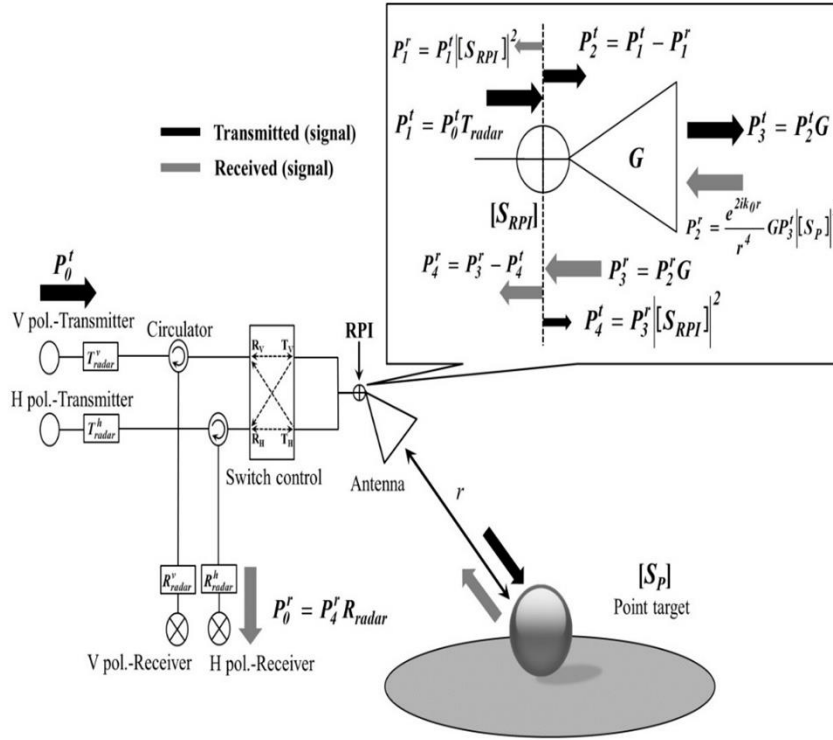


Figure 7. Geometry and block diagram of Polarimetric Radar System (PRS. P is the power generated by PRS. The superscript of P denotes direction of power transmission (e.g., t: transmitted or r: received direction). The subscript of P denotes a sequence of power transmission. [S] is a scattering matrix. The superscript of [S] denotes RPI or a point calibration target. G denotes the antenna gain. r is the distance between the antenna and a point calibration target.

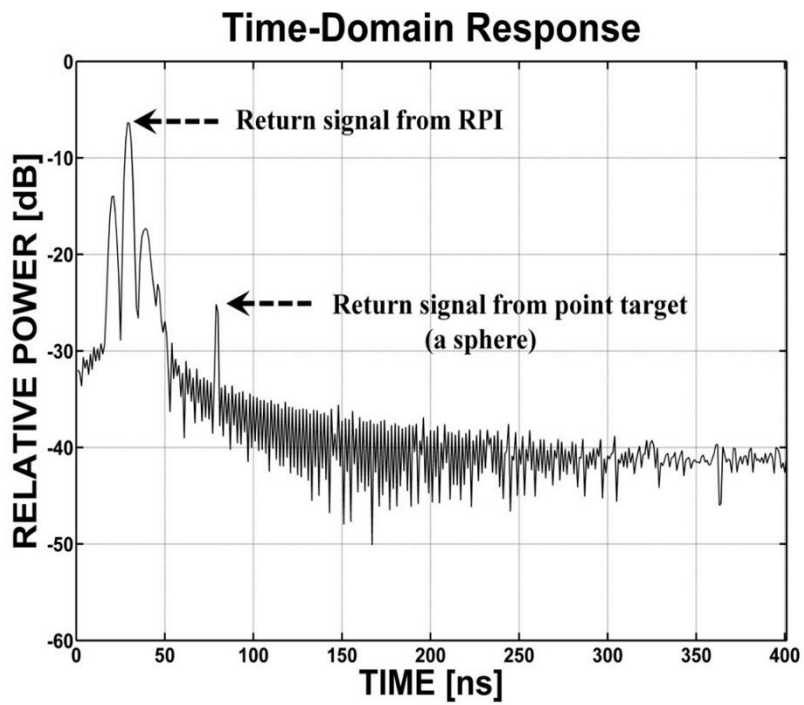


Figure 8. The measured radar response of the PRS in the anechoic chamber.

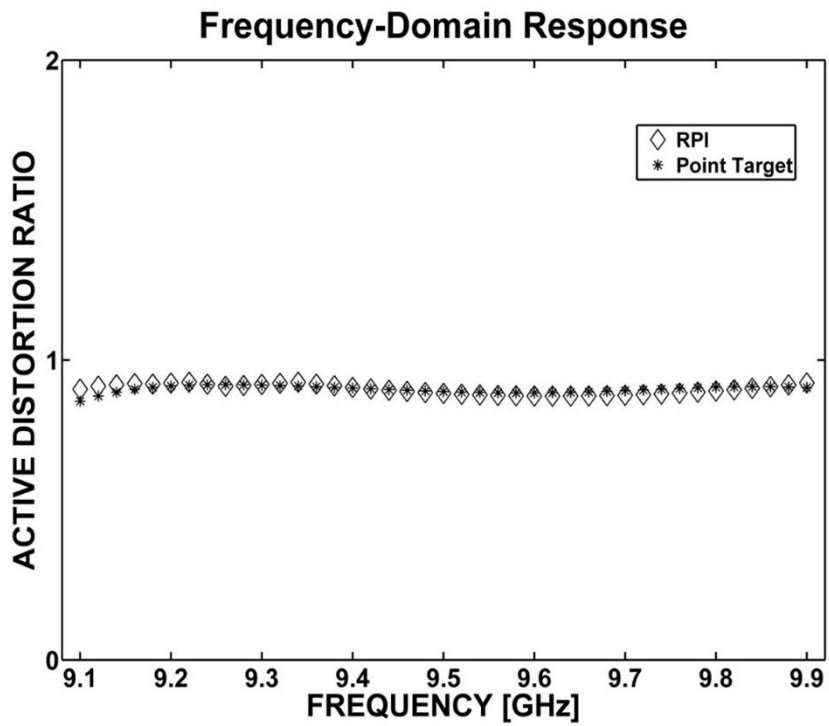


Figure 9. Active distortion estimated from field experiments.

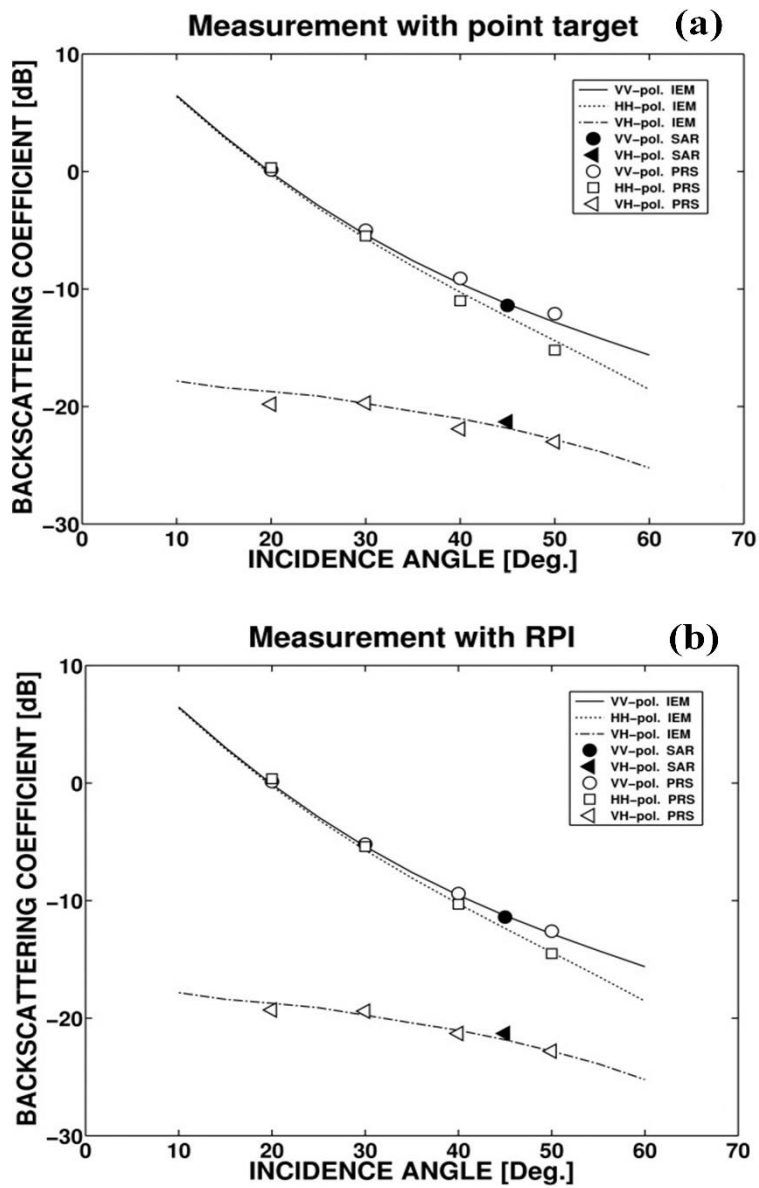


Figure 10. Comparison between simulated and measured backscattering coefficients.

2.2. Space-borne SAR systems

A. RADARSAT-2 and TerraSAR-X

In this thesis, the polarimetric space-borne SAR data were acquired by RADARSAT-2 and TerraSAR-X. RADARSAT-2 and TerraSAR-X are latest C- and X-band space-borne SAR systems, respectively. RADARSAT-2 was developed at the Canadian Space Agency (CSA), and was launched on December 14, 2007. TerraSAR-X was developed at the German Aerospace Center (DLR) and European Aeronautic Defense and Space Company (EADS) Astrium, and was launched on June 15, 2007. These radar earth observation satellites can operate with various imaging modes, combinations of full polarizations, high resolution capabilities (up to 1m), and precise radiometric and geometric accuracy (Figure 11). Detailed specifications of these systems are illustrated in Table 2. The data acquired by the space-borne SAR systems are basically calibrated by various radiometric and geometric calibration procedures. In particular, radiometric calibration is to determine the NRCS of distributed targets, and this procedure is main key to determine reliability of the acquired SAR data. The data acquired by TerraSAR-X and RADARSAT-2 need to reprocess in order to estimate exact NRCS of the data with the information which is given from MDA and DLR. Therefore, In order to reprocess exactly the data with the given information, it needs to understand basic concept of the radiometric calibration procedure. In this thesis, the procedure is explained with radiometric calibration experiments of air-borne SAR system

(NanoSAR-B, i.e. this system was used for the prospective study in chapter 4) operated by SNU since the radiometric calibration procedures of various SAR systems are similar.

Table 2. Specifications of RADARSAT-2 and TerraSAR-X.

| | <i>RADARSAT-2</i> | <i>TerraSAR-X</i> |
|-------------------------------|-------------------------------------|----------------------------|
| <i>Frequency</i> | 5.405 GHz (C-band) | 9.65 GHz (X-band) |
| <i>Polarizations</i> | HH/VV/HV/VH | HH/VV/HV/VH |
| <i>Antenna length</i> | 15m | 4.8m |
| <i>Antenna width</i> | 1.5m | 0.7m |
| <i>PRF</i> | 1.0 kHz ~ 3.8 kHz | 2.2 kHz ~ 6.5 kHz |
| <i>Range bandwidth</i> | 11.56, 17.28, 30.0, 50.0 MHz | 150 MHz and 300 MHz |
| <i>Revisit time</i> | 24 days | 11 days |
| <i>Resolution</i> | Up to 3m | Up to 1m |

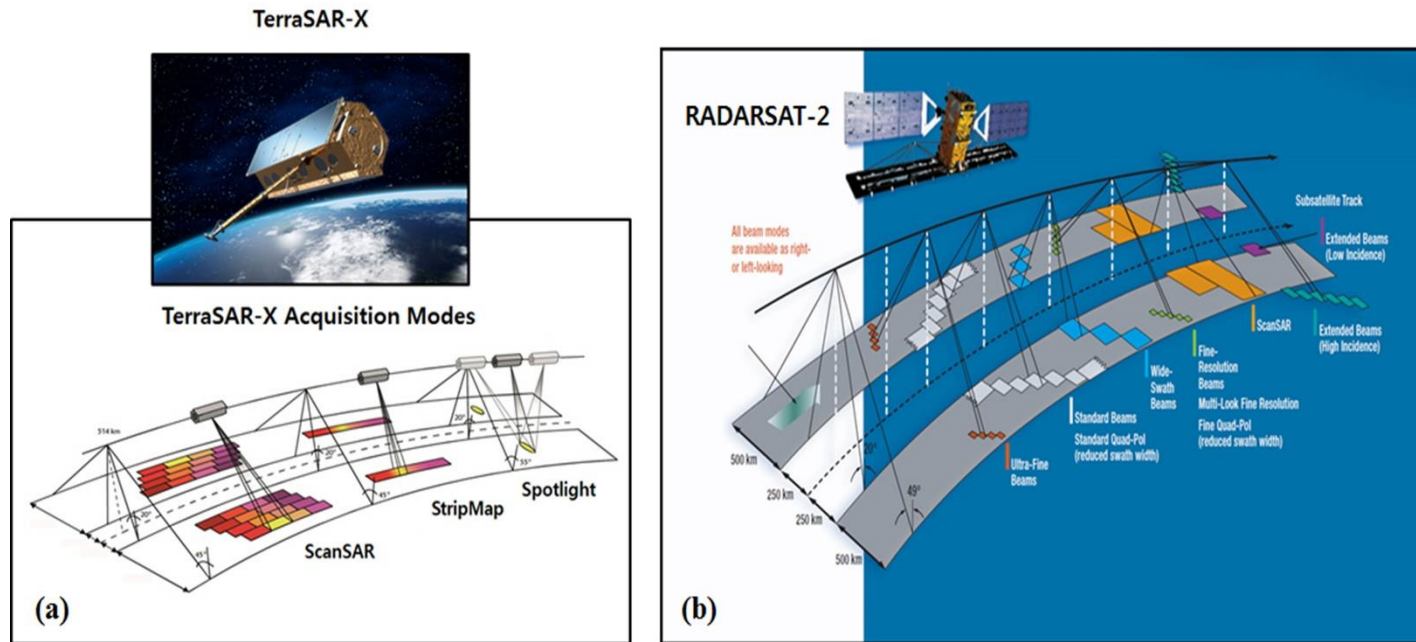


Figure 11. Various imaging modes of the space-borne SAR systems (a) TerraSAR-X (b) RADARSAT-2. [From DLR and MDA]

B. Radiometric calibration of the SAR systems

B.1. Background

Radiometric calibration allows to correct all the contributions in the radiometric values generated besides the target characteristics. This permits minimizing the differences in the image radiometry of air- and space-borne SAR system [45]. In order to acquire a highly qualified space-borne SAR data, accurate radiometric calibration is the essential procedure. Radiometric calibration is a correction for estimation of precise NRCS or backscattering coefficient (σ^0) of microwave signatures backscattered from a target. Basically, NRCS calculates with the following formula (11).

$$\sigma^0 = \frac{DN^2}{K} \frac{1}{G^2(\theta)} \left(\frac{R}{R_{ref}} \right)^3 \sin(\alpha) \quad (11)$$

where, K is the absolute calibration constant which compensates the power penalties which occurred from the internal system and the reference distance, R_{ref} , between the SAR antenna and the target. G is the unique antenna patterns transmitted and received from the antenna, which is defined as the function of elevation angle (θ). Here, it is assumed that transmitted and received antenna gain are same. R is the real distance between a target and an antenna. As K compensates the power loss from the reference distance, $(R/R_{ref})^3$ term plays the role of calibration for the power penalty

that occurred as much as the difference between the real distance and the reference distance. In general, these procedures are called “range spreading”. Lastly, α is the incidence angle of the main beam. In this regard, the antenna patterns and range spreading calibration are called “relative radiometric calibration” and the process of extracting the absolute calibration constant (K) with measuring known RCS of reference target (i.e. trihedral corner reflector) [46], [47] called “absolute radiometric calibration”.

B.2. Backscattering coefficient computation of TerraSAR-X and RADARSAT-2

Basically, DLR and MDA give to user respective radiometric calibrated TerraSAR-X and RADARSAT-2 data with above mentioned calibration procedures. However, the acquired SAR data need to be reprocessed in order to estimate exact backscattering coefficients. Here, it is explained to estimate the backscattering coefficients of the acquired TerraSAR-X and RADARSAT-2 data.

In case of TerraSAR-X, the Digital Number (DN) values are computed from the complex data given in the COSAR format file of delivered TerraSAR package files as following:

$$DN = \sqrt{I^2 + Q^2} \quad (12)$$

where I and Q are the real and imaginary parts of the complex data, respectively. Then, the radar brightness (β^0) is derived by the DN multiplying the calibration factor (K_s) given in the xml format file of delivered TerraSAR-X package files (Figure 12).

$$\beta^0 = K_s \cdot |DN|^2 \quad (13)$$

The radar brightness (β^0) is the RCS per unit area in the slant range, and the backscattering coefficient (σ^0) is the RCS per unit area in the ground range. Thus,

the relation of these values is as following

$$\beta^0 = \frac{\sigma^0}{\sin(\alpha)} \quad (14)$$

where α is a local incidence angle. Using this relationship, the backscattering coefficient is derived as following

$$\sigma^0 = \beta^0 \cdot \sin(\alpha) \quad (15)$$

DLR additionally provides the information of the system noise, Noise Equivalent Beta Naught (NEBN), in order to estimate exact radar brightness. Internal system of TerraSAR-X record the NEBN three times during the acquisition time. The acquisition start and stop times correspond to the first and last system noise records, respectively. Each NEBN is estimated as following equation

$$NEBN = K_s \cdot \sum_{i=0}^{deg} a_i (\tau - \tau_{ref})^i \quad \text{here, } \tau \in [\tau_{min}, \tau_{max}] \quad (16)$$

where i is polynomial degree. a is coefficient of the polynomial equation. τ_{ref} is reference point. τ_{min} and τ_{max} are validity range min and validity range max, respectively. The values of these parameters are given in the xml format file. At last, the NEBN is determined by the mean value of them, and then, exact backscattering coefficients of acquired TerraSAR-X data are derived as following equation (Figure 13)

$$\sigma^0 = (\beta^0 - NEBN) \cdot \sin(\alpha) \quad (17)$$

In case of RADARSAT-2, the process to estimate the backscattering coefficients is simpler than the one of TerraSAR-X. The DN values are computed from the complex data given in the tiff format file of delivered RADARSAT-2 package files, and the DN values can be selectively converted to the radar brightness (β^0) or the backscattering coefficients (σ^0) with scaling Look-up Tables (LUTs). Each LUT provides a constant offset and range dependent gain. Using these parameters, the calibrated values (i.e. the radar brightness and the backscattering coefficients) are directly derived as following equation (Figure 14 and 15)

$$\beta^0 \text{ or } \sigma^0 = \frac{(DN^2+B)}{A} \quad (18)$$

where A is the gains value. B is the constant offset

Beta naught of TerraSAR-X

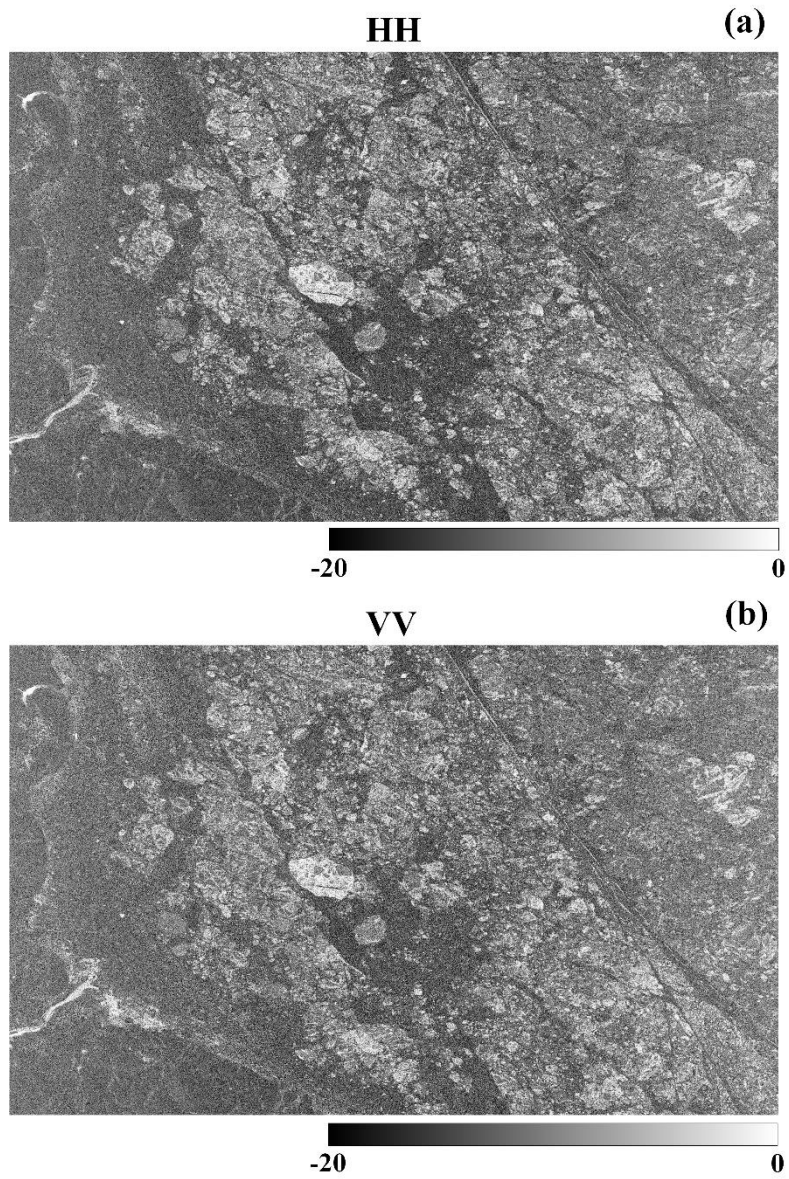


Figure 12. Estimated radar brightness of acquired TerraSAR-X. (a) HH (b) VV

Sigma naught of TerraSAR-X

HH

(a)



-20

0

VV

(b)



-20

0

Figure 13. Estimated backscattering coefficients of acquired TerraSAR-X data.
(a) HH (b) VV

Beta naught of RADARSAT-2

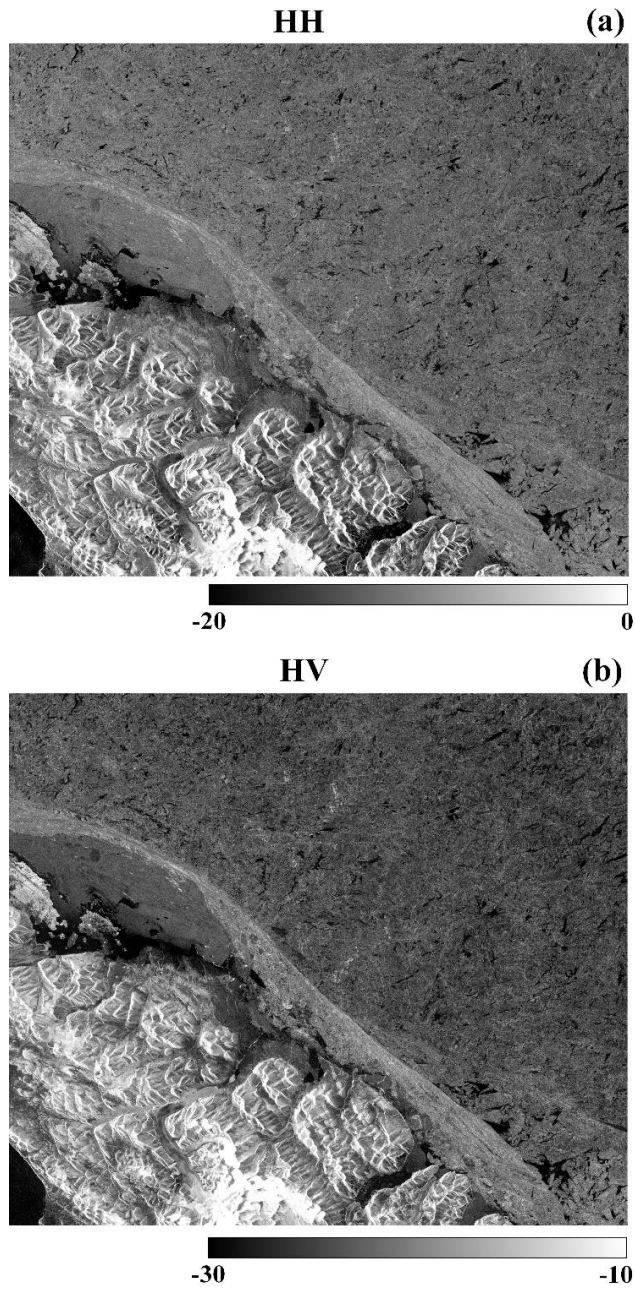


Figure 14. Estimated radar brightness of acquired RADARSAT-2 data.
(a) HH (b) HV

Sigma naught of RADARSAT-2

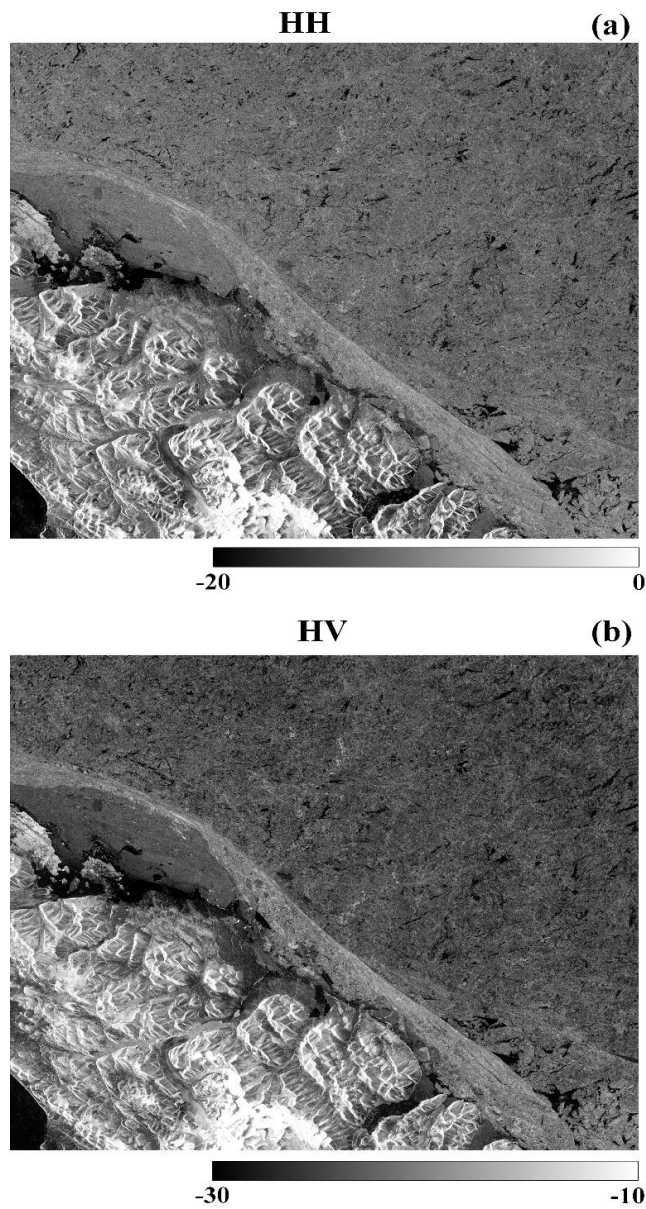


Figure 15. Estimated backscattering coefficients of acquired RADARSAT-2 data. (a) HH (b) HV

Chapter 3. Polarimetric signatures characterized by scattering features from sea ice and snow

3.1. Background

In the Arctic Ocean from the middle of September to the middle of March in next year (i.e. freezing season), sea ice is formed when the temperature of sea water decreases below its freezing point (i.e. about $-1.8\text{ }^{\circ}\text{C}$), and then, it grows. On the contrary to this, sea ice melts from the middle of March to the middle of September (i.e. melting season) due to increasing of the temperature above the freezing point (Figure 16a). In the Antarctic Ocean, the freezing season is from the middle of February to the middle of September, and the melting season is from the middle of September to the middle of February (Figure 16b). In general, sea ice formed during the freezing season can be broadly divided into First-Year ice (FYI) and Multi-Year ice (MYI). FYI has no more than one year growth while MYI has survived more than one melting season.

Figure 17 shows common life cycle of sea ice [48]. For the freezing season, FYI is formed and grows. The surface roughness of newly formed FYI is relatively smooth, and dry snow is covered on its surface. For the melting season, snow cover melts, and the surface roughness is relatively rougher. In this season, FYI are fully melted or survived. For next freezing season, the survived FYI changes into MYI, and the surface roughness of MYI is rougher and deformed due to mechanical growth processes where ice blocks collide with each other (i.e. ridging process). New dry

snow is covered on the surface. During the melting season, snow on surface of MYI becomes wet, and melting pond is formed by snow melting on surface of MYI. These processes are repeated every year. Thus, it is necessary to consider the realistic physical characteristics of sea ice such as snow cover, surface roughness, and dielectric constant in order to understand detail scattering features from sea ice under various conditions.

Polarimetric backscattering signatures from the ice are determined by various scattering features of microwave [48]. The features are simply classified into surface and volume scattering. Degree of surface scattering can be determined by surface roughness and dielectric constant of the ice surface, and the dielectric constant also decides on penetration of microwave into the ice surface. If microwave can penetrate into the ice surface due to low dielectric properties of the ice surface, degree of volume scattering must be determined by physical properties (i.e. shape, orientation, absorption, reflectivity, and etc.) of scatterers within the ice layer such as air bubbles and pockets of salty water (brine). The dielectric properties of sea ice are deeply related to the brine volume which is the fraction of brine [49], and temperature and salinity of sea ice govern the brine volume [50].

The salinity of sea ice is strongly related to its growth process. As sea ice grows, the brine within the ice layer is drained into the ice bottom, and the salinity is decreased (i.e. desalination). In addition, it was found that rapid desalination only occurs in thin sea ice (i.e. < 50 cm thickness), and the desalination slows down over time as the ice thickens, and Cox and Weeks (1973) [51] suggested that the average salinity in the Arctic Ocean is a piecewise linear decreasing function of the ice

thickness. This suggests that the variation of surface dielectric constant as the ice thickness may give us the solution to measure the ice thickness using space-borne SAR data.

As mentioned above, it is generally known that backscattering signatures from sea ice are dominated by surface roughness and complex dielectric constant of the ice surface [52]. These two factors have been decoupled to study relative contribution between these two [53]-[55]. The authors of [53]-[55] suggested the VV-to-HH backscattering coefficient ratio (BCR) of L-band air-borne SAR data could cancel out the surface roughness contribution, BCR can represent the remaining contribution from dielectric constant. They also showed a good correlation between BCR and thin FYI thickness. This relationship can be attributed to desalination of sea ice as the ice thickness increases. The rapid desalination of FYI decreases the surface dielectric constant resulting in decreasing BCR. However, as mentioned above, rapid desalination only occurs in thin FYI, and the desalination slows down over time as the ice thickens. That is, the variation of surface dielectric constant becomes very small in thicker ice (e.g. MYI). Furthermore, the ice is characterized by low-density surface layer with air bubbles, thus, unlike thin FYI, backscattering signatures from the ice are induced by not only surface scattering from surface roughness and dielectric properties but also volume scattering within the low-density layer [52]. These complexities of the scattering features from sea ice still make measuring of the ice thickness using the SAR data difficult. Therefore, it needs to understand detail scattering structures of microwave from sea ice exposed various conditions. In order to understand in detail the scattering features from sea ice, the

scattering structures of sea ice were departmentalized like Figure 18. As mentioned above, sea ice surfaces are generally covered with snow cover. Thus, the scattering structures can be classified into surface and volume scattering from snow, and surface and volume scattering from sea ice. Based on the scattering structures, it was explored optimized method to determine sea ice thickness in next section.

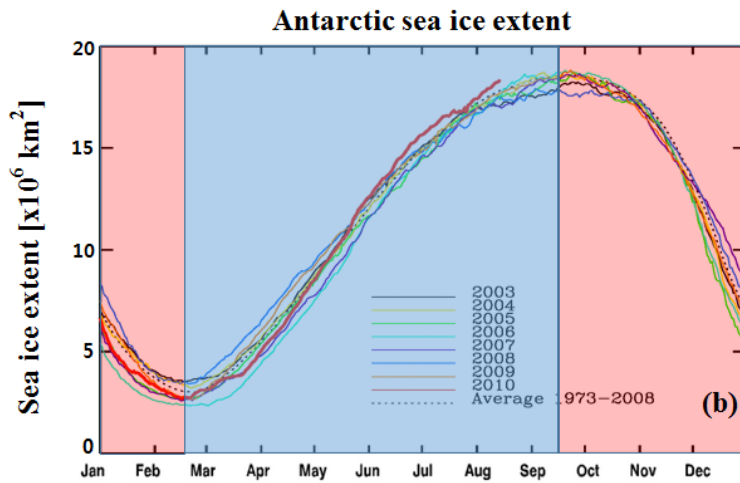
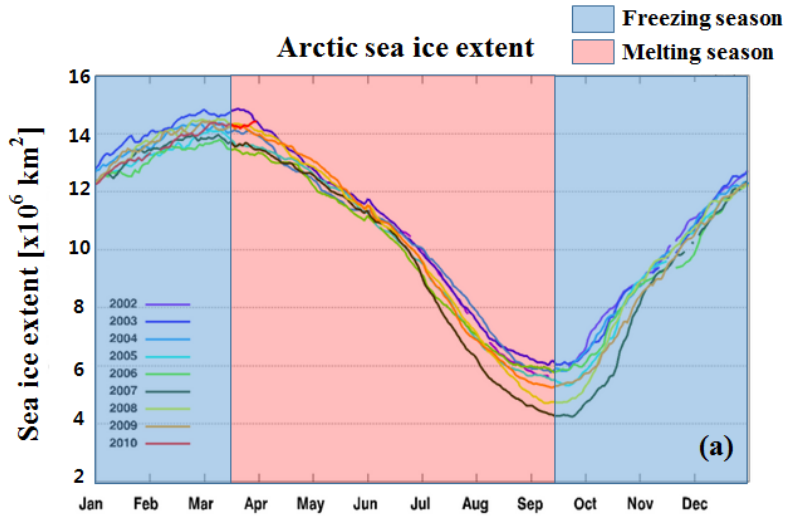


Figure 16. Variations of sea ice extent for the melting and freezing season.
 (a) Arctic sea ice (b) Antarctic sea ice

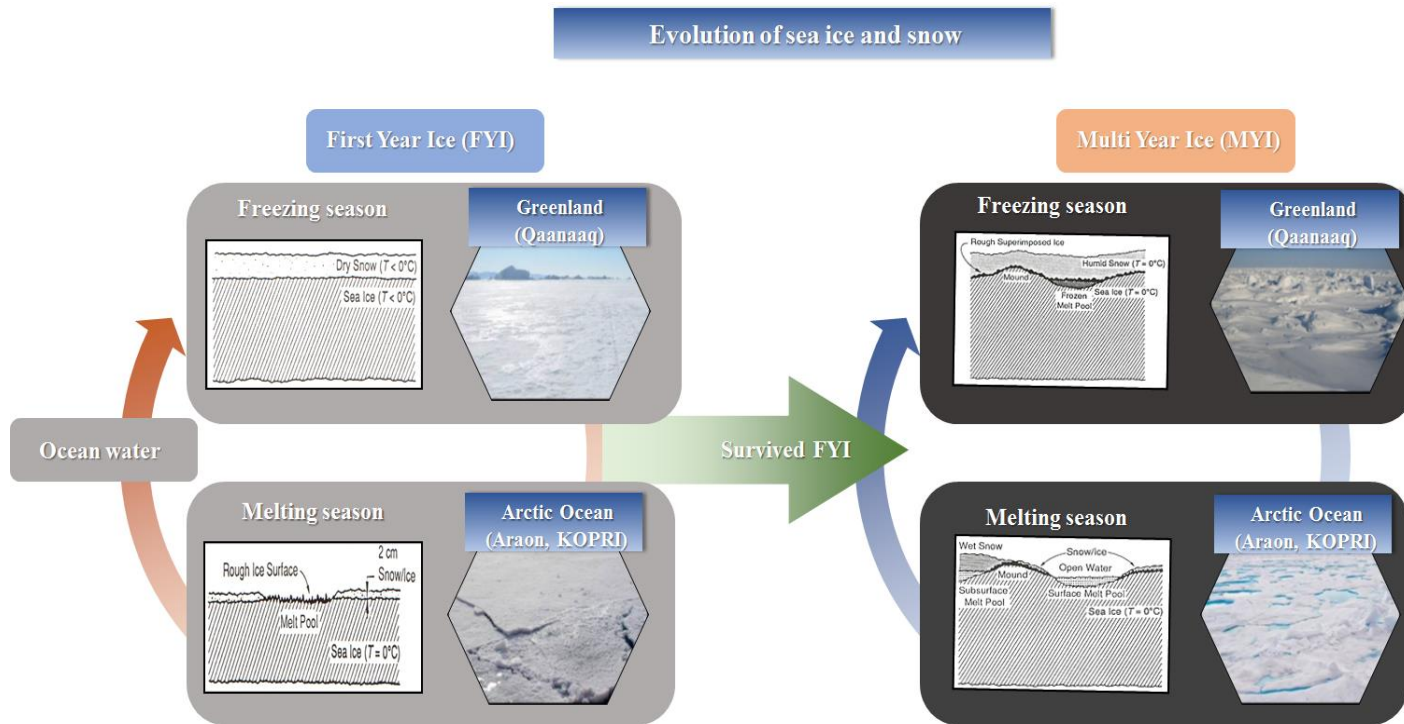


Figure 17. Life cycles of sea ice.

Backscattering structure of microwave at sea ice and snow

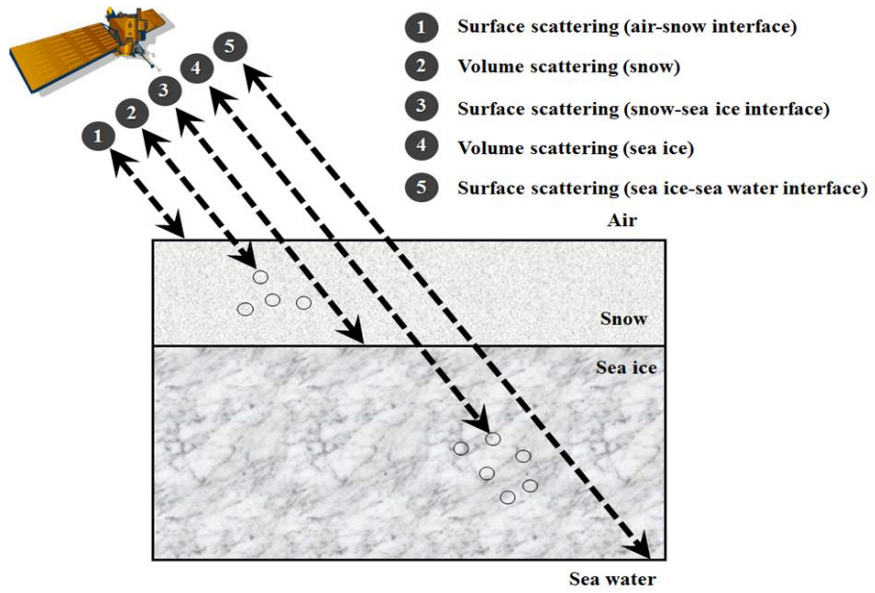


Figure 18. Scattering structures of sea ice and snow.

3.2. Polarimetric scattering features of snow

A. Dielectric properties of snow

In general, snow becomes dry when the surface temperature of snow fall below the freezing point (0 °C), causing this snow to have a minimal amount of water content. In contrast to wet snow, whose average snow to water content ratio is about ten to one, dry snow may have the ratio as high as 30 to one. There are more air pockets between the snow crystals within dry snow layer. Previous study [56] showed that the dielectric properties of dry snow are only dependent on the density of snow although wet snow is dependent on not only the density of snow but also water content [57], and it is difficult to know the amount of liquid within snow layer. Thus, many studies [58]-[59] developed the dielectric constant model of dry snow. Typical dielectric constant model is as following [60]

$$\varepsilon'_{ds} = 1.0 + 1.9\rho_s \quad (\rho_s < 0.5) \quad \varepsilon'_{ds} = 0.51 + 2.88\rho_s \quad (\rho_s \geq 0.5) \quad (19)$$

$$\varepsilon''_{ds} = \frac{\varepsilon'_i}{v_i} \left(\frac{\varepsilon'_{ds} - 1}{\varepsilon'_i - 1} \right)^2, \text{ here } \varepsilon'_i = 3.15 \text{ and } v_i = \frac{\rho_s}{0.916} \quad (20)$$

where ε'_{ds} and ε''_{ds} denote real and imaginary part of dielectric constant of dry snow, respectively. ρ_s is the density of snow. ε'_i denotes real part of dielectric constant of pure ice, and this is about 3.15.

Strozzi (1996) [36] measured the air temperature, the density of snow, and the

dielectric constant of snow at Moosseedorf, Swiss from January 1994 to June 1995 (Figure 19), and these data could show the variation of the density and dielectric constant as air temperature changes (Table 3). In figure 20, mean air temperature was below 0 °C during the freezing season in 1994 and 1995, and the density of snow was distributed between 100 and 200 g/cm³. In contrast, mean air temperature was above 0 °C during the melting season, and the density of snow was rapidly increased by more than 500 g/ cm³. In a comparison between observed real part of dielectric constant and the one simulated by equation (13), the simulated values during the freezing season (blue box) were perfectly matched with the observed values unlike the simulated values during the melting season (Figure 21). Thus, it is clear that the range of dielectric constant (real part) is from 1.1 to 1.25 during the freezing season, and based on the range, it is expected that the backscattering signatures from dry snow cover may be induced by not only surface scattering from surface roughness and dielectric properties of snow cover but also volume scattering within the low-density layer during the freezing season. However, the backscattering signatures from wet snow cover may be induced by only surface scattering from surface roughness and relatively high dielectric constant of snow cover. In next section, it shows that the scattering features measured by GB-POLSCAT with Strozzi's method and newly proposed method to quantitatively estimate normalized intensity of surface, bottom-surface, and volume scattering from snow cover.

Test site : Moosseedorf, Swiss

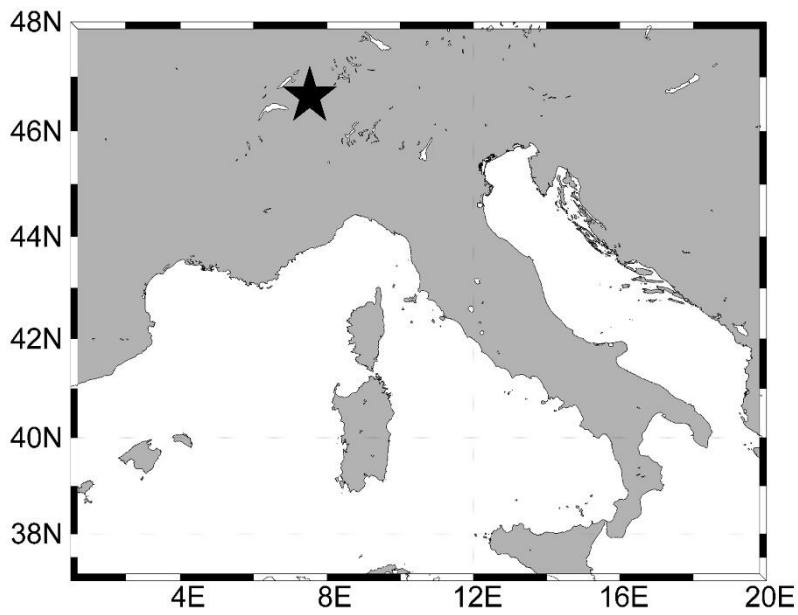


Figure 19. Test site of Strozzi's measurements.

Table 3. Specifications of Strozzi's measurements.

| Specifications | |
|---------------------------|--|
| Center Frequency | 5.3 GHz (C-band) |
| Sweep time | 1s |
| Bandwidth | 1.4 GHz |
| Transmitted Power | 10 dBm |
| Polarization | HH/VV/HV/VH |
| Incidence Angle | 0° ~ 70° |
| Platform Height | ~ 4m |
| Calibration method | GCT |
| Measurement item | Radar response / air temp. / Snow density / Dielectric constant of snow |

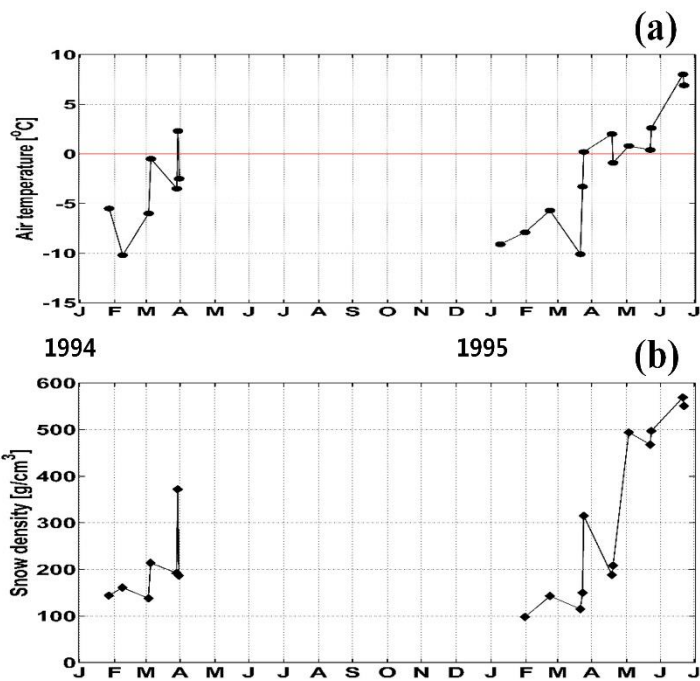


Figure 20. (a) measured air temperature and (b) snow density for the melting and freezing seasons. [Strozzi, 1996]

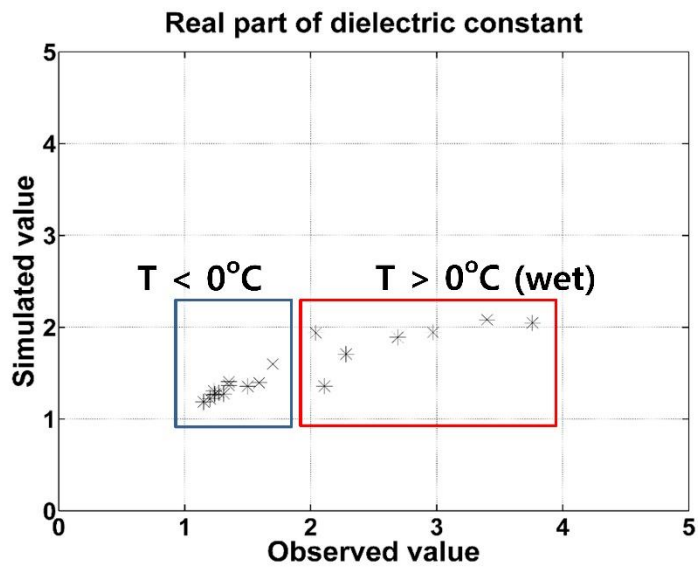


Figure 21. Comparison of observed dielectric constant (real) of snow surface and simulated dielectric constant (real) for the melting (red box) and freezing (blue box) season.

B. The scattering features from snow

It is difficult to understand the scattering features from snow cover with the conventional measurements of various GB-POLSCATs. Because the backscattering coefficient estimated by the measurements simply indicates the NRCS of snow cover, and the NRCS is determined by ensemble average of all backscattered signals induced by the surface and volume scattering from snow cover [60]. Therefore, it cannot explain in detail the scattering features from snow cover. On the other hand, Strozzi (1996) [36] showed the scattering profiles from the snow cover with the 5.3 GHz GB-POLSCAT with broad bandwidth (i.e. 1.4 GHz) (Table 3). Firstly, they measured the received electric field at 201 frequency points for the 4 polarizations (i.e. HH, VV, VH, and HV) at incidence angles between 0° and 70° on the snow cover, and converted the signal of frequency domain to the signal of time domain with inverse FFT method. They then computed the traveling times of signals from antennas to the snow surface and to the bottom at each incidence angles. To compute the correct travel times, the effect of the refraction by the snow cover was considered. Finally, they showed the scattering amplitude as a function of the snow height for the different incidence angles and polarizations.

In this study, the normalized intensity of the surface, bottom-surface, and volume scattering from snow cover was estimated with the scattering profiles. In order to distinguish each of the scattering features, time or distance range of each scattering feature was estimated by the pulse duration time (τ) of the GB-POLSCAT, and τ

can be easily determined as following

$$\tau = k_r B \quad (21)$$

where k_r is the sweep time, and B denotes the band width. These values of the GB-POLSCAT are described in Table 3.

As you can see in Figure 22, the intensity of the surface and bottom-surface scattering was estimated by the intensity summation of the backscattered signal for a pulse duration time at the snow surface and bottom, respectively, and the intensity of the volume scattering was estimated by the intensity summation of the backscattered signal between the snow surface and bottom. Finally, the normalized intensity of each scattering feature was calculated as following

$$\overline{P}_{surf} = \frac{\int_{t_{s2}}^{t_{s1}} |E_{pq}^r|^2 dt}{\int_{t_{b2}}^{t_{s1}} |E_{pq}^r|^2 dt} \quad (22)$$

$$\overline{P}_{bottom-surf} = \frac{\int_{t_{b2}}^{t_{b1}} |E_{pq}^r|^2 dt}{\int_{t_{b2}}^{t_{s1}} |E_{pq}^r|^2 dt} \quad (23)$$

$$\overline{P}_{vol} = \frac{\int_{t_{b1}}^{t_{s2}} |E_{pq}^r|^2 dt}{\int_{t_{b2}}^{t_{s1}} |E_{pq}^r|^2 dt} \quad (24)$$

where boundary conditions of each equation are described in Figure 22.

As a results, Figure 23 and Table 4 shows that the normalized intensity of each

scattering feature for 10° incidence angle and all polarizations. For the freezing season, the volume scattering (green bar) is relatively dominant than the other scattering features for HH and VV polarization. $\overline{P_{vol}}$ of HH and VV is about 55 and 56.1%, respectively. In case of cross polarizations (i.e. HV and VH), the bottom-surface scattering (red bar) is relatively dominant than the other scattering features. $\overline{P_{bottom-surf}}$ of HV and VH is about 54.3 and 56.1%, respectively. On the other hand, it shows completely different scattering patterns for the melting season. In this season, the surface scattering (blue bar) is strongly dominant for all polarizations. $\overline{P_{surf}}$ of HH, VV, HV, and VH is 88.5, 95, 76.7, and 72.5 %, respectively. In Figure 24 and Table 5, the bottom-surface scattering is predominant than the other scattering features for 40° incidence angle and all polarizations during the freezing season. $\overline{P_{bottom-surf}}$ of HH, VV, HV, and VH is 64.1, 66.4, 71.5, and 68.2 %, respectively, and the surface scattering is absolutely dominant for the melting season similar. $\overline{P_{surf}}$ is HH, VV, HV, and VH is 77.8, 84.9, 81.4, and 78.8 %, respectively.

These results show that most of the traveling signals are backscattered from the snow surface for the melting season because dielectric constant of the snow surface becomes high due to strong surface melting (Figure 21). In other words, it can say that polarimetric signatures of microwave must have been backscattered from the surface of the snow cover on sea ice for the melting season. That is, the backscattered signatures are not almost affected by the physical properties of sea ice, so it may be difficult to measure sea ice thickness using polarimetric scattering features of SAR data for the melting season. On the other hand, although the backscattered signal for low incidence angles and co-polarizations is relatively dominated by volume

scattering within the snow layer, the backscattered signal for high incidence angle and all polarizations is strongly dominated by the bottom-surface scattering from the snow cover during the freezing season. This shows that the polarimetric signatures can interact with the physical properties of sea ice for the freezing season. It is clear that first optimized condition to determine sea ice thickness is to acquire SAR data with high incidence angles (i.e. 40°) for the freezing season. In this condition, it can be ignored the scattering features from snow cover.

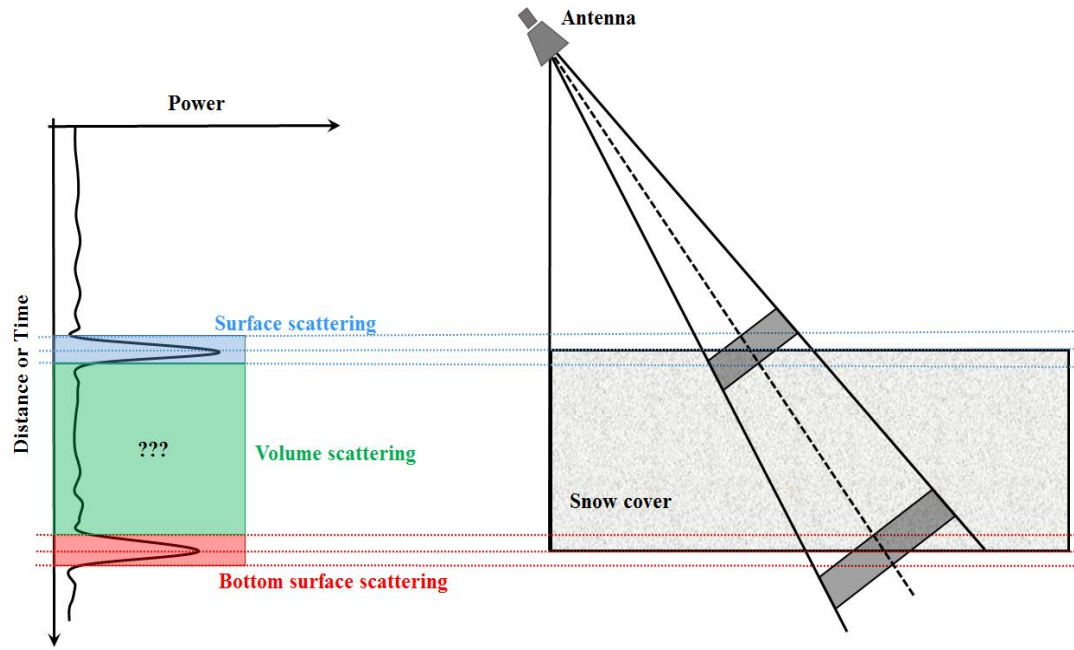


Figure 22. Scheme of scattering structures from snow cover in the GB-POLSCAT measurements.

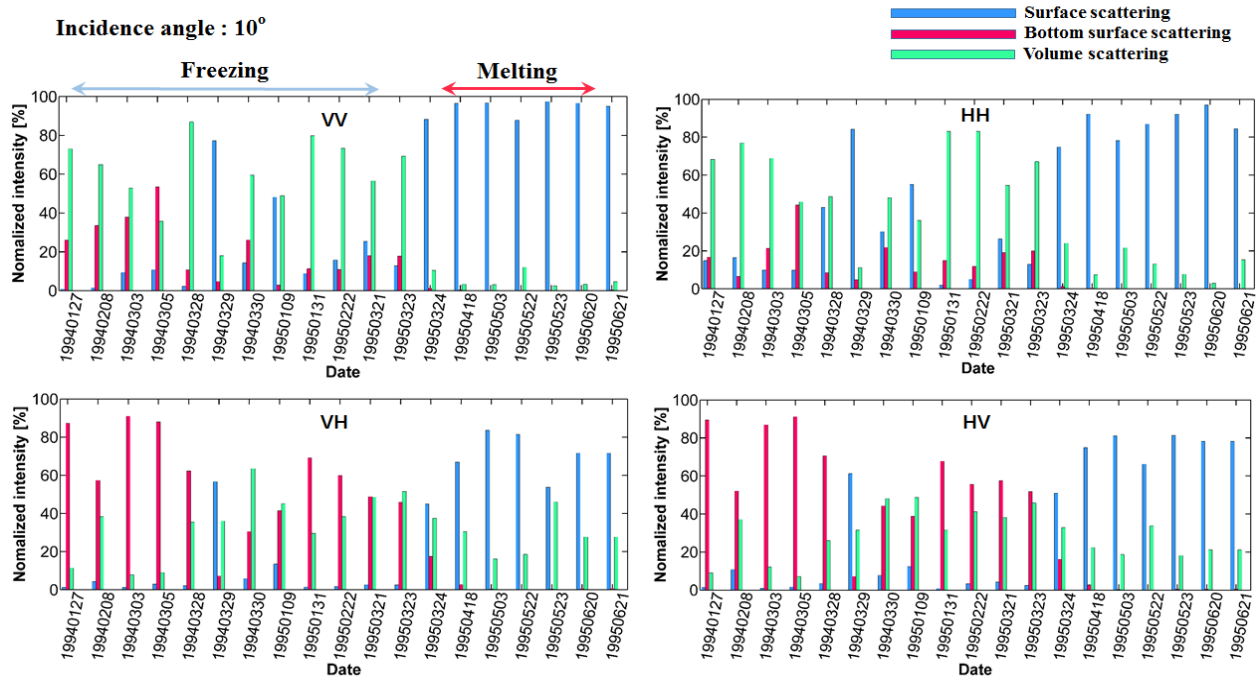


Figure 23. Normalized scattering intensity from snow cover with Strozzi's data for the melting and freezing season (Incidence angle: 10°).

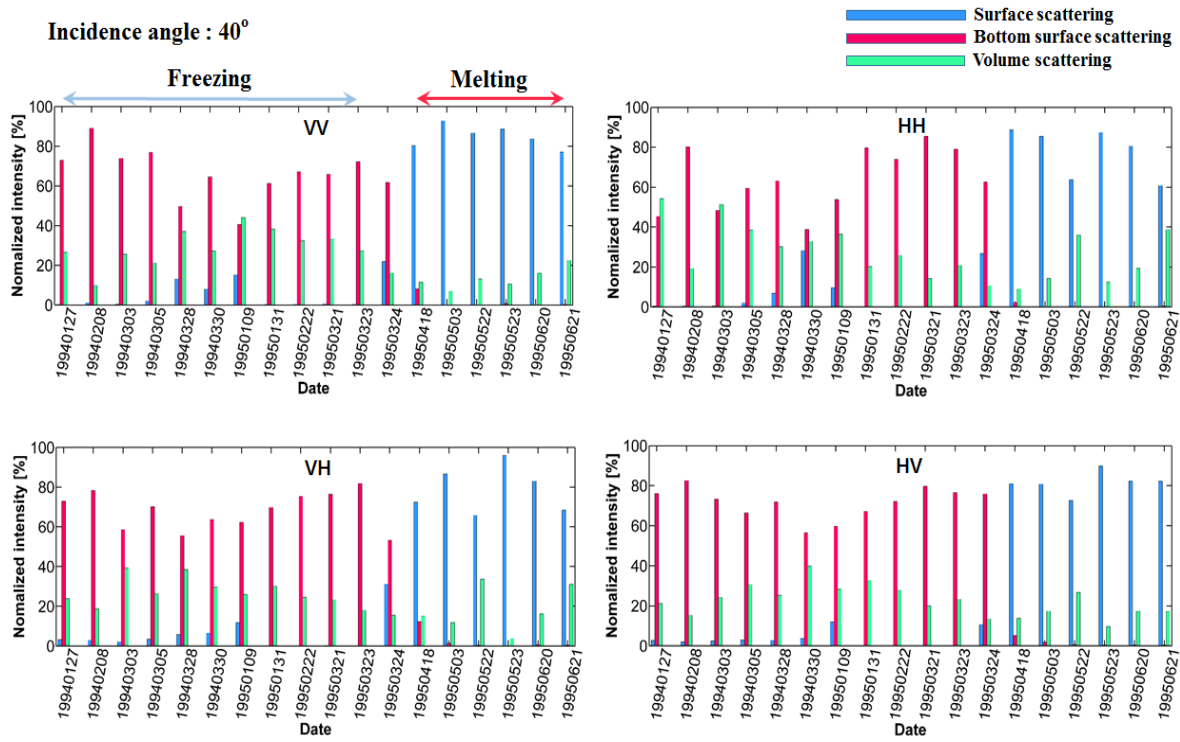


Figure 24. Normalized scattering intensity from snow cover with Strozzi's data for the melting and freezing season (Incidence angle: 40°).

Table 4. Averaged scattering intensities from snow cover for the freezing season.

| | Surface scattering | | Bottom-surface scattering | | Volume scattering | |
|-----------|--------------------|----------|---------------------------|---------------|-------------------|----------|
| | Inc. 10° | Inc. 40° | Inc. 10° | Inc. 40° | Inc. 10° | Inc. 40° |
| HH | 29.6 % | 6.3 % | 15.4 % | 64.1 % | 55 % | 29.6 % |
| VV | 24.3 % | 5.4 % | 19.6 % | 66.4 % | 56.1 % | 28.2 % |
| VH | 10.9 % | 5.6 % | 54.3 % | 68.2 % | 34.8 % | 26.2 % |
| HV | 12.4 % | 3.3 % | 56.1 % | 71.5 % | 31.5 % | 25.2 % |

Table 5. Averaged scattering intensities from snow cover for the melting season.

| | Surface scattering | | Bottom-surface scattering | | Volume scattering | |
|-----------|--------------------|---------------|---------------------------|----------|-------------------|----------|
| | Inc. 10° | Inc. 40° | Inc. 10° | Inc. 40° | Inc. 10° | Inc. 40° |
| HH | 88.5% | 77.8 % | 0.2 % | 0.6 % | 11.3 % | 21.6 % |
| VV | 95 % | 84.9 % | 0.2 % | 1.6 % | 4.8 % | 13.5 % |
| VH | 72.5 % | 78.8 % | 0.8 % | 2.6 % | 26.7 % | 18.6 % |
| HV | 76.7 % | 81.4 % | 0.7 % | 1.5 % | 22.6 % | 17.1 % |

3.3. Polarimetric scattering features of sea ice

Dielectric constant and surface roughness of sea ice can control the amount of a traveling radar signals with reflection, transmission, absorption, and dissipation. In order to understand the scattering features from the ice, it needs to understand these physical properties of sea ice. In the following sections, the physical properties were explored in detail with conditions determined in section 3.1.

A. Dielectric properties of sea ice

As mentioned above, dielectric constant of sea ice is strongly dependent on the salinity of the ice. In order to understand fluctuations of the salinity for the freezing season, it was used ice buoy data of Professor Hajo Eicken's research group at Alaska University from 1999 to 2009. The buoy was deployed on land-fast sea ice in the Chukchi Sea at Barrow, Alaska (Figure 25). Figure 26a shows the observed salinity profiles of FYI with various thicknesses for the freezing season. The profiles agree well with [51]'s results. As FYI grows, the salinity of the ice surface is rapidly decreased from 15 to 5 psu (i.e. real red line a \rightarrow d). In case of MYI, [51] showed the averaged profiles (real blue line e). The salinity of the ice surface is almost zero. In addition, [61]'s the profiles of MYI (Figure 26b) show that the salinity within the ice with MYI grows is gradually decreased from 1 to 0 psu although the salinity of all MYI surfaces is almost 0 psu.

Based on the salinity profiles as the ice grows, the dielectric constant model of sea

ice have been developed with various frequencies in several studies [49], [62]-[63]. In the frequency band of the space-borne SAR sensors introduced in Chapter 2, the models are as following

$$\varepsilon_i' = 3.04 + 0.0072 \frac{V_b}{V} \quad \varepsilon_i'' = 0.02 + 0.0033 \frac{V_b}{V} \quad (C - band) \quad (25)$$

$$\varepsilon_i' = 3.00 + 0.0120 \frac{V_b}{V} \quad \varepsilon_i'' = 0.00 + 0.010 \frac{V_b}{V} \quad (X - band) \quad (26)$$

where ε_i' and ε_i'' is the real and imaginary part of the sea ice dielectric constant, respectively. $\frac{V_b}{V}$ is the relative brine volume, and can be determined as following

$$\frac{V_b}{V} = \frac{\rho S_i}{\rho_b S_b} \quad (27)$$

Where ρ is the bulk ice density. S_b is the brine salinity. ρ_b is the brine density. S_i is the salinity of sea ice. These values can be determined as following, respectively [54].

$$\rho = \frac{\rho_i \rho_b S_b}{\rho_b S_b - S_i (\rho_b - \rho_i)} \quad (28)$$

$$\rho_b = 1 + 0.0008 S_b \quad (29)$$

$$S_i = 14.24 - 19.39 h_i \quad (h_i \leq 0.4) \quad | \quad S_i = 14.24 - 19.39 h_i \quad (h_i > 0.4) \quad (30)$$

where h_i is the thickness of sea ice

$$S_b = -3.9921 - 22.7T_i - 1.0015T_i^2 - 0.019956T_i^3 \quad (31)$$

where T_i is the temperature of sea ice, and can be determined as following [54]

$$T_i = \frac{h_s k_i T_w + h_i k_s T_a}{h_s k_i + h_i k_s} - 273.0 \quad (32)$$

where h_s is the snow depth, T_w is the sea temperature beneath the ice, T_a is the air temperature, k_s is the thermal conductivity of snow, and k_i is the thermal conductivity of the ice.

As mentioned above, thin FYI grows into thick FYI, it loses its brine (i.e., desalination), and thick FYI further loses its salinity during the melting season. These processes control the complex dielectric constants and the penetration depth of microwave into the ice. Here it is introduced a simple demonstration of evolution of complex dielectric constants as a function of ice thickness using the dielectric constant model. The penetration depth (δ) can be as following [64].

$$\delta = \frac{\lambda}{4\pi} \left\{ \left[\left(1 + \left(\frac{\varepsilon_i''}{\varepsilon_i'} \right)^2 \right) - 1 \right]^{0.5} \frac{\varepsilon_i'}{2} \right\}^{-0.5} \quad (33)$$

where λ is the wave length of microwave for the free space.

Figure 27 shows the calculated penetration depth of C- and X-band as a function of sea ice thickness. While the calculated dielectric constants decrease as the ice thickness increases, the penetration depth of C- and X-band increases as the ice thickness increases, mainly due to its lower salinity and subsequent decrease in both real and imaginary parts of complex dielectric constants. This suggests that the volume scattering within the ice can be increased as the ice grows due to the desalination process.

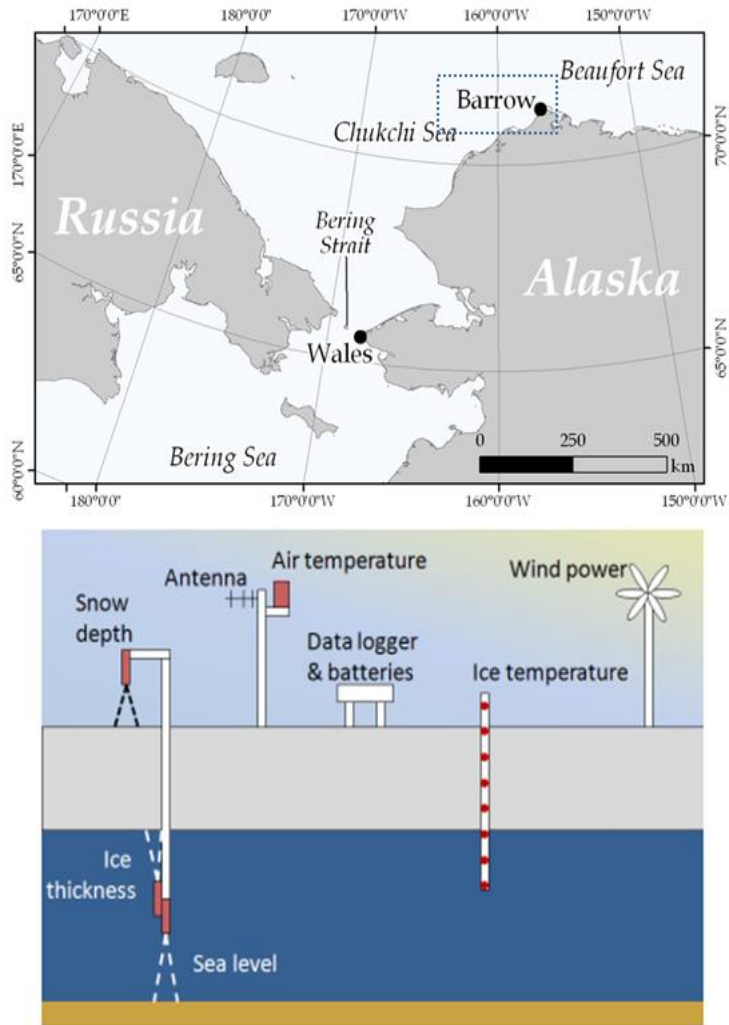


Figure 25. Measurement site of the ice buoy (top) and structures of the ice buoy (bottom) [from Prof. Hajo Eicken's homepage at Alaska University].

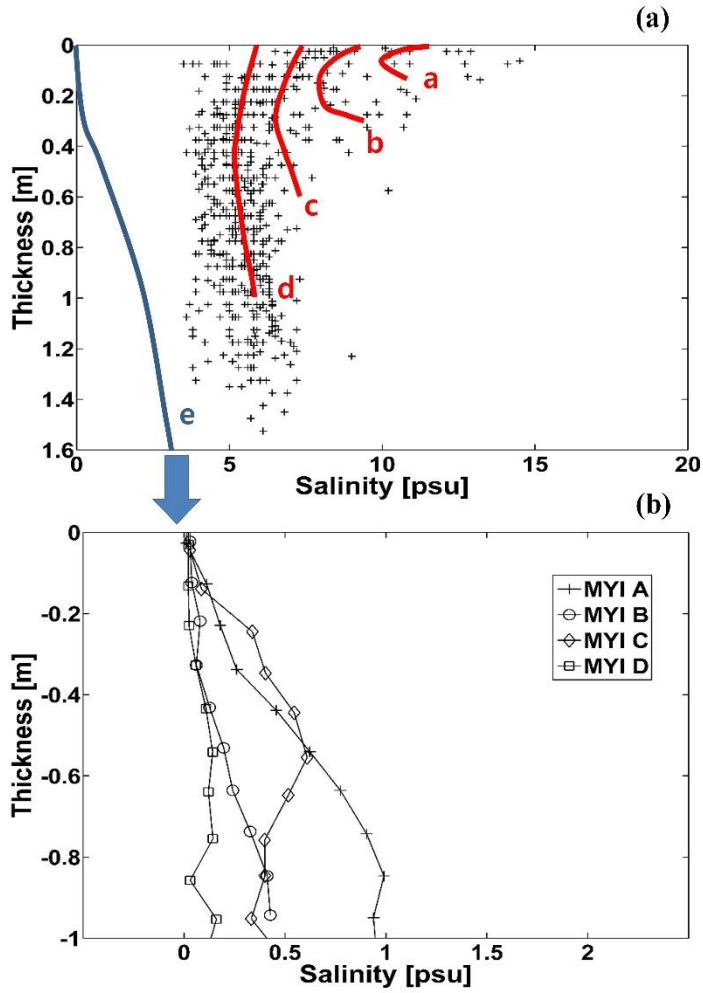


Figure 26. (a) the salinity profiles of FYI for the freezing season (red line a-d denote averaged salinity profiles as FYI grows, and blue line is averaged salinity profile of MYI in [51]) (b) the salinity profiles of MYI for the freezing season. From MYI A to MYI D, the thickness are gradually increased [61].

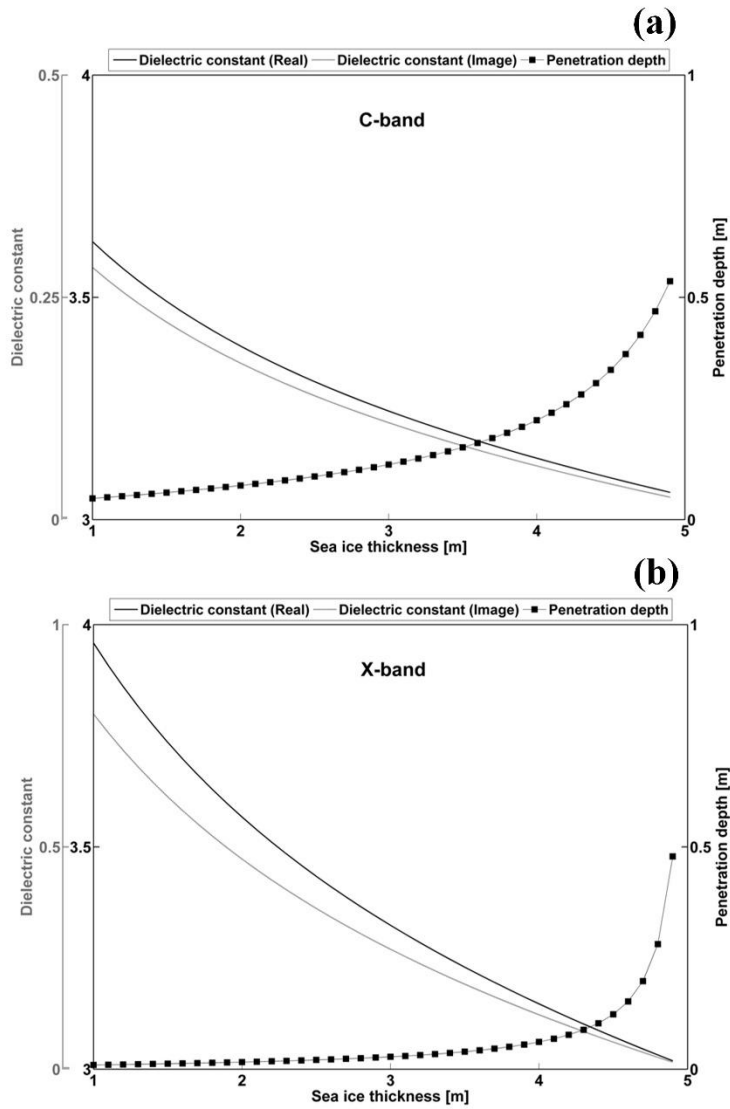


Figure 27. Dielectric constant (real and imaginary parts) and penetration depth as a function of sea ice thickness for C- and X-band frequencies. Left Y-axis represents the values of dielectric constant (black: real part, gray: imaginary part) and right Y-axis represents penetration depth. (a) C-band (b) X-band

B. Surface roughness of sea ice

The amount of surface roughness can control the amount of the backscattered signal on the ice surface. In general, small-scale (comparable with radar wavelength: a few cm) surface roughness of sea ice is important for the interpretation of SAR data. The small-scale surface roughness is usually induced by factors such as surface wind stress, snow-ice interface temperature, and so forth [65]. In particular, snow-ice interface temperature plays an important role in creating the differences in small-scale surface roughness between MYI and FYI during the sea ice growing season (Figure 28). The superimposed ice is ice created by re-frozen snow melt water at the snow-sea ice interface and can be one of the important factors in the determination of the short scale surface roughness of the sea ice [52]. Such a superimposed ice does not observe on the snow-FYI interface. Aside from small-scale surface roughness, large-scale surface (slope) can induce multiple scattering at the sea ice surface. Large-scale surface roughness (i.e., a few tens of cm) is primarily caused by sea ice compression and ridging processes, as shown in Figure 28. Peterson et al. [66] and Toyota et al. [67], [68] have showed that this scale of surface roughness is closely related to sea ice thickness due to ridging and drafting process that may occur as sea ice ages.

Gupta et al [69] showed that the distributions of surface roughness on the ice surface in the southeastern Beaufort Sea and the Amundsen Gulf in the western Canadian High Arctic with ship-based laser profiler. In case of FYI (Figure 29a), the

distribution of the surface is concentrated in Root Mean Square (RMS) height 0.02m. In case of MYI (Figure 29b), the RMS height is relatively concentrated between 0.05 and 0.08 m although the distribution is broadly dispersed. Therefore, it is reasonable to say that the scale of surface roughness is relatively increased as sea ice grows due to various process mentioned above although relationship between surface roughness and thickness of the ice thickness is relatively weak unlike dielectric properties of sea ice.

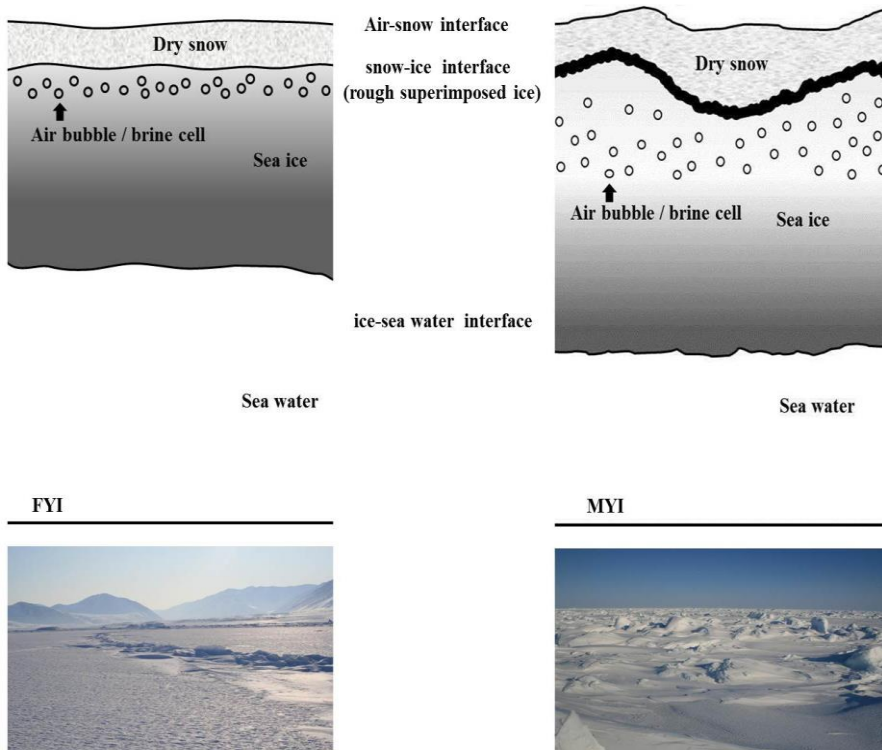


Figure 28. Cross-sectional view of FYI (left) and MYI (right) during the sea ice growing season. The lower bottom photographs show typical scenes of the corresponding sea ice type.

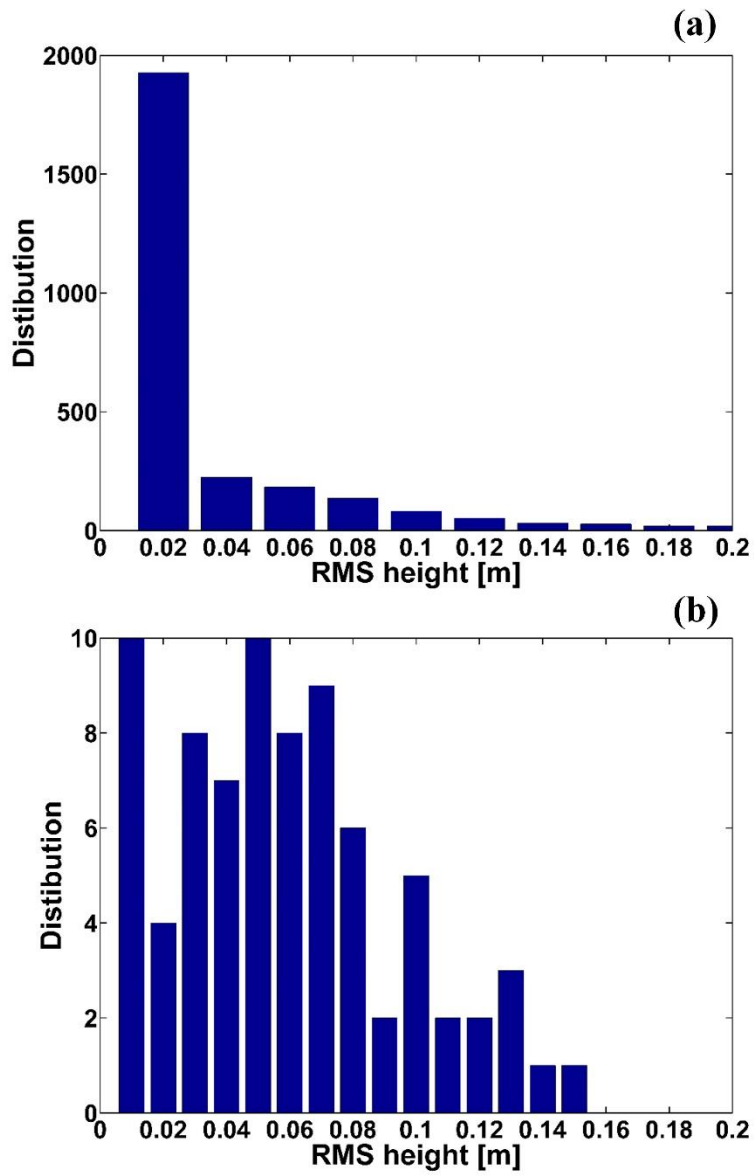


Figure 29. Distributions of FYI and FYI in [69]. (a) FYI (b) MYI

C. The scattering features from sea ice

Based on the contributions of the physical properties explained above, microwave is strongly backscattered from the surface of FYI due to high dielectric properties of the surface. Then, thicker and older sea ice tends to be rougher and less saline, and the backscattering signatures from the ice are not only originated from rough surface scattering but also from volume scattering within a low-density sub-surface layer [7],[11],[12]. Based on this, Kim et al [70] showed the NRCS distribution (5-18GHz, incidence angle: 40°, and HH polarization) of FYI and MYI with smooth and rough surface roughness estimated by field measurements and numerical simulations for the freezing season (Figure 30). The distribution can distinguish MYI from FYI for C- and X-band. That is, it is possible that the backscattering coefficient allow us to distinguish the sea ice type (i.e. FYI and MYI) in the optimized conditions. However, this result do not explain perfectly the optimized method to determine sea ice thickness. In next section, it is explored more distinct method to determine sea ice thickness using polarimetric signatures with physical interpretations.

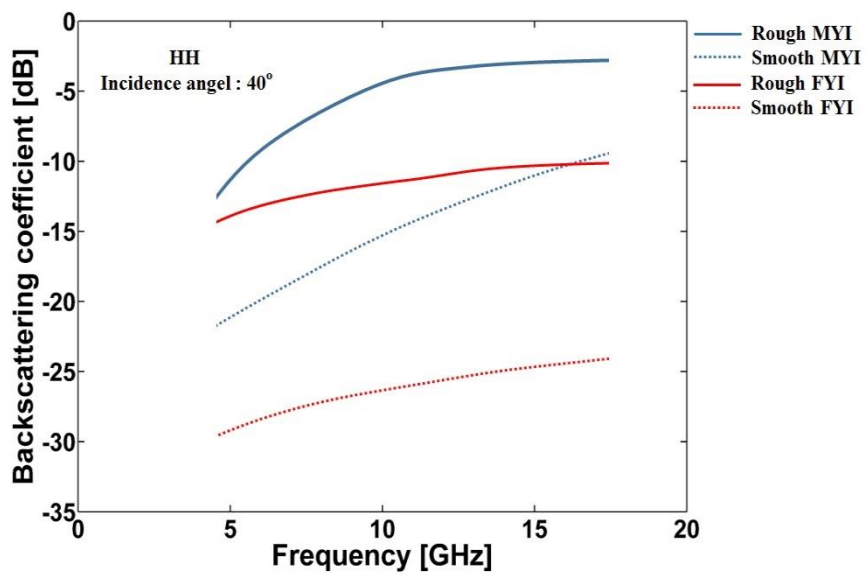


Figure 30. The distribution of backscattering coefficients from FYI and MYI [70] (red real line: rough FYI, red dotted line: smooth FYI, blue real line: rough MYI, and blue dotted line: smooth MYI).

3.4. Depolarization effects based on the polarimetric scattering features of sea ice

If the surface is rough, the scattered wave can be altered from the desired state of wave polarization – “depolarized”. The mechanism of multiple scattering at the rough surface causes the depolarization effects [71]. This depolarization effects can also be occurred within inhomogeneous bulk materials due to volume scattering. The co-polarized correlation and cross-polarized ratio have been used to measure the degree of depolarization effects [71], [72]. These depolarization factors have been used to snow mapping [72] and land classification applications [73]. For sea ice studies, Isleifson et al [74] calculated the co-polarized correlation from ship-mounted scatterometer measurements over thin FYI (2 - 69 cm) and tried to correlate the values with the ice thickness. No one-to-one relationship was found in that study, but they found two distinct the ice-thickness regimes (i.e. < 6 cm and > 8 cm). They suggested that the division of the two thickness regimes (two regimes of depolarization) was attributed to the difference in surface roughness and/or brine cells between the two thickness regimes. This experiment was however carried out only in newly formed thin sea ice (< 69 cm), and the relationship between the depolarization factors and the thickness of thicker and older sea ice has not been explored.

As mentioned above, thicker and older sea ice tends to be rougher and less saline. Small-scale surface roughness of older ice (i.e. MYI) can be higher than younger ice (i.e. FYI), mainly due to the presence of superimposed ice at the snow/ice interface

formed by re-frozen snow melt water [52]. Deformed (ridged and rafted) sea ice also tends to be thicker and rougher as previous studies [67], [68] have shown a good correlation between large-scale surface roughness and sea ice thickness due to ridging and rafting processes. MYI is thicker (mean wintertime thickness of about 3.2 m) and much less saline (about 2 ppt) than FYI (mean wintertime thickness of 2.1 m and bulk salinity of about 2-20 ppt). As the salinity of sea ice decreases, complex dielectric constants decrease, and it in turn increases the penetration depth of radar wave. Volume scattering become significantly enhanced with the presence of a low-density sub-surface layer of MYI. As surface roughness increases and desalination significantly slows down in thicker and older sea ice, it is the multiple scattering from snow/ice interface (e.g. superimposed ice, deformation-related) and volume scattering (e.g. low density layer) that affect depolarization for those ice types. Although it is a rather complex matter, these approaches were investigated via both in-situ observations and numerical modeling works. In numerical modeling works, we aim at estimating the degree of depolarization due to the multiple scattering from rough surface and volume scattering within sea ice with reasonable range of sea ice physical parameters.

A. Numerical experiments of the depolarization effects due to surface scattering from rough surface

In case of small-scale surface roughness, IEM model explained in Appendix A is used in order to simulate the depolarization factors (i.e. cross-polarization ratio) due to small-scale surface roughness. The depolarization factor of C- and X-band as a function of RMS height were simulated. The correlation length and the dielectric constant values suggested in [75] for typical sea ice types were used for the calculations. The results show increases in the calculated cross-polarized ratios with the RMS height (Figure 31). For the mean RMS values of small-scale surface roughness reported in [48] (0.48 cm for MYI and 0.27 cm for FYI), the calculated cross-polarized ratios of MYI (0.004 for C-band and 0.008 for X-band) are about two times higher than the ones of FYI (0.002 for C-band and 0.004 for X-band).

The extended Bragg model [76] would be a suitable surface scattering model that can implement the effects of those large-scale surface slopes. The coherence matrix determined from the pure Bragg scattering model cannot estimate depolarization power (i.e., HV power). However, the coherence matrix determined by the extended Bragg scattering model can estimate the depolarization power due to the azimuthally oriented surface angle (i.e., large-scale surface slopes, but less than a SAR resolution cell). Further details of extended Bragg model is described in Appendix B. In addition, we have converted the coherency matrix of the extended Bragg model to the covariance matrix using a special unitary transformation matrix in order to estimate the depolarization effects. The transformation equation is given by

$$[C] = [U][T][U]^{-1} \quad \text{here, } [U] = \frac{1}{\sqrt{2}} \begin{bmatrix} 1 & 1 & 0 \\ 1 & -1 & 0 \\ 0 & 0 & \sqrt{2} \end{bmatrix} \quad (34)$$

where C is the covariance matrix, T is the coherency matrix, and U is the special unitary transformation matrix. The converted covariance matrix of the extended Bragg model is given by the following:

$$[C] = \begin{bmatrix} \langle |S_{HH}|^2 \rangle & \langle S_{HH}S_{VV}^* \rangle & \sqrt{2}\langle S_{HH}S_{HV}^* \rangle \\ \langle S_{VV}S_{HH}^* \rangle & \langle |S_{VV}|^2 \rangle & \sqrt{2}\langle S_{VV}S_{HV}^* \rangle \\ \sqrt{2}\langle S_{HV}S_{HH}^* \rangle & \sqrt{2}\langle S_{HV}S_{VV}^* \rangle & 2\langle |S_{HV}|^2 \rangle \end{bmatrix} = \frac{m_s^2}{4} \begin{bmatrix} a & b & 0 \\ b & c & 0 \\ 0 & 0 & d \end{bmatrix} \quad (35)$$

$$\text{here, } a = C_1 + 2C_2 \text{sinc}(2\beta_1) + C_3[1 + \text{sinc}(4\beta_1)]$$

$$b = C_1 - C_3[1 + \text{sinc}(4\beta_1)]$$

$$c = C_1 - 2C_2 \text{sinc}(2\beta_1) + C_3[1 + \text{sinc}(4\beta_1)]$$

$$d = \sqrt{2}C_3[1 + \text{sinc}(4\beta_1)]$$

where C_1 , C_2 , and C_3 describe the Bragg components of the surface (Appendix B), m_s is the backscatter amplitude that contains information about the small-scale surface roughness condition of the surface, and β_1 denotes the azimuthally oriented surface angle (slope). The cross-polarized ratios and the co-polarized correlation can be estimated from the converted covariance matrix. In the simulation, the width of azimuthally oriented surface angle (β_1) was used as a measure of large-scale

roughness, because the width (range) of azimuthally oriented surface angles increases as the surface slope increases.

The results show increases in the depolarization for the higher large-scale surface roughness, showing a positive trend for cross-polarized ratios (Figure 32). It is important to note that cross-polarized ratio is almost insensitive of variations in the dielectric constant caused by changes between thick FYI and MYI. The results suggest that higher large-scale roughness (steeper surface slopes) caused by ridging or rafting could significantly increase depolarization. It should be noted that depolarization can be caused by the interaction between small-scale and large-scale roughness. These results clearly show significant depolarization due to both small-scale and large-scale surface roughness.

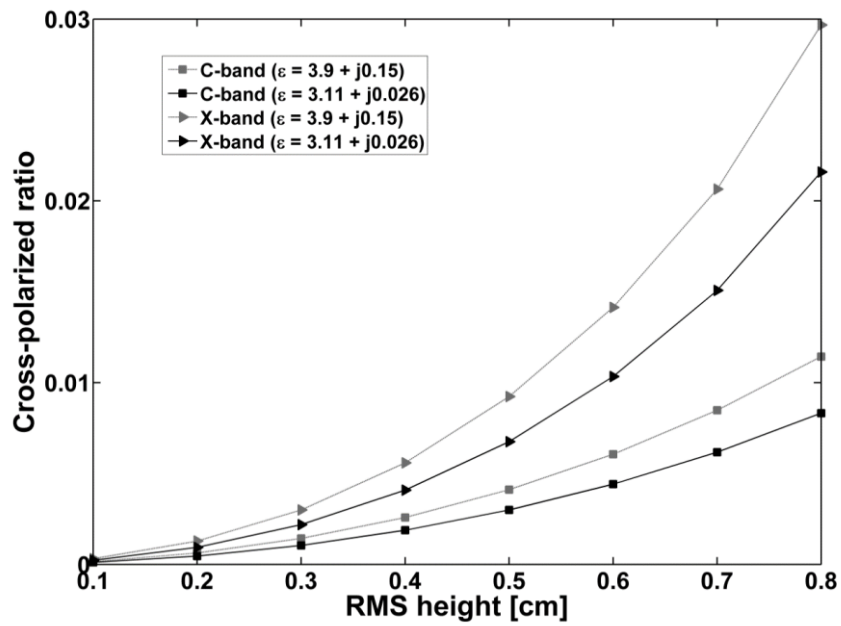


Figure 31. The variation of cross-polarized ratio (HV/HH) as a function of RMS height (small-scale roughness) for the C- and X-band.

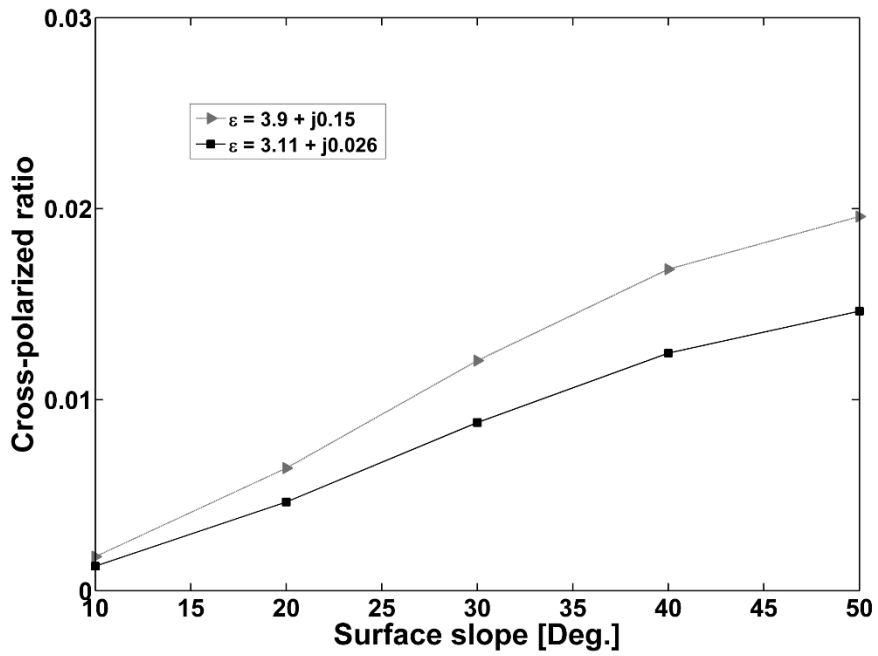


Figure 32. The variation of depolarization factors (cross polarized ratio) as a function of surface slope width (large-scale surface roughness) for the dielectric constants of thick FYI and MYI using extended-Bragg model.

B. Numerical experiments of the depolarization effects due to volume scattering within sea ice layer

As mentioned above, sea ice grows into thick ice, it loses its brine (i.e., desalination), and further loses its salinity during summer melt. These processes control the complex dielectric constants (penetration depth) and depolarization due to volume scattering. The volume scattering within sea ice have been generally simulated by Vector Radiative Transfer (VRT) theory [80],[81]. Detail description of VRT is introduced in Appendix C.

In order to simulate the relationship between the depolarization factors induced by volume scattering and sea ice thickness in the optimized conditions, the experiments of two case studies were set up. The first case is assumed that the surface of sea ice is flat, and the second case is assumed that the surface of sea ice is rougher as sea ice grows. For the simulation, changes of dielectric constant and penetration depth as sea ice grows (i.e. 0.1 ~ 5m) were first simulated by equations (19)-(27). Detail conditions of each simulation are illustrated by Figure 33a and b. Figure 34 shows that the changes of dielectric constant of C- and X-band agree well with the patterns of dielectric constant as sea ice grows explained by [77]-[79]. Using these results, polarimetric backscattering coefficients were simulated by the IEM and VRT models (Figure 35 - 38), and the cross polarized ratio (VH/VV) was estimated. The simulated cross polarized ratio (i.e. VH/VV) is increased as sea ice grows regardless of the change of incidence angle (Figure 39). In addition, the ratios simulated by case 1 and 2 experiments are almost same. That is, the ratio induced by volume scattering is

larger than the one induced by surface scattering. This shows that the backscattered signatures from sea ice can be dominantly depolarized by volume scattering within sea ice layer. Based on this, field experiments were conducted to mediate verify one-to-one relationship between the depolarization factors induced by volume scattering and the artificial ice thickness.

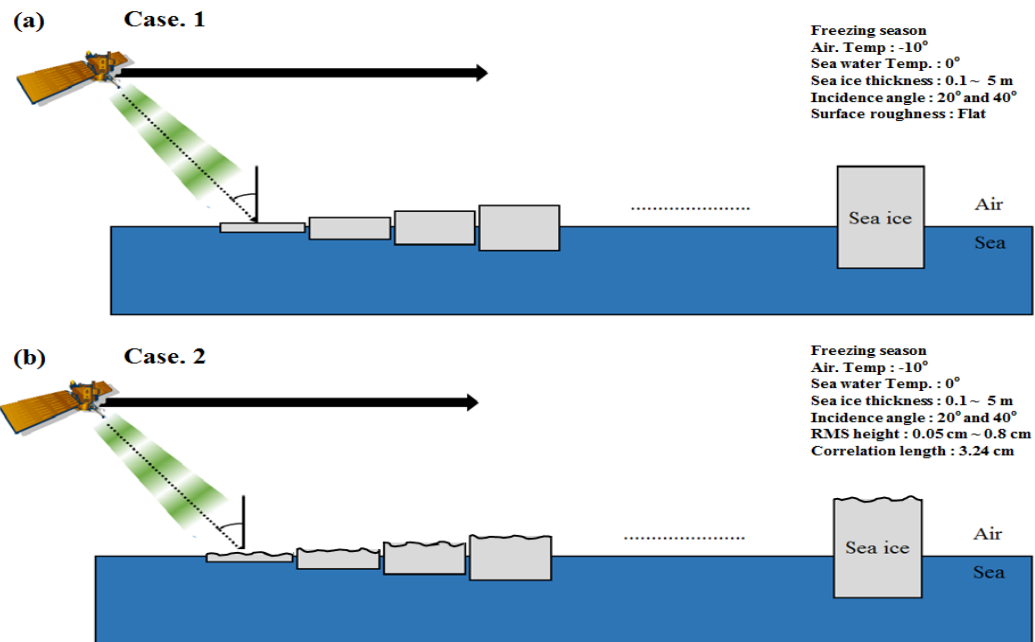


Figure 33. Set-up of VRT model simulation. (a) flat surface (only volume scattering) (b) relatively rough surface as sea ice grows (surface + volume scattering).

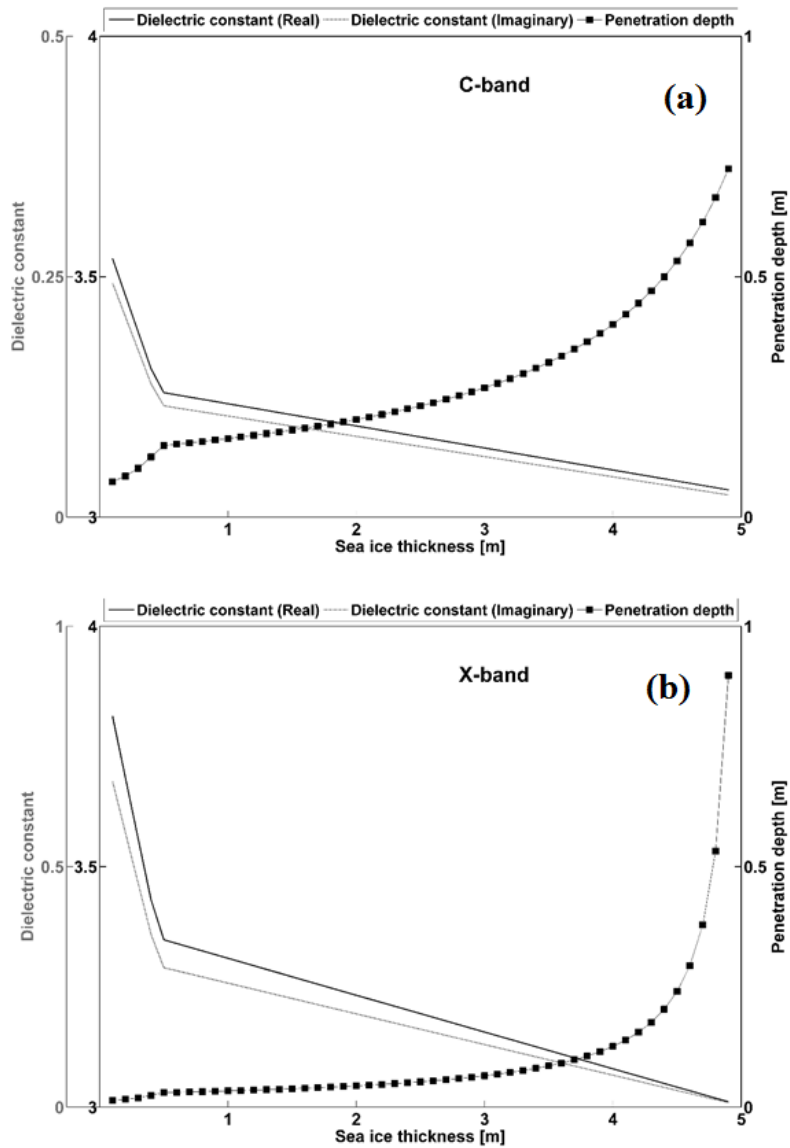


Figure 34. In the VRT simulation, dielectric constant (real and imaginary parts) and penetration depth as a function of sea ice thickness (i.e. 0.1 ~ 5 m) for C- and X-band frequencies. Left Y-axis represents the values of dielectric constant (black: real part, gray: imaginary part) and right Y-axis represents penetration depth.

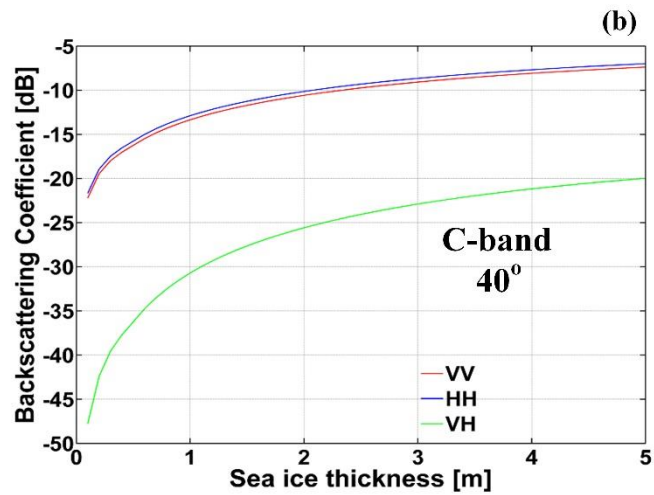
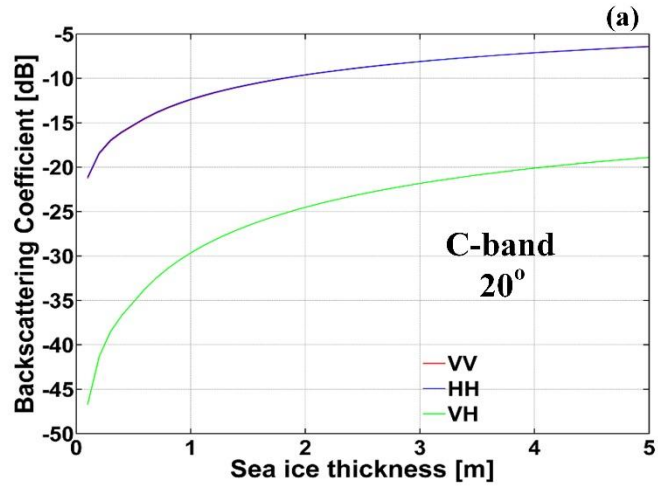


Figure 35. Backscattering coefficients (C-band) simulated by the VRT (Case 1, only volume scattering) as sea ice grows (red: VV, blue: HH, and green: VH). (a) incidence angle: 20° (b) incidence angle: 40°

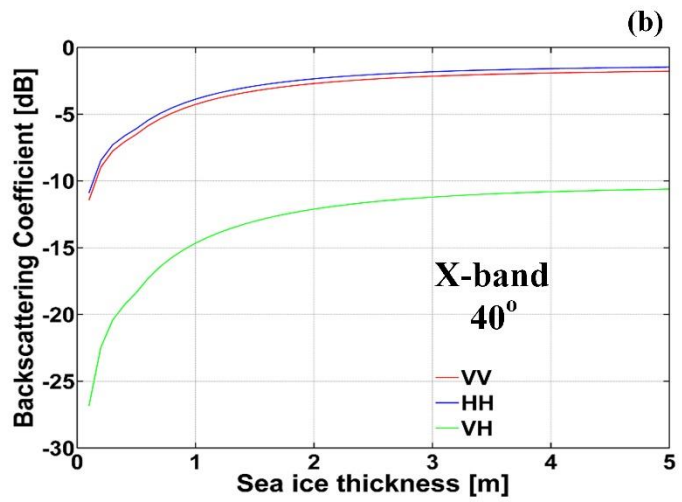
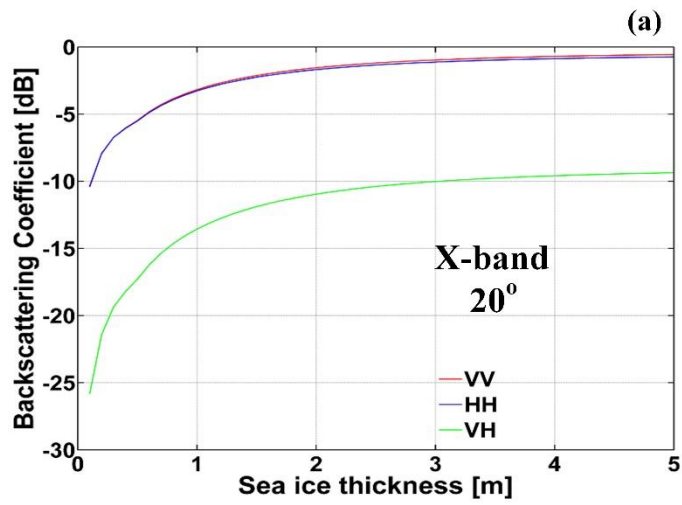


Figure 36. Backscattering coefficients (X-band) simulated by the VRT (Case 1, only volume scattering) as sea ice grows (red: VV, blue: HH, and green: VH). (a) incidence angle: 20° (b) incidence angle: 40°

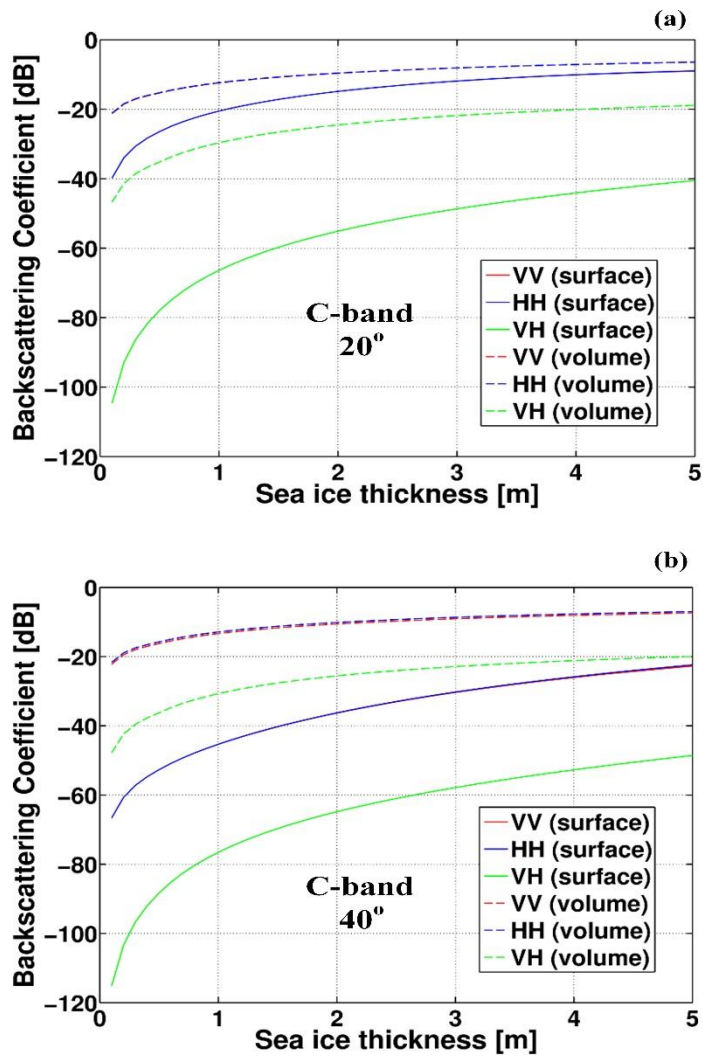


Figure 37. Backscattering coefficients (C-band) simulated by the VRT (Case 2, surface and volume scattering) as sea ice grows. Real line denotes simulated value by surface scattering, and dotted line denotes simulated value by volume scattering (red: VV, blue: HH, and green: VH). (a) incidence angle: 20° (b) incidence angle: 40°

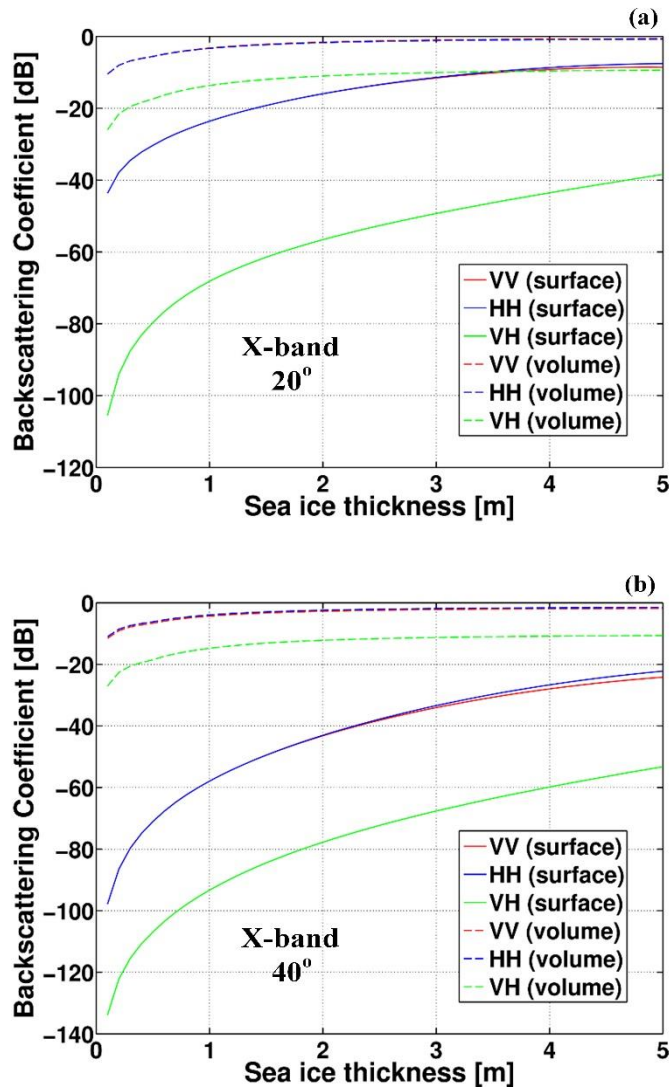


Figure 38. Backscattering coefficients (X-band) simulated by the VRT (Case 2, surface and volume scattering) as sea ice grows. Real line denotes simulated value by surface scattering, and dotted line denotes simulated value by volume scattering (red: VV, blue: HH, and green: VH). (a) incidence angle: 20° (b) incidence angle: 40°

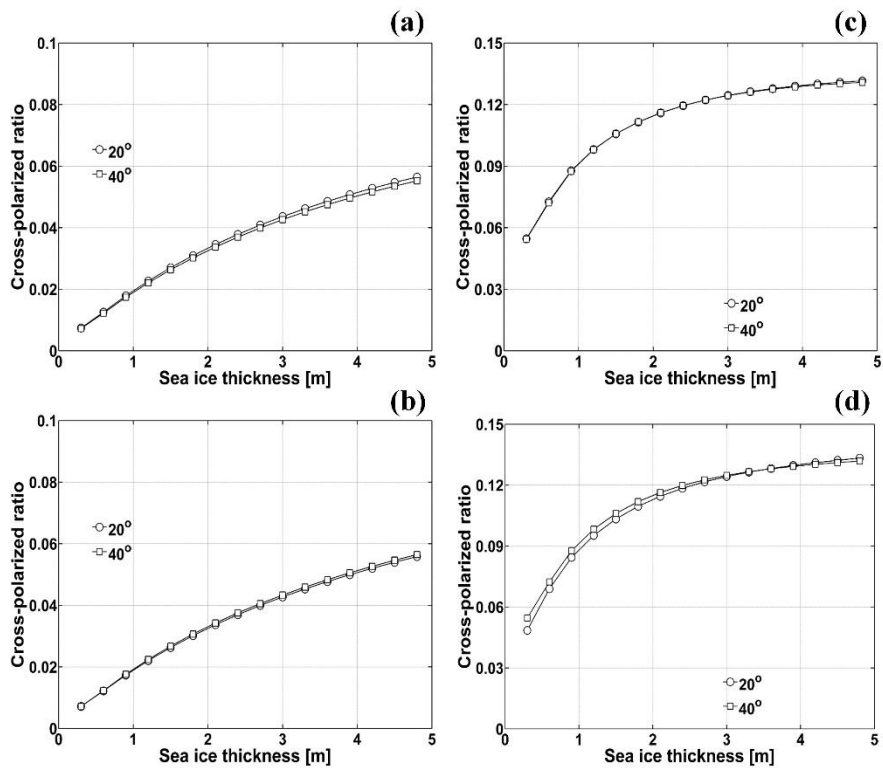


Figure 39. The relationship between depolarization factor (VH/VV) simulated by case 1 and 2 experiments and sea ice thickness. (a) C-band (case 1) (b) C-band (case 2) (c) X-band (case 1) (d) X-band (case 2)

C. Field experiments of the depolarization effects due to volume scattering within ice layer

Although the numerical simulations showed that the cross polarized ratio can be closely related to sea ice thickness due to the volume scattering within sea ice layer, it needs to verify this using field experiments. Here, the relationship between the ratio induced by volume scattering and the ice thickness was explored using measurements of artificially frozen ice with GB-POLSCAT (Figure 40). It measured the backscattered signatures from the ice with 140 and 190 cm of ice thickness, respectively. Detail specifications of the measurements are demonstrated in Table 6.

Figure 41 shows the backscattered signatures from the ice in the distance domain. In order to determine the position of ice surface, the backscattered signature was measured from the metal plate on the antenna aperture (dotted green line) and the ice surface (dotted black line). The position of ice bottom was determined by traveling distance of microwave estimated by Snell's law (Figure 42). The traveling distance within the ice (d_t) can be as following

$$\theta_t = \arcsin\left(\frac{\sqrt{\varepsilon'_{air}}}{\sqrt{\varepsilon'_{ice}}} \sin\theta_i\right) \quad (36)$$

$$d_t = \frac{d_i}{\cos\theta_t} \quad (37)$$

where θ_t is the transition angle. θ_i is the incidence angle. ε'_{air} is real part of

dielectric constant of air. ϵ'_{air} is real part of dielectric constant of ice. d_i is the ice thickness. The dielectric constant (real part) of air is 1, and of the ice is 3.15. It is assumed that the propagation velocity of microwave is same to the one of light. The backscattered signature from the antenna input was used the calibration of GB-POLSCAT based on new calibration method explained in Chapter 2.1.C

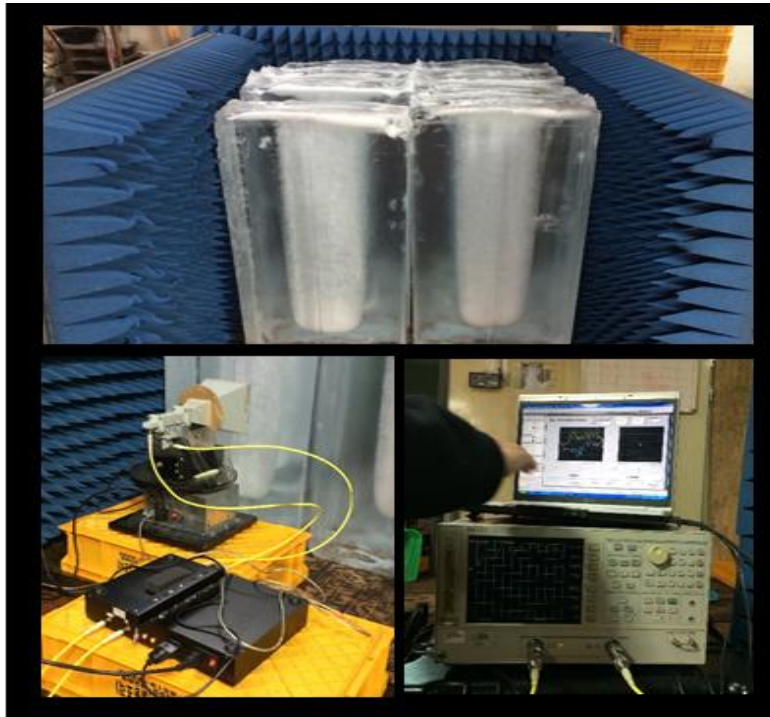


Figure 40. GB-POLSCAT measurement of artificially frozen ice.

Table 6. The specifications of the GB-POLSCAT measurement.

| Specifications | |
|---------------------------|---------------------------------------|
| Center Frequency | 5.275 GHz (C-band) |
| Sweep time | 1s |
| Bandwidth | 1.5 GHz |
| Transmitted Power | 20 dBm |
| Polarization | HH/VV/HV/VH |
| Incidence Angle | 0° ~ 40° |
| Calibration method | Kim et al [2012] |
| Measurement item | Radar response / Ice thickness |

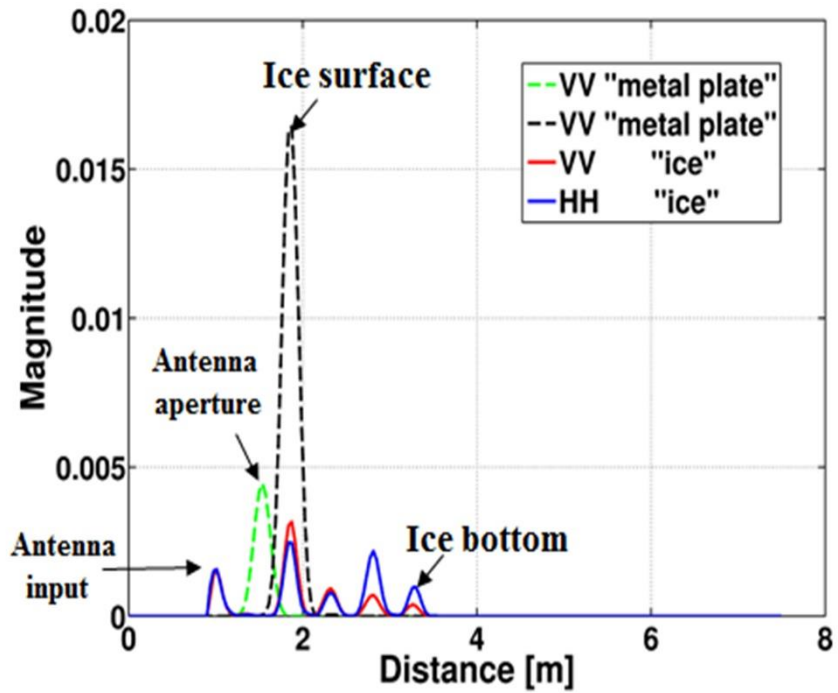


Figure 41. The measured backscattered signatures from the ice (blue real line: HH, red real line: VV). The green and black dotted line denotes the backscattered signatures from metal plate on the antenna aperture and the ice surface, respectively.

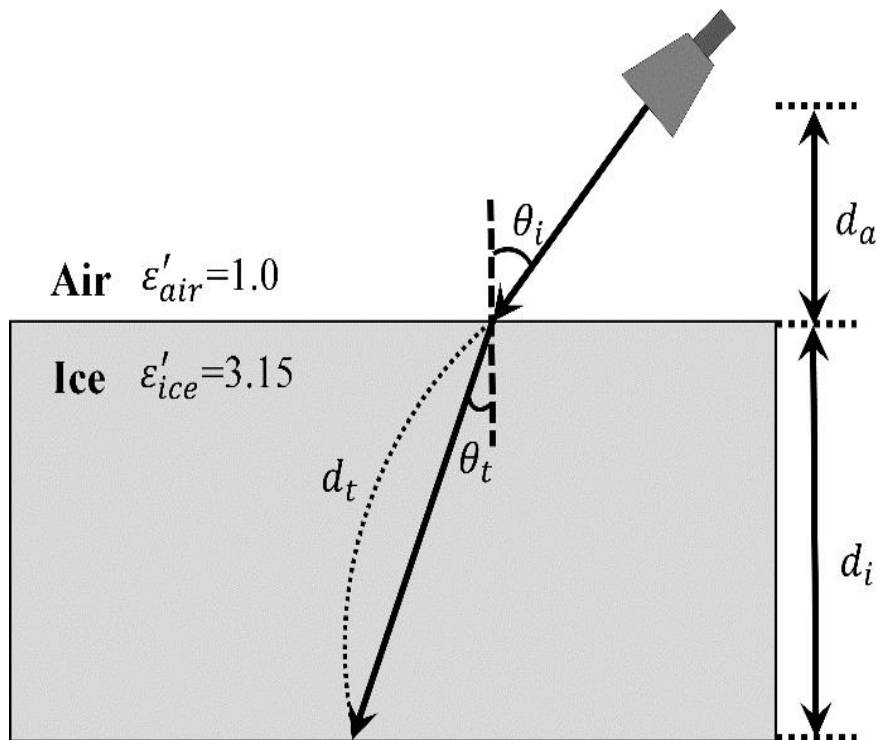


Figure 42. Refraction of microwave at the interface between the air and the ice based on Snell's law.

Figure 43 and 44 shows the backscattered signatures from each ice thickness. The range of incidence angle is from 0° to 40° (red dotted line: 0° , blue dotted line: 20° , and green dotted line: 40°). As incidence angle increases, the received power of the signals gradually decreases, and the phase is shifted due to the increase of the traveling distance. On the basis of this phase shift, each received power from surface, volume, and bottom of the ice is estimated using equation (16)-(18).

Figure 45 shows the normalized magnitude of each scattering feature. In all case experiments, volume scattering due to air bubbles within the ice is strongly dominant at 20° and 40° of incidence angle. Thus, it can be estimated that variation of the cross polarized ratio as the increase of the ice thickness. Table 7 shows the cross polarized ratio with the ice thickness. In the case 1 (the ice thickness = 140 cm), the ratio is 0.00097 and 0.00075 at 20° and 40° of incidence angle, respectively. In the case 2 (the ice thickness = 150 cm), the ratio is 0.0018 and 0.0016, respectively. That is, the increase of the ratio is 0.00083 and 0.00085 when the ice thickness increases from 140 to 190 cm. Through the numerical and the field studies, it is reasonable to say that the depolarization factors (i.e. the cross polarized ratio) are efficient parameter to determine sea ice thickness in the optimized conditions. Based on this, field experiments using space-borne SAR data were explored as case study, and it is described in next section.

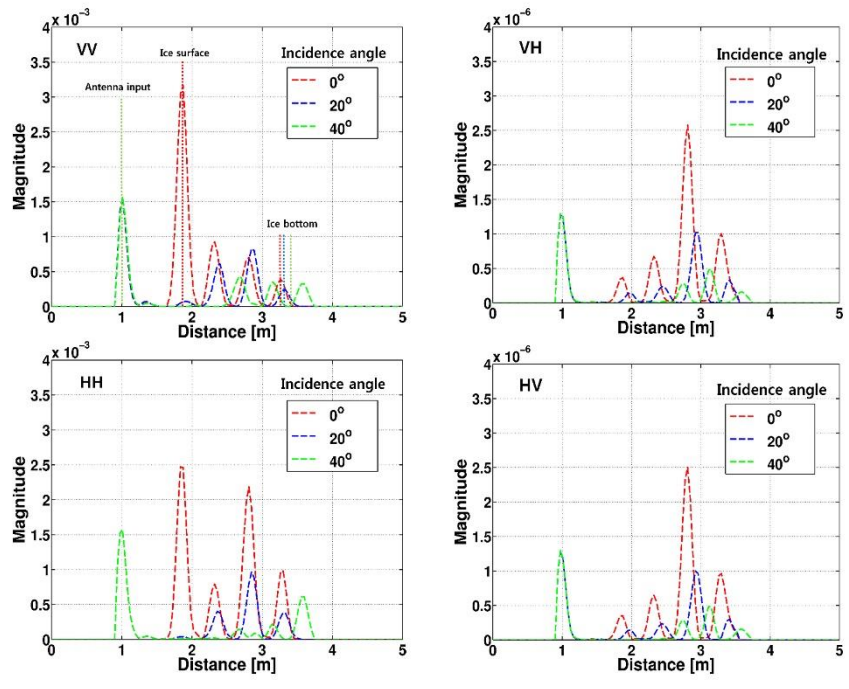


Figure 43. The backscattered signatures from the ice at 0°, 20°, and 40° of incidence angle. (the ice thickness = 140 cm)

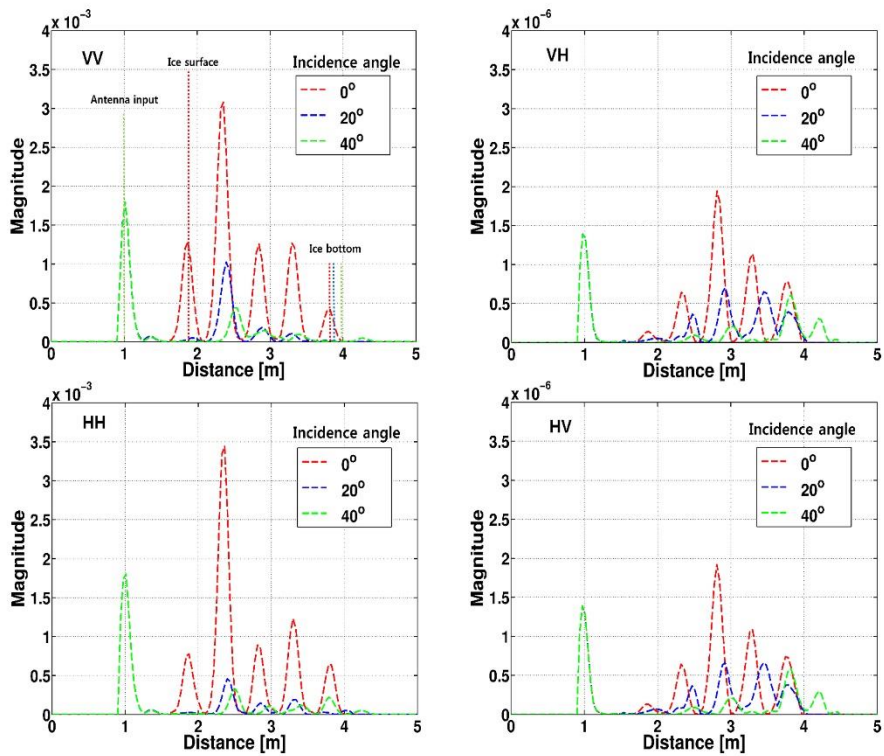


Figure 44. The backscattered signatures from the ice at 0°, 20°, and 40° of incidence angle. (the ice thickness = 190 cm)

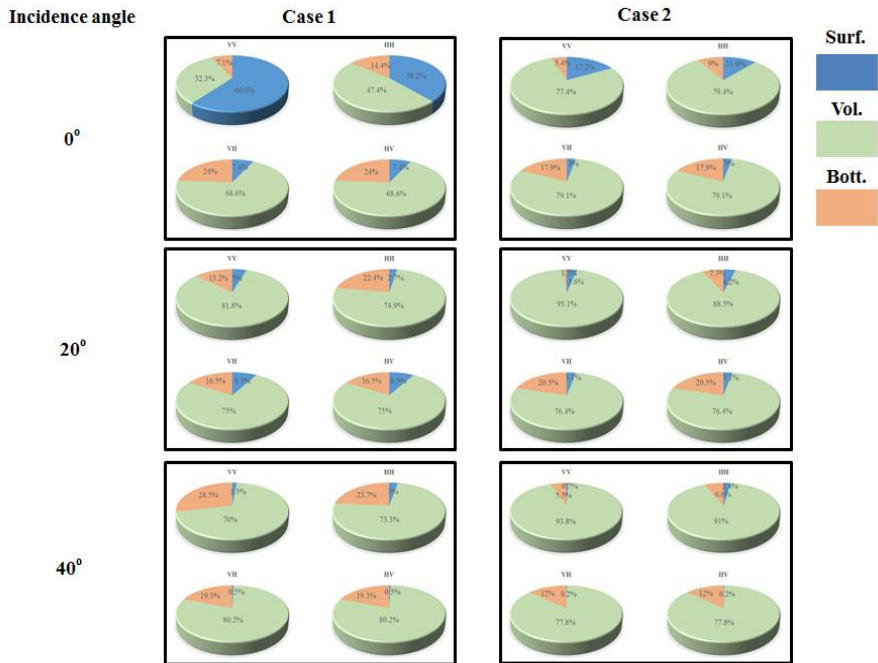


Figure 45. The normalized magnitude of surface, volume, and bottom-surface scattering from the ice at 0°, 20°, and 40° of incidence angle.

Table 7. The estimated cross polarized ratio in the case studies.

| | 20° | 40° |
|--|-----------------|-----------------|
| Case 1 (the ice thickness = 140 cm) | 0.00097 | 0.00075 |
| Case 2 (the ice thickness = 190 cm) | 0.0018 | 0.0016 |
| Difference | +0.00083 | +0.00085 |

Chapter 4. Measurement of sea ice thickness using space-borne SAR data in the Arctic Ocean

4.1. In-situ measurements and SAR data acquisition

An ice camp was set up on land-fast ice in the north of Greenland (Lat.: 83° 38.622 N, Lon.: 32° 14.245W) (Figure 46). This was part of an inter-disciplinary, scientific ice camp coordinated by the Danish Meteorological Institute (DMI) and the Danish Technological University (DTU). The land-fast ice camp was erected on May 1, 2009, and operated until May 6, 2009. Throughout the use of the ice camp, snow and ice thickness were measured using a snow probe and Electromagnetic Induction system (Model: Geonics EM31-SH). The EM31 can measure the magnitude of the in-phase and quadrature components of the secondary electro-magnetic field induced in the ground by the instrument's 9.8 kHz transmitted electro-magnetic field [22]. In the case of sea ice, the secondary field is primarily induced in the highly conductive sea water underneath the sea ice because of the low conductivity of sea ice. The magnitude of the secondary field is related directly to the distance between the instrument and the sea water below, and sea ice thickness can be estimated with known snow depth and instrument height above the snow surface.

At the ice camp, ice thickness were measured along the validation line, which stretched 1.5 km from smooth thick FYI in the south to rubble MYI in the North (Figure 47). The ice thickness of FYI was very stable at approximately 2 m, while the ice thickness of rubble MYI varied significantly. The mean air temperature was

about -18°C during ice camp. This presents an ideal case study to explore the possibility of using C- and X-band SAR data to estimate the ice thickness of both FYI and MYI.

Dual polarization TerraSAR-X data was acquired at 11:44 (UTC) on May 2, 2009, and two scenes of RADARSAT-2 were acquired at 10:42 (UTC) on April 28 and at 09:43 (UTC) on April 30, 2009, respectively (Figure 46). TerraSAR-X collected VV and HH polarization data in the Strip Map mode and RADARSAT-2 collected HH and HV (4/28), and VV and VH (4/30) dual-polarization data in the Standard Mode. All data were processed in Single-Look Complex (SLC) and slant-range projection to be used for polarimetric analysis. A speckle reduction filter (7×7 Lee filter) and radiometric calibration procedures were applied for the calculation of more accurate and reliable backscattering coefficients. Figure 48 shows the resulting backscattering coefficient images for TerraSAR-X and RADARSAT-2, respectively. The summary of the SAR data specifications are presented in Table 8.

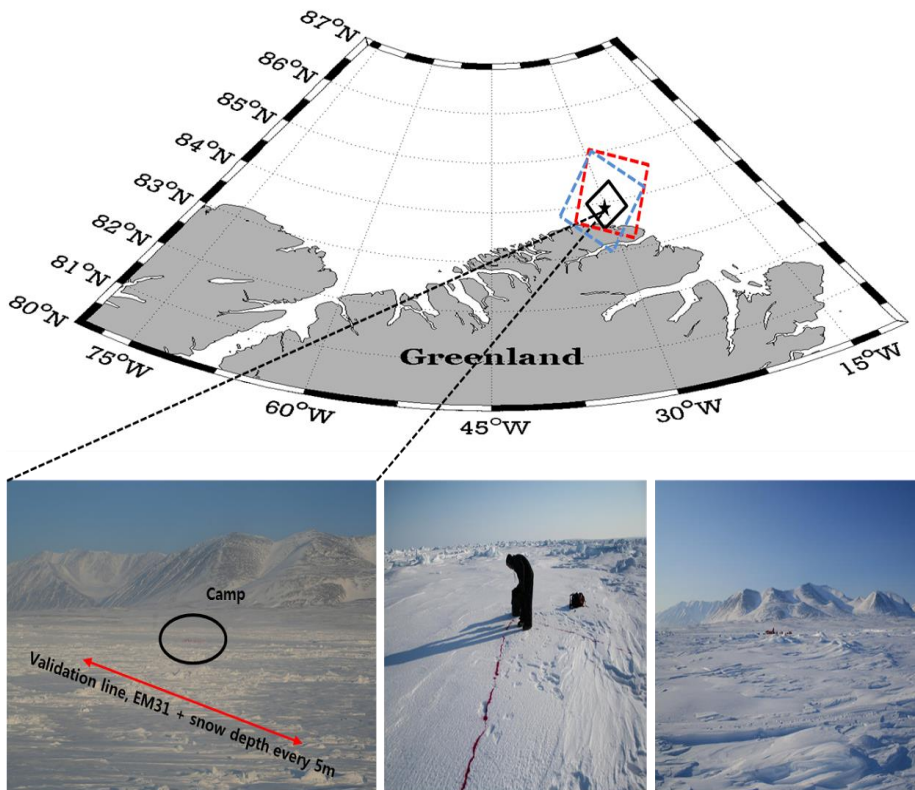


Figure 46. Study area off the northern coast of Greenland. The TerraSAR-X data was acquired on May 2, 2009 (black solid square). Two RADARSAT-2 data were acquired on April 28, 2009 (dotted blue square) and on April 30, 2009 (dotted red square), respectively. Ground truth data were obtained on May 01, 2009 (black star). The red line shown in lower left photograph represents the validation line on which the sea ice thickness and snow depth were measured using an EM31 instrument.

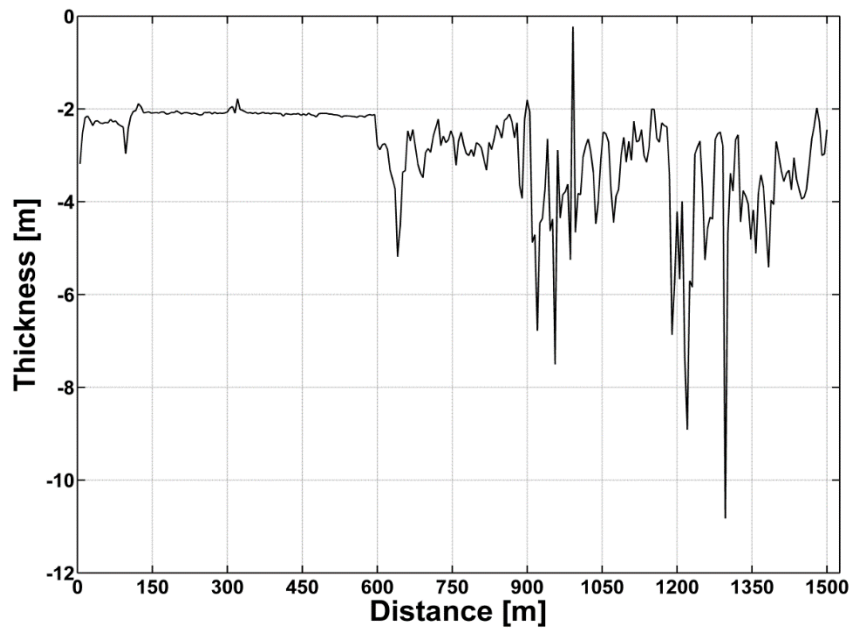


Figure 47. Sea ice thickness profile measured by the EM31 along the validation line (smooth thick FYI: 0~580 m, rubble MYI: 580~1500 m).

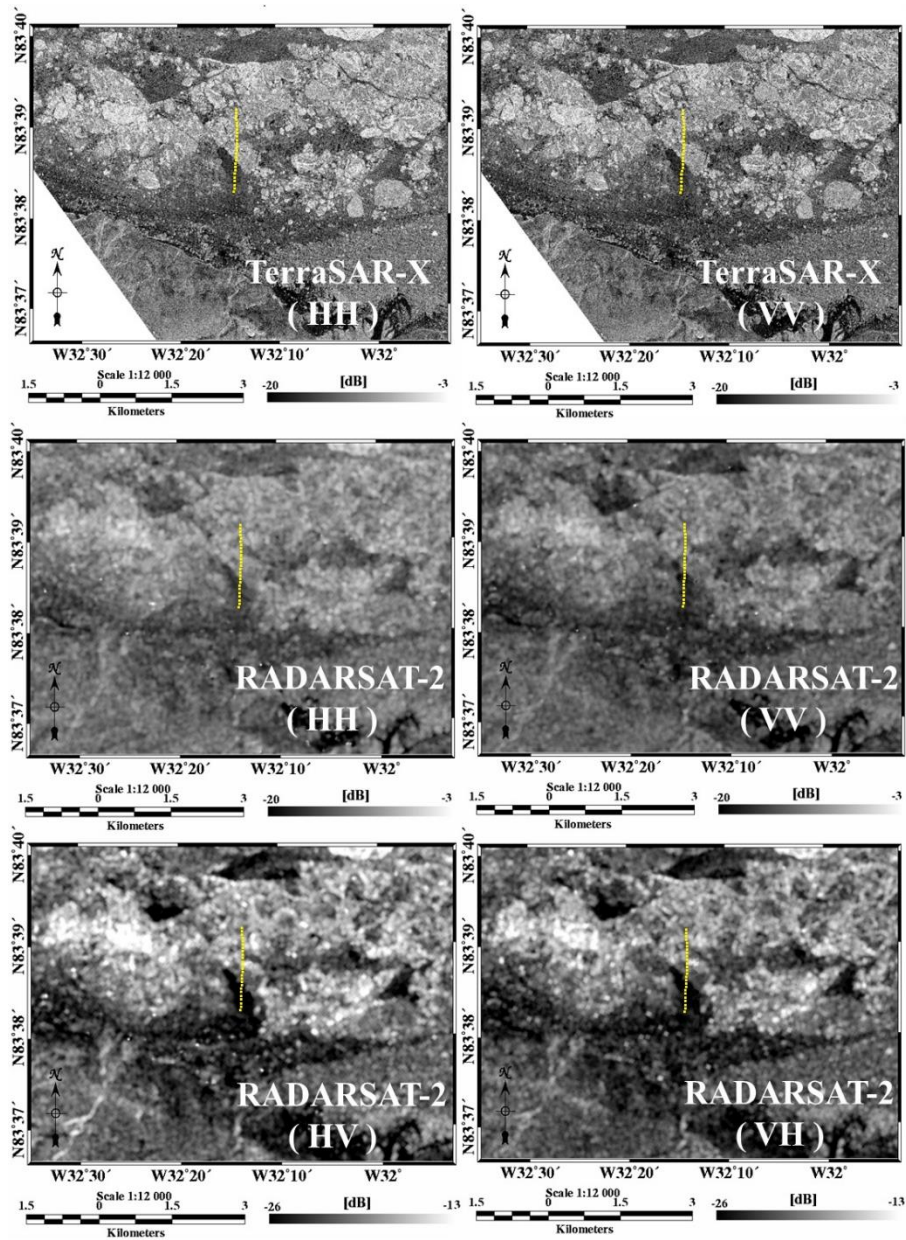


Figure 48. Radiometrically and geometrically calibrated SAR images (backscattering coefficients) of TerraSAR-X and RADARSAT-2. The yellow dots indicated in each figure represent the positions where sea ice thickness and snow depth were measured.

Table 8. Specifications of acquired TerraSAR-X and RADARSAT-2.

| <i>Acquisition date/time (UTC)</i> | <i>TerraSAR-X</i> | | <i>RADARSAT-2</i> | |
|------------------------------------|------------------------------|---------------------------------|---------------------------------|--|
| | May 2, 2009 17:40 | April 28, 2009 10:42 | April 30, 2009 09:43 | |
| <i>Center frequency</i> | 9.65 GHz (X-band) | 5.405 GHz (C-band) | 5.405 GHz (C-band) | |
| <i>Polarization</i> | HH and VV | HH and HV | VV and VH | |
| <i>Pixel spacing</i> | 3 m | 12.5 m | 12.5 m | |
| <i>Incident angle</i> | 27.3° ~ 29.0° | 33.6° ~ 39.8° | 41.4° ~ 46.6° | |

4.2. Depolarization-to-sea ice thickness relationship using space-borne SAR data

Both co-polarized correlation and cross-polarized ratio as depolarization factors were calculated from the SAR data, and the calculated values for each pixel were correlated to in-situ ice thickness. The results are presented as one-to-one scatter plots in Figure 49, showing strong and significant correlation coefficients (0.76 to 0.88) for both TerraSAR-X and RADARSAT-2. Co-polarized correlation for X-band varies 0.4 to 0.9 for the ice thickness range of 2.0 m to 5 m. Cross-polarized ratios for C-band range about 0.05 to 0.25 for the same range of sea ice thickness.

In first glance, the good correlation we found in this case study is likely due to contrast between smooth FYI and rubble MYI, however a close look reveals an interesting feature. The data points are rather continuous than clustered, especially for the case of RADARSAT-2 VH/VV. If the correlations are simply caused by a categorical difference in scattering mechanism between FYI and MYI, those data points should be more clustered. The continuous feature indicates that there might be a mechanism that thicker ice becomes rougher or higher volume scattering and in turn increases depolarization. In our case this mechanism involves ridging and rafting processes that increase the ice thickness and surface roughness as well as lower density layers within lifted ice blocks. Model simulation results for surface roughness showed a maximum of about 0.05 increases in cross-polarized ratio between FYI and

MYI, while about 0.05 (C-band) and 0.1 (X-band) increases for volume scattering. The combined value (about 0.1 ~ 0.2) from simulation is slightly smaller than the observed difference of 0.2. While considering uncertainty in model simulations, this suggests that depolarization in MYI can be attributed to both surface roughness and volume scattering which is closely related to ridging and rafting processes. Over smooth FYI, the cross-polarized ratio values are scattered at the same ice thickness. This indicates a case for de-correlation between ice thickness and roughness/volume scattering. In other words, FYI with the same ice thickness can have different surface roughness or/and volume scattering, and depolarization. In our case we observed patches of small rafting and higher snow on the surface of the smooth FYI. The effect of this scatter is relatively smaller than the correlation in MYI.

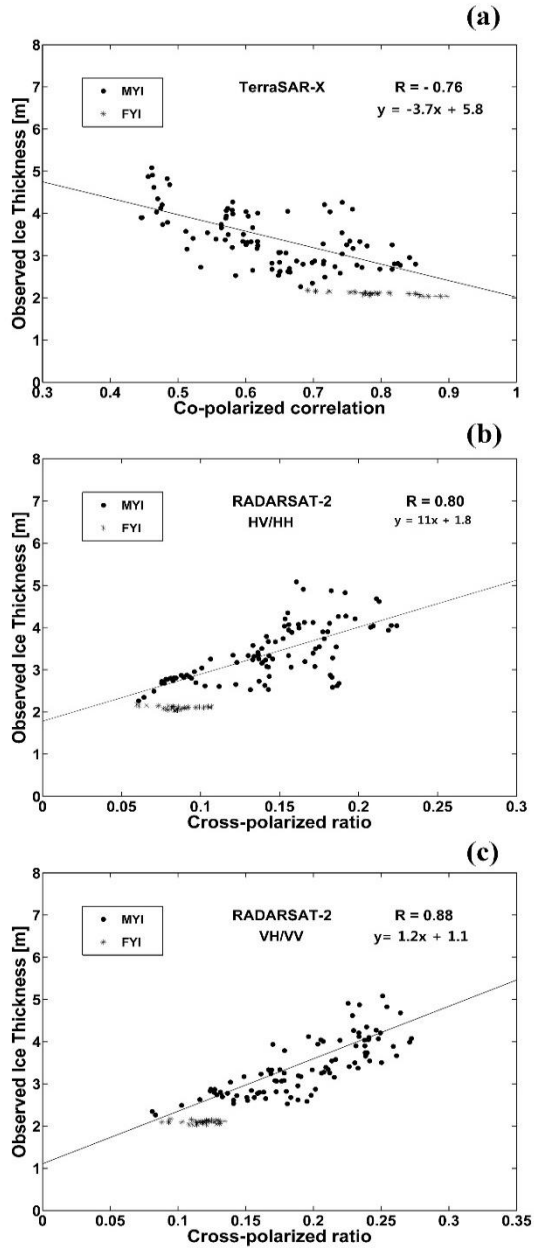


Figure 49. Relationship between the depolarization factors and observed sea ice thickness. (a) TerraSAR-X (5/02) (b) RADARSAT-2 (4/28) (c) RADARSAT-2 (4/30)

Chapter 5. Conclusion

5.1. Summary

This thesis presents numerical microwave scattering simulations and in-situ measurements with polarimetric RADAR (i.e. GB-POLSCAT and space-borne SAR) systems in order to investigate the optimum method for estimating sea ice thickness. Reanalysis of Strozzi's GB-POLSCAT measurements informed us that the backscattered signatures of microwave (C-band) from the surface of snow cover on sea ice can predominantly affect the space-borne SAR measurements for the melting season due to the high dielectric properties of the surface melting water. On the other hand, for the freezing season, the signatures with all polarization and high incidence angles can predominantly originate from the interface between the snow cover and the sea ice. Furthermore, in-situ measurements and numerical simulations of the physical properties (i.e. salinity, dielectric constant, and surface roughness) of sea ice as sea ice grows showed that sea ice tends to be rougher and less saline as sea ice grows during the freezing season. These mean that the multiple scattering of microwave from the surface and volume of sea ice can increase as the sea ice thickness increases during the freezing season. Thus, it could be proposed that relationship between sea ice thickness and the depolarization effect might exist because the depolarization effect of the backscattered signatures are strongly

dominated by the multiple scattering from a target.

Here, the degree of depolarization due to surface scattering from sea ice were simulated by dividing the roughness scales into small and large scales. IEM and extended Bragg models were used to simulate the degree of depolarization by small-scale and large-scale roughness, respectively, within a reasonable range of sea ice parameters. Furthermore, the degree of depolarization due to volume scattering was estimated by VRT simulation and GB-POLSCAT measurements. As a results, the cross-polarized ratio, one of the depolarization factors, has a distinct one-to-one relationship with sea ice thickness due to dominant depolarization effect induced by volume scattering within the ice layer. Based on these experiments, space-borne SAR data (one TerraSAR-X and two RADARSAT-2 scenes) were acquired along with in-situ sea ice thickness measurements. The depolarization factors (i.e., co-polarized correlation and cross-polarized ratio) were then calculated from acquired SAR data. At last, a strong and significant correlation between the ice thickness and the depolarization factors (correlation coefficients of 0.76 to 0.88) for both TerraSAR-X and RADARSAT-2 was found. Therefore, it is reasonable to say that the depolarization factors (i.e. the cross polarized ratio) extracted by space-borne SAR data are efficient parameters to determine sea ice thickness in the optimized conditions.

5.2. Discussion

The determination of sea ice thickness is the main issue of space-borne SAR measurements in the cryosphere, and various researches for this are being investigated. In this thesis, sensitivity studies conducted using numerical experiments and the observed results from polarimetric RADAR data have shown that the depolarization factors extracted by space-borne SAR data are effective parameters for the estimation of sea ice thickness.

However, this study restricts to conclude whether the ice thickness-to-depolarization relationship is an operational method to determine sea ice thickness. Because this relationship is not always able to satisfy under all dynamic nature of sea ice. For example, although pancake ice is a thin sea ice (i.e. its thickness is up to 10 cm), its surface roughness is relatively rougher than the one of universal thin sea ice due to periodic compressions of oceanic wave. Thus, the degree of depolarization estimated from pancake ice can be stronger than the one of universal thin sea ice due to multiple scattering from surface of the ice while the thickness of these ice are similar, and these can weaken the ice thickness-to-depolarization relationship.

Based on this view, in order to improve the operational applicability for determination of sea ice thickness using space-borne SAR data, the weakening factors of the ice thickness-to-depolarization relationship should be resolved. Although this thesis showed that the ice thickness and depolarization induced by multiple scattering

from surface of the ice can be correlated under optimized conditions, this relationship can break under specific conditions as mentioned above. On the other hand, the ice thickness and depolarization induced by volume scattering within the ice layer are strongly correlated by the desalination process as sea ice grows. That is, the operational capability can improve if depolarization effects induced by only volume scattering within the ice layer can be extracted from space-borne SAR data. Unfortunately, it is not easy because the backscattering coefficients estimated by space-borne SAR measurements are determined by the summation of the backscattered signatures induced by surface and volume scattering. Recent works have tried to quantitatively distinguish the contributions of each scattering from polarimetric SAR data with polarimetric decomposition and Polarimetric SAR Interferometry (Pol-InSAR) techniques. Therefore, future works require the investigations of capability for measuring sea ice thickness with these techniques, and if the operational method to measuring sea thickness using space-borne SAR data is successfully developed, it can be expected that global climate change process can understand more effectively such as thermal feedback between ocean, atmosphere, and the ice.

Appendix

In this appendix, the models used in this thesis are explained. The models can be classified into IEM, the extended Bragg, and VRT model. IEM and the extended Bragg model were used to simulate the backscattering features induced by the ice surface for small- and large-scale surface roughness, respectively. VRT was used to simulate the backscattering features induced within the ice layer.

A. Integral Equation Method (IEM)

This model can simulate backscattering coefficients from a target surface (σ_{pq}^S), the backscattering coefficients can be classified into single and multiple scattering ($\sigma_{pq}^S = \sigma_{pq}^s + \sigma_{pq}^m$) Single scattering can only induce the backscattering signatures of co-polarization while multiple scattering can induce the signatures of co- and cross-polarization [43]. In this model, the backscattering coefficients due to single or multiple scattering are as following

$$\sigma_{pq}^s = \frac{k^2}{2} \exp(2k_z^2 s^2) \sum_{n=1}^{\infty} |I_{pq}^n|^2 \frac{W^{(n)}(2k_x, 0)}{n!} \quad (\text{A.1})$$

$$\text{here, } |I_{pq}^n| = f_{pq} (2sk_z)^n \exp(-k_z^2 s^2) + \frac{(sk_z)^n [F_{pq}(-k_x, 0) + F_{pq}(k_x, 0)]}{2}$$

$$\sigma_{pq}^m = \frac{k^2}{16\pi} \exp(-2k_z^2 s^2) \sum_{n=1}^{\infty} \sum_{m=1}^{\infty} \frac{(k_z^2 s^2)^{n+m}}{n!m!} \quad (\text{A.2})$$

$$\cdot \int \left[|F_{pq}(u, v)|^2 + F_{pq}(u, v)F_{pq}^*(-u, -v) \right] W^{(n)}(-k_x, v)W^{(m)}(u + k_x, v) dudv$$

where superscripts s and m denote single and multiple scattering, respectively. k is the wave number. $k_x = k\sin\theta$, $k_z = k\cos\theta$, and θ is the incidence angle. u and v are scattering vector directions, s is the surface RMS height. $W^{(n)}$ and $W^{(m)}$ are the Fourier transform of the n^{th} or m^{th} power of the surface correlation function. f_{pq} is the Kirchhoff coefficient, and F_{pq} represents the complementary field coefficients.

B. Extended Bragg model

The extended Bragg model for a wider range of roughness conditions proposed by [76] is summarized. First, Bragg scattering coefficients are functions of the complex permittivity and the local incidence angle. Hence, it can write the following:

$$R_s = \frac{\cos\theta - \sqrt{\varepsilon - \sin^2\theta}}{\cos\theta + \sqrt{\varepsilon - \sin^2\theta}} \quad R_p = \frac{(\varepsilon - 1)[\sin^2\theta - \varepsilon(1 + \sin^2\theta)]}{(\varepsilon\cos\theta + \sqrt{\varepsilon - \sin^2\theta})^2} \quad (\text{B.1})$$

where R_s and R_p denote the horizontal and the vertical Bragg scattering coefficients, respectively. ε is the complex permittivity and θ is the local

incidence angle. The polarimetric scattering matrix S for a Bragg surface can be written as

$$[S] = \begin{bmatrix} S_{HH} & S_{HV} \\ S_{VH} & S_{VV} \end{bmatrix} = m_s \begin{bmatrix} R_s & 0 \\ 0 & R_p \end{bmatrix} \quad (\text{B.2})$$

where m_s is the backscatter amplitude that contains information regarding the roughness condition of the surface. The coherency matrix can be formed by employing a scattering vector \underline{k} as the vectorization of the scattering matrix using the Pauli spin matrices basis set. Its formation can be described as follows:

$$\underline{k} = \frac{1}{2} \text{Trace}([S][\Psi]) = \frac{1}{\sqrt{2}} [S_{HH+VV} \quad S_{HH-VV} \quad 2S_{HV}]^T$$

here, $[\Psi] = \left\{ \sqrt{2} \begin{bmatrix} 1 & 0 \\ 0 & 1 \end{bmatrix} \quad \sqrt{2} \begin{bmatrix} 1 & 0 \\ 0 & -1 \end{bmatrix} \quad \sqrt{2} \begin{bmatrix} 0 & 1 \\ 1 & 0 \end{bmatrix} \right\}$ (B.3)

$$[T] = \langle \underline{k} \cdot \underline{k}^{-1} \rangle = \begin{bmatrix} T_{11} & T_{12} & T_{13} \\ T_{21} & T_{22} & T_{23} \\ T_{31} & T_{32} & T_{33} \end{bmatrix}$$

where $[\Psi]$ denotes the Pauli spin matrices basis set. In order to extend the Bragg scattering model for a wider range of roughness conditions, Hajnsek et al. [76]

introduced a method of modeling the surface disturbance as a reflection symmetric depolarizer by rotating the Bragg coherency matrix about an angle, β , in the plane perpendicular to the scattering plane. This rotation of the Bragg coherency matrix can be expressed as follows:

$$[T] = m_s^2 [A] \begin{bmatrix} \langle |R_s + R_p|^2 \rangle & \langle (R_s + R_p)(R_s - R_p)^* \rangle & 0 \\ \langle (R_s - R_p)(R_s + R_p)^* \rangle & \langle |R_s - R_p|^2 \rangle & 0 \\ 0 & 0 & 0 \end{bmatrix} [A]^T \quad (\text{B.4})$$

$$\text{here, } [A] = \begin{bmatrix} 1 & 0 & 0 \\ 0 & \cos 2\beta & \sin 2\beta \\ 0 & -\sin 2\beta & \cos 2\beta \end{bmatrix}$$

Using a uniform distribution density function of β

$$P(\beta) = \begin{cases} \frac{1}{2\beta_1} & |\beta| \leq \beta_1 \\ 0 & 0 \leq \beta_1 \leq \frac{\pi}{2} \end{cases} \quad (\text{B.5})$$

The coherency matrix for a rough surface can be determined as follows:

$$\begin{aligned}
[T] &= \int_0^{2\pi} T(\beta)P(\beta)d\beta \\
&= \frac{m_s^2}{2} \begin{bmatrix} C_1 & C_2 \text{sinc}(2\beta_1) & 0 \\ C_2 \text{sinc}(2\beta_1) & C_3[1 + \text{sinc}(4\beta_1)] & 0 \\ 0 & 0 & C_3[1 - \text{sinc}(4\beta_1)] \end{bmatrix} \quad (\text{B.6})
\end{aligned}$$

The coefficients C_1 , C_2 , and C_3 describe the Bragg components of the surface and are given by

$$C_1 = |R_s + R_p|^2 \quad C_2 = (R_s + R_p)(R_s^* - R_p^*) \quad C_3 = \frac{1}{2}|R_s - R_p|^2 \quad (\text{B.7})$$

C. Vector Radiative Transfer (VRT)

In this model, the scattering and propagation of the traveling signal with a specific intensity in a medium can be defined by [77]

$$\cos\theta \frac{dI}{dz} = -\kappa_e I + \int P I dz \quad (\text{C.1})$$

where I is the specific intensity which is defined by the Stokes vector. κ_e is the extinction matrix, and P is the phase matrix of scatterer within a target layer. z denotes the penetration depth of microwave. κ_e can be estimated to sum between the scattering and the absorption coefficient of the scatterer [77]. P is strongly

connected with the shape, reflectivity, and etc. of the scatterer. In general, many sea ice simulations with VRT [60], [77], it was assumed that the scatterer within the ice layer is Rayleigh scatterer (i.e. the shape of the scatterer is a sphere and radius of the scatterer \ll wave length of microwave). The phase matrix of Rayleigh scatterer was well explained in [80]. Equation (C.1) is generally solved by iterative method with 2nd order solution [80], and the physical meanings of each order solutions were described minutely in [81].

Total backscattering coefficients simulated by VRT is as following

$$\sigma_{pq}^{total} = \sigma_{pq}^0 + \sigma_{pq}^1 + \sigma_{pq}^2 \quad (C.2)$$

where superscripts 0, 1, and 2 denote zeroth-, first-, and second-order backscattering coefficient, respectively. The zeroth-order solution is surface scattering component (Figure 50). Thus, the component was solved by IEM simulation (i.e. σ_{pq}^S) like [81]. Figure 51 shows the backscattering coefficients of first and second order solution with the physical meanings. The first order solution of VRT can be classified into three components (Figure 51a, b, and c). First and second are interaction components between bottom-surface and the scatterer within the layer, and third is single scattering component from the scatterer within the layer. Backscattering coefficients of the each component are as following

$$\sigma_{pq}^{VS} = \cos\theta_s T_p^i T_q^s \sec\theta_s^t L_p L_q \sigma_{pq}^S \quad (\text{C.3})$$

$$\begin{aligned} \sigma_{pq}^a &= \cos\theta_{t0} T_{10p}(\theta_{t0}, \theta_{i1}) T_{01q}(\theta_{t1}, \theta_{i0}) L_q(\theta_{t1}) \sec\theta_{s2} \\ &\cdot \int_0^{2\pi} \int_0^{\frac{\pi}{2}} \sin\theta \sec\theta \cdot \sum_{u=v,h} \sigma_{uq}^{VS}(\theta, \phi | \pi - \theta_{i2}, \phi_{i2}) \\ &\cdot P_{pu}(\phi_{ss1}, \theta_{ss1} | \theta, \phi) \frac{L_p(\theta_{ss1}) - L_u(\theta)}{\kappa_{eu}(\theta) \sec\theta - \kappa_{ep}(\theta_{ss1}) \sec\theta_{ss1}} d\phi d\theta \end{aligned} \quad (\text{C.4})$$

$$\begin{aligned} \sigma_{pq}^b &= \cos\theta_{t0} T_{10p}(\theta_{t0}, \theta_{i1}) T_{01q}(\theta_{t1}, \theta_{i0}) L_q(\theta_{t1}) \sec\theta_{s2} \\ &\cdot \int_0^{2\pi} \int_0^{\frac{\pi}{2}} \sin\theta \sec\theta \cdot \sum_{u=v,h} \sigma_{pu}^{VS}(\theta_{s2}, \phi_{s2} | \pi - \theta, \phi) \\ &\cdot P_{uq}(\pi - \theta, \phi | \pi - \theta_{si1}, \phi_{si1}) \frac{L_u(\theta) - L_q(\theta_{si1})}{\kappa_{eq}(\theta_{si1}) \sec\theta_{si1} - \kappa_{eu}(\theta) \sec\theta} d\phi d\theta \end{aligned} \quad (\text{C.5})$$

$$\begin{aligned} \sigma_{pq}^c &= 4\pi \cos\theta_{t0} T_{10p}(\theta_{t0}, \theta_{i1}) T_{01q}(\theta_{t1}, \theta_{i0}) \sec\theta_{ss1} \\ &\cdot P_{pq}(\theta_{ss1}, \theta_{ss1} | \pi - \theta_{si1}, \phi_{si1}) \frac{1 - L_p(\theta_{ss1}) L_q(\theta_{si1})}{\kappa_{ep}(\theta_{ss1}) \sec\theta_{ss1} - \kappa_{eq}(\theta_{si1}) \sec\theta_{si1}} \end{aligned} \quad (\text{C.6})$$

where σ_{pq}^{VS} is the backscattering coefficient of the bottom-surface. Superscripts i and s denote the incident and scattered direction, respectively. Incident or scattered angles of each layer are described in Figure 52 (i.e. $\pi - \theta$ denotes downward direction and ϕ is azimuth angle). T is the transmission coefficient on the interface of the each layer. Subscripts of T denote the propagation direction of microwave on the interface of each layer. For example, T_{01} means that the transmission coefficient

of microwave which propagates from 0 layer to 1 layer. L is power attenuation term, and can be estimated by

$$L_p(\theta) = \exp[-\kappa_{ep}d\sec\theta] \quad (C.7)$$

where d is the layer depth. The second order solution of VRT can be classified into two components (Figure 51d and e). These components mean the interaction between the scatterer within the layer. Backscattering coefficients of the each component are as following

$$\begin{aligned} \sigma_{pq}^d &= 4\pi\cos\theta_{t0}T_{10p}(\theta_{t0},\theta_{i1})T_{01q}(\theta_{t1},\theta_{i0})\sec\theta_{ss2} \\ &\cdot \int_0^{2\pi} \int_0^{\frac{\pi}{2}} \sin\theta\sec\theta \cdot \sum_{u=v,h} \frac{P_{pu}(\theta_{ss2},\phi_{ss2}|\theta,\phi)P_{uq}(\theta,\phi|\pi-\theta_{si1},\phi_{si1})}{\kappa_{eq}(\theta_{si1})\sec\theta_{si1}+\kappa_{eu}(\theta)\sec\theta} \quad (C.8) \\ &\cdot \left[\frac{1-L_p(\theta_{ss2})L_q(\theta_{si1})}{\kappa_{ep}(\theta_{ss2})\sec\theta_{ss2}+\kappa_{eq}(\theta_{si1})\sec\theta_{si1}} + \frac{L_q(\theta_{si1})[L_u(\theta)-L_p(\theta_{ss2})]}{\kappa_{eu}(\theta)\sec\theta-\kappa_{ep}(\theta_{ss2})\sec\theta_{ss2}} \right] d\phi d\theta \end{aligned}$$

$$\begin{aligned} \sigma_{pq}^e &= 4\pi\cos\theta_{t0}T_{10p}(\theta_{t0},\theta_{i1})T_{01q}(\theta_{t1},\theta_{i0})\sec\theta_{ss2} \\ &\cdot \int_0^{2\pi} \int_0^{\frac{\pi}{2}} \sin\theta\sec\theta \cdot \sum_{u=v,h} \frac{P_{pu}(\theta_{ss2},\phi_{ss2}|\pi-\theta,\phi)P_{uq}(\pi-\theta,\phi|\pi-\theta_{si1},\phi_{si1})}{\kappa_{ep}(\theta_{ss2})\sec\theta_{ss2}+\kappa_{eu}(\theta)\sec\theta} \quad (C.9) \\ &\cdot \left[\frac{1-L_p(\theta_{ss2})L_q(\theta_{si1})}{\kappa_{ep}(\theta_{ss2})\sec\theta_{ss2}+\kappa_{eq}(\theta_{si1})\sec\theta_{si1}} + \frac{L_p(\theta_{ss2})[L_u(\theta)-L_q(\theta_{si1})]}{\kappa_{eu}(\theta)\sec\theta-\kappa_{eq}(\theta_{si1})\sec\theta_{si1}} \right] d\phi d\theta \end{aligned}$$

Finally, Backscattering coefficients of the volume scattering (σ_{pq}^V) within the layer can be calculated by

$$\sigma_{pq}^V = \sigma_{pq}^a + \sigma_{pq}^b + \sigma_{pq}^c + \sigma_{pq}^d + \sigma_{pq}^e \quad (\text{C.10})$$

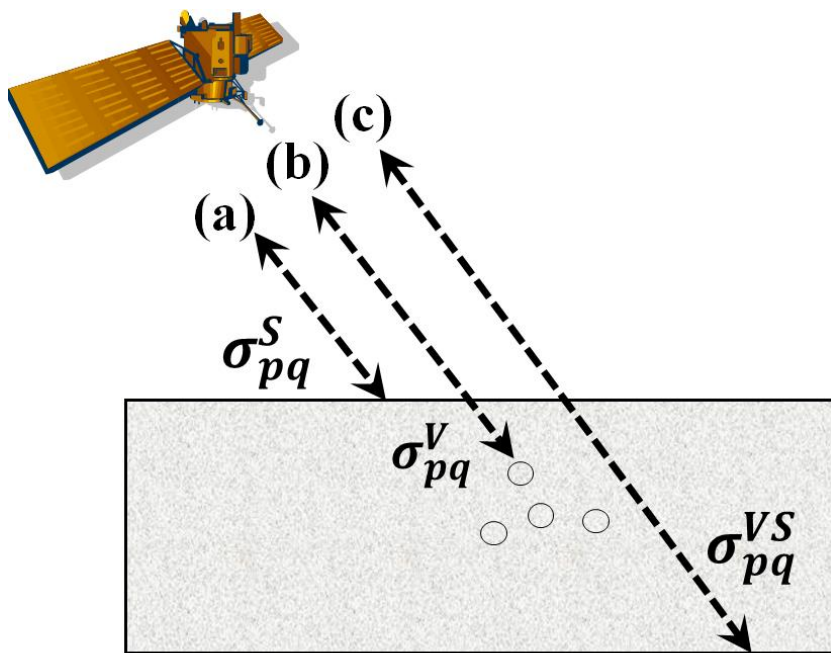


Figure 50. Scattering structures of VRT model simulation. (a) surface scattering (b) volume scattering (c) bottom-surface scattering

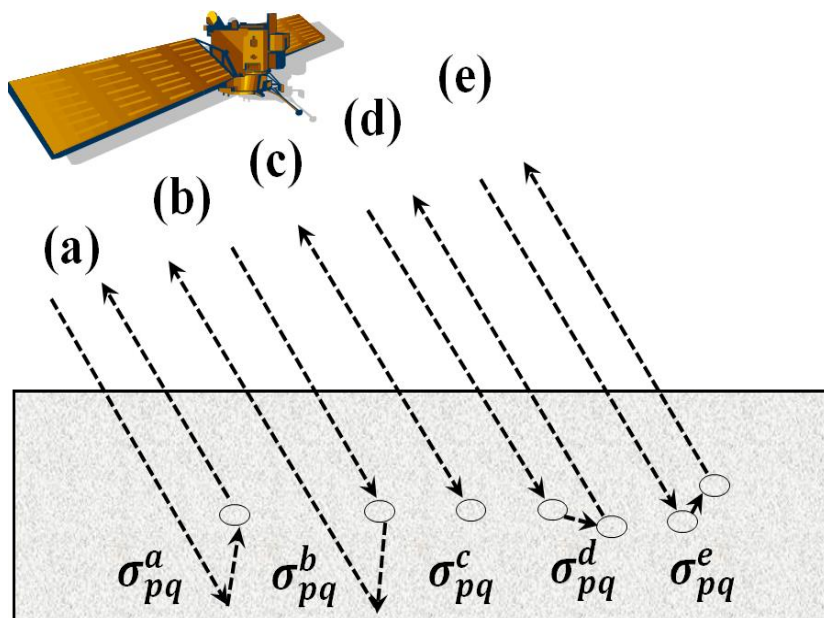


Figure 51. Volume scattering structure of VRT simulation. (a)-(c) first order solution (d)-(e) second order solution.

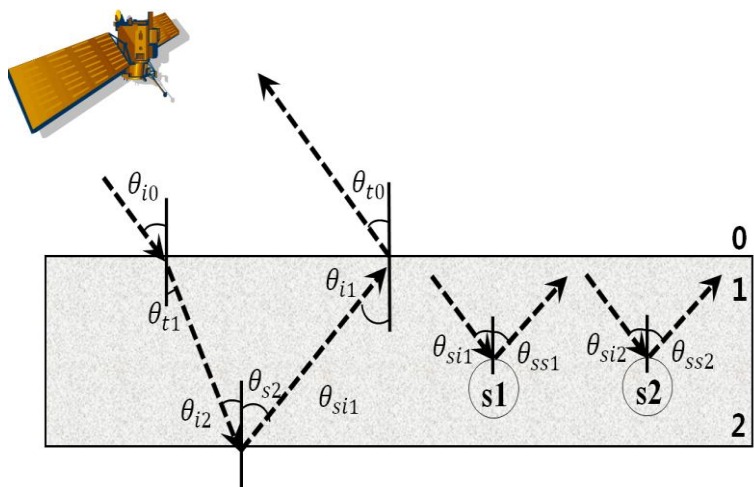


Figure 52. Geometry of incident and scattered angle at the each layer for VRT simulation.

References

1. Fitzharris, B. B. (1996). *The cryosphere: changes and their impacts*. Cambridge university press, New York, NY(USA)., pp. 241-265
2. Hall, D. K., & Martinec, J. (1985). *Remote sensing of ice and snow* (pp. 109-155). New York: Chapman and Hall.
3. Chapman, W. L., & Walsh, J. E. (1993). Recent variations of sea ice and air temperature in high latitudes. *Bulletin of the American Meteorological Society*, 74(1), 33-47.
4. <http://www.cocorahs-albedo.org/>
5. Coakley, J. A. (2002). Reflectance and albedo, surface.
6. Parkinson, C. L., & Cavalieri, D. J. (2008). Arctic sea ice variability and trends, 1979–2006. *Journal of geophysical research*, 113(C7), C07003.
7. Pritchard, H. D., Ligtenberg, S. R. M., Fricker, H. A., Vaughan, D. G., Van den Broeke, M. R., & Padman, L. (2012). Antarctic ice-sheet loss driven by basal melting of ice shelves. *Nature*, 484(7395), 502-505.
8. Stroeve, J., Holland, M. M., Meier, W., Scambos, T., & Serreze, M. (2007). Arctic sea ice decline: Faster than forecast. *Geophysical research letters*, 34(9).
9. Boé, J., Hall, A., & Qu, X. (2009). September sea-ice cover in the Arctic Ocean projected to vanish by 2100. *Nature Geoscience*, 2(5), 341-343.

10. Wang, M., & Overland, J. E. (2009). A sea ice free summer Arctic within 30 years?. *Geophysical Research Letters*, 36(7), L07502.
11. Haas, C., Gerland, S., Eicken, H., & Miller, H. (1997). Comparison of sea-ice thickness measurements under summer and winter conditions in the Arctic using a small electromagnetic induction device. *Geophysics*, 62(3), 749-757.
12. Van der Kruk, J., Arcone, S. A., & Liu, L. (2007). Fundamental and higher mode inversion of dispersed GPR waves propagating in an ice layer. *Geoscience and Remote Sensing, IEEE Transactions on*, 45(8), 2483-2491.
13. Mittelholzer W and others (1925) By airplane towards the north pole (trans: Paul E, Paul C). Houghton Mifflin, Boston, 176p
14. Wilkins, H. (1929). The Wilkins-Hearst Antarctic Expedition, 1928-1929. *Geographical Review*, 19(3), 353-376.
15. McDonald, R. A. (1995). CORONA-Success for Space Reconnaissance, a Look into the Cold-War, and a Revolution for Intelligence. *Photogrammetric Engineering and Remote Sensing*, 61(6), 689-720.
16. Peebles, C. (1997). *The CORONA project: America's first spy satellites* (p. 246). Annapolis, MD: Naval Institute Press.
17. Wheelon, A. D. (1997). Corona: The first reconnaissance satellites. *Physics today*, 50, 24.
18. Sohn, H. G., Jezek, K. C., & Van der Veen, C. J. (1998). Jakobshavn Glacier, West Greenland: 30 years of spaceborne observations. *Geophysical Research Letters*, 25(14), 2699-2702.
19. Bindshadler, R., & Vornberger, P. (1998). Changes in the West Antarctic ice sheet since 1963 from declassified satellite photography. *Science*, 279(5351),

689-692.

20. Comiso, J. C., Cavalieri, D. J., & Markus, T. (2003). Sea ice concentration, ice temperature, and snow depth using AMSR-E data. *Geoscience and Remote Sensing, IEEE Transactions on*, 41(2), 243-252.
21. Zhao, Y., Liu, A. K., & Long, D. G. (2002). Validation of sea ice motion from QuikSCAT with those from SSM/I and buoy. *Geoscience and Remote Sensing, IEEE Transactions on*, 40(6), 1241-1246.
22. Haas, C. (2001). The seasonal cycle of ERS scatterometer signatures over perennial Antarctic sea ice and associated surface ice properties and processes. *Annals of Glaciology*, 33(1), 69-73.
23. Matzler, C. (1998). Microwave properties of ice and snow. In *Solar System Ices* (pp. 241-257). Springer Netherlands.
24. Waite, A. H., & Schmidt, S. J. (1962). Gross errors in height indication from pulsed radar altimeters operating over thick ice or snow. *Proceedings of the IRE*, 50(6), 1515-1520.
25. Laxon, S. (1994). Sea ice altimeter processing scheme at the EODC. *International Journal of Remote Sensing*, 15(4), 915-924.
26. Zwally, H. J., Bindschadler, R. A., BRENNER, A. C., MAJOR, J. A., & Marsh, J. G. (1989). Growth of Greenland ice sheet: Measurement. *Science*, 246(4937), 1587-1589.
27. Wingham, D. J., Francis, C. R., Baker, S., Bouzinac, C., Brockley, D., Cullen, R., ... & Wallis, D. W. (2006). CryoSat: A mission to determine the fluctuations in Earth's land and marine ice fields. *Advances in Space Research*, 37(4), 841-871.

28. Zwally, H. J., Schutz, B., Abdalati, W., Abshire, J., Bentley, C., Brenner, A., ... & Thomas, R. (2002). ICESat's laser measurements of polar ice, atmosphere, ocean, and land. *Journal of Geodynamics*, 34(3), 405-445.
29. Koenig, L., Martin, S., Studinger, M., & Sonntag, J. (2010). Polar airborne observations fill gap in satellite data. *Eos, Transactions American Geophysical Union*, 91(38), 333-334.
30. Freeman, A., & Durden, S. L. (1998). A three-component scattering model for polarimetric SAR data. *Geoscience and Remote Sensing, IEEE Transactions on*, 36(3), 963-973.
31. Pottier, E., & Lee, J. S. (2000, March). Application of the «H/A/alpha» Polarimetric Decomposition Theorem for Unsupervised Classification of Fully Polarimetric SAR Data Based on the Wishart Distribution. In *SAR workshop: CEOS Committee on Earth Observation Satellites* (Vol. 450, p. 335).
32. Yamaguchi, Y., Moriyama, T., Ishido, M., & Yamada, H. (2005). Four-component scattering model for polarimetric SAR image decomposition. *Geoscience and Remote Sensing, IEEE Transactions on*, 43(8), 1699-1706.
33. Shi, J., Wang, J., Hsu, A. Y., O'Neill, P. E., & Engman, E. T. (1997). Estimation of bare surface soil moisture and surface roughness parameter using L-band SAR image data. *Geoscience and Remote Sensing, IEEE Transactions on*, 35(5), 1254-1266.
34. Srivastava, H. S., Patel, P., Manchanda, M. L., & Adiga, S. (2003). Use of multiincidence angle RADARSAT-1 SAR data to incorporate the effect of surface roughness in soil moisture estimation. *Geoscience and Remote Sensing, IEEE Transactions on*, 41(7), 1638-1640.
35. Rott, H. (1984). The analysis of backscattering properties from SAR data of

- mountain regions. *Oceanic Engineering, IEEE Journal of*, 9(5), 347-355.
36. Strozzi, T. (1996). *Backscattering measurements of snowcovers at 5.3 and 35 GHz*. Universitat Bern, Fakultat der Philosophisch-naturwissenschaftlichen.
 37. Barton, D. K. (2005). *Radar system analysis and modeling* (p. 122). Norwood, MA, USA: Artech House.
 38. Sarabandi, K., Ulaby, F. T., & Tassoudji, M. A. (1990). Calibration of polarimetric radar systems with good polarization isolation. *Geoscience and Remote Sensing, IEEE Transactions on*, 28(1), 70-75.
 39. Whitt, M. W., Ulaby, F. T., Polatin, P., & Liepa, V. V. (1991). A general polarimetric radar calibration technique. *Antennas and Propagation, IEEE Transactions on*, 39(1), 62-67.
 40. Barnes, R. M. (1986). Polarimetric calibration using in-scene reflectors. *Rep. TT-65, MIT Lincoln Lab, MA*.
 41. Sarabandi, K., Oh, Y., & Ulaby, F. T. (1992). Measurement and calibration of differential Mueller matrix of distributed targets. *Antennas and Propagation, IEEE Transactions on*, 40(12), 1524-1532.
 42. Bird, T. S. (2009). Definition and Misuse of Return Loss [Report of the Transactions Editor-in-Chief]. *Antennas and Propagation Magazine, IEEE*, 51(2), 166-167.
 43. Fung, A. K., Li, Z., & Chen, K. S. (1992). Backscattering from a randomly rough dielectric surface. *Geoscience and Remote Sensing, IEEE Transactions on*, 30(2), 356-369.
 44. Fung, A. K., & Chen, K. S. (2004). An update on the IEM surface backscattering model. *Geoscience and Remote Sensing Letters, IEEE*, 1(2), 75-77.

45. Matsuoka, T., Umehara, T., Nadai, A., Kobayashi, T., Satake, M., & Uratsuka, S. (2009, July). Calibration of the high performance airborne SAR system (Pi-SAR2). In *Geoscience and Remote Sensing Symposium, 2009 IEEE International, IGARSS 2009* (Vol. 4, pp. IV-582). IEEE.
46. Ruck, G., Barrick, D. E., Stuart, W. D., & Krichbaum, C. K. (1970). RCS handbook.
47. Ferrara, G., Mattia, F., & Posa, F. (1995, December). Backscattering study on non-orthogonal trihedral corner reflectors. In *Microwaves, Antennas and Propagation, IEE Proceedings* (Vol. 142, No. 6, pp. 441-446). IET.
48. Carsey, F. D. (1992). *Microwave remote sensing of sea ice* (Vol. 68, pp. 1-462). American Geophysical Union.
49. Vant, M. R., Ramseier, R. O., & Makios, V. (1978). The complex-dielectric constant of sea ice at frequencies in the range 0.1–40 GHz. *Journal of Applied Physics*, 49(3), 1264-1280.
50. Cox, G. F., & Weeks, W. F. (1982). *Equations for determining the gas and brine volumes in sea ice samples*. US Army Corps of Engineers, Cold Regions Research & Engineering Laboratory.
51. Cox, G. F., & Weeks, W. F. (1973). *Salinity variations in sea ice* (No. CRREL-RR-310). Cold Regions Research and Engineering Lab Hanover NH.
52. Onstott, R. G. (1992). SAR and scatterometer signatures of sea ice. *Microwave remote sensing of sea ice*, 73-104.
53. Wakabayashi, H., Matsuoka, T., Nakamura, K., & Nishio, F. (2004). Polarimetric characteristics of sea ice in the Sea of Okhotsk observed by airborne L-band SAR. *Geoscience and Remote Sensing, IEEE Transactions on*,

- 42(11), 2412-2425.
54. Nakamura, K., Wakabayashi, H., Naoki, K., Nishio, F., Moriyama, T., & Uratsuka, S. (2005). Observation of sea-ice thickness in the Sea of Okhotsk by using dual-frequency and fully polarimetric airborne SAR (Pi-SAR) data. *Geoscience and Remote Sensing, IEEE Transactions on*, 43(11), 2460-2469.
 55. Nakamura, K., Wakabayashi, H., Uto, S., Naoki, K., Nishio, F., & Uratsuka, S. (2006). Sea-ice thickness retrieval in the Sea of Okhotsk using dual-polarization SAR data. *Annals of Glaciology*, 44(1), 261-268.
 56. Tiuri, M., Sihvola, A., Nyfors, E., & Hallikaiken, M. (1984). The complex dielectric constant of snow at microwave frequencies. *Oceanic Engineering, IEEE Journal of*, 9(5), 377-382.
 57. Sweeny, B. D., & Colbeck, S. C. (1974). *Measurements of the Dielectric Properties of Wet Snow Using a Microwave Technique* (No. CRREL-RR-325). Cold Regions Research and Engineering Lab Hanover NH.
 58. Hallikainen, M., Ulaby, F., & Abdelrazik, M. (1986). Dielectric properties of snow in the 3 to 37 GHz range. *Antennas and Propagation, IEEE Transactions on*, 34(11), 1329-1340.
 59. Cumming, W. A. (1952). The dielectric properties of ice and snow at 3.2 centimeters. *Journal of Applied Physics*, 23(7), 768-773.
 60. Ulaby, F. T., Moore, R. K., & Fung, A. K. (1986). *Microwave Remote Sensing: Active and Passive*, vol. III, Volume Scattering and Emission Theory, Advanced Systems and Applications. *Inc., Dedham, Massachusetts*, 1797-1848.
 61. Isleifson, D., Langlois, A., Barber, D. G., & Shafai, L. (2009). C-band scatterometer measurements of multiyear sea ice before fall freeze-up in the

- Canadian Arctic. *Geoscience and Remote Sensing, IEEE Transactions on*, 47(6), 1651-1661.
62. Arcone, S. A., Gow, A. J., & McGrew, S. (1986). Structure and dielectric properties at 4.8 and 9.5 GHz of saline ice. *Journal of Geophysical Research: Oceans (1978–2012)*, 91(C12), 14281-14303.
63. Hallikainen, M. T., Toikka, M. V. O., & Hyypä, J. M. (1988, September). Microwave dielectric properties of low-salinity sea ice. In *Geoscience and Remote Sensing Symposium, 1988. IGARSS'88. Remote Sensing: Moving Toward the 21st Century., International (Vol. 1, pp. 419-420)*. IEEE.
64. Kim, J. W., Kim, D. J., & Hwang, B. J. (2012). Characterization of Arctic sea ice thickness using high-resolution spaceborne polarimetric SAR data. *Geoscience and Remote Sensing, IEEE Transactions on*, 50(1), 13-22.
65. Nghiem, S. V., Kwok, R., Yueh, S. H., & Drinkwater, M. R. (1995). Polarimetric signatures of sea ice: 1. Theoretical model. *Journal of Geophysical Research: Oceans (1978–2012)*, 100(C7), 13665-13679.
66. Peterson, I. K., Prinsenber, S. J., & Holladay, J. S. (2008). Observations of sea ice thickness, surface roughness and ice motion in Amundsen Gulf. *Journal of Geophysical Research*, 113(C6), C06016.
67. Toyota, T., Ukita, J., Ohshima, K., Wakatsuchi, M., & Muramoto, K. (1990). A measurement of sea ice albedo over the southwestern Okhotsk Sea. *Journal of the Meteorological Society of Japan. Ser. II*, 77(1), 117-133.
68. Toyota, T., Nakamura, K., Uto, S., Ohshima, K. I., & Ebuchi, N. (2009). Retrieval of sea ice thickness distribution in the seasonal ice zone from airborne L-band SAR. *International Journal of Remote Sensing*, 30(12), 3171-3189.

69. Gupta, M., Barber, D. G., Scharien, R. K., & Isleifson, D. (2012). Detection and classification of surface roughness in an Arctic marginal sea ice zone. *Hydrological Processes*.
70. Kim, Y. S., Moore, R. K., Onstott, R. G., & Gogineni, S. (1985). Towards identification of optimum radar parameters for sea ice monitoring. *Journal of Glaciology*, 31(109), 214-219.
71. Kasilingam, D., Schuler, D., & Lee, J. S. (2001). The depolarization of radar backscatter from rough surfaces due to surface roughness and slopes. In *Geoscience and Remote Sensing Symposium, 2001. IGARSS'01. IEEE 2001 International* (Vol. 2, pp. 925-927). IEEE.
72. Shi, J., Dozier, J., & Rott, H. (1994). Snow mapping in alpine regions with synthetic aperture radar. *Geoscience and Remote Sensing, IEEE Transactions on*, 32(1), 152-158.
73. Li, Z., & Guo, H. (2000). Permafrost mapping in the Tibet plateau using polarimetric SAR. In *Geoscience and Remote Sensing Symposium, 2000. Proceedings. IGARSS 2000. IEEE 2000 International* (Vol. 5, pp. 2024-2026). IEEE.
74. Isleifson, D., Hwang, B., Barber, D. G., Scharien, R. K., & Shafai, L. (2010). C-band polarimetric backscattering signatures of newly formed sea ice during fall freeze-up. *Geoscience and Remote Sensing, IEEE Transactions on*, 48(8), 3256-3267.
75. Onstott, R. G., Moore, R. K., & Weeks, W. F. (1979). Surface-based scatterometer results of Arctic sea ice. *Geoscience Electronics, IEEE Transactions on*, 17(3), 78-85.
76. Hajnsek, I., Pottier, E., & Cloude, S. R. (2003). Inversion of surface parameters

- from polarimetric SAR. *Geoscience and Remote Sensing, IEEE Transactions on*, 41(4), 727-744.
77. Fung, A. K., & Eom, H. J. (1982). Application of a combined rough surface and volume scattering theory to sea ice and snow backscatter. *Geoscience and Remote Sensing, IEEE Transactions on*, (4), 528-536.
78. Winebrenner, D. P., Tsang, L., Wen, B., & West, R. (1989). Sea-ice characterization measurements needed for testing of microwave remote sensing models. *Oceanic Engineering, IEEE Journal of*, 14(2), 149-158.
79. West, R., Tsang, L., & Winebrenner, D. P. (1993). Dense medium radiative transfer theory for two scattering layers with a Rayleigh distribution of particle sizes. *Geoscience and Remote Sensing, IEEE Transactions on*, 31(2), 426-437.
80. Jin, Y. Q. (1993). *Electromagnetic scattering modelling for quantitative remote sensing*. World Scientific.
81. Ewe, H. T., Chuah, H. T., & Fung, A. K. (1998). A backscatter model for a dense discrete medium: Analysis and numerical results. *Remote Sensing of Environment*, 65(2), 195-203.

Abstract (in Korean)

본 논문은 고해상도 다중편파 레이더 시스템의 측정자료로부터 북·남극에 존재하는 해빙두께를 효율적으로 추출할 수 있는 방법에 대한 것이다. 이를 위해, 지상기반 다중편파 산란계 시스템과 다양한 전자기파 산란 모델을 이용하여 해빙의 생성·소멸 시기에 따라 유전율과 표면 거칠기와 같은 물리적 특성에 따라 전자기파의 산란특징이 어떻게 변하는지를 이해하고자 하였다. 이를 위하여, 전자기파의 산란구조를 해빙 표면 위에 적설된 눈의 표층산란, 눈의 체적산란, 눈과 해빙의 경계면에서 발생하는 산란, 해빙의 체적산란으로 나누어 살펴 보았다.

지상기반 다중편파 산란계 시스템의 측정실험을 통하여 해빙 소멸시기에 해빙표면 위에 적설된 눈은 높은 대기온도로 인하여 눈 표면이 녹아 유전율이 높아지기 때문에 산란계로부터 송신된 대부분의 전자기파 신호가 눈 표면에서 산란 (표층산란)되어 수신되는 특징을 보였다. 반면에, 해빙 생성시기에는 대기온도가 항상 영하로 유지되면서 눈 표면의 유전율이 낮아져 전자기파 신호가 눈 표면을 투과하여 눈의 체적 내부 또는 눈과 해빙 표면의 경계면에서 산란되어 수신될 수 있는 가능성을 보였다. 더욱이, 전자기파의 입사각이 작으면 HH와 VV 편파의 전자기파는 눈의 체적 내부에서 체적산란이 우세하게 발생하였고 HV와 VH 편파의 전자기파는 눈과 해빙의 경계면에서 우세하게 산란될 수 있는 가능성을 보였다. 반면에 입사각이 상대적으로 커지면 모든 편파의 전자기파가 눈과 해빙의 경계면에서 우세하게 산란될 수 있는 가능성을 보였다.

다음으로, 다양한 현장조사 자료를 통하여 해빙 생성시기가 길어질수록 해빙의 담수화 현상으로 인하여 해빙두께에 따라 해빙 표면의 유전율이 감소하고 전자기파의 투과 깊이가 증가할 수 있는 가능성을 확인 하였다. 이에 더하여, 해빙 생성시기가 길어질수록 해빙 표면 용해수의 재결빙과 유빙들의 충돌 현상으로 인해 해빙두께에 따라 표면 거칠기가 상대적으로 증가할 수 있는 가능성을 확인 하였다. 따라서, 해빙의 두께가 두꺼워질수록 해빙의 표면에서는 거친 표면으로 인하여 다중표층산란이 증가하고 해빙 체적 내부의 체적산란 또한 증가한다는 것을 다양한 전자기파 산란 모델의 수치해석 결과를 통하여 확인 하였다. 이러한 결과를 바탕으로 전자기파 산란 모델을 이용하여 해빙 두께에 따라 다중표층산란과 체적산란이 증가하고 이는 송·수신된 전자기파의 편파 손실정도 (참고, 편파손실 정도는 VH/VV 또는 HV/HH와 같은 편파비로 계산된다.)와 선형관계가 있다는 것을 확인하였다. 그리고 북극해에서 실측된 해빙 두께 정보와 동시간대에 관측된 TerraSAR-X와 RADARSAT-2 SAR 자료로부터 추출된 VH/VV와 HV/HH 편파비가 매우 높은 상관관계가 있다는 것을 추가적으로 확인 하였다. 이러한 결과를 통하여, 다중편파 레이다 시스템에서 관측된 편파 손실정도가 해빙두께를 추출하기 위한 매우 유용한 정보가 될 수 있다는 사실을 확인 하였다.

주요어: 해빙두께, 눈, 다중편파 레이다 시스템, 표층산란, 체적산란, 편파 손실 효과

학번: 2008-30820